Ultrasound imaging of the ultrasound thrombolysis

Paul Boulos

N°d'ordre NNT : 2017LYSE1251

THESE de DOCTORAT DE L'UNIVERSITE DE LYON
opérée au sein de
l'Université Claude Bernard Lyon 1

Ecole Doctorale 162
Mécanique, Energétique, Génie civil, Acoustique

Spécialité de doctorat : GENIE BIOMEDICAL
Discipline : Imagerie ultrasonore

Soutenue publiquement le 30/11/2017, par :
Paul BOULOS

Ultrasound imaging of the ultrasound thrombolysis

Devant le jury composé de :

Aubry, Jean-François	DR CNRS, Langevin, Paris	Rapporteur
Franceschini, Emilie	CR CNRS, LMA, Marseille	Rapporteure
Albouy-Kissi, Adélaïde	MC, FabLab, Puy-en-Velay	Examinatrice
Bridal, Lori	DR CNRS, LIB, Paris	Examinatrice
Tortoli, Piero	Professeur, MSDlab, Florence	Examinateur
Varray, François	MC, CREATIS, Lyon	Examinateur
Cachard, Christian	Professeur, CREATIS, Lyon	Directeur de thèse
Bera, Jean-Christophe	Professeur, LabTAU, Lyon	Co- Directeur de thèse
Gilles, Bruno	MC, LabTAU, Lyon	Invité

UNIVERSITE CLAUDE BERNARD - LYON 1

Président de l'Université	**M. le Professeur Frédéric FLEURY**
Président du Conseil Académique	M. le Professeur Hamda BEN HADID
Vice-président du Conseil d'Administration	M. le Professeur Didier REVEL
Vice-président du Conseil Formation et Vie Universitaire	M. le Professeur Philippe CHEVALIER
Vice-président de la Commission Recherche	M. Fabrice VALLÉE
Directrice Générale des Services	Mme Dominique MARCHAND

COMPOSANTES SANTE

Faculté de Médecine Lyon Est – Claude Bernard	Directeur : M. le Professeur G.RODE
Faculté de Médecine et de Maïeutique Lyon Sud – Charles Mérieux	Directeur : Mme la Professeure C. BURILLON
Faculté d'Odontologie	Directeur : M. le Professeur D. BOURGEOIS
Institut des Sciences Pharmaceutiques et Biologiques	Directeur : Mme la Professeure C. VINCIGUERRA
Institut des Sciences et Techniques de la Réadaptation	Directeur : M. X. PERROT
Département de formation et Centre de Recherche en Biologie Humaine	Directeur : Mme la Professeure A-M. SCHOTT

COMPOSANTES ET DEPARTEMENTS DE SCIENCES ET TECHNOLOGIE

Faculté des Sciences et Technologies	Directeur : M. F. DE MARCHI
Département Biologie	Directeur : M. le Professeur F. THEVENARD
Département Chimie Biochimie	Directeur : Mme C. FELIX
Département GEP	Directeur : M. Hassan HAMMOURI
Département Informatique	Directeur : M. le Professeur S. AKKOUCHE
Département Mathématiques	Directeur : M. le Professeur G. TOMANOV
Département Mécanique	Directeur : M. le Professeur H. BEN HADID
Département Physique	Directeur : M. le Professeur J-C PLENET
UFR Sciences et Techniques des Activités Physiques et Sportives	Directeur : M. Y.VANPOULLE
Observatoire des Sciences de l'Univers de Lyon	Directeur : M. B. GUIDERDONI
Polytech Lyon	Directeur : M. le Professeur E.PERRIN
Ecole Supérieure de Chimie Physique Electronique	Directeur : M. G. PIGNAULT
Institut Universitaire de Technologie de Lyon 1	Directeur : M. le Professeur C. VITON
Ecole Supérieure du Professorat et de l'Education	Directeur : M. le Professeur A. MOUGNIOTTE
Institut de Science Financière et d'Assurances	Directeur : M. N. LEBOISNE

N.B : Un résumé étendu en Français du mémoire de thèse est pourvu à la page 93 de ce manuscrit.

N.B : Un résumé étendu en Français du mémoire de thèse est pourvu à la page 93 de ce manuscrit.

INTRODUCTION

Ultrasound (US) is often adopted for medical diagnostic imaging because of its known advantages as noninvasive, ease of use, real time display, and limited cost. Innovative ultrasound therapy techniques emerged recently with the discovery of high intensity focused ultrasound (HIFU) technology which could induce mechanical or thermal damage caused by acoustic cavitation mechanisms. It has the main advantage of being able to externally treat deep organs without altering the tissues between the transducer and its focal spot. Such therapeutic modalities have already clinical applications as for example the treatment of prostate cancers and the destruction of kidney stones. On the other hand, cardiovascular diseases as thrombosis, corresponding to blood clots obstructing vessels, are currently treated with thrombolysis techniques as: drug treatment (anticoagulants or thrombolytic agents) and surgeries (balloon angioplasty, thrombectomy, or bypass). Yet these techniques have high risk of failure caused most of the time by bleeding issues. Therefore, a novel low-invasive therapeutic technique is being investigated: extracorporeal ultrasound thrombolysis by exploiting the mechanical damage to destroy the thrombus. Moreover, in order to control the cavitation power activity a prototype has been recently designed and improved with a real-time feedback loop. Yet, this therapeutic technique still needs a monitoring system which would be essential to ensure the perfect and entire destruction of thrombus without damaging vessels. It should be able to first image and localize the thrombus and second follow and quantify the cavitation activities in both spatial and temporal dimensions. Thus, this work focuses on the development and assessment of an advanced ultrasound monitoring system integrated to the ultrasound thrombolysis treatment: ultrasound imaging of the ultrasound thrombolysis.

This PhD thesis is divided in four Chapters. Chapter I includes an overview of the thrombosis pathology, its actual treatment, ultrasound background, and the regulated ultrasound-induced cavitation generator system. Chapter II deals with the development of the ultrasound imaging system with especially passive imaging techniques corresponding to different beamforming algorithms. They are investigated using validation protocols as simulation on a point source and experiment on a wire. Chapter III introduces the cavitation experiments achieved in water tank situation with different protocols as one-spot, multi-spots, or non-regulated versus regulated cavitation experiments. Moreover, *in vivo* testing on an animal model of acute limb ischemia using specifically an ovine model of arterial thrombosis is investigated. Finally, the Chapter IV carries on with some enhanced imaging system optimizations as a 3D implementation, improved probe characteristics, a frequency domain analysis, and finally a real-time hybrid monitoring mode combining both active anatomical images and passive cavitation maps.

Chapter I: Introduction

I.1Thrombolysis

I.1.1 Thrombosis

Thrombosis is the formation of a blood clot, also called thrombus. It is the result of the aggregation of different components as platelets, red blood cells, and fibrin. It is formed in vessels mostly during hemostasis process corresponding to a healthy response to an injured vessel. When the endothelium surface is damaged, the platelets interact with the revealed sub-endothelium surface, forming a thrombus to stop the bleeding. Then after the injury, fibrinolysis natural process takes place to chemically disintegrate the blood clot [1], [2]. Most of the time, the thrombus is locally constrained in the injured vessel and do not cause major ischemia risks. However thrombosis could pathologically emerge in a healthy vessel, caused by three inter-dependent risk factors known as Virchow's triad which includes endothelium lesion (hemostasis), blood flow anomaly (stasis), and hypercoagulability (genetic deficiencies) [3], [4]. Sometimes, the thrombus can even breaks free and wanders in the blood circulation, it is known as an embolus, which could then obstructs healthy vessels. This pathology is called thromboembolism [5]. There are two types of thrombosis depending on where it occurs: venous or arterial thrombosis [6], [7].

For venous thromboses, the most severe fallout is the pulmonary thromboembolism caused by the obstruction of the arterial pulmonary system by a thrombus detached upstream [8]. For arterial thromboses, the severity is more important and can result either in an acute myocardial infarction [9] or a brain ischemia [10] corresponding to the blockage respectively of the coronary artery supplying the cardiac muscle and the carotid artery supplying the brain. Less but still high risks could be noticed for acute limb ischemia corresponding to the blockage of blood supply to a limb [11]. If not quickly treated, it could result in permanent disability, amputation or even death of the patient.

I.1.2 Clinical treatment

These pathologies need quick adapted treatments, called thrombolysis techniques, which disaggregate chemically or mechanically the blood clot obstructing partially or totally the vessel. Depending on the location, the gravity, the composition, and the age of the thrombus different techniques can be used as drug treatments or invasive surgery.

I.1.2.1 Drug treatment

The drug treatments, allowing the chemical disaggregation of the thrombus, can be classified in two general types: anticoagulants or thrombolytic agents.

Anticoagulants, also called "blood thinners", as heparins, direct thrombin inhibitor, factor Xa inhibitors and vitamins K antagonist (VKA) suppress the coagulation cascade mechanisms during hemostasis process by mainly inhibiting the thrombin generation step [12]–[14]. It is mostly used for minor thromboses (as venous thromboembolism) and for stroke prevention [15].

Plasminogen, produced in the liver, is the inactive form of the plasmin enzyme. Plasminogen has an affinity for fibrin and so is incorporated to the clot when it is formed. Thrombolytic agents as urokinase, streptokinase (SK), and tissue activator plasminogen (tPA) induce the fibrinolysis mechanism by converting plasminogen into plasmin which then promotes the cleavage operation of the fibrin and so dismantle the thrombus [16]–[18]. As these agents fracture only fibrin, they are specifically useful for just one type of blood clot and so pretty useless for the other (as example clots essentially composed of platelets) [19]. Also, these drug treatments do not target locally the pathological vessel and therefore bleeding problems have been observed [20]–[22].

I.1.2.2 Surgical procedure

More direct and invasive techniques could be considered with the use of surgery allowing the total ablation of any type of thrombosis. It is commonly used for more violent and severe pathologies which could not be fully treated with drugs. There are three surgery techniques used in clinic: angioplasty, thrombectomy, or bypass.

Angioplasty, or commonly called balloon angioplasty, is an endovascular procedure consisting in the insertion of a deflated balloon catheter up to the stenosed area of the vessel [23]. The balloon is then inflated, forcing mechanically the expansion of the lumen. Finally the balloon is deflated and withdrawn. To prevent relapse or collapse of the treated vessel, a metal or plastic tube (stent) is frequently added to the balloon catheter keeping permanently the lumen wide open [24]. Research and development are being conducted on the mechanical properties as well as on the biocompatibility aspect of the stent [25], [26]. This technique is exclusively used for atherosclerosis pathology (formation of plaques on the artery walls).

Thrombectomy technique is considered for more advanced thrombosis and especially planned for medical emergency [27]. It consists in the fragmentation and removal of the thrombus by the use of diverse catheter devices. They cover a large panel of design based on mechanical, hydraulic, suction, pressure, or laser mechanisms [28].

Vascular bypass surgery redirects the blood flow around the thrombus by sewing a graft on both edges of the ischemic area. The more preferred graft is patient's own vein (autograft) which for example could be the great saphenous vein during coronary artery bypass surgery restoring myocardial blood supply [29]. Nevertheless artificial grafts are also used as Teflon or Dacron material [30], [31]. Compared with the previous thrombolysis techniques, the bypass is the most invasive and risky one. This is why it is restricted to very severe pathology with extremely high damaged vessel.

The combination of drug treatments with surgery was also considered. Thanks to a catheter the drugs are directly delivered on the thrombus site to prevent global bleeding problems in other part of the body [32]. It also decreases the time of disaggregation of the thrombus and improves its efficiency. Moreover, the choice of the best thrombolysis treatment depends entirely on the personal preference of the cardiologist. Due to the non-exhaustive disadvantages of the actual clinical thrombolysis techniques (bleeding, complications, high risk, great cost, and time consuming), many studies and developments are recently emerging around innovative lower invasive approaches. Overcoming these limitations, the use of high intensity focalized ultrasound to induce or increase the destruction of the thrombus is greatly explored which are presented afterwards in section I.3. The

next section outlines ultrasound field and its benefits for ultrasonography and therapy on which this project is based.

I.2 Ultrasound

I.2.1 Basics

I.2.1.1 Physical principles

In physics, a wave is the oscillation of a physical quantity combined with energy transfer propagating through a medium. Two oscillation direction types exist: transverse or longitudinal corresponding respectively to oscillations perpendicular or oscillations parallel to the wave propagation (Figure I-1).

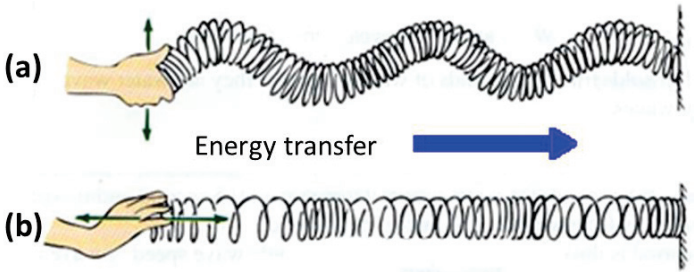

Figure I-1: (a) Transverse wave with oscillations perpendicular to the energy transfer propagation. (b) Longitudinal wave with oscillations parallel to the energy transfer propagation [33].

There are two main types of waves: electromagnetic or mechanical waves. The electromagnetic wave, propagating only as a transverse wave, consists of oscillations of electric and magnetic fields which both are synchronized, in phase, and perpendicular to each other. It does not require a medium to travel and so can propagate in vacuum (for example, the light). On the contrary, the mechanical wave requires a medium to propagate through and consists of oscillations of matter around an initial equilibrium position meaning that it transports energy and not matter (adiabatic process). The transmission medium should have elasticity properties to be able to locally be deformed by the disturbance and then get back to its original shape. For longitudinal waves, the medium resistance to compressibility is defined by the isentropic coefficient of compressibility χ_S or the isentropic bulk modulus κ_S, which both are connected by the following relations:

$$\chi_S = -\frac{1}{V}\left(\frac{\partial V}{\partial P}\right)_S, \qquad \kappa_S = 1/\chi_S \tag{I.1}$$

with V the volume, P the pressure, and S the entropy. For transverse waves, the medium stiffness is defined by the shear modulus G. Mechanical waves could be both transverse or/and longitudinal waves. Its propagation relies on the wave equation represented by a second-order linear differential equation namely d'Alembert's formula:

$$\Delta g(\boldsymbol{r},t) = \frac{\partial^2 g(\boldsymbol{r},t)}{{c_0}^2 \partial t^2} \tag{I.2}$$

with Δ the Laplace operator, and g a scalar or vector quantity at position $\boldsymbol{r}$ and time t. c_0 is the wave propagation speed which is equal for longitudinal wave to $\left(K_S/\rho\right)^{1/2}$ and for transverse wave to $\left(G/\rho\right)^{1/2}$ with ρ the medium density. This wave propagation equation (I.2) represents a space-time conservation equation meaning that any variation in time is compensated by a variation in space neglecting thereby any diffusion and anisotropic effect. Moreover, as this relation is linear, a wave is not deformed along its propagation. This is the simplest model of the wave propagation. More complex and ultrasound propagation mechanisms are outlined in section I.2.2.4

A particular mechanical wave, commonly called acoustic wave, is defined as the oscillations in pressure, stress, particle displacement, and particle velocity traveling through a transmission medium. In this case, the scalar quantity g in the wave equation (I.2) is replaced by the pressure variation p (compression or rarefaction) or the particle displacement u. Human audible sound corresponds to acoustic waves with frequencies between 20 Hz and 20 kHz. Sounds with frequencies lower than 20 Hz are called infrasound and with frequencies higher than 20 kHz are called ultrasound.

I.2.1.2 Pioneer discoveries

Ultrasound was discovered and recognized for the first time by Lazzaro Spallanzani in 1794 with echolocation used by bats to hunt and navigate. During the 19th century, minor observations and discoveries were made regarding ultrasound. The direct piezoelectric effect of a material was discovered in 1880 by both brothers Jacques and Pierre Curie. It corresponds to the internal generation of an electrical charge resulting from an applied mechanical force (pressure). It was then demonstrated that this effect is a reversible process meaning that a material manifesting the direct piezoelectric effect (creation of electricity when a force is applied) can also manifest the converse piezoelectric effect (creation of a force when an electric field is applied). Thanks to this discovery, piezoelectric sensors were developed which could be used as ultrasound transceiver (transmitter plus receiver). It is after the Titanic disaster of 1912 that navigation underwater ultrasound devices emerged as example with an iceberg detection system designed by Reginald Fessenden in 1915. During the First World War, in 1917, Paul Langevin and Constantin Chilowski developed the first technological application of ultrasound used for the detection of submarine which is now called SONAR (SOund Navigation And Ranging).

I.2.2 Ultrasonography

Nowadays, ultrasound has applications in many different fields mostly used to detect, localize and analyze object structures. Thanks to its inexpansive, portable, non-ionizing and non-invasive properties, ultrasound imaging or namely ultrasonography is highly used for diagnostic in medicine. In the following, a general overview of ultrasound imaging is given with three main steps: acquisition of radio-frequency (RF) signal, image formation (beamforming), and the US images visualization (display). Finally, an additional overview of diverse US mechanisms which could occur during propagation of the US wave in the tissue is also presented.

I.2.2.1 RF signal acquisition

The first step for classical ultrasound imaging (pulse-echo) is the acquisition of the RF signal corresponding to US backscattered echoes. This step includes first, the emission of an US pulse second, its propagation in the medium combining different wave mechanisms (as reflection or scattering) and finally, the reception of the US echoes. Thanks to the reversible piezoelectric effects, the transmission (converse piezoelectric effect) and reception (direct piezoelectric effect) of an US pulse is supported by a transceiver (commonly called US transducer). The US transducer is held against the area of interest and an US beam is sent into the body. The ultrasound propagates through the tissue and interacts with heterogeneities as different tissue types, muscle, cysts, tumors, fat, air, bone, etc. Each one of them is characterized by a specific acoustic impedance $Z = (\rho K_S)^{1/2} = \rho c$. It is defined as the cause/effect ratio between the pressure variation p and the particle velocity v. When the US wave, with amplitude p_i, reaches an interface between two medium M_1 and M_2 with corresponding acoustic impedance Z_1 and Z_2, the wave is partially reflected and transmitted with respective amplitudes p_r and p_t. The wave's amplitude depends on the pressure reflection $R = \frac{p_r}{p_i}$ and transmission $T = \frac{p_t}{p_i}$ coefficients defined as follows:

$$R = \frac{Z_2 - Z_1}{Z_2 + Z_1}, \qquad T = \frac{2Z_2}{Z_2 + Z_1} \tag{I.3}$$

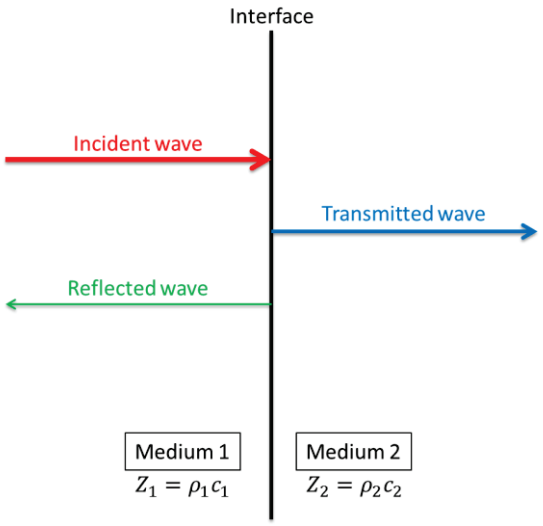

Figure I-2: Reflection and transmission wave mechanisms.

Scattering mechanism occurs when a small heterogeneity (smaller than the wavelength of the US wave) is considered. The US pulse is hence scattered in all directions. Finally, the reflected and backscattered waves (echoes) propagate back to the same transducer where they are detected and recorded as a RF signal.

I.2.2.2 Beamforming

Now that the RF signals, including the echoes, are acquired they need to be processed to extract the necessary data (distance and amplitude). As seen before in (I.2), the US propagates through a

medium with a constant speed of sound c (in soft tissue c=1540 m/s). Therefore as $c = \frac{distance}{time}$, the round-trip distance $d_{\rightleftharpoons}$ travelled by the US can be recovered using the total time-of-flight (tof) : $d_{\rightleftharpoons} = tof.c$. Thus finally the depth position of the heterogeneity accounted for its corresponding US backscattered echo is $d_{\rightharpoonup} = {}^{d_{\rightleftharpoons}}/_{2}$.

For higher quality images and two dimensions access, a stack of US transducers (called array or probe) is required. A beamforming reconstruction algorithm, called the delay and sum (DAS), is applied. It consists in coherently summing the RF signals, by first applying appropriate delays τ_i and then adding the delayed signals together to form finally the post-beamformed signal (Figure I-3.a). It enables focalization in reception. The beamforming process can also be applied in transmission for US beam focusing or/and steering achieved with electronic phased array technology. The beam-steering is very useful in cardiac imaging to bypass the ribs issue.

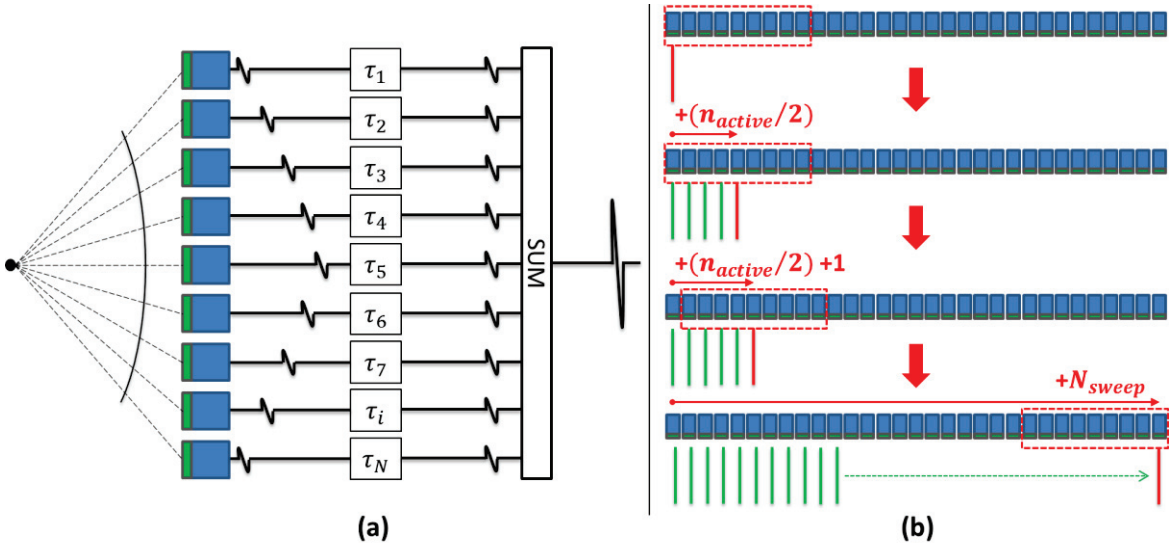

Figure I-3: (a) Delay and sum (DAS) beamforming method allowing focalization in reception. (b) Electronic sweep of the active elements (n_{active}) on the entire imaging array. The vertical lines correspond to the post-beamformed lines.

In classic ultrasonography scanners, it is common to use a portion of the probe with n_{active} elements and then sweep it on the entire probe by shifting it element by element. For each sweep, the focalization in reception (DAS beamforming algorithm) is applied to generate one post-beamformed line. This operation is repeated on the entire probe and the final image is computed by adding successively the entire N_{sweep} post-beamformed lines (Figure I-3.b). On the extremities of the array, for the first and last $n_{active}/2$ sweeps, no shift of the active elements is executed but instead the post-beamformed line is steered on the right sweep.

I.2.2.3 Display

The classical display of ultrasound images is called brightness mode (B-mode) and correspond to echogram images in grayscale (Figure I-4.a). The white areas correspond to hyperechoic structures (higher amplitude echoes) and on the opposite the black areas correspond to hypoechoic structures (lower amplitude echoes). The B-mode image is computed by using envelope detection on the post-beamformed signals. It could be achieved either by demodulating the signal around a lower frequency (low pass filter) to suppress the high-frequency carrier, or by applying the absolute value

of the Hilbert transform. For better visualization, a logarithm compression is applied to increase the dynamic range of the B-mode image and to highlight the different regions (Figure I-4.b).

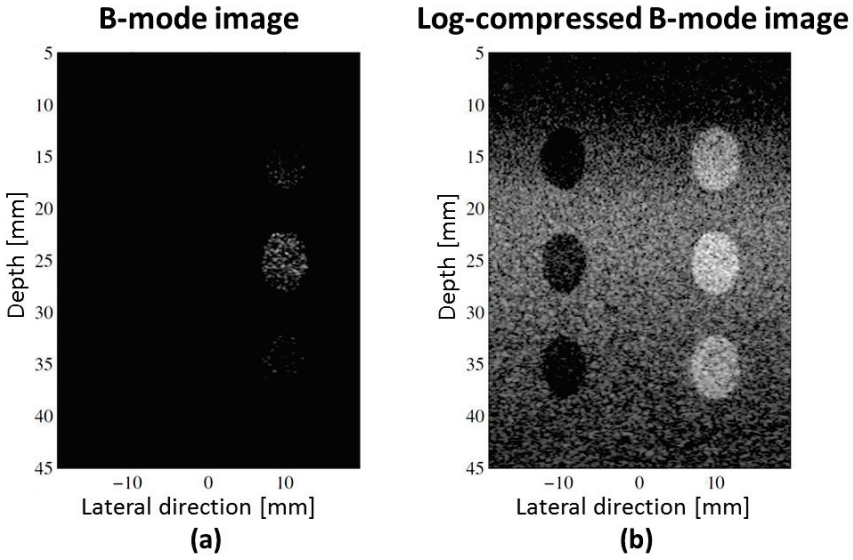

Figure I-4: An example of the classic different ultrasound images illustrating a cyst phantom with different echogenicity proprieties. (a) The B-mode image and (b) the log-compressed B-mode image with a dynamic range of 50 dB [34].

I.2.2.4 Ultrasound propagation mechanism overview

In ultrasonography for medicine, the human body transmission medium (soft tissue) is considered, for mathematical simplicity modeling, as a fluid instead of an elastic solid (or soft solid), meaning that the transverse wave (also called shear wave) is neglected relative to the longitudinal wave (also called compressional wave). The main reasons why it could be neglected are multiple. First, the generation of shear wave using US transducers is not efficient second, shear waves are strongly absorbed by soft tissue and third, they travel slower than the compressional waves (1m/s versus 1540m/s). However, for application as elastography (study of tissue stiffness), the use of shear wave is relevant and is no more neglected.

In term with the previous physical mechanism reflection on interfaces in section I.2.2.1, a coupling gel is *a priori* deposited between the patient's skin and the probe to avoid the skin-air-probe interface and so to increase the transmission of the US into the body. Furthermore, in this case, the wave was normally incident on the interface representing a simple case compared to an oblique incidence yielding the refraction mechanism described by Snell-Descartes law (Figure I-5). The incident angle θ_i is this time considered and influences both reflected and transmitted waves.

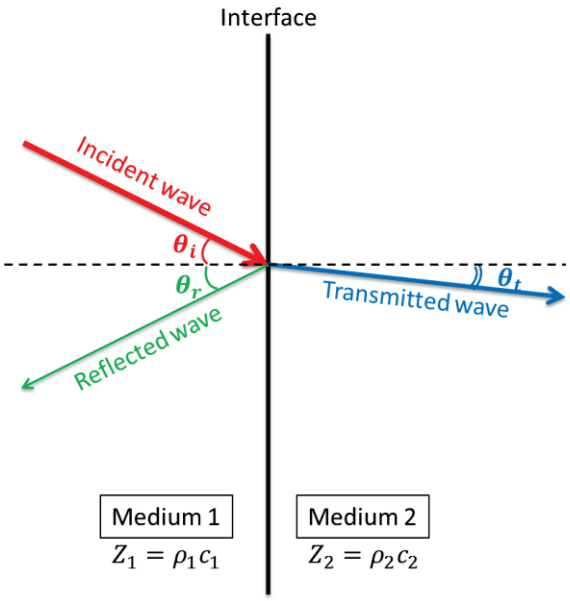

Figure I-5: Snell-Descartes law defining the reflection and refraction mechanism for an oblique incident wave.

The incident angle θ_i equals the reflected angle θ_r and is related to the transmitted angle θ_t by the following relation:

$$\frac{\sin\theta_i}{c_1} = \frac{\sin\theta_t}{c_2} \tag{I.4}$$

The reflection and transmission coefficients are therefore defined as:

$$R = \frac{Z_2\cos\theta_i - Z_1\cos\theta_t}{Z_2\cos\theta_i + Z_1\cos\theta_t}, \qquad T = \frac{2Z_2\cos\theta_i}{Z_2\cos\theta_i + Z_1\cos\theta_t} \tag{I.5}$$

This refraction mechanism enhances the ultrasound pulse amplitude attenuation corresponding to the sum of the energy losses due to ultrasound physical phenomena as reflection, scattering, diffraction, spherical spreading, diffusion, and tissue absorption. Still ultrasonography is operator dependent, have depth limitation because of attenuation mechanisms, is limited to some organs (not possible in lungs and difficult to penetrate through the skull), and could yield some artefacts.

I.2.3 Ultrasound therapy

High intensity ultrasound can be harmful and even damage tissue. It was first observed with the submarine detection device in World War I (Langevin and Chilowski developments) during which the use of very high ultrasound intensity induced the death of many fish. Therefore, if ultrasound can kill fish it could be used for therapeutic purposes as the destruction of tumors. This led to researches and developments of innovative therapeutic ultrasound devices. The first ultrasound therapy application was achieved in the 1940th using focused transducers to enhance the ultrasound intensity at the focus. This application is now called high intensity focalized ultrasound (HIFU) and is used to locally increase the temperature in a tissue and thus thermally destroy it [35], [36]. At the end of the 20th century, with technological breakthrough in fields as electronics and informatics, many ultrasound therapy applications emerged relying on thermal, mechanical, or/and chemical

mechanisms. When US propagates in the tissue, an absorption process occurs corresponding to the conversion of the acoustic energy into thermal energy caused by the vibration and friction of mater. It is already considered in ultrasonography partially contributing to the attenuation in depth of the US (with lower amplitude compared to therapeutic applications). Significant mechanical stresses could also be observed as the generation of shock waves, violent microstreaming, and micro-flows [37]–[41]. The chemical mechanism corresponds mainly to the generation of free radicals (OH* and H*) due to the local increase of acoustic energy [42]. The free radicals are highly reactive and play an important role in a number of biological processes resulting most of the time in cell damage (sonochemistry) [43]. However the main phenomenon taking part in ultrasound therapy and in charge of most of these destructive mechanisms is the acoustic cavitation.

I.2.3.1 Ultrasound cavitation

Cavitation phenomenon is the nucleation of bubbles (nuclei) induced in a liquid exposed to a high rarefaction pressure causing a significant quick decrease of the local pressure at constant temperature (green vertical arrow in Figure I-6). Therefore cavitation arises when the pressure is lower than the equilibrium vapor pressure. It is thermodynamically very similar to the boiling phenomenon where on the contrary the rapid increase in temperature at a constant pressure induces bubbles (red horizontal arrow in Figure I-6). This rarefaction pressure could be generated either by ultrasound waves (ultrasound cavitation) or by a very fast flowing liquid observed for example on propeller's blade (hydrodynamic cavitation) [44]. In the following work, only the ultrasound cavitation phenomenon is investigated.

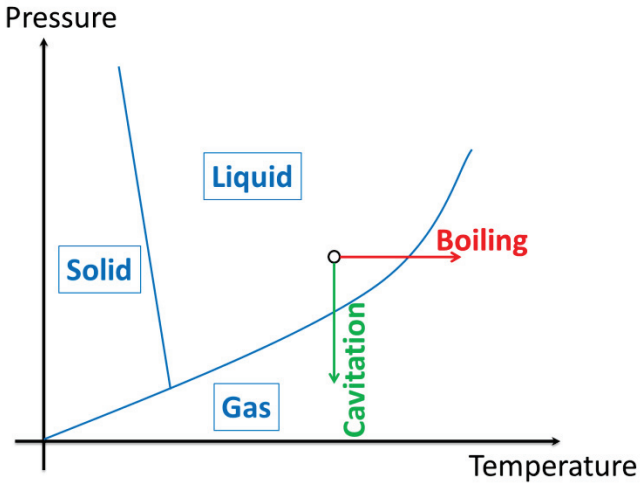

Figure I-6: Pressure-temperature diagram for water.

When bubbles are subject to an ultrasound field, their radius varies inversely proportional to the pressure (radial oscillation): rarefaction pressures ($p<0$) promote gas penetration in the bubble which will expand and on the contrary compression pressures ($p>0$) promote gas withdrawing from the bubble which will shrink. The quantity of gas diffused from one phase to the other is proportional to the surface area of the bubble (exchange surface). Because of the difference in this exchange surface between expansion and compression bubble cycles, there will be in average a net gas flow into the bubble. So the bubble's radius tends to increase. This theory is called rectified diffusion of mass and allows the bubble to reach their resonant radius [45].

The nucleation, when there is no prior presence of additional phases in the liquid, is called homogeneous nucleation. However in practice the heterogeneous nucleation is more likely to be detected. It consists in the presence in the liquid of impurities connected to small pockets of gas. Because of the oscillating pressure field, these gas pockets will then be released in the liquid and will grow larger in radius (rectified diffusion) to become nuclei [46]. Therefore, the cavitation bubbles could enclose either vapor of the medium or gas a priory dissolved in the medium. Both cases could also simultaneously co-exist.

Once the nucleation initiated, the cavitation could evolve, depending on the pressure amplitude of the ultrasound field, in different regimes [47], [48]. For low amplitudes, the bubble radial oscillation is stable and is described as a linear oscillation [49]. For higher amplitudes, the bubble still stably oscillates thought it tends to behave more as a non-linear oscillator including harmonics response and even sub-harmonics [50]. These two regimes representing a stable radial oscillation of the bubble is called the non-inertial cavitation regime [51]. In this case the absorption by the tissue is enhanced caused by the diffusion of the acoustic energy at different harmonic frequencies. Hence, the thermal mechanism is amplified. For even higher amplitudes, the bubble becomes highly unstable. It grows quickly and chaotically to size up to a dozen times its initial radius, causing its violent collapse followed by many rebounds [52], [53] . This collapse causes many mechanical (shock waves), thermal (local temperature up to 5000 K), and chemical (free radicals) fallouts. This regime is called the inertial cavitation regime and is acoustically defined by a broadband aspect related to the quick temporal condition of the collapse [54], [55]. These different regimes could co-exist in the same bubble cloud. Moreover in this work, the cavitation appellation is used for the nucleation, the radial oscillation, and the collapse of bubbles.

Thereby the cavitation phenomenon depends on a high number of parameters as the ultrasound field (amplitude, shape, and frequency), the medium (acoustic impedance, temperature, impurities and dissolved gas concentration). It is a complex phenomenon and with the actual knowledge it is considered as a random behavior [56].

I.2.3.2 Therapeutic applications

Ultrasound is increasingly used in the therapy field because of its obvious advantages in enabling low-invasive and inexpensive treatments.

In clinic, ultrasound is already used for therapeutic outcomes: physiotherapy, hyperthermia, and lithotripsy [57]. Physiotherapy uses thermal ultrasound effects (up to 40°C) to heat tissue and muscles for analgesic and anti-inflammatory treatments. However its effectiveness remains questionable [58]. With higher temperature (between 40°C and 60°C) and few minutes of exposure times (up to 30 minutes), hyperthermia is induced and consists in the thermal necrosis of tissue. It is mostly used for cancer treatments in combination with radiotherapy and chemotherapy. It sensitizes tumors to radiation and anti-cancers drugs, making those treatments more effective [59]. However it is difficult to maintain a uniform temperature in tumors during the entire exposure time due to blood perfusion effects. Therefore, even higher temperature rise (>60°C) and shorter exposure time (few seconds) are used with ablathermia techniques consisting mostly in tumor ablation with for example pathologies as prostate, uterine fibroids, breast, brain, and liver cancer [60]–[65]. Lithotripsy corresponds to kidney stones destruction using the mechanical destructive effects of ultrasound cavitation mostly with shock waves [66]. It is also applied to gallstones and pancreatic stones.

In research phase, innovative low-invasive ultrasound therapeutic techniques are still in investigation for applications as sonoporation, targeted drug delivery, histotripsy, and thrombolysis. Sonoporation consists in the use of ultrasound cavitation, normally enhanced by injected microbubbles, to disturb cell membrane structures (creating micro-pores), thus increasing its permeability to biomaterials [67], [68]. Targeted drug delivery technique uses ultrasound cavitation to release drugs at a specific site: drugs are a priory incorporated into microbubbles which will then, thanks to the inertial cavitation regime, implode at the radiated site [69]–[72]. The microbubbles employed could target a specific disease by using ligands such as antibodies. Histotripsy, similar to lithotripsy sonication principle, is the mechanical fractionation of tissue using very short (few microseconds) and very high intensity (over 20 MPa rarefaction peak pressure) ultrasound pulses for vast applications [73]–[76]. Ultrasound thrombolysis is the use of cavitation mechanisms to destroy blood clots.

I.3 Ultrasound thrombolysis

I.3.1 State of the art

Many thrombolysis alternative techniques using ultrasound have already been explored. First, a mechanical thrombolysis with direct contact on thrombus using a catheter combined with a tiny transducer [77]–[79]. It is similar to thrombectomy techniques and hence features the same risks and disadvantages. Therefore, to counter the catheter drawbacks an extracorporeal technique, commonly called sonothrombolysis, was considered by exploiting low intensity ultrasound principle and non-inertial cavitation mechanisms to enhance thrombolysis drugs effects [80]–[82]. It was shown that the use of a low dose of drug combined with moderate HIFU sonication is more efficient than the exclusive use of a higher dose of drug [83], [84]. Moreover, instead of thrombolysis drugs, encapsulated microbubbles could be used combined with inertial cavitation mechanisms to mechanically destroy the blood clot [85], [86]. However to overcome the side effects of intravascular or drug interventions, the exclusive use of ultrasound without any additional treatment (catheter insertion, drugs, encapsulated microbubbles) could be adopted. The corresponding technique uses transcutaneous pulsed HIFU sonication relying on inertial cavitation process. It is called extracorporeal ultrasound thrombolysis [37], [87], [88].

The cavitation behavior (nucleation, radial oscillation, and collapse), depending on the medium and ultrasound parameters, is random and chaotic. Nevertheless, the use of microbubbles injection or pulsed ultrasound sonication with very high intensity (histotripsy) promotes the inertial cavitation initiation and process [86], [89]–[92]. Moreover, other studies have proposed the use of multi-frequency ultrasound sonication to decrease the cavitation threshold [93]. However, the use of ultrasound cavitation for therapeutic fallouts remains complex and its dynamic needs to be temporally controlled in real-time.

Hence, several research works have been carried out to set up a cavitation temporal real-time control system using a regulation feed-back loop. A first system was developed to control cavitation activity in a continuous sonication regime using a 5 ms retroaction feedback loop [94]. Still, nowadays most of ultrasound therapy applications use pulsed ultrasound sonication for better control over the treatment area and to avoid overheating of the irradiated tissue. Moreover, in a

continuous regime once the bubble cloud is initiated its activity control is not that difficult to maintain compared to the pulsed regime where it is necessary to reinitiate the bubble cloud at the beginning of each burst. The temporal characteristics of the cavitation dynamics in a pulsed regime are of the order of few milliseconds. Thanks to recent development in field-programmable gate array (FPGA) technology, the computational speed was highly improved and hence the design of systems capable of regulating cavitation in pulsed mode with very low feedback retroaction time was achieved. Therefore, recently a more efficient control system with a 0.4 ms retroaction feedback loop was considered particularly for pulsed regime and inertial cavitation activity regulation [95], [96]. It was specifically developed for ultrasound thrombolysis application and is described in the next section.

I.3.2 Regulated ultrasound-induced cavitation generator

To counter the random behavior of ultrasound cavitation, a regulated focused ultrasound-induced cavitation generator was developed for specific inertial cavitation activity control in pulsed mode [95]. It includes a 1 MHz custom-manufactured piezo-composite transducer (IMASONIC SAS, Voray, France) focalized at 8 cm, a needle-hydrophone (HNC-1500, ONDA, Sunnyvale, CA, USA) recording the acoustic signal, and a FPGA card (field-programmable gate array, PXIe-7966R, NI, Austin, TX, USA) operating the real-time feed-back loop. The therapeutic transducer is excited with a pulsed sinusoidal signal at 1 MHz, 4 Hz pulse repetition, and 10 % duty cycle and is pre-amplified by a power amplifier (69 dB, GN 1000, PRANA, Malemort, France). The hydrophone signal is 31 dB pre-amplified and is then processed in real-time by the FPGA module to extract a cavitation index (CI) defined as the average along the frequencies of the logarithm compression of the Fourier transform of the hydrophone signal [95]. It represents the broadband acoustic noise corresponding to the inertial cavitation contribution.

When the regulation is OFF (open loop), the amplitude tension $U(t)$ delivered to the therapeutic transducer is equal to a constant value. When the regulation is ON (close loop), $U(t)$ is defined in real-time t by the temporal cavitation regulation algorithm (I.6):

$$U(t) = U(t - t_r) + G.(CI_{desired} - CI(t - t_r)) \quad \text{(I.7)}$$

Where t_r is the feedback loop retroaction time, G is the adjustable gain, and $CI_{desired}$ the desired cavitation index.

This system was first tested in water tank experiment (Figure I-7.a). A PVC tank with dimensions of 80 cm × 35 cm × 21 cm was filled with deionized-filtered (particles <5 µm) and degassed (7 mg O_2/L) water. The therapeutic transducer was completely emerged in the water, inducing at 8 cm the cavitation bubble cloud. The hydrophone, also emerged in water, was placed at 90° to the transducer and recorded the cavitation signal. An acoustic absorber was placed at the extremity of the tank to reduce echo-waves reflected from the tank's wall. A retroaction time t_r of 0.4 ms was achieved, which maintains a constant cavitation activity. The cavitation activity is random for the non-regulated strategy (Figure I-7.b) compared to the regulated strategy (Figure I-7.c) where it is stable. The real time computed cavitation index CI tends towards $CI_{desired}$.

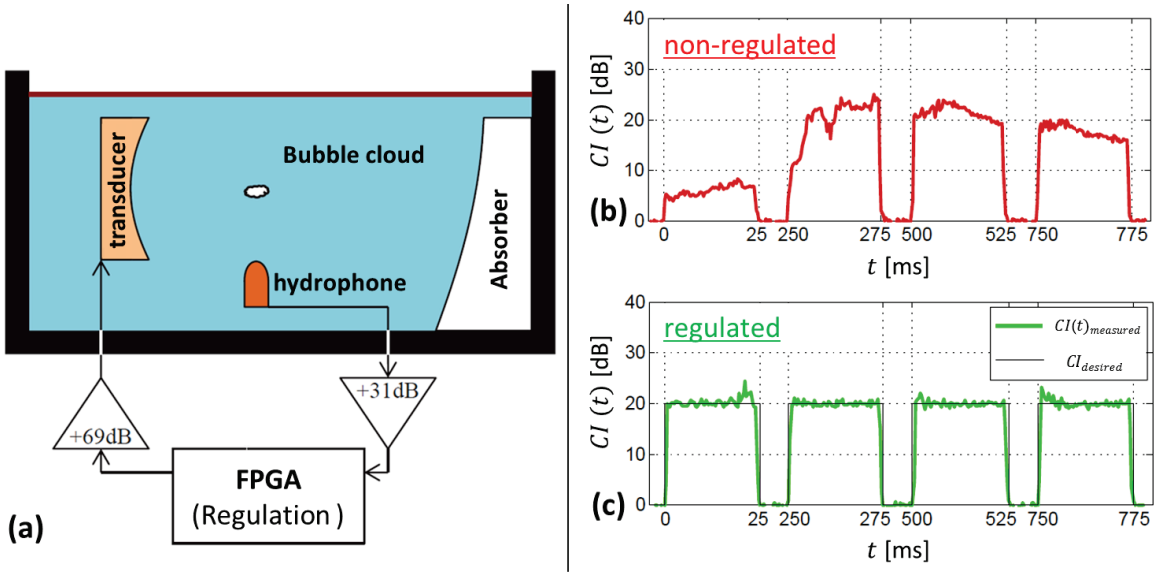

Figure I-7: (a) experimental setup. Temporal evolution of the real time computed cavitation index $CI(t)$ (b) without regulation or (c) with regulation [97].

In previous studies, different parameters of this regulated ultrasound-induced cavitation generator were investigated [97]. The shape of the sonication signal was considered with different sinusoidal frequencies, pulse repetition frequencies, and duty cycle values. The regulation feedback loop was tested with different gains G and also the impact of dissolved gas ratio was considered. This therapeutic system with optimal parameters was defined in recent study to be efficient for destroying thrombus during *ex vivo* experiments [96]. This regulated cavitation generator system provides reproducible pulsed sonication in inertial cavitation regime.

I.3.3 Monitoring system development

The ultrasound-induced cavitation generator system is regulated in term of its acoustic power radiation (CI). Its regulation efficiency was already proven and observed. However, it still lacks the spatial information of the cavitation activity. Therefore, in order to target spatially the thrombus in the blood vessel and to spatially control the cavitation activity, an appropriate monitoring system needs to be developed. In current research and even clinical use, US therapy is normally monitored under magnetic resonance imaging (MRI) thermometry with temperature rise maps [98], [99] or ultrasonic B-mode active imaging with hyperechoic bubble localization information [100]–[102]. However, both methods cannot spatially monitor the cavitation activity in real-time since they cannot work simultaneously with the therapy tools. Moreover, MRI provides temperature maps which are not useful for thrombolysis therapy where the mechanical damage prevails on the thermal one. In ultrasonic B-mode imaging, the cavitating bubble cloud appears as a temporally moving hyperechoic area which even if it provides spatial localization information about bubbles does not yield quantitative information about cavitation activity. Plus, they represent “old” bubbles which when detected are not cavitating anymore. Indeed, both methods can be used to guide per-operatively US therapies but they are not adapted for real-time cavitation activity guidance. On the contrary, passive US imaging is a good candidate because it does not interfere with the therapy pulses and it has real-time monitoring capabilities [103]–[105]. Therefore, it could provide activity cavitation maps in real-time during US therapies.

The aim of the present thesis is to develop and integrate an optimized monitoring system to the pre-existing therapy system. It includes an advanced passive imaging technique providing accurate activity cavitation maps useful for the localization of the cavitation sources (bubble cloud). In the next chapter, the imaging system developed for passive cavitation imaging is presented including its general setup and a validation process.

Chapter II : Imaging system

In this chapter the imaging system developed for monitoring the US thrombolysis therapy is presented. First, in section II.1, passive imaging techniques are investigated. The bubble cloud generates spherical waves represented by wave fronts propagating in the medium and collected passively by the ultrasound imaging probe. Then, by using a beamforming algorithm the cavitation activity is mapped. Three different beamforming algorithms are presented and tested with preliminary dataset. In section II.2, the general setup is presented including the ultrasonic scanner (ULA-OP), the imaging probes characteristics, the synchronization established between both therapy and monitoring system, and finally the data acquisitions. Then in section II.3, for preliminary results featured as a validation process, simulations considering an acoustic point source and experiments on a wire were conducted.

II.1 Passive imaging

In conventional B-mode imaging, a pulse-echo acoustic signal is used for brightness modulation and the time-of-flight (tof) is computed to get the scatterer position. In passive cavitation imaging, the transmission pulse is turned off and the probe records the acoustic signals transmitted by the cavitating bubbles. After recording passively the pre-beamformed RF data the cavitation activity map could be reconstructed thanks to a beamforming algorithm. In a preliminary study, three beamforming reconstruction methods were developed and tested specifically for cavitation source localization: time reversal method (TRM), passive acoustic mapping (PAM), and PAM weighted with a phase coherence factor (PAM-PCF).

II.1.1 Beamforming algorithms

II.1.1.1 Time reversal method (TRM)

Time reversal techniques rely on the invariance of the wave propagation equation by temporal reverse. It was first introduced by Fink *et al.* [106] and is used in many fields as telecommunication [107], [108] or medical [109], [110]. In medical applications, few studies were conducted using time-reversal focusing mechanism [111], [112] as for example on lithotripsy with kidney stone tracking and destruction [113] or on transcranial ultrasonic therapy with bone aberration corrections [114], [115]. The time reversal mirror technique [116]–[118] consists in the use of piezoelectric transducer array which allows the received acoustic field to be recorded, time reversed and then re-transmitted by the same transducers. As a consequence, the US wave back-propagates and refocuses at the initial acoustic source as if time was going backwards (Figure II-1).

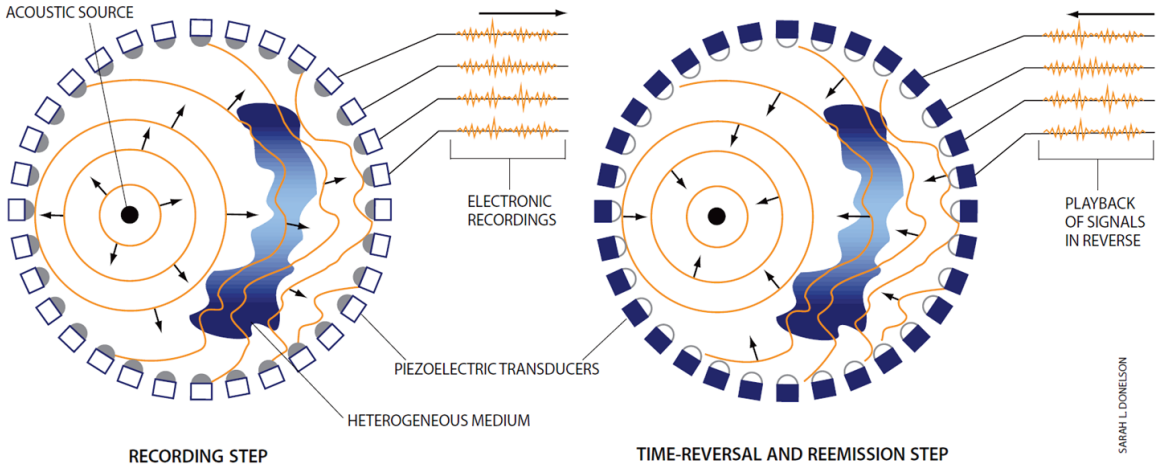

Figure II-1: Time reversal mirrors technique [118].

In our study a virtual time reversal method (TRM) was developed and applied on the recorded passive pre-beamformed RF signals. It consists in back-propagating the acoustic incident waves back to their sources and hence localizes the initial source (bubble cloud).

Treeby *et al.* [119] developed an acoustic toolbox in Matlab (The MathWorks Inc., Natick, MA, USA) called 'k-Wave" designed for time domain acoustic and ultrasound simulations based on k-space pseudo spectral method. It includes a flexible time reversal image reconstruction algorithm which reverses temporally the acoustic signals and virtually propagates the waves in the medium back to their sources. The wave's propagation simulation uses the first order wave's equation:

$$\begin{cases} \dfrac{\partial v}{\partial t} = -\dfrac{1}{\rho_0}\nabla p & \text{(a)} \\ \dfrac{\partial p}{\partial t} = -\rho_0 \nabla . v & \text{(b)} \\ p = c_0^2 \rho & \text{(c)} \end{cases} \qquad \text{(II.1)}$$

These equations are based on the conservation of momentum (a), conservation of mass (b) and the pressure-density relation (c). ρ_0 is the density of the medium and c_0 is the speed of sound in the medium. The acoustic power P_{TRM} is finally computed by averaging the squared pressure maps reconstructed by k-Wave toolbox over a time corresponding to the maximum depth of the backpropagation.

II.1.1.2 Passive acoustic mapping (PAM)

The passive acoustic mapping (PAM) reconstruction algorithm [120] consists in applying dynamic focalization in reception, *i.e.*, the delay-and-sum (DAS) algorithm. The delays τ_i to be applied to the RF data of each element i of the array for the specific pixel (x, y, z) of the reconstructed cavitation map are computed:

$$\tau_i(\boldsymbol{r}) = d_i(\boldsymbol{r}) / c_0 = \|\boldsymbol{r} - \boldsymbol{r_i}\| / c_0, \quad with \begin{cases} \boldsymbol{r} = (x, y, z) \\ \boldsymbol{r_i} = (x_i, y_i, z_i) \end{cases} \tag{II.2}$$

where d_i the propagation distance from the point at $\boldsymbol{r}$ to the i^{th} element at $\boldsymbol{r_i}$. However, since the imaging system works on passive acquisitions and the activity behavior of bubbles lacks its temporal knowledge, the round trip time of flight of the US wave cannot be used. The source strength q at a time $k\Delta t$ and pixel location at $\boldsymbol{r}$ is computed by summing the pressure information recovered from the delayed RF signals as follows:

$$q(\boldsymbol{r}, k\Delta t) = \frac{1}{N} \sum_{i=1}^{N} \alpha . s_i \left\{ k\Delta t + \tau_i(\boldsymbol{r}) - min\left[\tau(\boldsymbol{r}) \right] \right\} \tag{II.3}$$

where s_i is the RF signal recorded by the i^{th} element, α the compensation term for propagation attenuation, and N the number of elements of the linear array. To overcome the no-time-of-origin issue, the time exposure acoustic (TEA) principle [121] is applied, by averaging the square of the source strength q along a time $T = (K-1)\Delta t$. k represents the time segment offset integer number and K the total number of computed time segments. Finally, the acoustic power P_{PAM} is computed for each pixel:

$$P_{PAM}(\boldsymbol{r}) = \frac{1}{4\pi\rho_0 c_0} . \frac{1}{K} . \sum_{k=0}^{K-1} q^2(\boldsymbol{r}, k\Delta t) \tag{II.4}$$

II.1.1.3 PAM weighted with PCF (PAM-PCF)

To enhance the suppression of side-lobes, to correct out-of-focus points, and to rectify bubble interference artifacts that limit PAM reconstruction, different optimization methods have already been explored in previous studies such as the integration of the robust capon beamforming (PAM-RCB) [122] into the PAM. Here the PAM-PCF algorithm was used. It consists in adding a weighting factor, the phase coherence factor (PCF) [123], which is based on the estimation of the delayed signal phase dispersion σ_φ, and is computed:

$$PCF(\boldsymbol{r}, k\Delta t) = max\left[0; 1 - \frac{\gamma}{\sigma_0} \sigma_\varphi(\boldsymbol{r}, k\Delta t) \right] \tag{II.5}$$

where γ corresponds to the sensitivity of the PCF. The increase of the γ value favors suppression of out-of-focus signals, which will be chosen equal to 1 in the following studies. φ is the instantaneous phase of the delayed signal and σ_0 is the nominal standard deviation of a linear distribution in $[-\pi; \pi]$ modulo 2π and is equal to $\frac{\pi}{\sqrt{3}}$ [123]. Then the source strength q_{PCF} at a time $k\Delta t$ and pixel location at $\boldsymbol{r}$ is computed as follow:

$$q_{PCF}(\boldsymbol{r}, k\Delta t) = PCF(\boldsymbol{r}, k\Delta t) . q(\boldsymbol{r}, k\Delta t) \tag{II.6}$$

Finally as in PAM algorithm(II.4), the acoustic power $P_{PAM-PCF}$ is computed for each pixel:

$$P_{PAM-PCF}(\boldsymbol{r}) = \frac{1}{4\pi\rho_0 c_0} \cdot \frac{1}{K} \cdot \sum_{k=0}^{K-1} {q_{PCF}}^2(\boldsymbol{r}, k\Delta t) \quad \text{(II.7)}$$

II.2 General setup

To introduce a spatiotemporal monitoring system, an US imaging system was integrated into the previous therapy setup (the regulated ultrasound-induced cavitation generator). The imaging system is composed of an ultrasound advanced open platform (ULA-OP) paired with an imaging probe. The imaging system was synchronized with the regulated US cavitation generator so that radio frequency (RF) signals were acquired at a specific time. The general setup is displayed in Figure II-2.

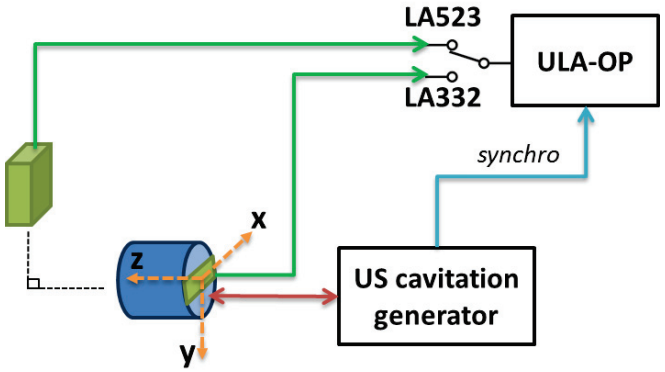

Figure II-2: General setup using both the therapeutic system (US cavitation generator) and the imaging system with ULA-OP paired with two imaging probes (LA523, LA332) synchronized with the therapeutic pulses.

II.2.1 ULA-OP

The ULA-OP-64 is an Ultrasound Advanced Open Platform developed by the microelectronics systems design laboratory (MSDlab) in Firenze, Italy [124]. It controls simultaneously and independently up to 64 channels in transmission and reception meaning that 64 elements of the imaging probe could individually transmit or record acoustic signals. It was designed to allow testing new US methods that include original beamforming strategies. This ultrasonic scanner consists in a metal rack of dimensions 33 cm x 23 cm x 18 cm connected to a PC with a dedicated software (Figure II-3). Therefore it is portable and very handy tool to move between research laboratory facilities.

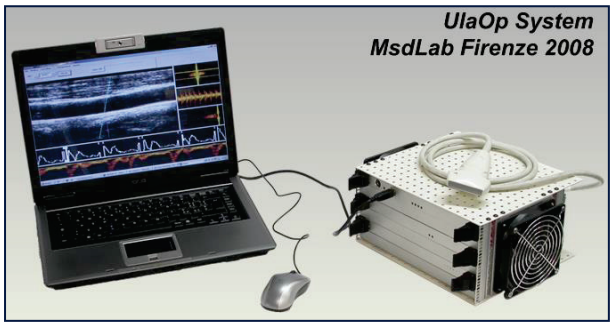

Figure II-3: ULA-OP ultrasonic scanner [124]

II.2.2 Imaging probes

Two imaging probes, LA523 and LA332 (Esaote S.p.A., Florence, Italy), are used separately in this work. They are piezoelectric linear array with the same pitch (distance between two consecutive elements) equal to 245 µm. They are placed perpendicular to each other and the LA332 array is incorporated into the therapeutic transducer. The characteristics of these two probes are displayed in Table II.1. The 64 central elements were used on both probes, corresponding to a 15.68 mm active aperture size.

Table II-1: Imaging probes characteristics.

Probe	Total number of elements	Bandwidth	Footprint
LA523	192	4–13 MHz	50x8 mm
LA332	144	3–11 MHz	36x8 mm

II.2.3 Synchronization

In addition to the therapy signal $U(t)$, defined in section I.3 as a 1 MHz sinusoidal pulsed signal at 4 Hz repetition frequency and 10 % duty cycle, a supplementary rectangular output signal is provided by the FPGA module. It represents the output synchronization signal $U_{synchro}(t)$ defined as a 25 ms width pulse (τ_{pulse}) occurring every 250 ms (T_{pulse}). It is displayed in Figure II-4.

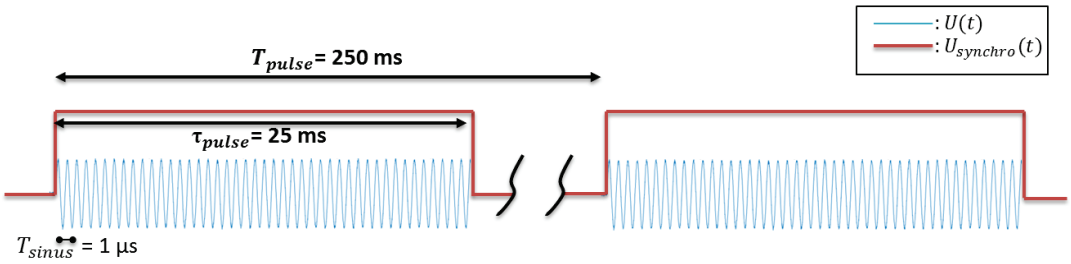

Figure II-4: Two synchronous signals are generated by the FPGA module of the US cavitation generator system: the sonication signal $U(t)$ sent to the therapeutic transducer and the output synchronization signal $U_{synchro}(t)$.

The ULA-OP ultrasonic scanner can be synchronized with any other external system. It can play as "master", sending out a pulse signal synchronous with the ULA-OP internal pulse repetition frequency (PRF), or as "slave", forcing the ULA-OP transmission to be synchronous with an external signal. In this work, the "slave" synchronization principle was largely used to grant monopoly to the therapy system. Two different configurations were established: "Synchro Out" or "Enable".

II.2.3.1 "Synchro Out" configuration

The "Synchro Out" configuration uses an external synchronism pulse $Synchro(t)$, which PRF defines the pulse repetition interval (PRI) sequence of the ULA-OP acquisition as shown in Figure II-5. The acquisition begins during the falling edge of the pulse.

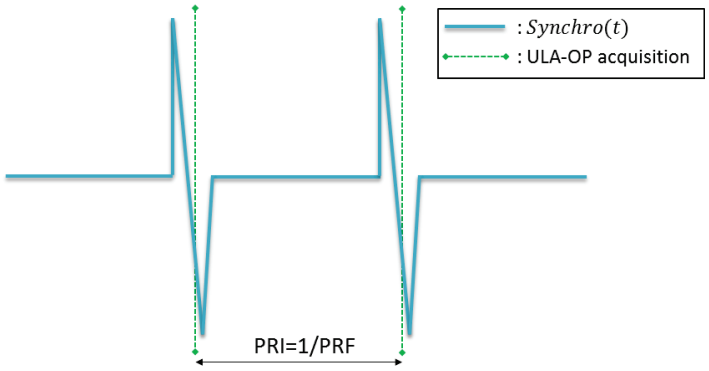

Figure II-5: The external pulse $Synchro(t)$ input signal used for ULA-OP acquisition synchronization.

In our work, the output synchronization signal $U_{synchro}(t)$ of the US cavitation generator is used to create the $Synchro(t)$ signal by adding a function generator. A phase shift $\phi_{synchro}$ between both signals can be directly tuned by the US cavitation generator system.

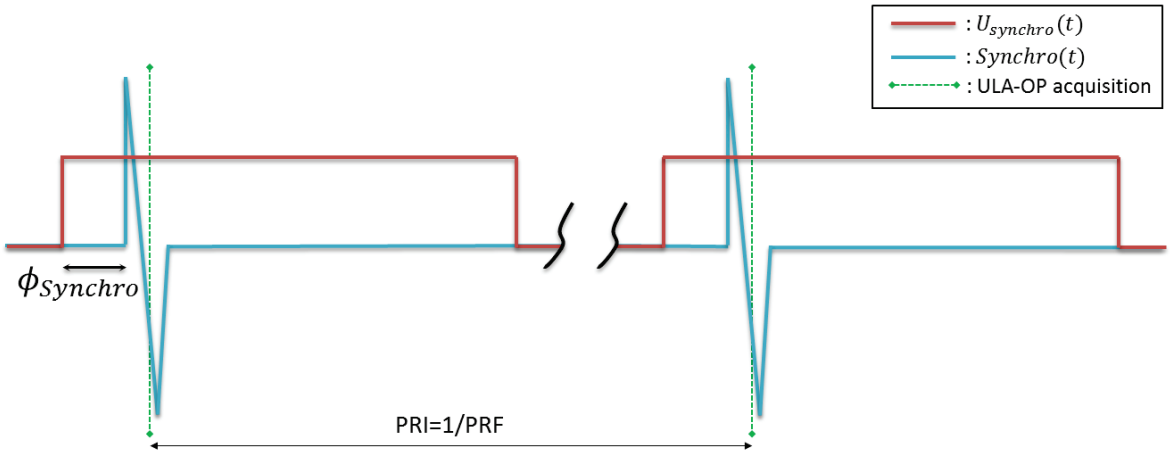

Figure II-6: "Synchro Out" configuration adapted to the US cavitation generator system.

This configuration, displayed in Figure II-6, favors punctual events recording (as wire pulsed excitation experiment) and is external PRF dependent (meaning that the PRF depends entirely on the sonication device repetition pulse). As it can record only one acquisition per sonication pulse, its main constraint is the low sonication information acquired.

II.2.3.2 "Enable" configuration

The "Enable" configuration uses a rectangular signal $Enable(t)$ as input to the ULA-OP synchronization. As shown in Figure II-7, ULA-OP acquisitions are executed, with the internal PRF available in ULA-OP settings, only when $Enable(t)$ is set to 1 by applying a voltage higher than 2 Volts (logical input).

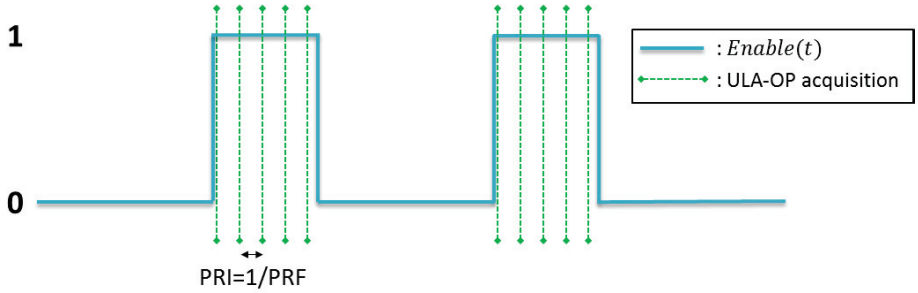

Figure II-7: The rectangular $Enable(t)$ input signal used for ULA-OP acquisition synchronization.

In our work, $U_{synchro}(t)$ signal can be used directly as $Enable(t)$ input signal and the phase shift ϕ_{Enable} can also be modified. Moreover, in this particular configuration, the $Enable(t)$ signal width (τ_{Enable}) could be adjusted thanks to a function generator.

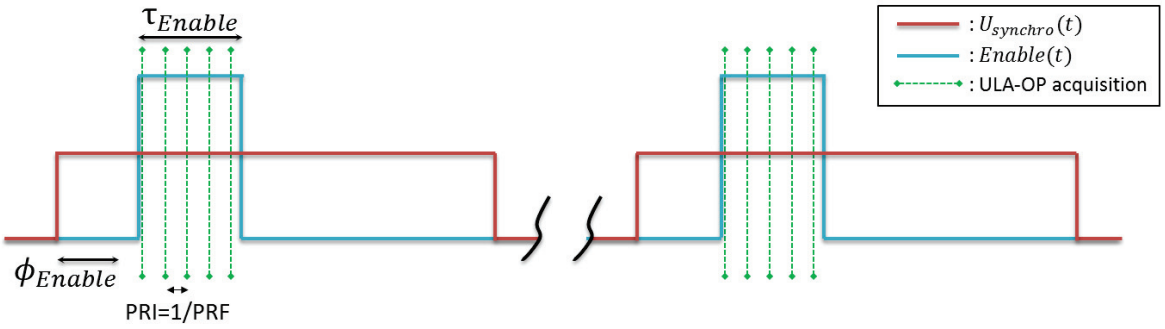

Figure II-8: "Enable" configuration adapted to the US cavitation generator system.

This configuration, presented in Figure II-8, merits of being simpler to set up and of acquiring more data thanks to the higher internal PRF dependency.

With the use of these two different synchronization configurations, data could be acquired during any moment of the sonication therapy signal. Hence it will be very helpful for different experimental applications as well as for the development of diverse imaging modes as B-mode, passive mode, and hybrid mode. More details are explained during material and method presentations in further sections.

II.2.4 Data acquisition

During ULA-OP acquisitions, transmission and reception strategies are carried out. In this work two simple transmission strategies were used: a 3-cycle pulse is sent in transmission for B-mode imaging versus no transmission for passive imaging.

For the reception step, pre- or post-beamformed data could be recorded. The ULA-OP scanner already includes an internal real-time DAS beamformer which allow post-beamformed data to be directly recorded for B-mode imaging. For both B-mode and passive imaging, thanks to the data acquisition (DAQ) technology, the pre-beamformed data (RF signals) could be recorded with a 12-bit sample quantization. At each PRI and for each channel, a number of samples ($n_{samples}$) is stored in the buffer at a 50 MHz sampling frequency rate (f_s). Hence, the total pre-beamformed data acquired for one ULA-OP acquisition (for one PRI) is represented in number of bytes (8 bits) as 64 channels x $n_{samples}$ x 12/8 bit. The maximum storage capacity is up to 1 Gigabyte for RF data.

The B-mode imaging mode is already established and used in almost all the clinical ultrasonic scanner. However, the passive imaging modes are still in research studies and needs more improvement. Therefore in the next section, the passive imaging mode is discussed.

II.3 Validation process

To test and assess the efficiency and the constraints of the three different beamforming methods, two different dataset were explored: simulations considering an acoustic point source and experiments on a wire.

II.3.1 Simulations on a point source

A first step to validate the reconstruction algorithms is to work on pre-beamformed simulated data using an acoustic point source corresponding to a singular cavitating bubble. This acoustic source is defined by its position, fundamental frequency f_0, and the number of harmonics assumed to be generated by nonlinearity. In this preliminary study, the source was characterized by a frequency f_0=1 MHz and a presence of seven harmonics of frequencies nf_0, n={2;…;8}, with an amplitude decrease proportional to $1/n$.

Firstly, for each reconstruction methods, two different positions were tested on the acoustic axis (lateral = 0 mm) at 40 or 80 mm depth (axial direction). For each position, 64 RF signals with 500 samples each are generated and are displayed in Figure II-9. Finally the three different beamforming algorithms (TRM, PAM, and PAM-PCF) are applied to the corresponding pre-beamformed data and the reconstructed maps are computed and are displayed in Figure II-10.(a-c) and Figure II-11.(a-c). Moreover, for a better quantitative interpretation the acoustic pattern profile in the lateral and axial direction are plotted for the three methods in Figure II-10.(d, e) and Figure II-11.(d, e).

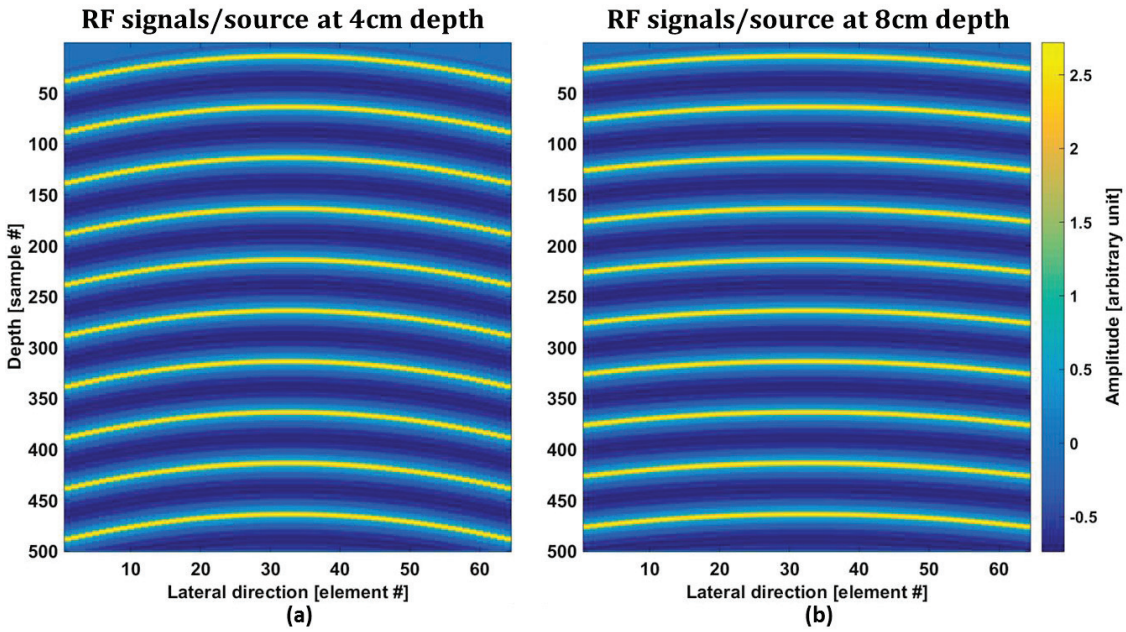

Figure II-9: Pre-beamformed simulated RF signals using 64 central elements.

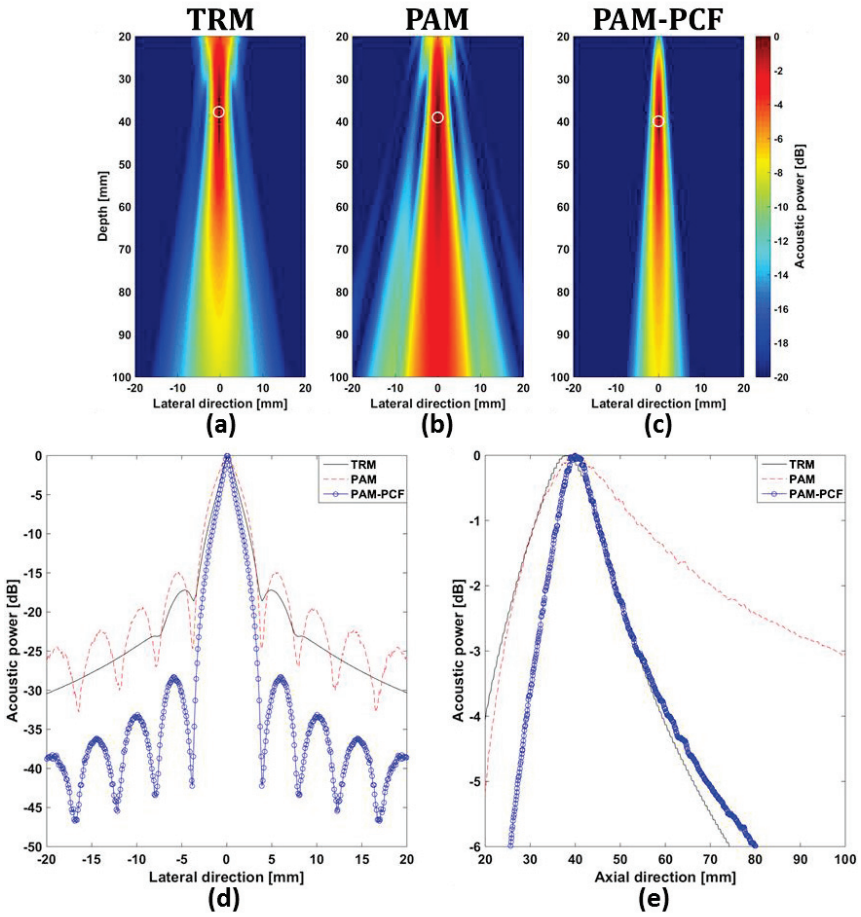

Figure II-10: On the top, acoustic power maps reconstructed using the three beamforming algorithms: (a) TRM, (b) PAM, (c) PAM-PCF applied to pre-beamformed simulated RF signals transmitted by an acoustic point source. In each subplot, the recovered focal point is marked by a white circle, with the (lateral; depth) coordinates in mm and the theoretical position equal to (0; 40). On the bottom, the acoustic pattern profiles in the (d) lateral and (e) axial direction=depth for the three beamforming algorithms (TRM, PAM, PAM-PCF).

In the acoustic maps (a-c), for the three methods, a “tail” aspect is noted representing a lateral resolution decrease in function of depth. It is quantitatively observed in (e) where its impact is stronger for PAM than TRM. This aspect could be explained mainly by the TEA process when in PAM the acoustic power is summed along a time T (II.4). Thanks to the PCF weighting factor implementation (PAM-PCF), the resolution was improved in both axial and lateral direction, especially decreasing this “tail” issue. For PAM-PCF, in lateral direction, a reduction of 13.4 dB in side lobes is achieved as well as the main lobe at -20 dB shrinked by 16.9 %. In the axial direction, the focal spot width at -3 dB was reduced by 69.8 %. In the axial direction (depth), the focal point (maximum intensity point) for TRM, PAM, and PAM-PCF is respectively localized at 37.7 mm, 39 mm, and 39.9 mm. Hence the point source localization is efficient and close to the theoretical one at 40 mm. The PAM have however a better localization efficiency than TRM.

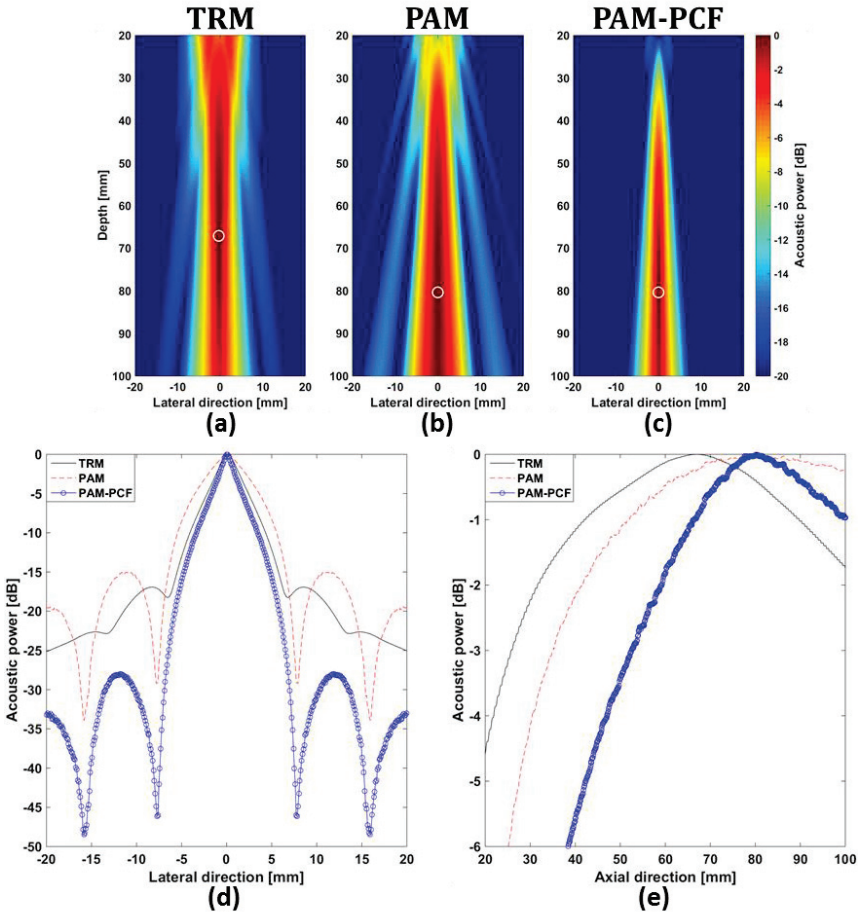

Figure II-11: On the top, acoustic power maps reconstructed using the three beamforming algorithms: (a) TRM, (b) PAM, (c) PAM-PCF applied to pre-beamformed simulated RF signals transmitted by an acoustic point source. In each subplot, the recovered focal point is marked by a white circle, with the (lateral; depth) coordinates in mm and the theoretical position equal to (0; 80). On the bottom, the acoustic pattern profiles in the (d) lateral and (e) axial direction=depth for the three beamforming algorithms (TRM, PAM, PAM-PCF).

Using a twice deeper punctual source (80 mm), the same interpretation about resolution and “tail” aspect is observed. Thanks to PCF, in lateral direction, a reduction of 12.9 dB in side lobes is achieved as well as the main lobe at -20 dB shrinked by 18.3 %. However, compared to the maps in Figure II-10, the resolution in both axial and lateral directions are degraded with wider width of the focal spot. This issue is dependent on the imaging system, especially on the aperture size (F-number).

Furthermore, in the axial direction (depth), the focal point for TRM, PAM, and PAM-PCF is respectively localized at 67.1 mm, 80.4 mm, and 80.4 mm. So a point source localization issue occurs for TRM when the depth of the acoustic source increases. This issue can be explained by the fact that time-reversal technique using K-Wave simulation tool for back-propagating the US wave back to the original punctual source is different in its way of computation process relative to the created simulated pre-beamformed RF signals. This is why most of the applications consider the physical aspect of the time-reversal by re-transmitting the reversed signal in the medium using the same physical transducer for focusing fallouts. Hence, PAM's superiority in performance relative to TRM is validated and so TRM won't be used or discussed anymore in the following work.

To investigate the beamforming accuracy outside of the acoustic axis two additional positions were explored with a 10 mm shift in the lateral direction. Hence, results for PAM and PAM-PCF are presented for the overall four different point sources located 40 or 80 mm deep and on the acoustic axis (lateral = 0 mm) or 10 mm apart from it. The acoustic power maps reconstructed are displayed in Figure II-12.

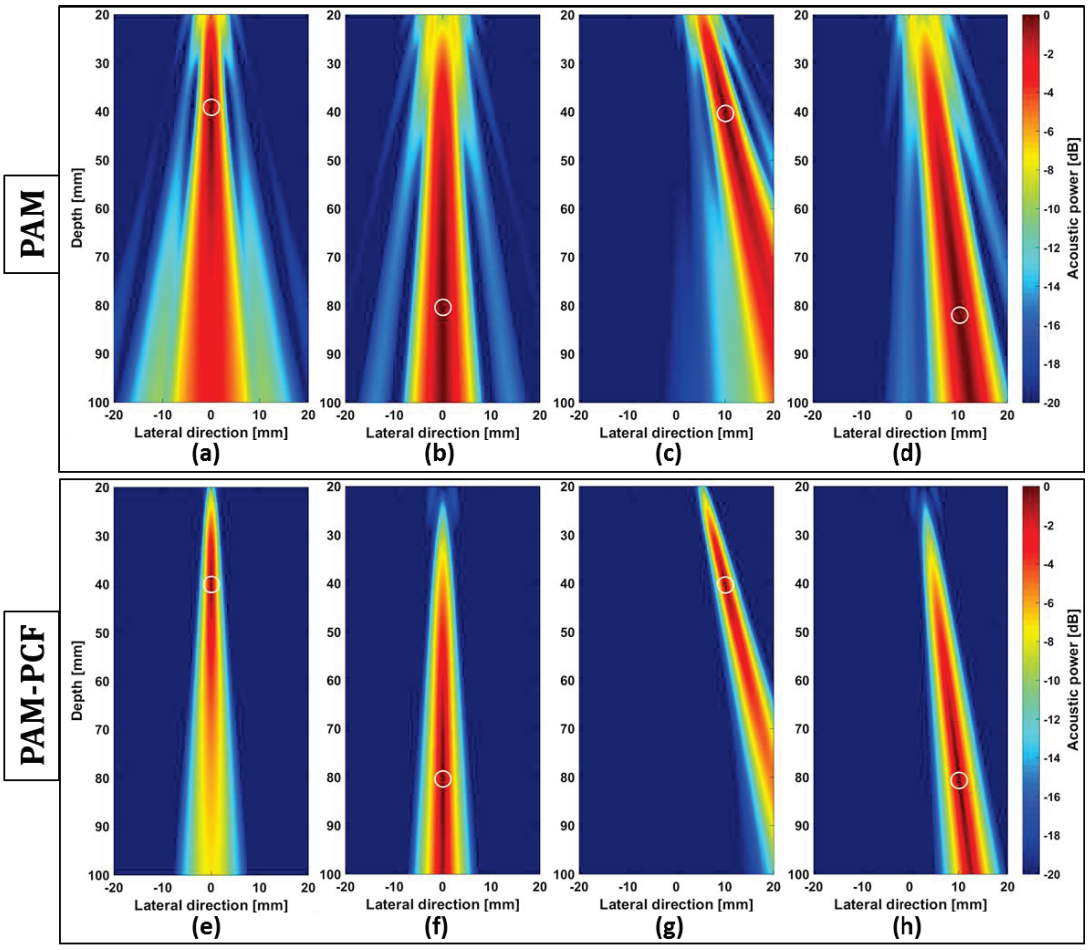

Figure II-12: From simulation dataset of a point source, images reconstructed using (a–d) PAM and (e–h) PAM-PCF. In each subplot, the theoretical position of the point source is marked by a white circle, with the (lateral; depth) coordinates in mm from left to right: (0; 40), (0; 80), (10; 40), and (10; 80).

For low space from the point source to the acoustic axis (here 10 mm apart), the results remain identical (Figure II-12 c–d). With the PCF weighting factor, the resolution improves in every case

(Figure II-12 e–h) as observed before with reduction in side and main lobes in both axial and lateral directions. Therefore, PAM-PCF has a better focal spot resolution as well as localization.

II.3.2 Experiment on a wire

To inspect the accuracy of the passive imaging technique (PAM-PCF), the point-spread-function (PSF) was considered using a 0.1 mm diameter nylon wire placed perpendicular to the imaging probe. A mono-element transducer (5 MHz, SL-0503-HP, Panametrics-Olympus, Tokyo, Japan) was used to excite the wire. It was powered with a pulser/receiver (5052PR, Sofranel Panametrics-Olympus, Tokyo, Japan) so that the scattering wire mimics a broadband point source providing information similar to an inertial cavitation event [120]. To study the localization ability of the PAM-PCF reconstruction technique, the position of the wire with respect to the probe position was axially and laterally shifted by moving the probe using a three-directional motorized positioning system (OWIS, Staufen, Germany) in the three orthonormal axes (x, y, z), as shown in Figure II-13. The wire was first positioned using B-mode visualization at (x = 0 mm; z = 20 mm). The y position was chosen so that the imaging plane remains in the transducer beam plane. Then, using the positioning system software (OWISoft), the imaging probe was shifted in 154 different positions: 11 lateral (in the x direction) and 14 axial (in the z direction), as shown in Figure II-14. Because of the lateral symmetry of the probe, only positive offsets for the lateral direction (0 to 20 mm) were considered. For each wire position, 100 passive acquisitions synchronized with the pulser/receiver were recorded. The "Synchro Out" synchronization configuration (Figure II-6) was used. After post-processing the acquisitions with the PAM-PCF method, 100 passive images were reconstructed. Then, on each map, the position of the maximum intensity pixel corresponding to the wire position was extracted. Finally, the mean wire position was recovered and plotted in Figure II-14 for all 154 positions.

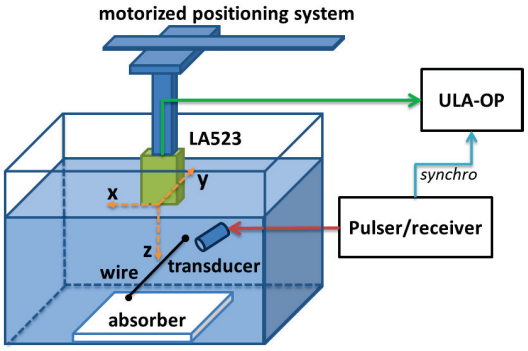

Figure II-13: Wire experiment setup where a 0.1-mm-diameter nylon wire is excited with a transducer driven by a pulser/receiver in a water tank. The LA523 imaging probe, recording the scattered acoustic signals with the ULAOP system, is shifted using a motorized positioning system in two directions (*x* =lateral and *z* =axial).

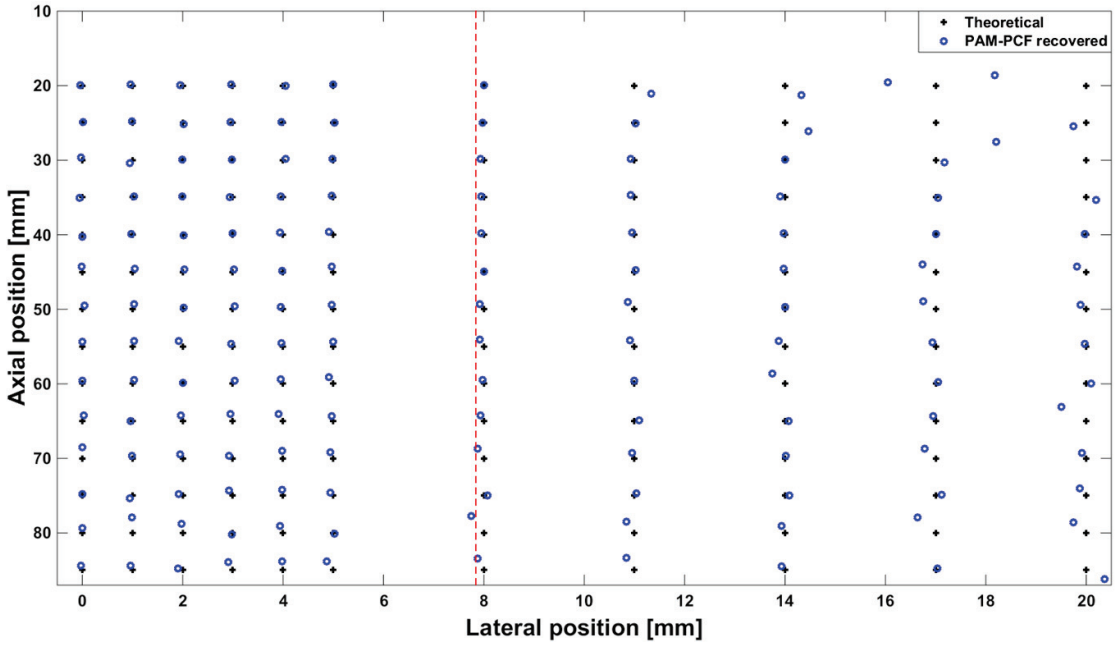

Figure II-14: The theoretical wire positions (black +) and those recovered with PAM-PCF (bleu o). The vertical red dashed line corresponds to the half array aperture limit equal to 7.84 mm (32 elements × 0.245 mm in pitch).

With the PAM-PCF algorithm, the wire positions were satisfactorily recovered: recovery errors (mean ± standard deviation), corresponding to the difference between the theoretical and recovered positions, are equal to 0.64 ± 0.52 mm and 0.13 ± 0.21 mm in the axial and lateral direction shifts, respectively. It is worth noting that the wire positions were better localized when in the active aperture of the probe (lateral positions < 7.84 mm) and close to the array (axial positions < 70 mm). In this region, the recovery errors in axial and lateral direction shifts, respectively, were equal to 0.44 ± 0.28 mm and 0.09 ± 0.04 mm. At greater depths (lateral positions < 7.84 mm and axial positions ≥ 70 mm), the localization was less robust and the recovery errors in the axial and lateral direction shifts were equal to 0.80 ± 0.52 mm and 0.06 ± 0.03 mm, respectively. Furthermore, for positions out of the active aperture's probe limit (lateral positions > 7.84 mm), the recovered positions were less accurate and the recovery errors in the axial and lateral direction shifts were equal to 0.76 ± 0.61 mm and 0.19 ± 0.30 mm, respectively. Indeed, because of the limited steering sensitivity of the imaging probe, the echoes backscattered from the wire were neglected in the recorded RF signal.

II.3.3 Conclusions

Therefore, the passive acoustic mapping weighted with the phase coherence factor (PAM-PCF) beamforming algorithm was investigated relative to the time reversal method (TRM) and PAM techniques considering the two previous validation protocols (simulations on a point source and experiment on a wire). Considering the simulations on a point source results first, PAM method overcomes TRM in the focal cavitation point (FCP) localization, and second PAM-PCF method overcomes PAM method in the focal spot resolution (reduction in main and side lobes). Then thanks to the experiments on a wire, the FCP localization accuracy for PAM-PCF technique was assessed and it was proven to be the most accurate in the active aperture of the imaging probe as well as at low depth correlated respectively with steering sensitivity and F-number probe aperture. Hence PAM-PCF beamforming technique is chosen as the referenced passive cavitation imaging technique for

reconstructing the cavitation activity maps in the following chapters. In the next Chapter III, it will be tested with cavitation experiments to assess the passive imaging technique in a closer real situation.

Chapter III : Cavitation experiments

PAM-PCF reconstruction algorithm was previously validated with simulation on a point source and experiments with a wire. For further validation process, cavitation experiments were conducted first to assess realistic passive imaging cavitation maps, and second to investigate and observe the cavitation activity behavior with its spatio-temporal evolution. Water tank experiments including one-spot, multi-spots, and non-regulated versus regulated cavitation experiments are considered. Additionally, preliminary *in vivo* experiments were assessed.

III.1 Water tank experiment

The primary way to investigate cavitation is to use water tank experiments allowing optical visualization of the bubble cloud generation and its motion tracking. First, one spot cavitation, with different medium parameters as well as ultrasound sonication intensity (CI), is investigated. Second, non-regulated versus regulated cavitation activity is assessed. Finally, multi-spots cavitation including multi cavitation sources are considered to assess PAM-PCF limitations.

III.1.1 One-spot cavitation

III.1.1.1 Experimental setup

To assess the spatiotemporal behavior of the cavitation activity and evaluate PAM-PCF reconstruction methods in real cavitation situation, a cavitation experiment setup was developed. US cavitation (bubble cloud) was induced in a water tank by the regulated US-induced cavitation generator. The tank was filled with deionized-filtered (particles <5 µm) and degassed (3 mgO_2/L) water. The ambient temperature was constant, equal to 22°C. Acoustic absorbers were used to reduce the echo-waves reflected from the tank walls. Two experimental cases, with or without an agar gel (4%), were considered. The agar gel, used as tissue-mimicking medium, was prepared with 4% agar dissolved in heated deionized water (85°C) and mixed using a magnetic stirrer. The homogeneous mixture was poured into a 10 cm × 10 cm × 10 cm mold and then cooled in a refrigerator overnight. When used, the agar gel was positioned 40 mm distance from the therapeutic transducer and in direct contact with the LA523 imaging probe. The bubble cloud was induced at 44 mm from LA523 and 80 mm from LA332. These positions were *a priori* checked using B-mode visualization with hyperechoic regions corresponding to the bubble cloud. The LA523 probe images the cavitation transversal plane (x, y) and the LA332 probe images the cavitation axial plane (x, z) as displayed in Figure III-1 and outlined in Figure III-3.

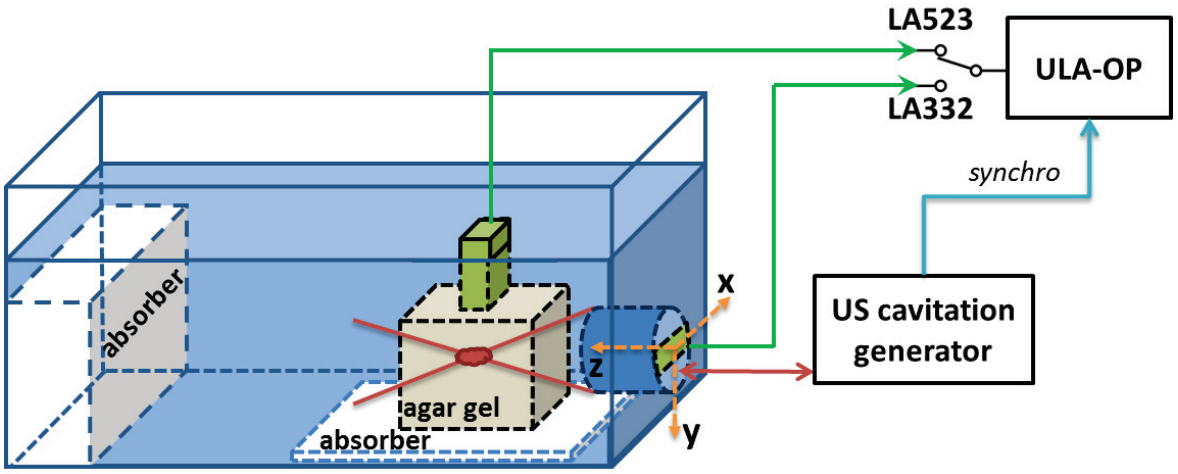

Figure III-1: Cavitation experiment setup using both the therapeutic system (US cavitation generator) to induce a bubble cloud and the imaging system with the two imaging probes (LA523, LA332) synchronized with the sonication pulses.

The "Enable" synchronization configuration (Chapter II) was used with a τ_{Enable} set to 25 ms which equals the width of the sonication pulse τ_{pulse}. Therefore, the RF signals were recorded only during the sonication pulses with an internal 3000 Hz PRF. Moreover, a phase shift ϕ_{Enable} was set to allow some first frames of the acquisition to be recorded outside of the sonication pulse. It was used to outline the start of the sonication pulses as well as to confirm the no-cavitation events. This configuration is displayed in Figure III-2. Three first frames for both LA523 and LA332 probes were recorded outside of the sonication pulse. The cavitation index (CI), introduced in section I.3.2, was used to control the cavitation activity intensity. Different experimental cases were investigated: with or without the agar gel, an increasing CI (10 to 40 dB with 5dB increment), and both imaging probes (LA523 or LA332). For each case, a total of 1500 passive acquisitions were achieved representing 20 sonication pulses of 75 RF signals each (72 acquisitions during sonication plus three outside).

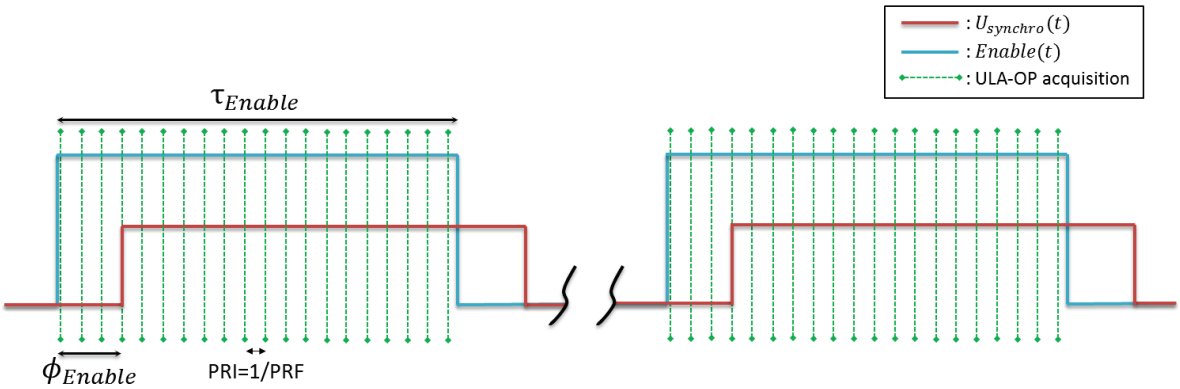

Figure III-2: Synchronization configuration established between the sonication pulse (US cavitation generator) and the ULA-OP acquisition using "Enable" configuration. The three first frames are acquired outside of each sonication pulse.

III.1.1.2 Computation step

For each passive recorded acquisition, one cavitation map was computed using PAM-PCF beamforming algorithm. The reconstruction parameters, used to compute the different maps, were set as follows. A 50 mm × 20 mm image [axial × lateral direction] with 200 pixels × 300 pixels were

used corresponding to a 0.166 mm × 0.1 mm pixel resolution. The minimum depth (axial imaging axis) was fixed at 20 mm and at 50 mm for the cavitation transversal plane (LA523 probe) and the cavitation axial plane (LA332 probe), respectively. The lateral imaging axis was centered at zero. These reconstruction parameters are displayed in Figure III-3. The time T used in the averaging process of TEA was set to 49.3 µs with a time step Δt of 0.1 µs which is coherent with bubble temporal activity.

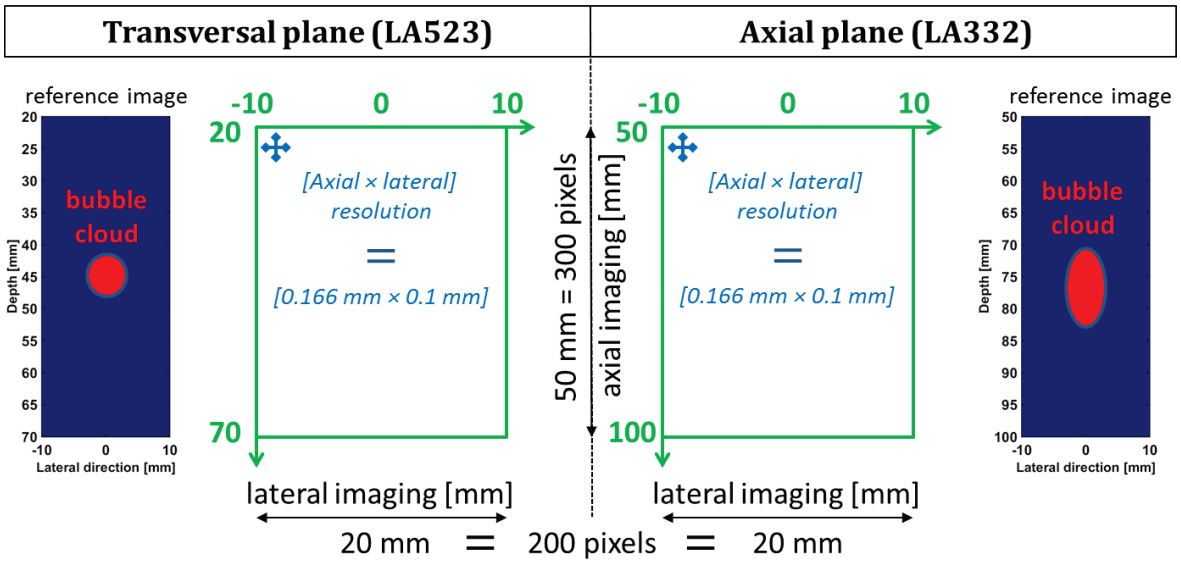

Figure III-3: Image reconstruction parameters for both probes LA523 and LA332 respectively imaging the cavitation transversal plane (x, y) and the cavitation axial plane (x, z). Reference images are displayed to outline the bubble cloud shape and focal point localization for each cavitation planes. The bubble cloud limits are not at the right scale, it is used as a representative reference image.

Hence, 1500 maps were reconstructed along 500 ms of overall sonication corresponding to 20 sonication pulses of 25 ms. For every map, the focal cavitation point (FCP) recovered was defined as the point with the maximum acoustic power and so as the center position of the cavitating bubble cloud. To remove low- or no-cavitation events (for example the three first frames recorded outside of each sonication pulses), a threshold of −40 dB was applied to the FCP acoustic power values. Exclusively for this threshold operation, the acoustic power was previously normalized over all 1500 maps. The changes in position of the FCP were then temporally computed for both axial and lateral imaging direction. One experimental case was chosen in this section to exhibit these different results: using degassed water, the agar gel, the cavitation transversal plane (LA523), and a cavitation index (CI) equal to 20 dB. First, the cavitation map reconstructed for the 4th passive acquisition frame and the cumulated map along the entire 1500 reconstructed maps are displayed in Figure III-4.(a, b). Then the FCP two dimensions position is displayed in Figure III-4.c. Likewise, its localization temporal profile in both axial (depth) and lateral imaging direction are displayed in in Figure III-4.(d, e).

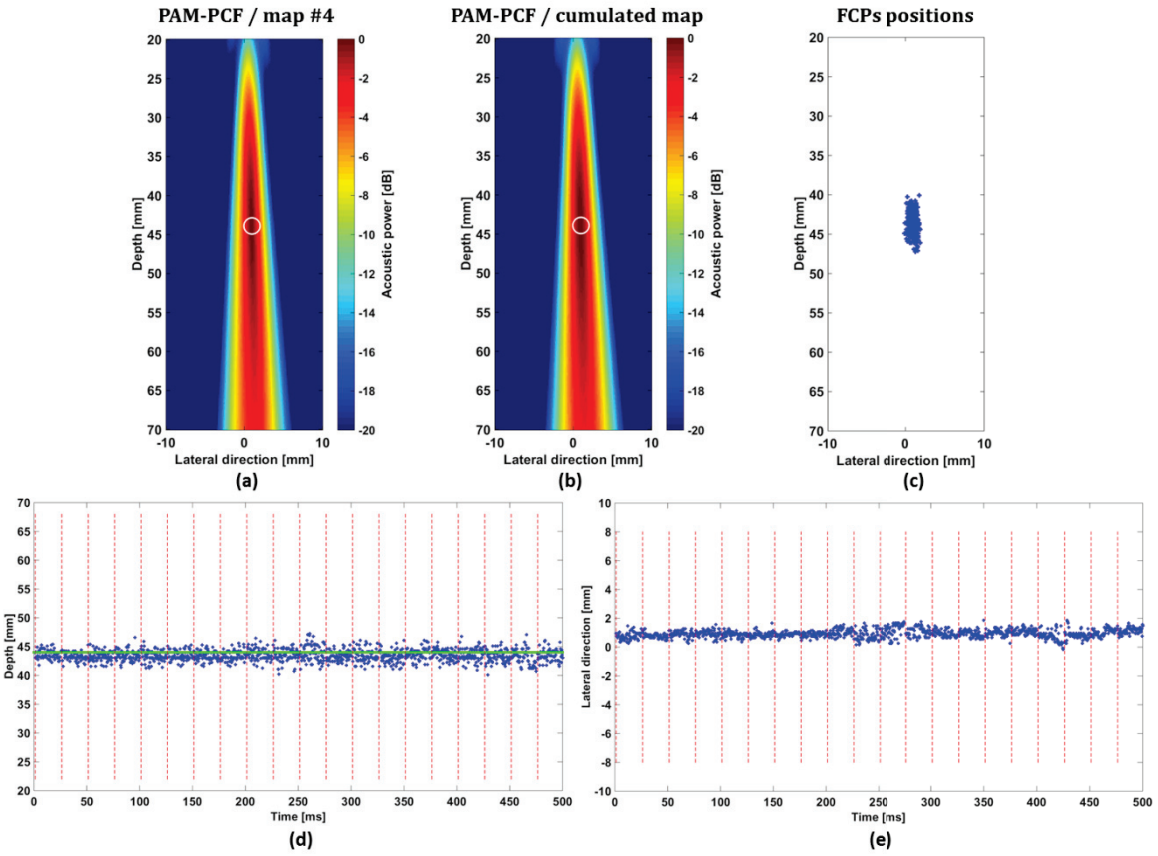

Figure III-4: Working in agar gel and using LA523 imaging probe with CI=20. (a) The cavitation map reconstructed with the PAM-PCF method for the 4th passive acquisition frame. (b) Cumulated map along 1500 maps. The white circle corresponds to the FCP localization. (c) The FCP 2D positions. The FCP localization temporal profile along 500 ms of sonication for both (d) depth and (e) lateral imaging direction. The horizontal green line represents the FCP theoretical depth reference and the vertical red dotted line corresponds to the start of each sonication pulse.

For a better visualization, the scales of the Figure III-4.(d, e) were enhanced and displayed in Figure III-5. The FCPs spatially oscillated in depth around the theoretical reference (44 ± 1.02 mm) and in the lateral direction (0.93 ± 0.28 mm) with no particular behavior. A “platform” aspect, more outlined in the lateral direction, is noted in Figure III-5.b. It corresponds to the discrete pixel positions values dependent to the resolution parameter set in the computation step. It can be partially resolved by increasing the pixel resolution of the reconstruction process. However, as we assess preliminary results with pixel resolution lower or equal to the pitch value of the imaging probe, there is no need to increase it. Likewise, the FCP recovery errors discussed in last chapter (experiment on a wire; section II.3.2) should be reminded. In this experiment, it could affect the FCP localization in the axial imaging direction when comparing results between cavitation transversal (LA523) and axial (LA332) planes. As asserted previously, the FCP recovery errors increases with the imaging depth which in this particular case is more pronounced for the cavitation axial plane (a 0.8 mm axial shift error average for focal depth at 80 mm > 70 mm) than for the cavitation transversal plane (a 0.4 mm axial shift error average for focal depth at 44 mm < 70 mm). Still, these errors are low compared to the actual FCP spatial extension (up to few mm). Therefore, in most of the cases it could be neglected.

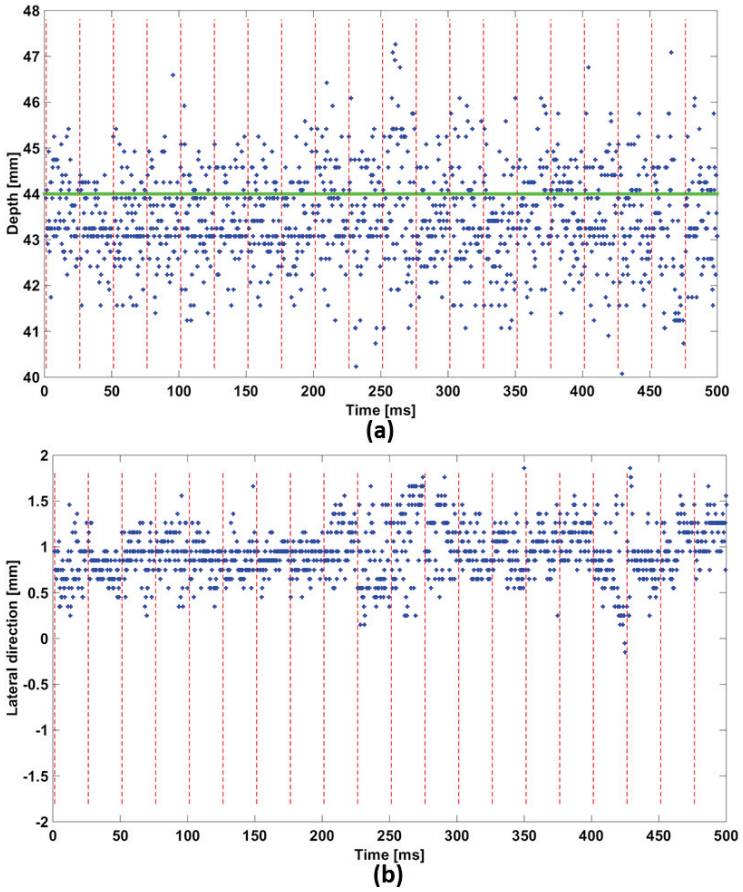

Figure III-5: Enhanced scale for the FCP localization temporal profile along 500 ms of sonication for both (a) depth and (b) lateral imaging direction.

III.1.1.3 Results

In this section an overview of the different results of the different cases are presented. The 2D FCP positions along the 500 ms of overall sonication are displayed for cases with or without agar gel, with an increasing CI, and for both cavitation planes in Figure III-6 (transversal plane) and Figure III-7 (axial plane). Moreover, for temporal investigation of the cavitation behavior, the FCP localization temporal profile in the imaging depth for CI equal to 10 or 25 are displayed for cavitation transversal plane in Figure III-8 and for cavitation axial plane in Figure III-9. However, having similar results and interpretations for the in-between cavitation activity intensity (CI=15 and 20), the FCP localization temporal profiles are not presented. Moreover, results for higher cavitation activity intensity (CI≥30), outlining some particular event and information, are presented and discussed progressively in the next section III.1.1.4.

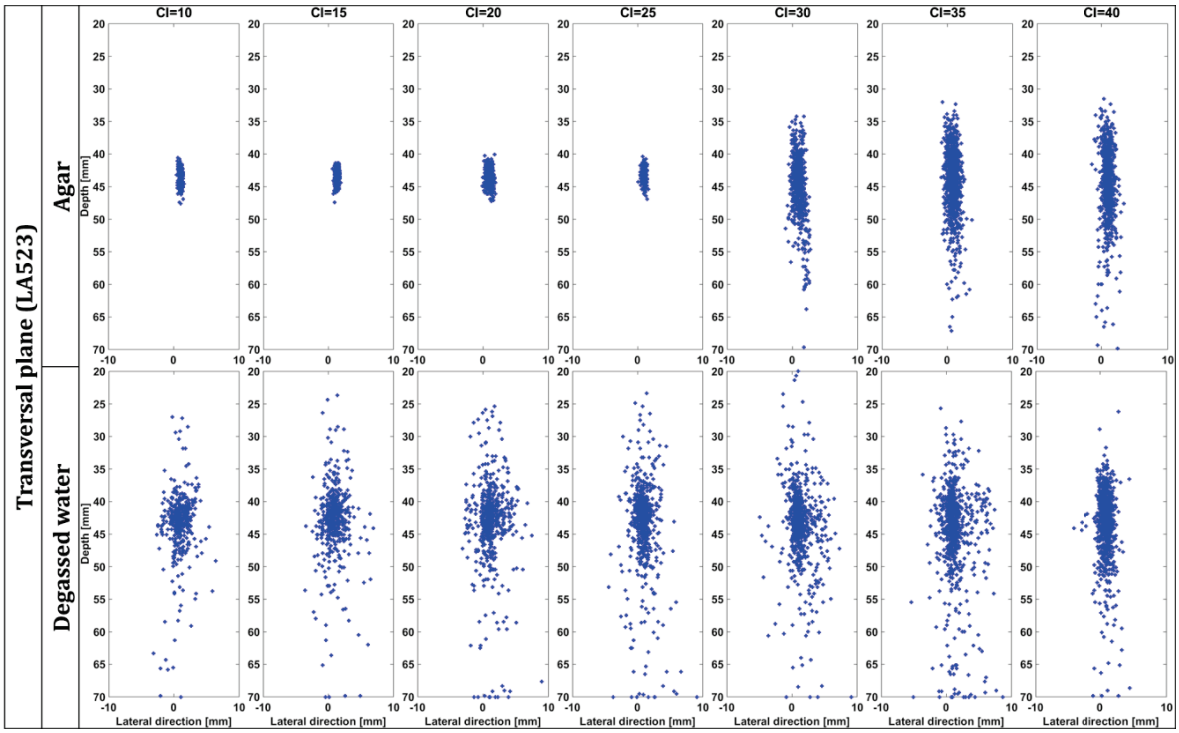

Figure III-6: Two dimensions focal cavitation point (FCP) positions along 500 ms of overall sonication for the cavitation transversal plane (LA523) with or without agar gel and with an increasing cavitation index (CI).

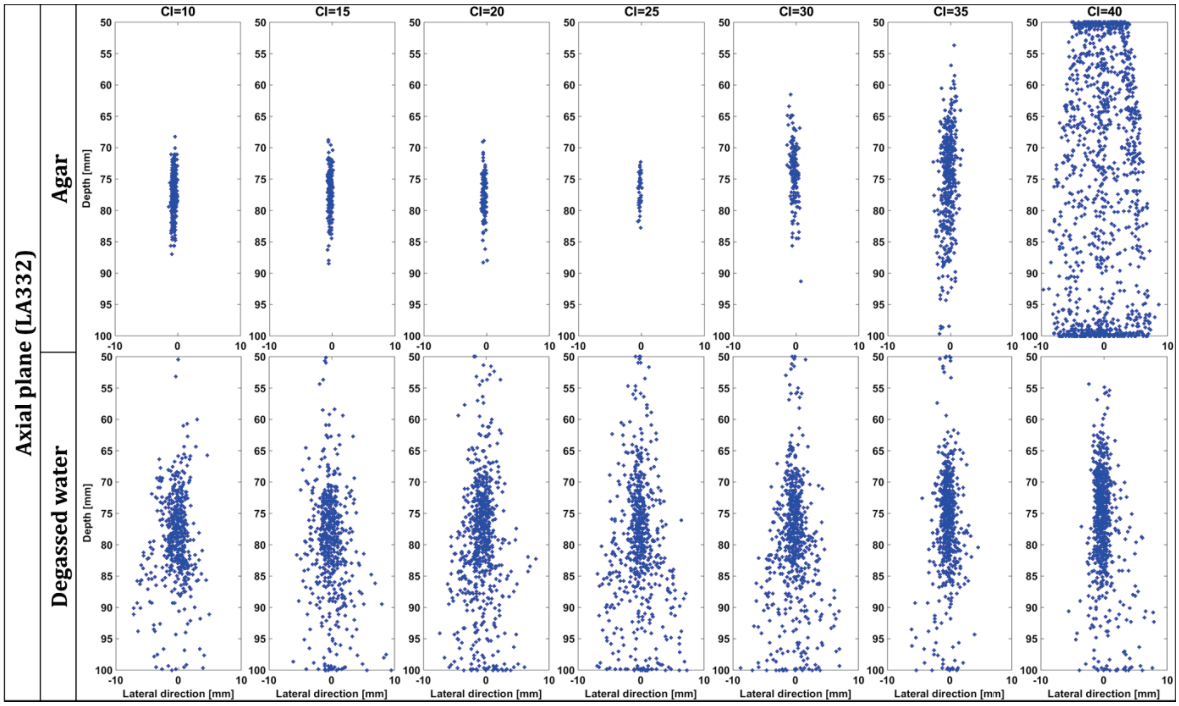

Figure III-7: Two dimensions focal cavitation point (FCP) positions along 500 ms of overall sonication for the cavitation axial plane (LA332) with or without agar gel and with an increasing cavitation index (CI).

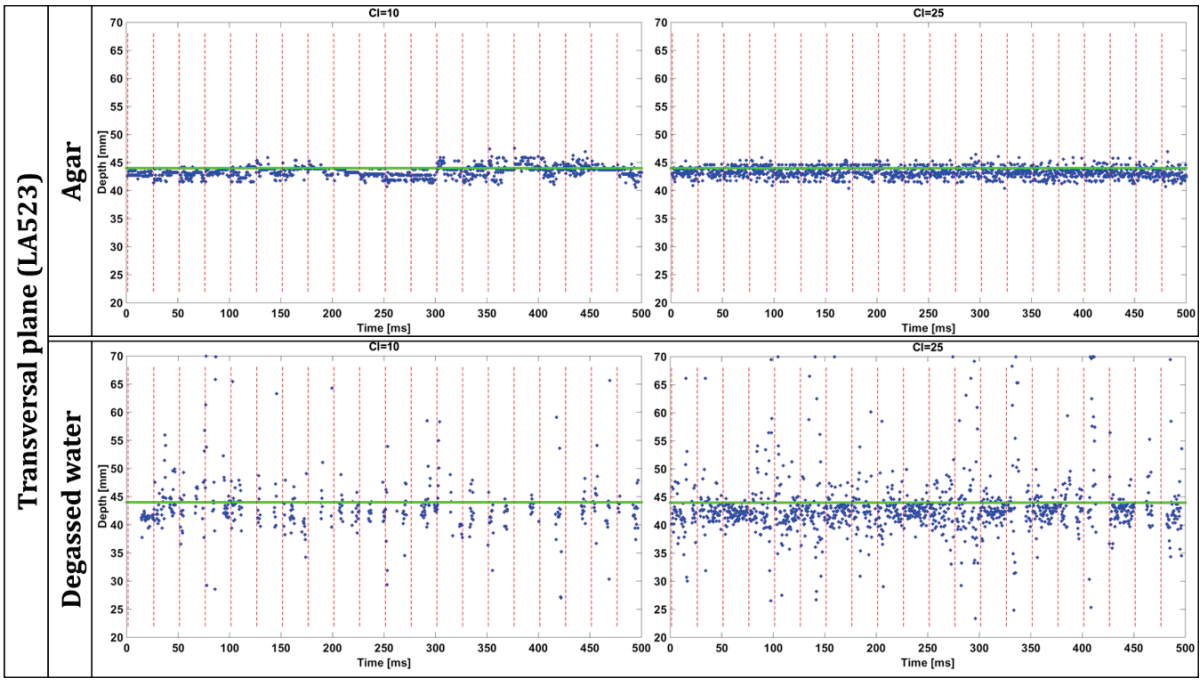

Figure III-8: The FCP localization temporal profile along 500 ms of sonication for the cavitation transversal plane (LA523), with or without agar gel and for cavitation index (CI) equal to 10 or 25. The horizontal green line represents the FCP theoretical depth reference and the vertical red dotted line corresponds to the start of each sonication pulse.

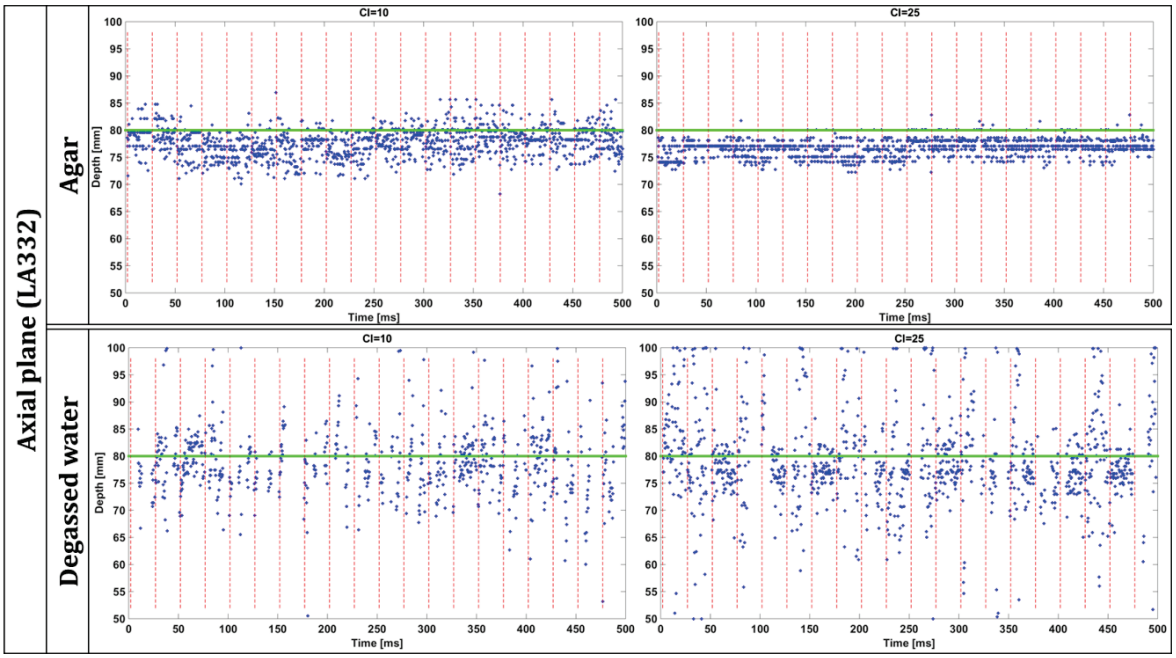

Figure III-9: The FCP localization temporal profile along 500 ms of sonication for the cavitation axial plane (LA332), with or without agar gel and for cavitation index (CI) equal to 10 or 25. The horizontal green line represents the FCP theoretical depth reference and the vertical red dotted line corresponds to the start of each sonication pulse.

In terms of spatiotemporal behavior, the US cavitation activity was investigated by analyzing the FCP spatial localization in depth for an increased CI. For every CI, the FCP was averaged along the 500 ms of sonication. It is displayed for the LA523 imaging probe corresponding to the cavitation

transversal plane in Figure III-10.(a, b) and for the LA332 imaging probe corresponding to the cavitation axial plane in Figure III-10.(c, d).

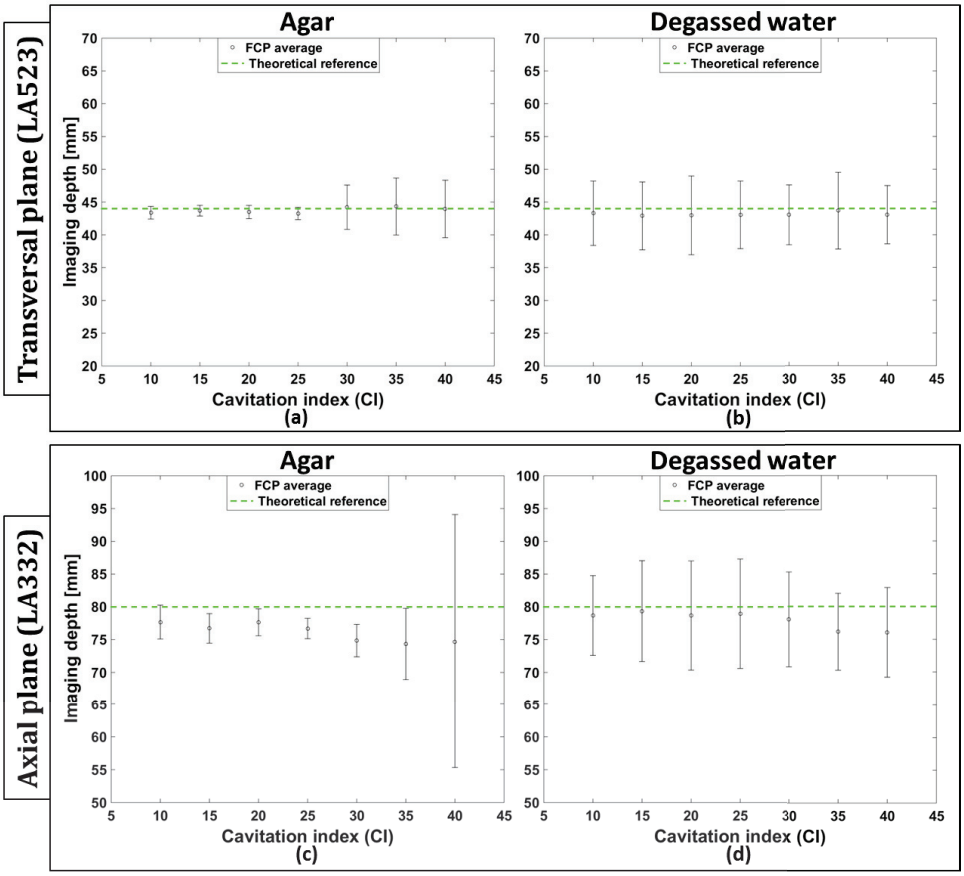

Figure III-10: FCP spatiotemporal evolutions for an increased CI and both transversal (LA523) and axial (LA332) cavitation planes with or without agar gel. The horizontal green dotted line represents the FCP theoretical reference.

III.1.1.4 Discussions

In the cavitation transversal plane (Figure III-10.(a, b)), the FCP average was constant and very close to the theoretical reference. In contrast, in the cavitation axial plane (Figure III-10.(c, d)), the FCP average was more discontinuous. With an increasing CI, it tends to migrate towards the therapeutic transducer. This observation is coherent with the physical already-known spatial behavior of the bubble cloud in this direction [60], [125]. Moreover, the FCP was spatially more extended in the cavitation axial plane than in the cavitation transversal plane which is coherent with the oval shape of the sonication beam in this direction. This extension is clearly noted when comparing the FCP positions in the imaging depth between both Figure III-6 and Figure III-7, mostly in agar case. However, as discussed in (III.1.1.2), it could also be partially due to the FCP recovery errors investigated during previous experiments on a wire.

In agar gel, bubbles are not free to move because of the gel's structure. The resulting confinement of the bubble cloud to a 2-mm-wide area was observed and confirmed in B-mode visualization of the bubbles remaining immediately after ultrasound shots at moderate cavitation activity (CI ≤25), and displayed in Figure III-11.a. For PAM-PCF during the shots, both axial and transversal cavitation planes (Figure III-10.(a, c)) showed very constant and reproducible patterns for such moderate cavitation: the FCP was spatially steady with an averaged standard deviation equal to 1.5 mm. This

confinement is also confirmed with 2D FCP positions in Figure III-6 and Figure III-7 as well as temporally observed with the FCP localization temporal profile for agar gel in Figure III-8 and Figure III-9.

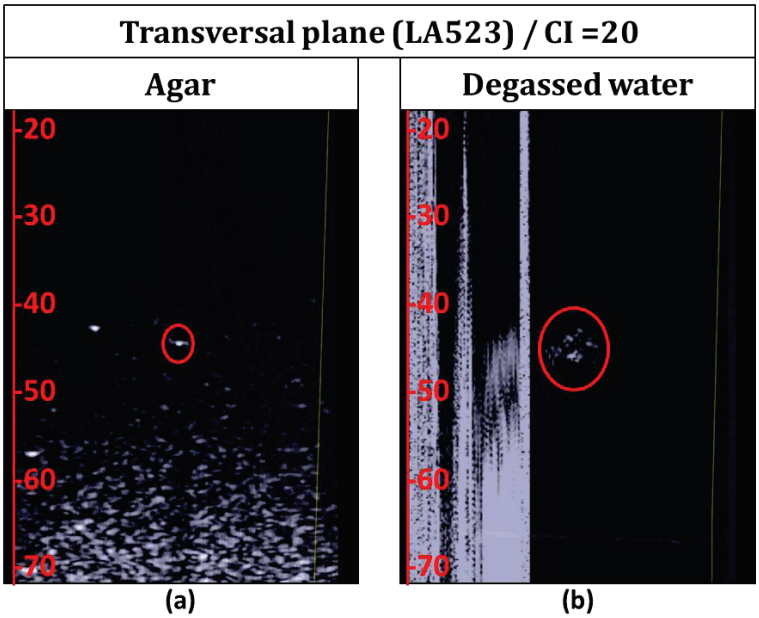

Figure III-11: Screenshots of the B-mode visualization for the cavitation transversal plane (LA523), for a cavitation index CI=20, and (a) with or (b) without agar gel. The white flash observed on the left side of the B-mode image in degassed water corresponds to the end of the sonication pulse. The red oval-circle delimits the hyperechoic area observed during the B-mode visualization.

On the other hand, in degassed water, bubbles were free to move (Figure III-11.b) and indeed they moved because they were subjected to external forces exerted by the acoustic wave and the water streaming: the acoustic wave was partially diffused by gas bubbles, resulting in acoustic radiation pressure on them, and the water flow (notably generated by acoustic streaming), which also results in drag force on immersed gas bubbles. The movement of the bubble cloud in degassed water for all sonication intensities was clearly visible during the ultrasound shots. In this experiment, this could be visually evaluated, and it was slightly greater in the acoustic axis direction where it equaled approximately 15 mm whatever the cavitation activity tested. The results obtained with PAM-PCF are coherent with this bubble cloud movement: in degassed water the FCP was enlarged (Figure III-10.(b, d)), with an averaged standard deviation equal to 6.2 mm. For degassed water and for decrease cavitation activity intensity (CI), an important increase in the gaps between each cavitation events was observed (Figure III-8 and Figure III-9). It is coherent with the gas ratio factor contributing to the nucleation mechanisms. When the gas dissolved in the medium is low, it is harder to initiate the nucleation. This is why higher sonication intensity (CI) is needed to nucleate and so to induce cavitation.

The mechanism of the cavity creation in agar gel, useful for the bubble cloud confinement discussed previously, is established by a progressive degradation of the agar gel at the focal therapeutic transducer focus in the early stage of the sonication pulses. This degradation was clearly observed during B-mode visualization with the progressive extension of the hyperechoic area limits (Figure III-14.a). In a particular case, recording at the very beginning of the sonication therapy for both cavitation planes, in agar gel, and for CI=30 (Figure III-12). The progressive confinement of the

bubble cloud was observed with the FCP localization in depth and in lateral direction where the FCP positions converged progressively. It could also correspond to the initiation of the bubble cloud (nucleation) at the focus.

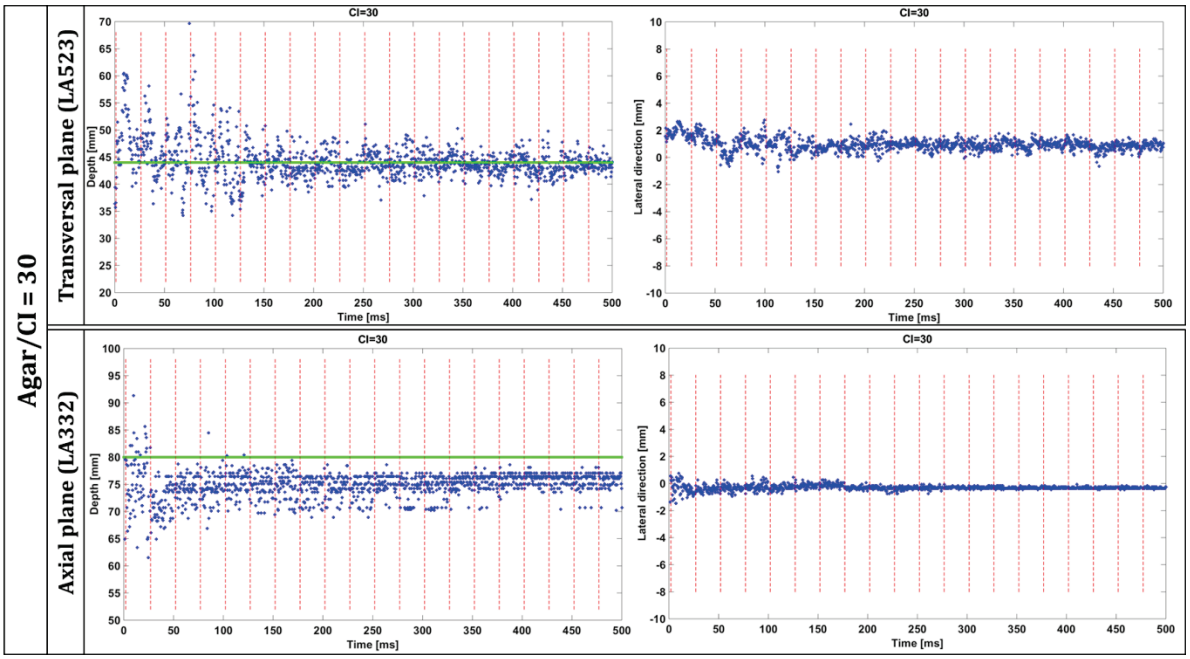

Figure III-12: The FCP localization temporal profile along 500 ms of sonication in agar gel, for a cavitation index (CI) equal 30, for both cavitation transversal plane (LA523) and the cavitation axial plane (LA332), and in both imaging depth or imaging lateral direction. The horizontal green line represents the FCP theoretical depth reference and the vertical red dotted line corresponds to the start of each sonication pulse.

Concerning higher cavitation activity intensities in agar gel (Figure III-10.(a, c); for CI=35), the FCP positions shows increased spatial variations which is quite constant along the entire 500 ms of sonication displayed in Figure III-13. This corresponds to an over-degradation of the agar gel, which leaves the bubbles freer to move, leading to a bubble behavior quite similar to that in degassed water (Figure III-6 and Figure III-7). It was confirmed with B-mode visualization in Figure III-14.(b, c). It could even be observed with lower cavitation intensities but with a slower and less marked over-degradation process meaning that it would need more overall sonication time to occur. Therefore, between each experiment case, the agar gel was displaced to prevent this over-degradation issue to be relayed to all experimental cases.

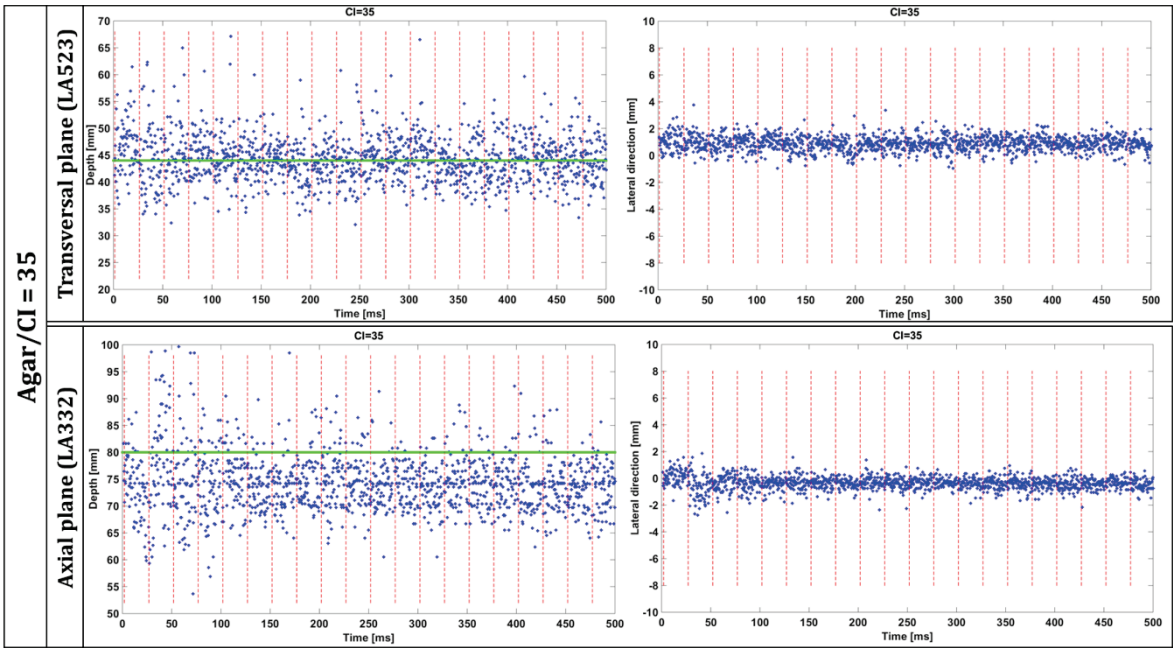

Figure III-13: The FCP localization temporal profile along 500 ms of sonication in agar gel, for a cavitation index (CI) equal 35, for both cavitation transversal plane (LA523) and the cavitation axial plane (LA332), and in both imaging depth or imaging lateral direction. The horizontal green line represents the FCP theoretical depth reference and the vertical red dotted line corresponds to the start of each sonication pulse.

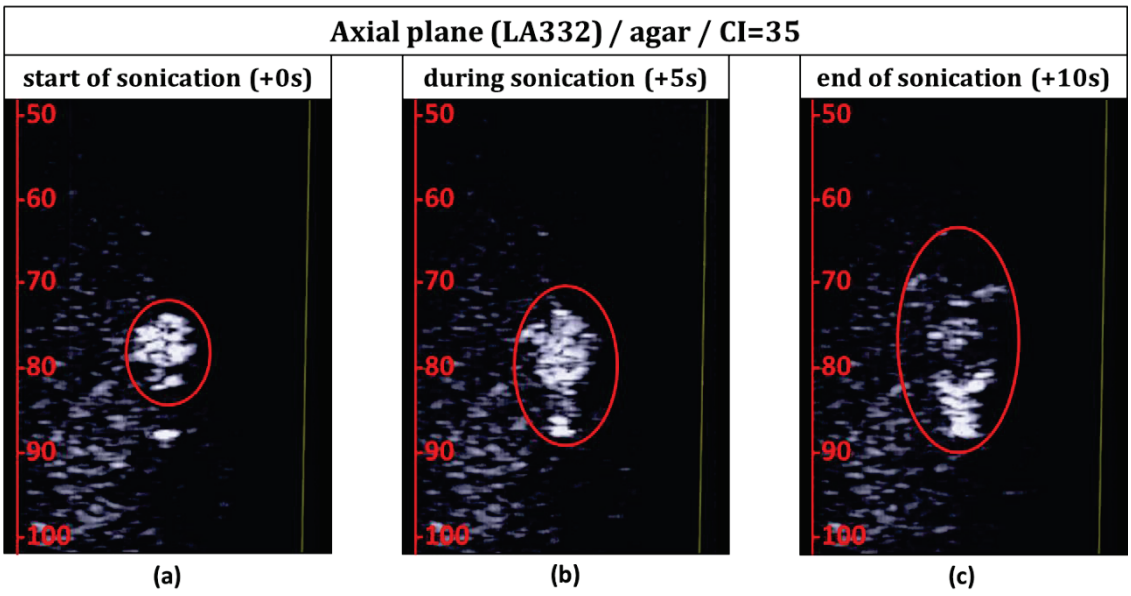

Figure III-14: Screenshots of the B-mode visualization for the cavitation axial plane (LA332), for a cavitation index CI=35, and with agar gel. (a) In the beginning of the sonication therapy, (b) during the sonication after 5 seconds, and (c) at the very end of the sonication session after 10 seconds. The red oval-circle delimits the hyperechoic area observed during the B-mode visualization.

Furthermore, at the highest cavitation activity intensity considered (CI=40), specifically for the cavitation axial plane (LA332), the FCP provided by PAM-PCF varied within a wide spatial range of tenths of centimeters (Figure III-10.c and Figure III-15). This corresponds to a situation of very high ultrasound amplitudes where some cavitating bubbles are sometimes visible on the water–agar interface, which is 40 mm from the imaging probe LA332, and in the travelling path of the focusing beam leading to the generation of multiple bubble cavitation clouds. It is worth noting in this case

that PAM-PCF detects a problem in the bubble cloud position, which should still be largely at the ultrasound focus. As observed with the cavitation map reconstructed with the PAM-PCF method from the 26th passive acquisition and displayed in Figure III-15.a, the FCP position is out-of-range of the image reconstruction limits in depth (50 mm → 100 mm). On that account and specifically for this frame, the reconstruction limits were increased (1 mm → 200 mm) and the zoomed out cavitation map for the 26th frame was reconstructed and displayed in Figure III-15.b. In this case, more than one cavitation clouds could be identified, and even if the bubbles at the ultrasound focus could be more than active and more numerous than those on the interface, searching for the FCP is no longer pertinent as observed in Figure III-15.(c-e). Besides, destructive and constructive interferences of the ultrasound waves transmitted by the multiples cavitation sources are recoded by the imaging probe and hence, are directly increasing the out-of-focus points corresponding to false positive cavitation sources. The fact that it is noticed only with the LA332 working in the therapeutic beam axis and with agar gel confirms the water-agar interface analysis. Likewise, this interface could also directly reflect a part of the incident sonication wave to the imaging probe. Basically these results and interpretations acknowledge the fact that this cavitation intensity CI=40 shouldn't be considered in the way of avoiding artifacts creation. Still, a more detailed study needs to be considered for this particular case and therefore, among other purposes, multi-spots cavitation experiment was proposed and is presented in the following (III.1.3).

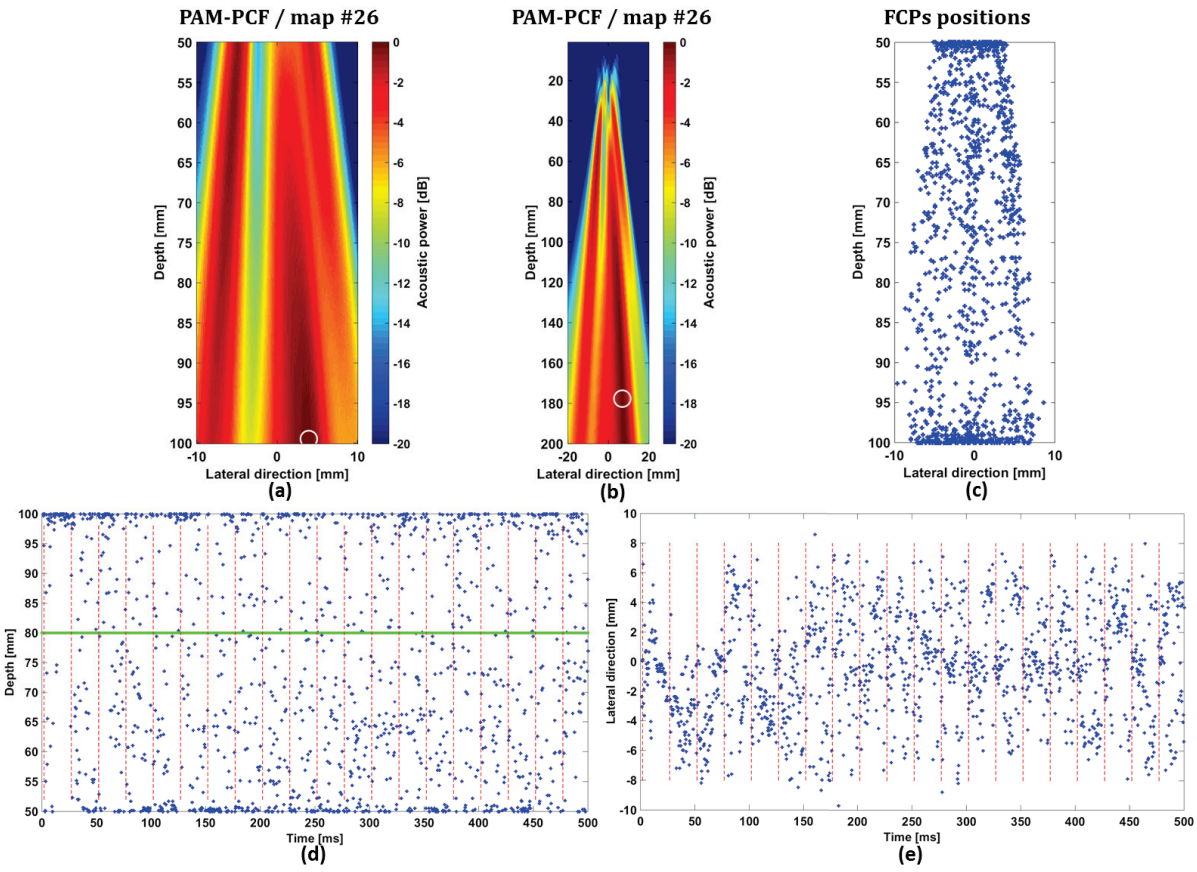

Figure III-15: Particular case in agar gel, in the cavitation axial plane (LA332), and for a cavitation index (CI) equal to 40. (a) The cavitation map reconstructed with the PAM-PCF method from the 26th passive acquisition. (b) The cavitation map reconstructed for the same 26th passive acquisition thought with a wider depth limits from 1mm to 200 mm. The white circle corresponds to the FCP localization. (c) The FCP 2D positions. The FCP localization temporal profile along 500 ms of sonication for both (d) depth and (e) lateral imaging direction. The horizontal green line represents the FCP theoretical depth reference and the vertical red dotted line corresponds to the start of each sonication pulse.

III.1.2 Non-regulated versus regulated cavitation

The activity behavior in term of FCP positions correlated with the radiated cavitation acoustic power are investigated and compared for both non-regulated (open loop) versus regulated (close loop) cavitation strategies.

III.1.2.1 Experimental setup and computation step

The same experimental setup and computation step as previous one-spot cavitation experiments (III.1.1.1 and III.1.1.2) was considered. But, only the LA332 imaging probe (axial cavitation plane) was used. Yet, as cavitation is easier to initiate in higher dissolved gas ratio, the dissolved gas in water was set this time at 7mgO2/L. To assess the unrestricted dispersion of the FCP positions and cavitation behavior, no agar gel was used for bubble cloud confinement. Moreover, it was already proved in previous study that the regulated cavitation system generator allowed better inertial cavitation activity initiation and behavior [97]. In the following study, the non-regulated cavitation strategy was investigated and thus the values of the radiated cavitation power are expected to be highly irregular. Therefore a more elaborated threshold operation was considered comprehending 4 threshold levels corresponding to 4 different matched colors:]-10;0] dB in black,]-20;-10] dB in red,]-30;-20] dB in green, and]-30;-40] dB in blue. The low- or no-cavitation events are as before omitted thanks to a -40 dB threshold.

In regulated cavitation strategy, the desired CI was set and then the temporal cavitation regulation algorithm (I.6) defined in real-time the amplitude tension $U(t)$ used as input of the therapeutic transducer. The averaged CI along the entire sonication was measured and it always converged to the desired one ($CI_{measured}$ = $CI_{desired}$). On opposite, in non-regulated cavitation strategy, a constant amplitude tension U(t) was manually set as input of the therapeutic transducer and the averaged CI along the entire sonication was still measured ($CI_{measured}$).

III.1.2.2 Results

For both regulated and non-regulated cavitation experiments the FCPs 2D positions are displayed in Figure III-16.

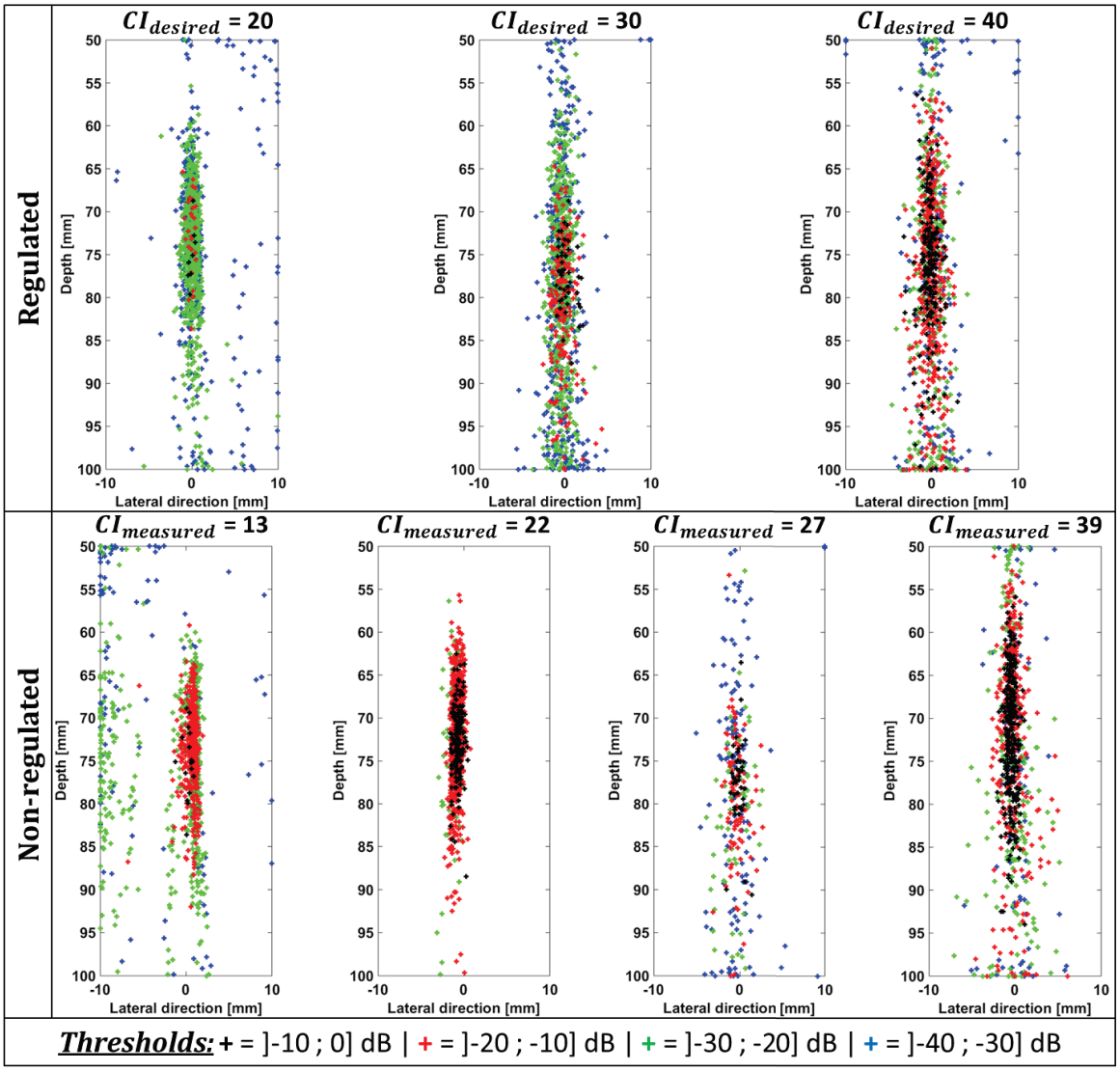

Figure III-16: The FCPs 2D positions for (on top) the regulated cavitation strategy and (on bottom) the non-regulated cavitation strategy. Four cavitation power threshold levels were used and outlined by four matching colors.

The FCP temporal profiles along 500 ms of sonication in the depth imaging direction are also displayed for regulated cavitation strategy in Figure III-17 and for non-regulated cavitation strategy in Figure III-18.

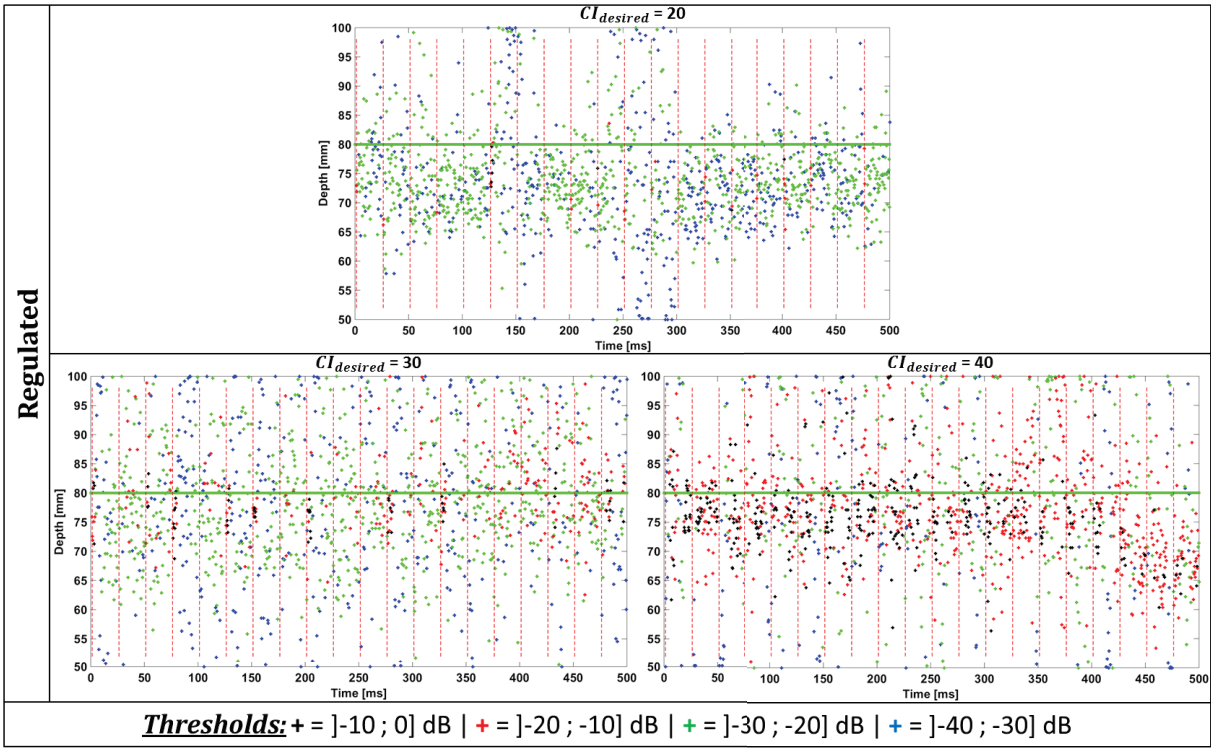

Figure III-17: The FCP temporal profile along 500 ms of sonication for depth imaging direction for the regulated cavitation strategy and for three desired CI = [20, 30, 40] dB. The horizontal green line represents the FCP theoretical depth reference and the vertical red dotted line corresponds to the start of each sonication pulse.

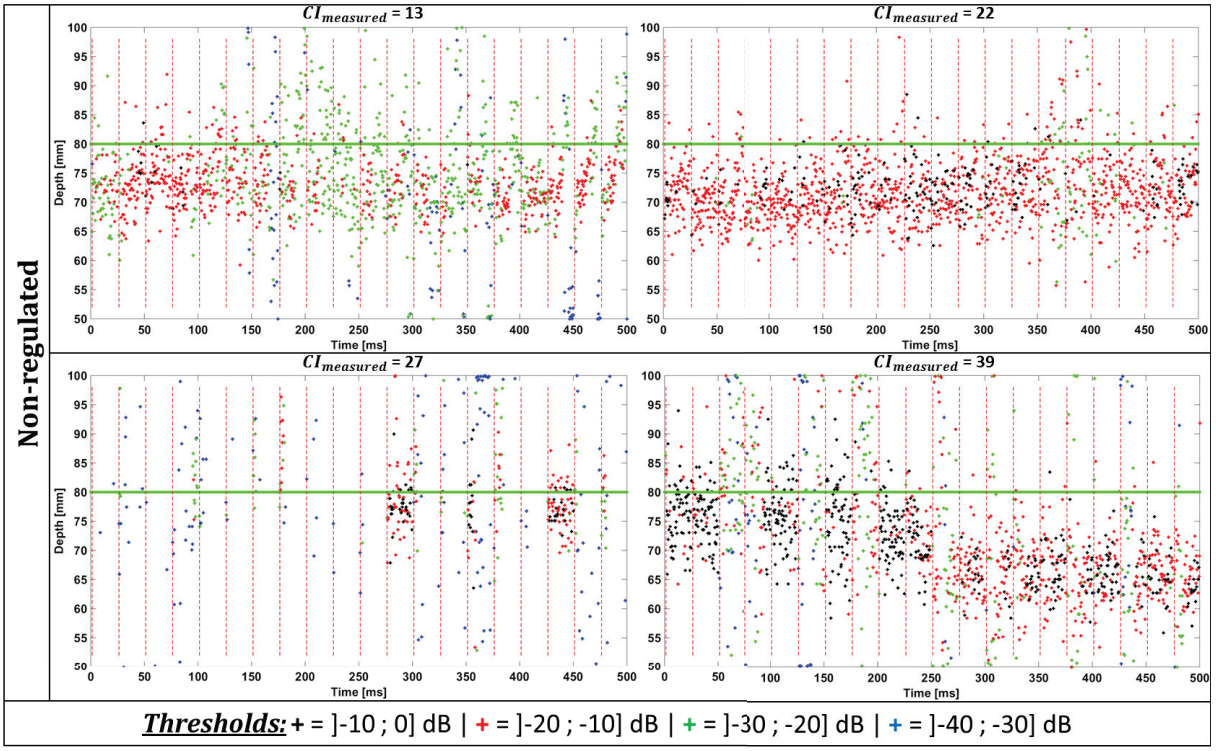

Figure III-18: The FCP temporal profile along 500 ms of sonication for depth imaging direction for the non-regulated cavitation strategy and for four different voltage outputs corresponding to four averaged measured CI = [13, 22, 27, 39] dB. The horizontal green line represents the FCP theoretical depth reference and the vertical red dotted line corresponds to the start of each sonication pulse.

The four levels threshold operation considered earlier is specific for each experimental case (regulated versus non-regulated and for the different CI) and hence the overall cavitation power cannot be compared between each case. Therefore, first to remove the low- or no-cavitation events, the global threshold of -40 dB operation was achieved separately for each case. Then the cavitation power of the FCP was normalized over the entire cases. Afterwards, for each case, the FCP cavitation power was averaged along the entire 500 ms of sonication and plotted for the whole cases in Figure III-19. Furthermore, for quantitative dispersion judgment, the standard deviations were also computed and were plotted as error bars in Figure III-19.

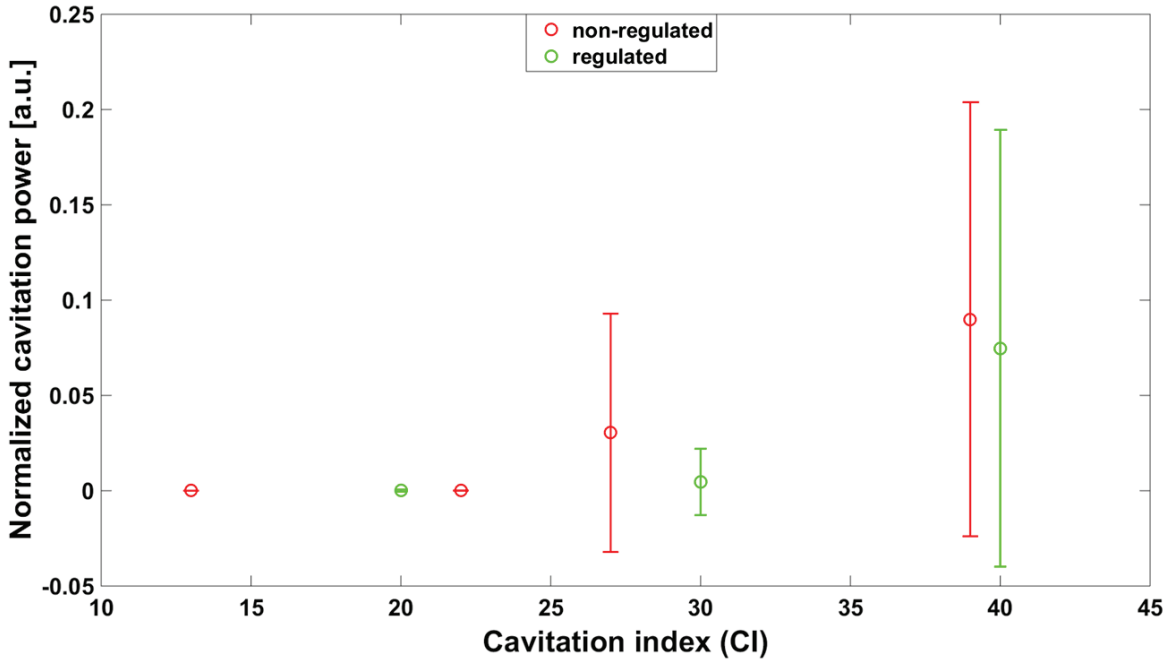

Figure III-19: Normalized cavitation acoustic power of the FCP averaged along the entire 500 ms of sonication for each experimental case and after a global threshold set at -40 dB. The regulated strategy is outlined in green and the non-regulated in red.

III.1.2.3 Discussions

First of all, for all the experimental cases, the majority of the highest cavitation power values, black and red color points representing a threshold of]-20;0] dB, are noticed for corresponding FCPs close to the focus. Still, the overall FCP positions tend to migrate towards the therapeutic transducer corresponding to the real-focus moving away from the theoretical-focus initially set at 8 cm deep (horizontal green line). This migration mechanism, previously observed and discussed in III.1.1.4, is temporally outlined in Figure III-18 specifically for the non-regulated strategy and with $CI_{measured}$ = 39 case. At approximatively 250 ms sonication time, a clear overall FCP position shift of around 1 cm occurred.

For the regulated strategy, when CI increases, the highest cavitation power values (black and red point) at the focus are more numerous. However, the global dispersion of the power values also increased with CI. This dispersion is outlined by the color diversity enhancement in Figure III-17 and by the standard deviation increase (green error bars) in Figure III-19. It means that even though for higher CI the cavitation power at the focus greatly increased, the global cavitation power is still

extended over a larger area around the focus. Therefore, a compromise must be made between high cavitation powers at the focus versus low global cavitation power dispersion.

For the non-regulated strategy, same interpretation could be noted with greater number of high cavitation power values (black and red points) at the focus with increase of the amplitude tension $U(t)$ (higher CI) observed in Figure III-18, as well as the increase of the global cavitation power dispersion outlined in Figure III-19 (red error bars). However the non-regulated cavitation behavior characteristic is clearly noticed in the specific experimental case for $CI_{measured}$ = 27 in Figure III-18 where a great number of low- or no-cavitation events were omitted.

However when comparing generally the FCP localization between non-regulated and regulated strategies, the FCP positions for the non-regulated one are more converging to the focus. It could be explained by the fact that to induce regulated inertial cavitation the cavitation generator system need to adapt the sonication intensity in real-time and so exert more random external dragging forces on the cavitating bubbles. Thus, the development of a monitoring system for cavitation localization specifically for its integration to the regulated focused ultrasound-induced cavitation generator is pertinent. Basically with regulated strategy, the reproducibility and the focus positions is more stable than with the non-regulated regime where probability of bad focus and power dispersion is much higher. As well with scenarios as case with $CI_{measured}$ = 27 could happen with very low number of exploitable cavitation events which is coherent with the results and discussions explored in previous studies for non-regulated versus regulated cavitation activity behavior in term of acoustic power [97].

III.1.3 Multi-spots cavitation

Until now, only one cavitation source corresponding to one cavitation bubble cloud was considered. However for more realistic experiments with high chaotic cavitation events, multiple cavitation separated bubble sources should be investigated to evaluate multi-localization ability of cavitation source of the PAM-PCF beamforming technique. Therefore a more complex method was developed with principally integrating another independent US cavitation generator.

From my knowledge, there is no existing multi-spots cavitation experiment developed using two independent US cavitation generator to induce separated bubble clouds. The closest works which could be mentioned is first the use of simulated cavitation records considering different number of sources [126], or second the use of two disjoint cavitation regions produced by insonifying an agar gel with two talc suspension channels [120].

III.1.3.1Experimental setup

The experimental setup developed was very similar to the previous one in section III.1.1.1 (same absorbers, degassed water, and ambient temperature). However, here two identical 1 MHz therapeutic transducers (IMASONIC SAS, Voray, France) focalized at 8 cm were used to induce two separate bubble cloud in agar gel. Hence, as only one regulated focused ultrasound-induced cavitation generator is available and could be exploited for one bubble cloud generation, a function generator with double outputs (out_1 and out_2) is instead used with a different power amplifier for each output: Amp_1 (69 dB, GN 1000, PRANA, Malemort, France) and Amp_2 (66 dB, AMPAR 801, PRANA, Malemort, France). Therefore, during this experiment the cavitation intensity activity (CI)

was not regulated and so the reproducibility cavitation activity factor was not considered. Both outputs (out_1 and out_2) were set as a pulsed sinusoidal signal at 1 MHz, 4-Hz pulse repetition, and 10% duty cycle similar to the therapy signal considered in the previous one-spot cavitation experiment. The LA332 imaging probe, incorporated into the therapeutic transducer, was exclusively operated. The agar gel was prepared with the same protocol as previous setup. However, as this time two bubble clouds need to be confined, a bigger mold (18 cm × 18 cm × 14 cm) was used. The agar gel was positioned 35 mm from the LA332 imaging probe. Both bubble clouds were induced at 80 mm from each corresponding therapeutic transducers. Thus, the bubble cloud induced by out_1 (bc_1) was localized at 80 mm from LA332 probe and centered in the lateral imaging direction. The bubble cloud induced by out_2 (bc_2) was localized at 95 mm from the LA332 probe and at 11.5 mm in the lateral imaging direction as displayed in Figure III-20. Therefore, the LA332 probe images the (z, y) plane corresponding to the cavitation axial plane of the bubble cloud (bc_1) and the cavitation frontal plane of the bubble cloud (bc_2) as outlined in Figure III-25.

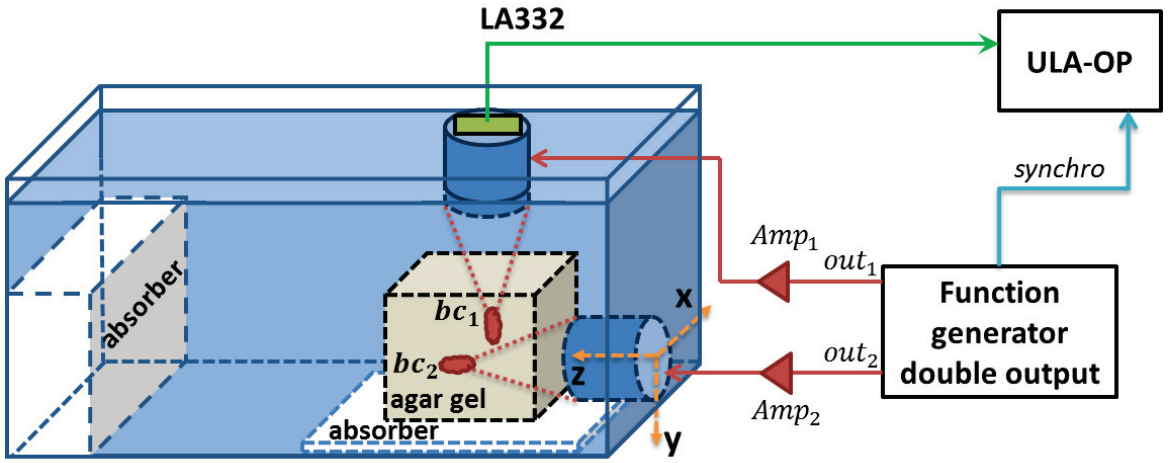

Figure III-20: Cavitation experiment setup using two therapeutic transducers to induce two separate bubble clouds (bc_1 and bc_2). The imaging system with one imaging probe (LA332) is synchronized with both sonication pulses.

The RF data were acquired and the ULA-OP acquisitions were synchronized with the double output function generator thanks to the "Enable" synchronization configuration displayed in Figure III-21. The τ_{Enable} width was set to 25.7 ms and the phase shift ϕ_{Enable} was tuned to allow acquisitions just during the sonication pulses with the first and the last frame of each sonication pulses additionally recorded. The ULA-OP acquisitions were performed with an internal 3000 Hz PRF.

Three different cases were considered: only out_1 is ON (case #1), only out_2 is ON (case #2), or both out_1 and out_2 are ON (case #3). For each case, a total of 616 passive acquisitions (RF signals) were recorded representing 8 pulses of 77 RF signals each (75 lines during sonication plus two outside).

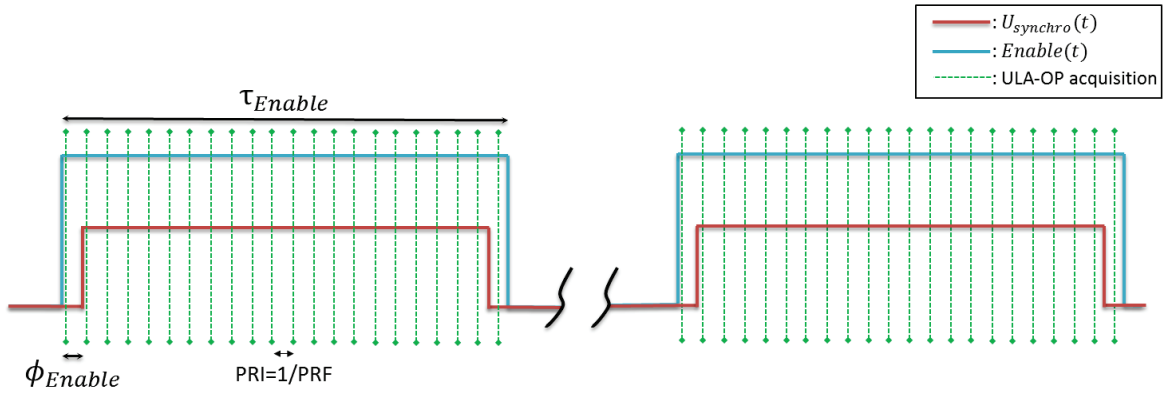

Figure III-21: Synchronization configuration established between the two simultaneous sonication pulses (function generator double output) and the ULA-OP acquisition using "Enable" configuration. The first and last frames are acquired outside of each sonication pulse.

III.1.3.2 RF signal electronic saturation

As discussed before, the US cavitation in this case was not regulated. Hence, because of the non-regulated cavitation activity and mostly because of the difficulty to perfectly calibrate the cavitation intensity generated simultaneously from both outputs with their corresponding power amplifier, the pre-beamformed RF signals recorded by the LA332 imaging probe exhibited electronic analogical saturation. It is recognized as a square signal instead of sinusoidal signal observed for example in Figure III-22.b. and outlined with the averaged spectrum over the total 64 active elements of the probe (Figure III-22.c). For visualization aspect not the entire spectrum was displayed in Figure III-22.c, instead the spectrum scale was limited to 10 MHz maximum. However, a high harmonic numbers of the 1 MHz signal could be identified for at least 20 MHz corresponding partially to the square signal shape. It means that the frequency analysis of these saturated RF signals is not considered for cavitation interpretation. The harmonics generated from the square signal cannot be differentiated from the ones generated by the cavitation. However, the hyperbolic delay shapes, the most essential information for PAM reconstruction algorithm, is still available and observed in Figure III-22.a. Moreover, as the acoustic intensity is maximized (saturation) then the acoustic cavitation radiated power values cannot be investigated, meaning that when applying the threshold operation to remove low- or no-cavitation events only the no-cavitation events are omitted. Therefore, when looking at the FCP localization results, some FCP positions could correspond to very low cavitation intensity events and hence this issue would need to be dealt with in future experimental protocol.

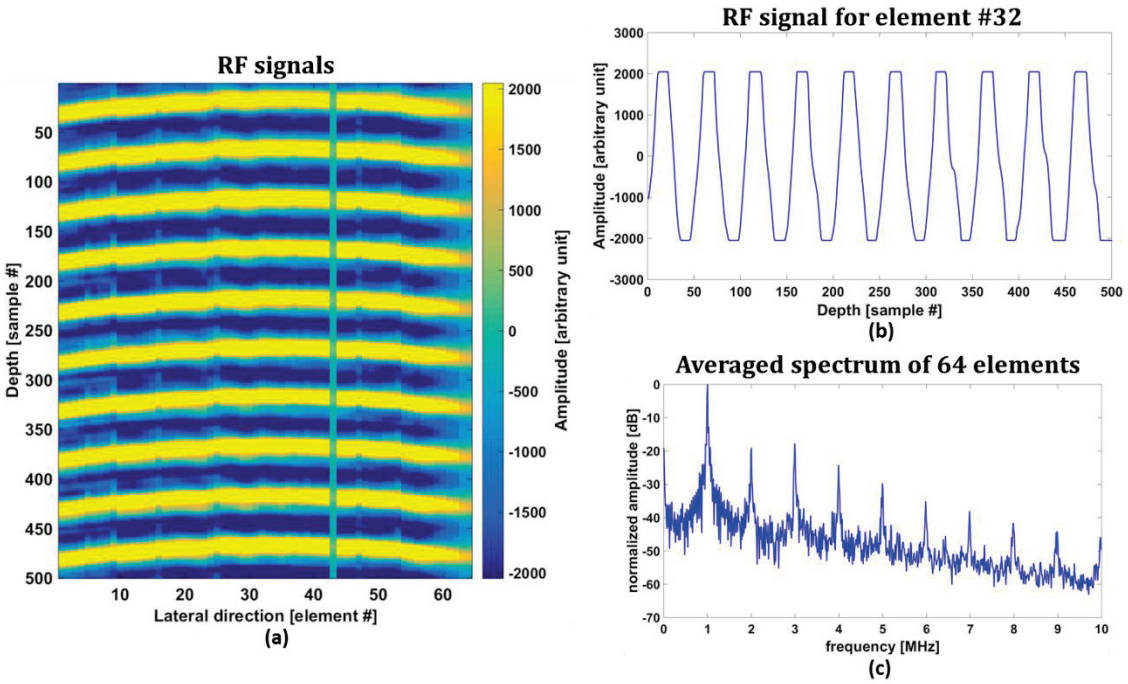

Figure III-22: Electronically saturated RF pre-beamformed signal recorded by the LA332 probe for case #1 of the multi-spots cavitation experiments and for frame #5: (a) the 64 total RF signals, (b) the RF signal plot for central element number 32, and (c) the averaged spectrum over the entire 64 total active elements. Element number 43 was damaged and so the corresponding RF signal wasn't considered.

Furthermore, for a closer acoustic signature to the one for non-saturated data, the saturated signals were filtered with a high-pass Butterworth filter of 5^{th} order and with a 1.25 MHz cutoff frequency. The non-saturated reference RF signals is displayed in Figure III-24 and it corresponds to the pre-beamformed data recorded by the same LA332 probe during the one-spot cavitation experiment in degassed water, with a CI=20 and for frame #36. The filtered RF data displayed in Figure III-23 look very similar to the non-saturated reference RF signals (Figure III-24) in term of frequency signature and sinusoidal shape.

Actually, for all the computation process, the same filtering step was already applied to the pre-beamformed data prior to the beamforming step for first, removing the DC component from the RF data (ULA-OP material specific), and second to indirectly lower the linear scattering for cavitation prevailing over linear scatterers in the medium.

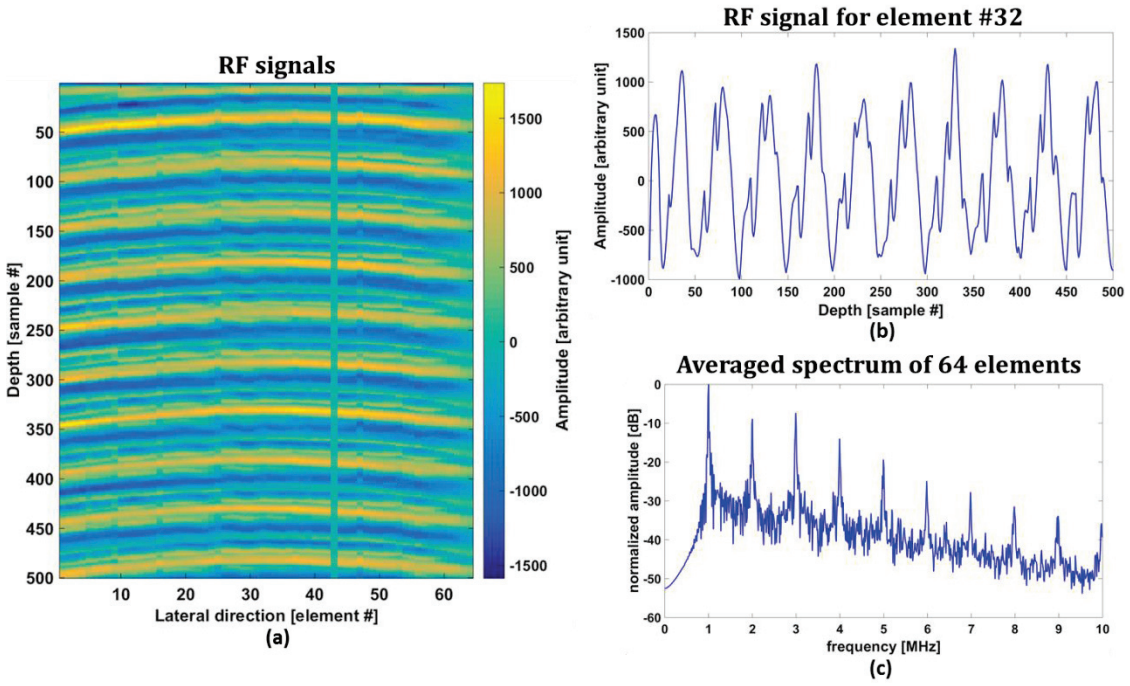

Figure III-23: Electronically saturated RF pre-beamformed signal recorded by the LA332 probe for case #1 of the multi-spots cavitation experiments and for frame #5 and filtered by a high-pass Butterworth filter: (a) the 64 total RF signals, (b) the RF signal plot for central element number 32, and (c) the averaged spectrum over the entire 64 total active elements. Element number 43 was damaged and so the corresponding RF signal wasn't considered.

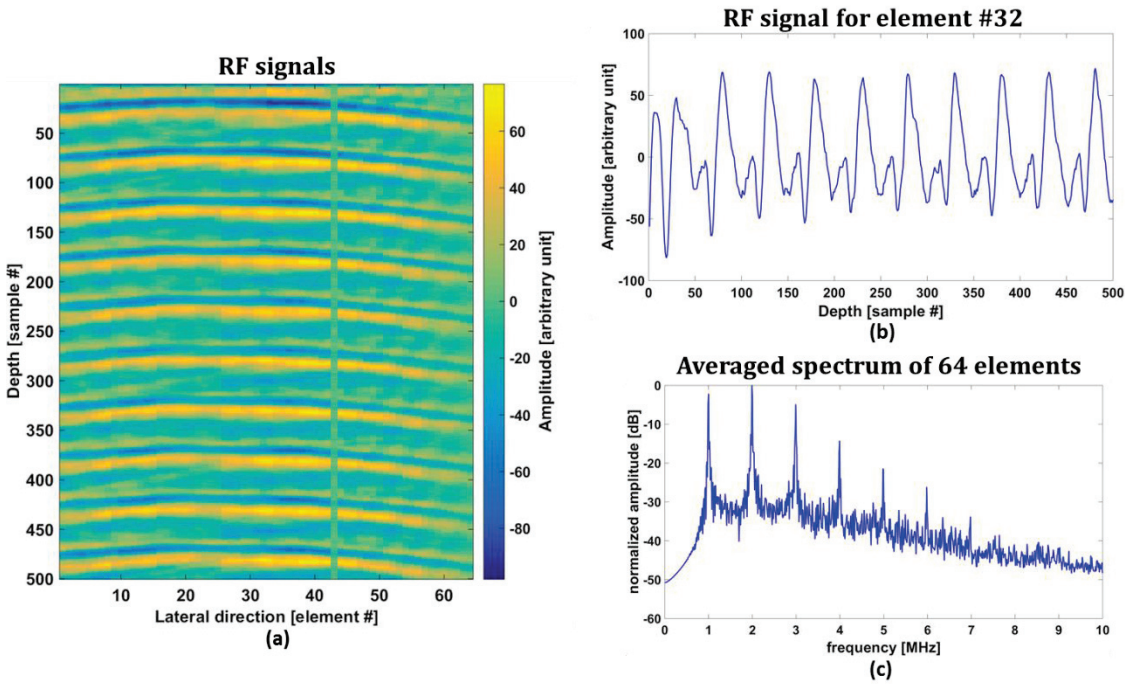

Figure III-24: Reference non-saturated RF pre-beamformed signal recorded by the LA332 probe during the one-spot cavitation experiment in degassed water, with CI=20, and for frame #36: (a) the 64 total RF signals, (b) the RF signal plot for central element number 32, and (c) the averaged spectrum over the entire 64 total active elements. Element number 43 was damaged and so the corresponding RF signal wasn't considered.

III.1.3.3 Computation step

Same computation steps as in section III.1.1.2 was applied to each RF data for all three cases. However different passive image reconstruction parameters were adapted, as displayed in Figure III-25. 70 mm × 40 mm [axial × lateral direction] images were reconstructed thanks to PAM-PCF with 400 pixels × 300 pixels corresponding to a 0.175 mm × 0.133 mm pixel resolution. The minimum depth (axial imaging axis) was set at 50 mm and the lateral imaging axis was centered at zero. 616 cavitation maps were computed along 205.33 ms of overall sonication corresponding to 8 pulses of 25.66 ms.

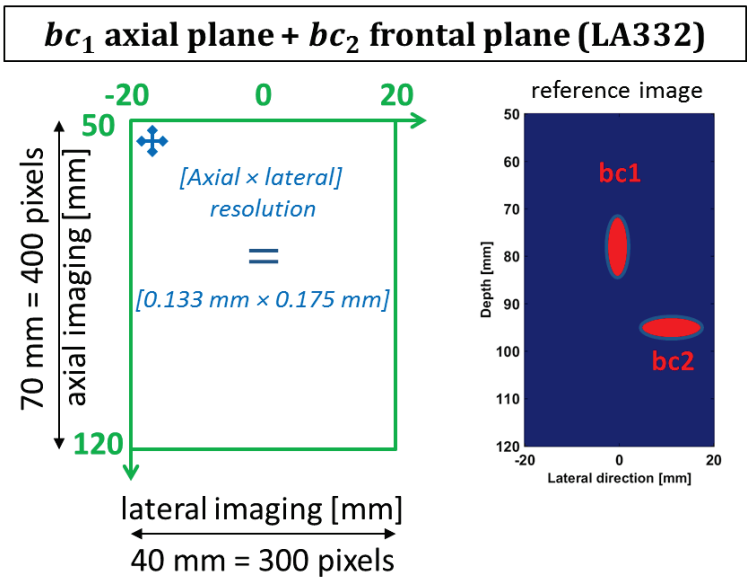

Figure III-25: Image reconstruction parameters for LA332 probe imaging the (z, y) plane corresponding to the cavitation axial plane of the bubble cloud (bc_1) and the cavitation frontal plane of the bubble cloud (bc_2). A reference image is displayed to outline the bubble cloud shape and focal point localization. The bubble cloud limits are not at the right scale, it is used as a representative reference image.

III.1.3.4 Results

Results were displayed for case #1 in Figure III-26, for case #2 in Figure III-27, and for case #3 in Figure III-28. For each case, different frames of PAM-PCF reconstructed cavitation maps are outlined. As well as the cumulated map along the entire 616 maps and the two dimensions FCPs positions are presented.

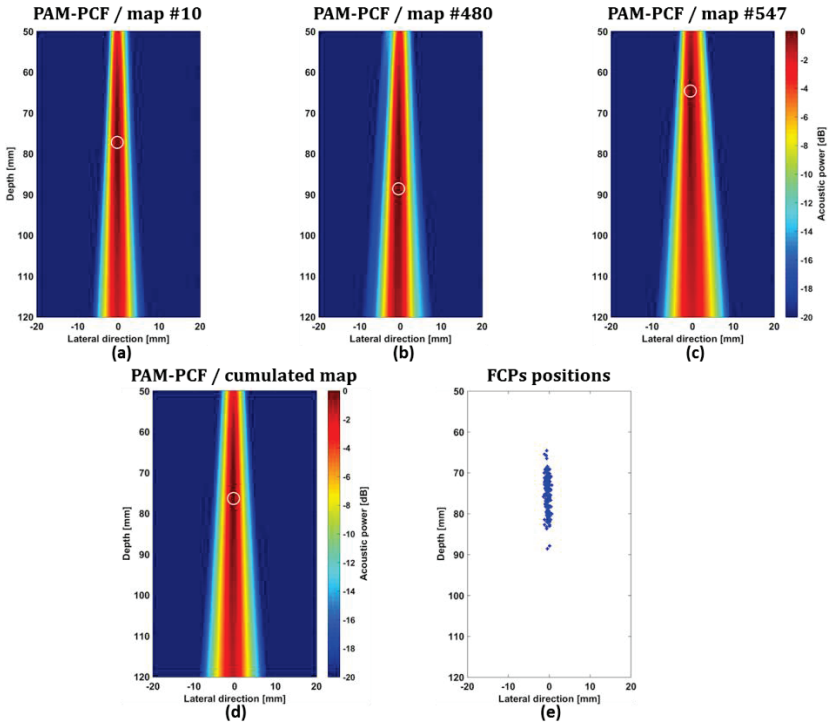

Figure III-26: Results for case #1 where only the out_1 was ON (only bc_1 bubble cloud was present). (a-c) The cavitation map reconstructed with the PAM-PCF method from three different passive acquisition frames. (d) The cumulated map along 616 maps and (e) the FCP 2D positions. The white circle corresponds to the FCP localization.

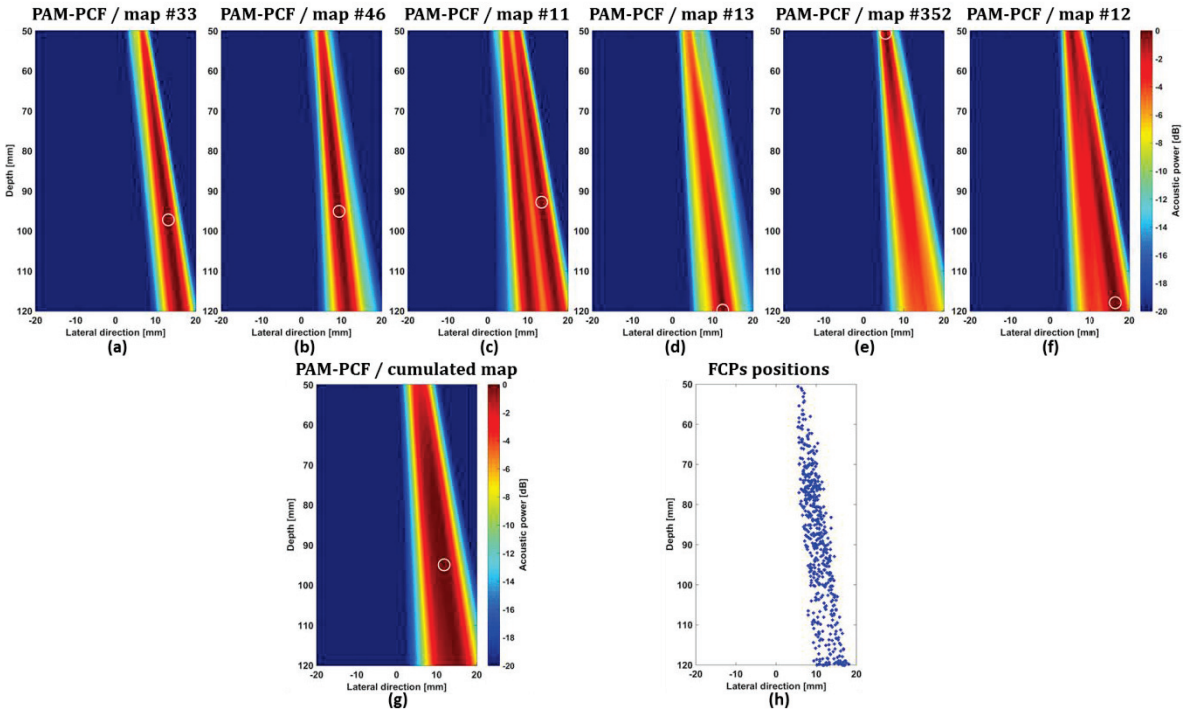

Figure III-27: Results for case #2 where only the out_2 was ON (only bc_2 bubble cloud was present). (a-f) The cavitation map reconstructed with the PAM-PCF method from six different passive acquisition frames. (g) The cumulated map along 616 maps and (h) the FCP 2D positions. The white circle corresponds to the FCP localization.

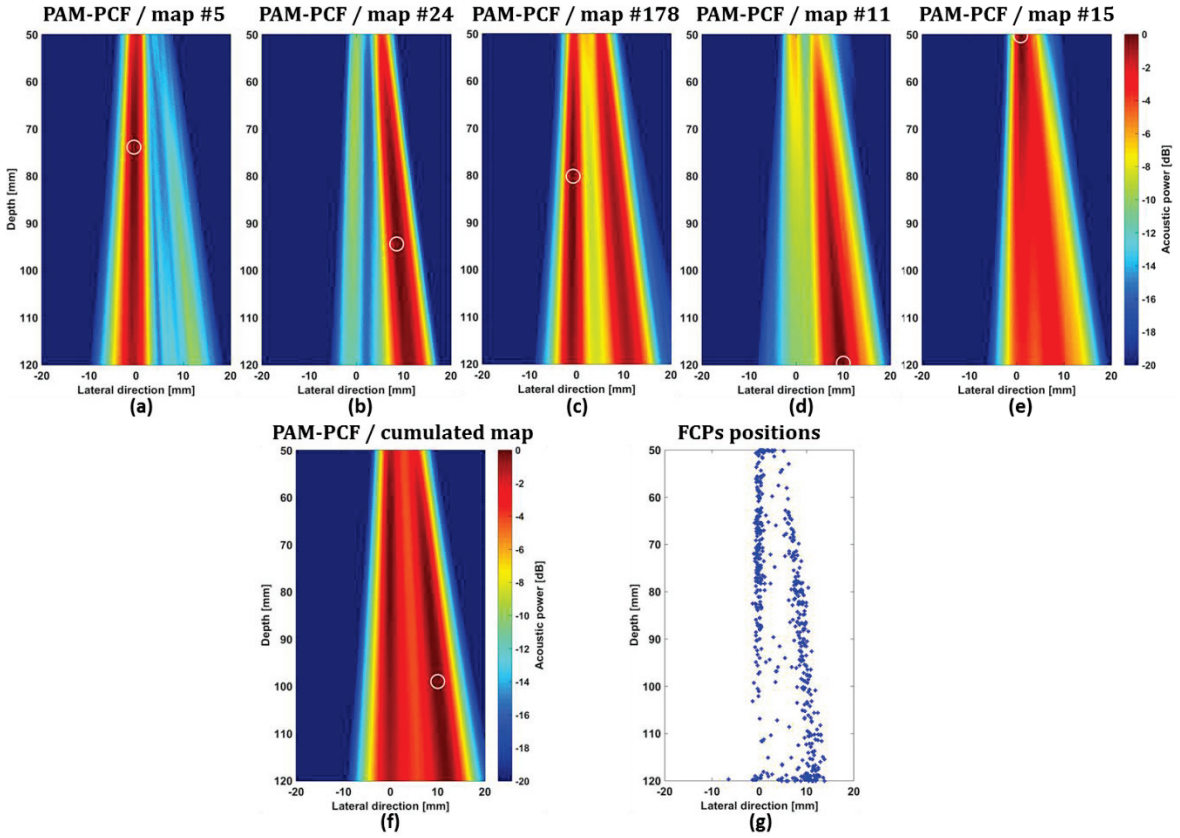

Figure III-28: Results for case #3 where both out_1 and out_2 was ON (both bc_1 and bc_2 bubble clouds were present). (a-e) The cavitation map reconstructed with the PAM-PCF method from five different passive acquisition frames. (f) The cumulated map along 616 maps and (g) the FCP 2D positions. The white circle corresponds to the FCP localization.

III.1.3.5 Discussions

For case #1 where only the out_1 was ON (bc_1 bubble cloud), the same observations and interpretations as for the one-spot cavitation in the cavitation axial plane are noticed. The bubble cloud is confined in the agar gel and the FCP positions are more extended in the cavitation axial direction.

For case #2 where only the out_2 was ON (bc_2 bubble cloud), the cavitation frontal plane is considered meaning that we are imaging the oval longer side shape of the bubble cloud. Moreover, the cavitation sources (cavitating bubbles) were distributed in the lateral imaging direction centered at 11.5 mm with a total extension of around 7 mm (distribution from 8 mm to 15 mm). This distribution was confirmed in B-mode visualization and was confirmed in PAM-PCF results with the three frames (Figure III-27.(a-c)) and the FCPs positions (Figure III-27.h). In the frame #11 (Figure III-27.c), two different cavitation spots could be observed however when applying the FCP localization it does not consider both of them. Therefore a more complex and automatic multi-focal cavitation spots localization was developed. It includes a segmentation labeling tool (label connected components) combined with a threshold operation. After applying this automatic cavitation spots localization step to the frame #11, both cavitation spots were recognized and the FCPs for each spot was localized (Figure III-29.(a,b)). Furthermore, it was also applied to the entire 616 cavitation maps and hence the overall 2D FCPs positions were computed and displayed in Figure III-29.c.

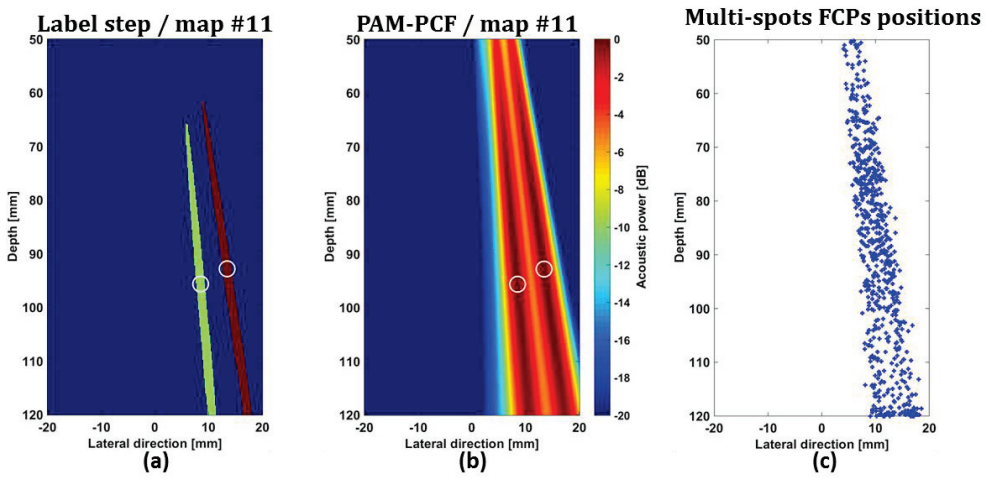

Figure III-29: For case #2 where only the out_2 was ON (only bc_2 bubble cloud was present). (a) The 2 connected objects (cavitation spots) recognition after applying the threshold then the label segmentation step on the PAM-PCF cavitation map frame #11. (b) The PAM-PCF cavitation map frame #11 with multi-spots FCP localization. The white circle corresponds to the FCPs localization. (c) The overall 2D FCPs positions including all multi-spots cavitation recognized.

For case #3 where both out_1 and out_2 was ON (bc_1 and bc_2 bubble clouds), both cavitation spots were predominantly observed during the entire sonication which is confirmed by the cumulated map (Figure III-28.f). However both bubble clouds are not always simultaneously induced because of the non-regulated and not perfectly synchronous cavitation sonication pulses. As confirmed in Figure III-28.(a,b), the non-synchronous effect is observed where only one-spot cavitation (bc_1 or bc_2) is alternatively dominant. Figure III-28.c. exhibits one frame example where both cavitation spots are presents and localized with PAM-PCF. Hence, same as for case #2, the new automatic multi-spots detection step was applied to the entire cavitation maps. The labeling segmentation step and the multi-spots maps for 5 frames (the same as in Figure III-28) are respectively displayed in Figure III-30.(a-e) and in Figure III-30.(f-j). Additionally, the cumulated multi-spots map and the overall 2D FCPs positions are presented in Figure III-30.(k-m).

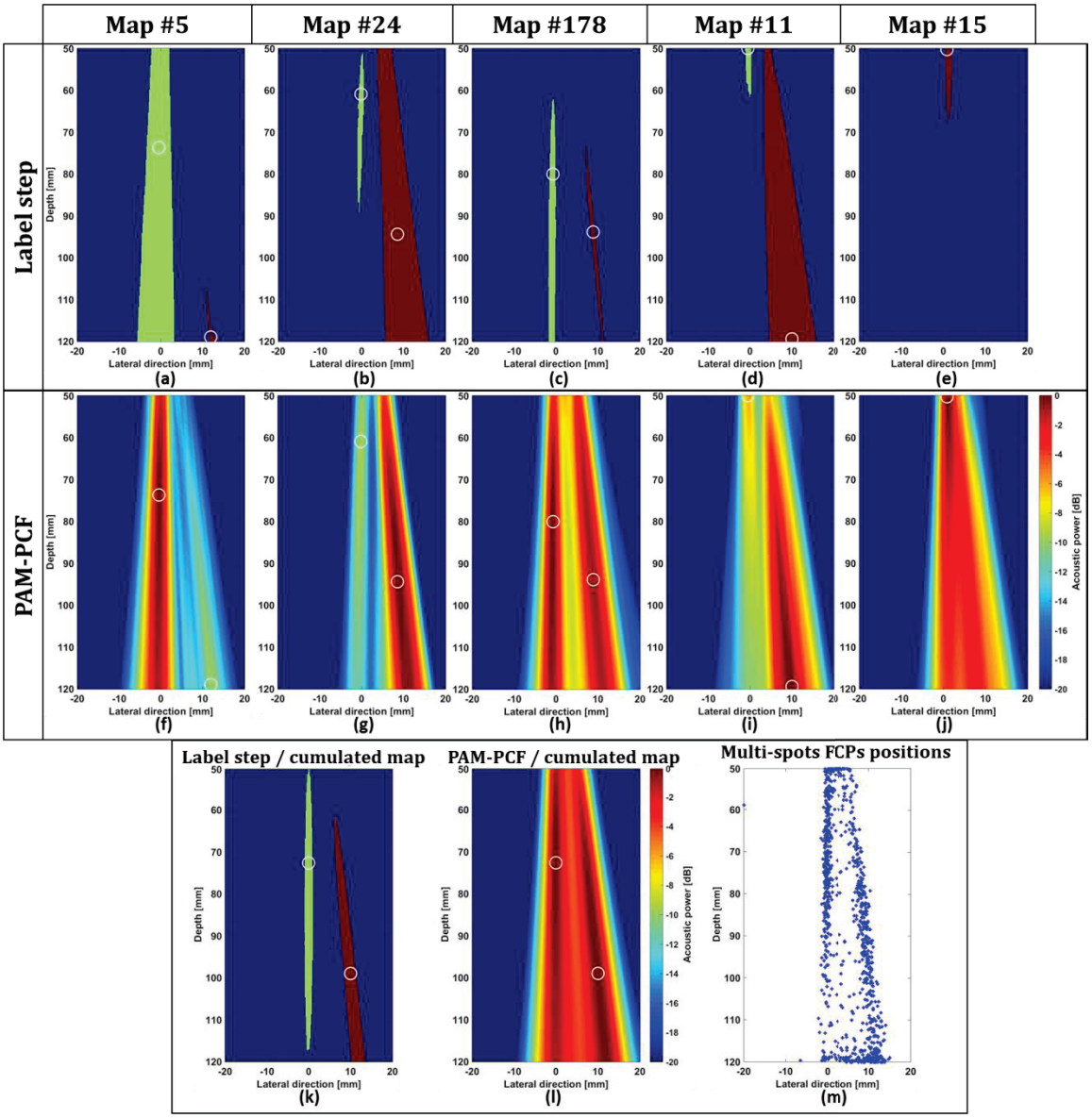

Figure III-30: For case #3 where both out_1 and out_2 was ON (both bc_1 and bc_2 bubble clouds were present). (a-e) The 2 connected objects (cavitation spots) recognition after applying the threshold then the label segmentation step on 5 frames of PAM-PCF cavitation map. (f-j) The 5 frames PAM-PCF cavitation maps with multi-spots FCP localization for both cavitation spots. The white circle corresponds to the FCP localization. (k) The cumulated label step and (l) PAM-PCF multi-spots cavitation map. (m) The overall 2D FCPs positions including all multi-spots cavitation recognized.

Yet, another issue is noticed for both case #2 and #3, in Figure III-27.(d-f) and Figure III-28.(d, e) where the FCP is out of range of the reconstructed image. It was already observed with the particular case with one-spot cavitation experiment and very high cavitation intensity (CI=40) in Figure III-15. It could be explained mainly by interferences of the wave fronts emitted by different cavitation sources (bubble clouds) arriving at the same time on the imaging probe. For better understanding of this case and of bubble emission interferences issues, a more controlled ground truth protocol need to be developed as example the use of a scattering wire shifted in many positions (same experimental protocol than the one in Chapter II). But this time the corresponding RF pre-beamformed recorded signals are summed for different position of the wire to get a pseudo-multi-sources spots dataset.

III.2 *In vivo* experiment

Many more experimental investigations and validation process before *in vivo* animal ultrasound thrombolysis testing is required. However, as the opportunity of performing *in vivo* experiment on animals turned up, the use of our passive imaging system incorporated within *in vivo* protocol was achieved. The main objective of this *in vivo* experiment was to test the innovative ultrasound thrombolysis technique on an ovine model in order to demonstrate its efficiency in real situation. Specifically for this experiment, a "three offset aperture" passive image acquisition sequence was developed and is presented in section III.2.3. In the following, first a quick overview of the *in vivo* setup and protocol is presented, and second some preliminary *in vivo* PAM-PCF results are computed and outlined. For more detailed information about the full *in vivo* protocol please refer to the last chapter in "Adrien POIZAT" PhD thesis [97].

III.2.1 *In vivo* thrombolysis experimental setup

A specific *in vivo* thrombolysis setup was developed, displayed in Figure III-31.b, involving the previous regulated induced-cavitation generator system partially defined by the therapy device, the FPGA module, and the power amplifier. The therapy device, which cut plane is outlined in Figure III-31.a, incorporates principally the therapeutic transducer (same transducer used in the previous water tank cavitation experiments), the hydrophone used for measuring the inertial cavitation index (CI), the imaging probe LA332, and a coupling balloon filled with degassed and filtered water. A portable ultrasound scanner (ESAOTE MYLAB 30 GOLD) was combined with the incorporated imaging probe, helpful for B-mode and Doppler visualization and localization of the stenosed area. Moreover, a 6-axis robotic arm (DENSO VS050) coupled to a controller (DENSO RC8) and a joystick was implemented. It is very useful, first to accurately and manually position the therapy device on the desired area, and second to automatically scan the entire thrombus for a total controlled destruction.

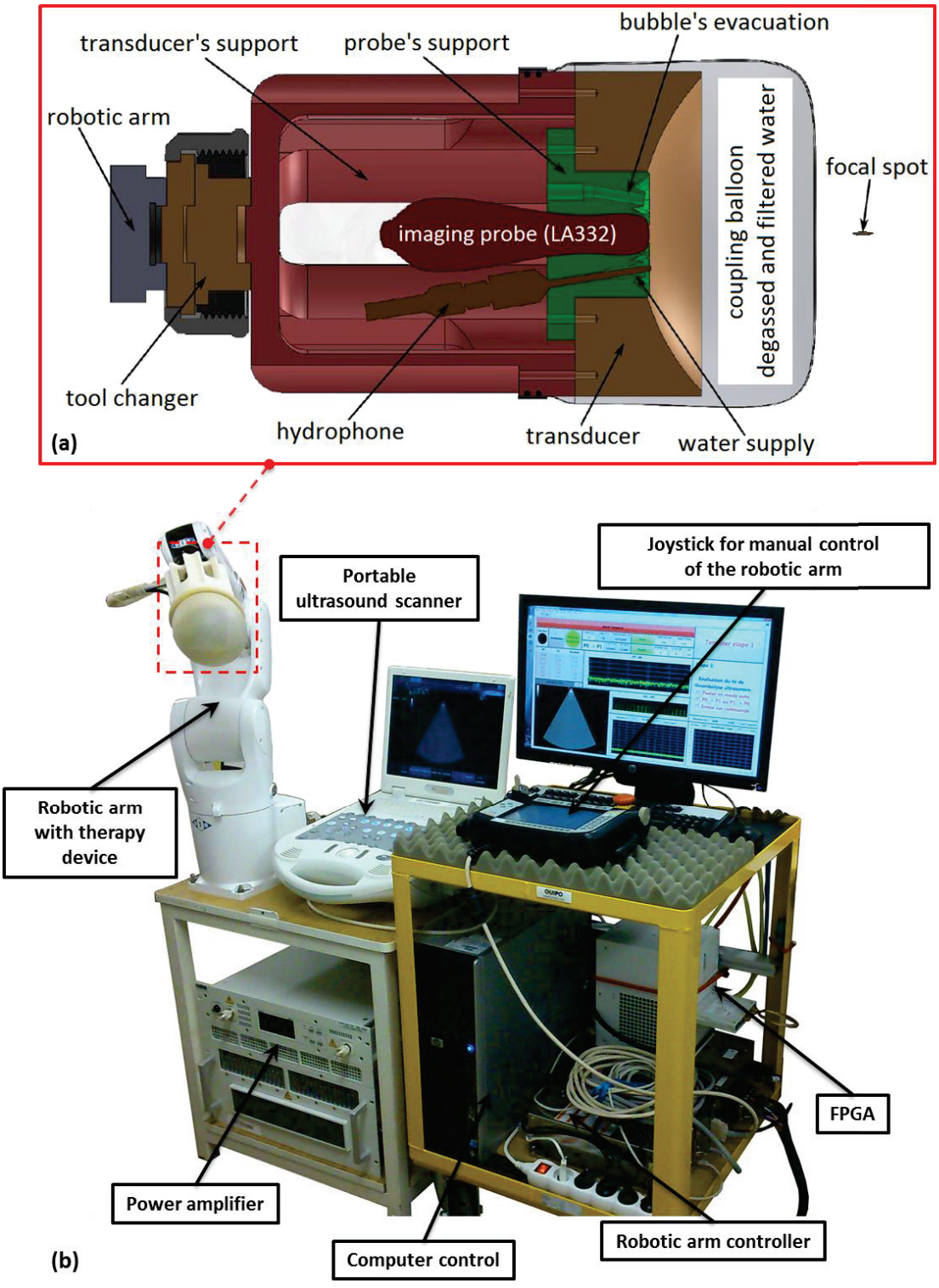

Figure III-31: (a) Cut plane of the *in vivo* therapy device including mainly the therapeutic transducer, the hydrophone, the imaging probe LA332, and a coupling balloon. (b) *In vivo* complete experimental thrombolysis setup including the regulated induced-cavitation generator system, an ultrasound scanner, and a 6-axis robotic arm system. [97]

III.2.2 *In vivo* thrombolysis protocol

The *in vivo* experimental protocols have previously been inspected and validated by an ethics committee. All animal experiments were carried out on the NAMSA platform site located in Chasse-sur-Rhone, France in collaboration with the diagnostic and therapeutic imaging department of

Professor Didier Revel of the “Louis Pradel “Hospital in Bron, France. There are two main steps in the *in vivo* thrombolysis experimental protocol: first, the creation of a thrombus, and second its destruction using the ultrasound extracorporeal thrombolysis setup previously presented.

For preliminary *in vivo* experiments, the acute lower limb ischemia protocol was chosen because it is less difficult to perform than more complex models as myocardial infarction or brain ischemia. Moreover, specifically for this experimental testing, a protocol was developed for ovine models. Sheep species was chosen because of its high cardiovascular resistance system and its closer cardiovascular anatomy to human one. The protocol model consists in the creation of a controlled sized thrombus in the femoral artery of a goat by blocking and slowing down the blood circulation specifically in the desired area thanks to coils deposited with a catheter. The thrombus formation is monitored thanks to first ultrasonography imaging combining B-mode images for anatomical visualization and Doppler imaging for blood flow circulation information, and second angiography images. If the thrombus took too much time to form (longer than 1 hour) then a thrombin bolus was injected within the catheter directly to the desired site to enhance thrombosis mechanisms.

Once the thrombus is formed and blocks the femoral artery, the ultrasound sonication can be planned. The therapeutic device is manually placed thanks to the robotic arm on the sheep’s leg as observed in Figure III-32. A coupling gel is deposited *a priori* between the skin and the balloon. Then, thanks to B-mode ultrasonography anatomical visualization, the two extremities of the thrombus (two points A and B outlined in Figure III-33) are located and their positions (three dimensions coordinates) are saved. Finally, ultrasound sonication shots are performed during 180 seconds along the entire 1 cm length thrombus thanks to a linear sweep between both points A and B at a constant speed of movement of 0.055 mm/s. The sonication therapy signal used was the same as with the water tank cavitation experiments: pulsed sinusoidal signal at 1 MHz, 4 Hz pulse repetition, and 10 % duty cycle. The regulation feedback loop was turned on and the inertial cavitation index was set at CI=25 dB. Sometimes, if deemed necessary, a repetition of the sonication shots in reversed direction (from point B to A) is also performed. At the end of the testing, the sheep is sacrificed.

To know if the thrombolysis procedure worked and destroyed the thrombus, three imaging modalities were alternatively used: ultrasound imaging coupled with Doppler imaging, angiography images, and post-surgery histology procedure of the vessel cross-section in the targeted area.

Figure III-32: Picture of the *in vivo* experimental testing during ultrasound sonication shots. The therapy device is placed on the sheep's leg thanks to the robotic arm system. [97]

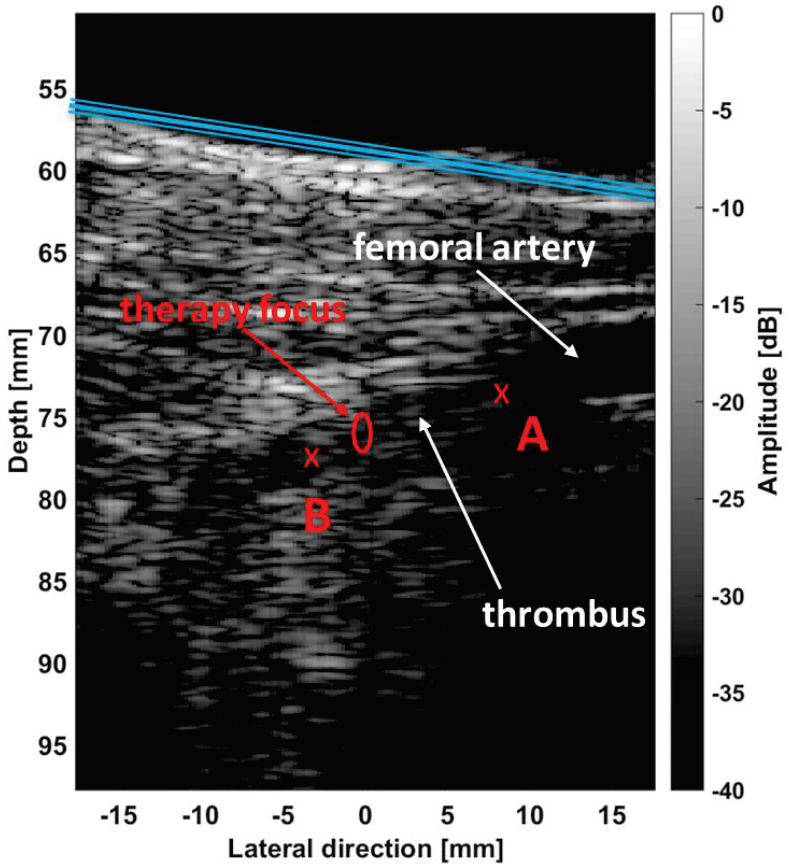

Figure III-33: The In-phase and Quadrature (I/Q) post-beamformed image representing the femoral artery blocked by a thrombus. The image was acquired with the LA332 imaging probe between ultrasound sonication shots performed during a linear sweep between both points A and B. The blue triple line corresponds to the water-balloon-skin-tissue interface.

III.2.3 Passive data acquisition

During the ultrasound sonication shots, passive data acquisitions were achieved. Hence, instead of using the portable ultrasound scanner (ESAOTE MYLAB 30 GOLD), the ULA-OP system was used combined with the imaging probe LA332 incorporated in the therapy device. As this *in vivo* experiment took place in the early stage of the PhD project, the synchronization configuration system presented in Chapter II was not developed yet. Thus, the passive ULA-OP acquisitions were not synchronized with the therapy signal and so were achieved during the entire signal with a 6000 Hz PRF as displayed in Figure III-34. Moreover, to take advantage of the entire aperture imaging probe, a particular "three offset aperture" passive image acquisition sequence was developed and presented in Figure III-34 and Figure III-35. It consists in using 64 consecutive active elements at three different location of the probe using three different offsets: left (in green), central (in red), or right (in blue) active probe aperture. For each ULA-OP acquisition, the active apertures are alternatively switched on in this sequential order: left, central, then right. It also allows during post-processing step to apply an additional "triangulation process" by summing the three offset reconstructed maps.

A total of 1500 ULA-OP acquisitions corresponding to 250 ms were carried out and therefore, because of lack of the synchronization configuration, only 150 of them occurred during the 25 ms therapy pulse. Meaning that for each three active aperture offsets, 50 pre-beamformed RF signals were recorded with a corresponding new specific $PRF_{aperture}$ of 2000 Hz. Because of bad calibration step, same electronic saturation as discussed in section III.1.3.2 was observed. Hence, the amplitude and threshold operations are not enabled and the same high-pass filtering process was applied. Moreover, since the passive acquisitions are achieved during the sweep of the thrombus, motion compensation should be advised. However here as only 25 ms of the entire 180 seconds of therapy is considered then the total motion for one sonication pulse equals approximatively 1.4 µm and hence can be neglected.

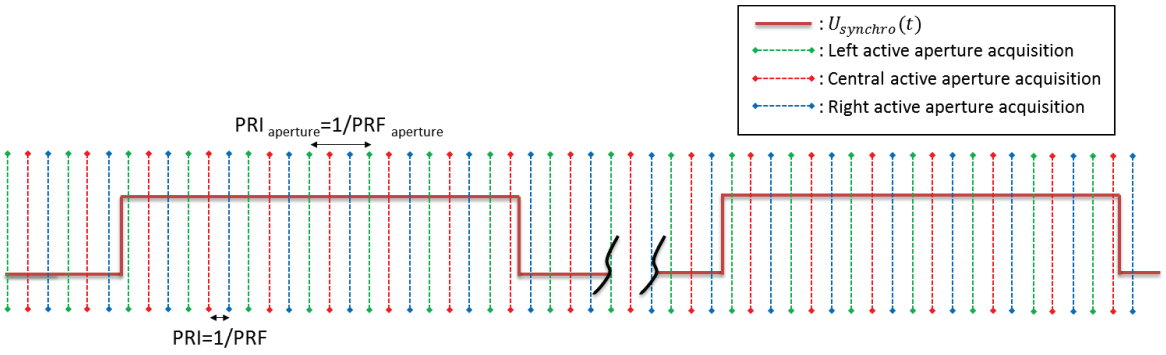

Figure III-34: "three offset aperture" passive image acquisition sequence with no synchronization configuration and corresponding to the use of three different active aperture probes alternatively switched on.

III.2.4 Computation step

For each passive recorded acquisition, one cavitation map was reconstructed using PAM-PCF beamforming algorithm. The reconstruction parameters displayed in Figure III-35, used to compute the different maps, were set as follows. A 110 mm × 40 mm image [axial × lateral direction] with 1100 pixels × 400 pixels were used corresponding to a 0.1 mm × 0.1 mm pixel resolution. The depth

(axial imaging axis) ranged from 10 mm to 120 mm. The lateral imaging axis was centered at zero. The time T used in the averaging process of TEA was set to 15.7 µs with a time step Δt of 0.1 µs. Hence, 50 maps were reconstructed for each three active apertures and the FCP 2D positions were recovered. In addition as mentioned before, a triangulation process was considered and achieved by simply summing the 3 active aperture maps and therefore providing a more accurate focal localization.

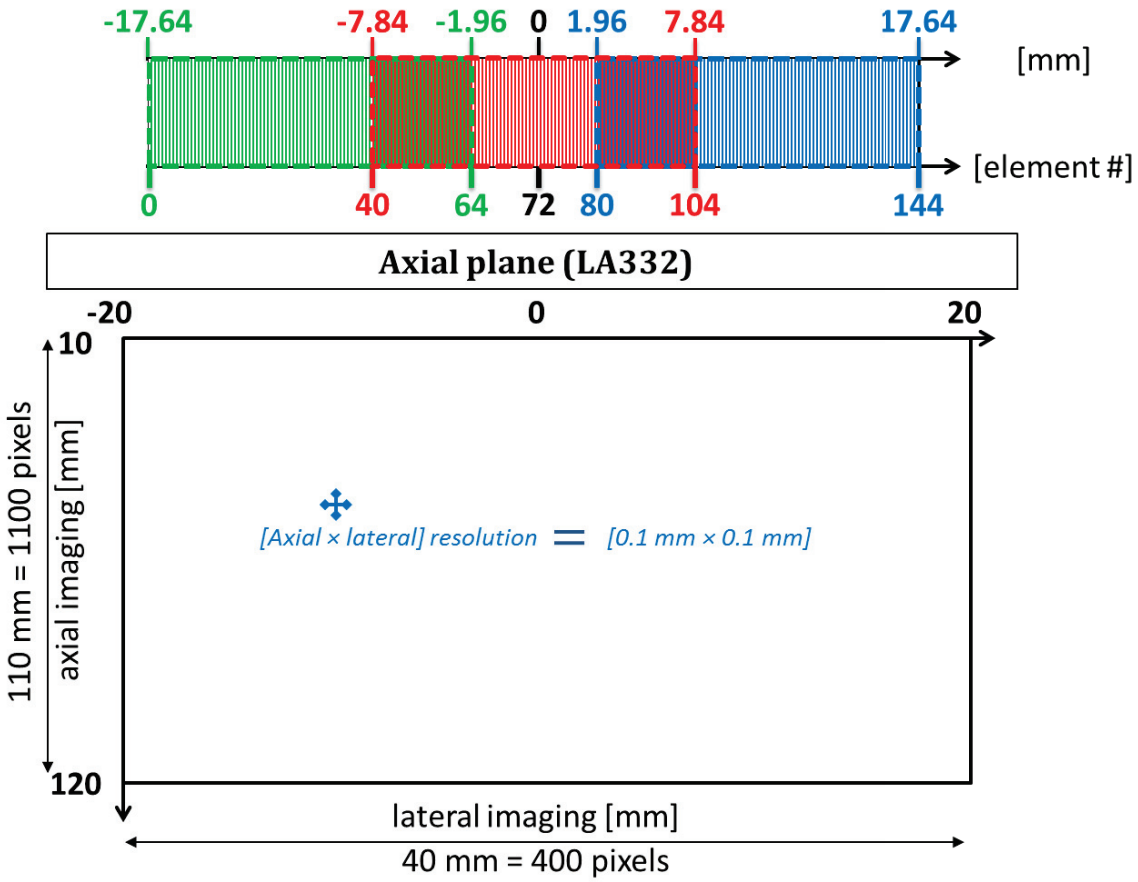

Figure III-35: On top the illustration of the LA332 imaging probe with the three active apertures corresponding to three different offsets: left (in green), central (in red), and right (in blue). On bottom the image reconstruction parameters for probe LA332 imaging the cavitation axial plane (x, z).

III.2.5 Results

The different results are represented in Figure III-36 and Figure III-37. The post-processed cavitation maps for the three different active apertures are displayed for one frame among the 50 in Figure III-36.(a-c) and the three apertures summation cavitation map is displayed in Figure III-36.d. Moreover, the FCP 2D positions for the entire 50 frames are outlined in Figure III-36.(e, f). Likewise, the FCP localization in the temporal profile along 25 ms of ultrasound sonication, corresponding to one pulse, is outlined for both axial imaging direction (depth) and lateral imaging direction in Figure III-37.a and Figure III-37.b, respectively.

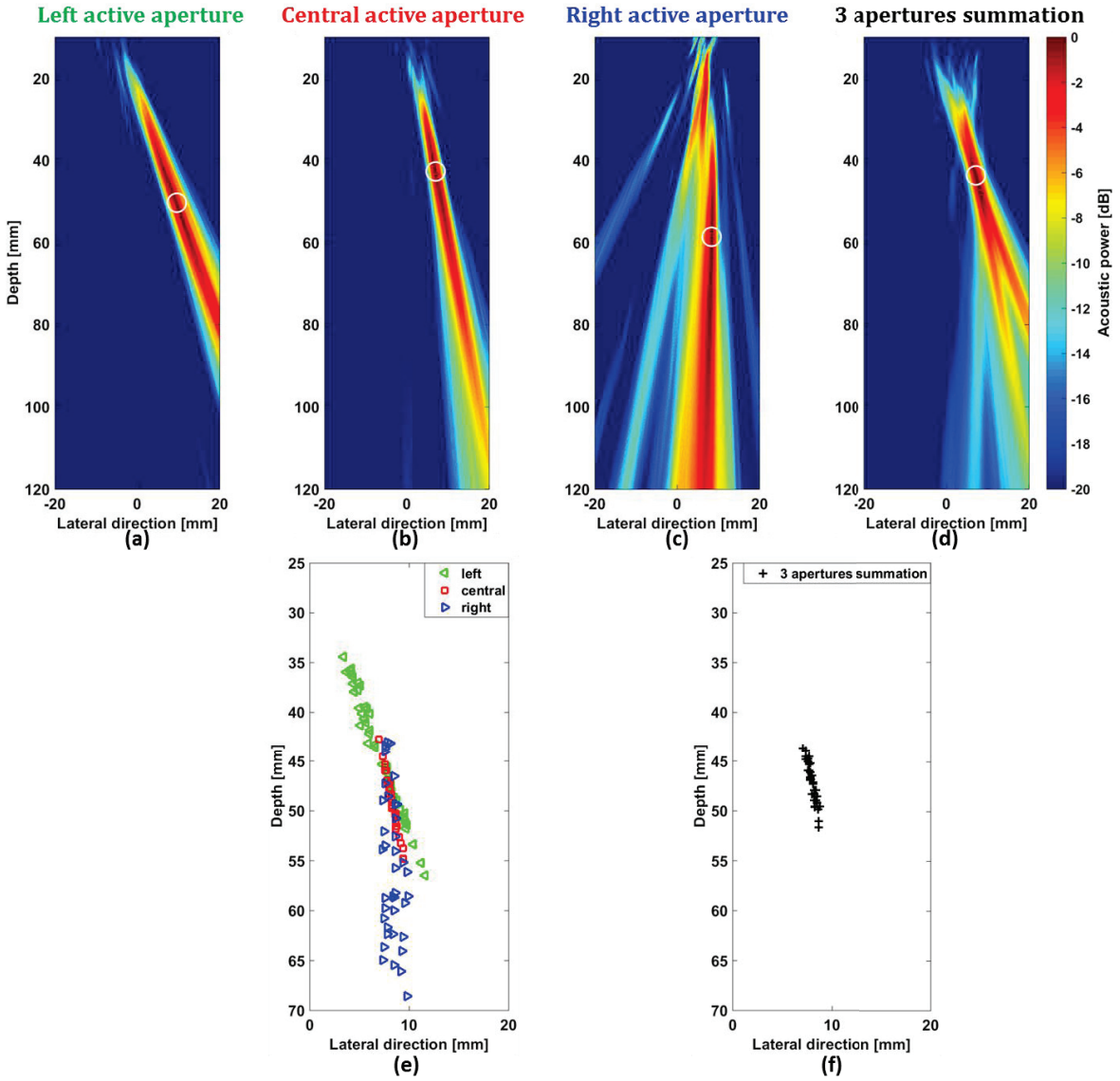

Figure III-36: The cavitation map reconstructed with the PAM-PCF method for one frame among 50 for (a) left aperture, (b) central aperture, (c) right aperture, and (d) three apertures summation. The white circle corresponds to the FCP localization. For the entire 50 frames, along 25 ms of ultrasound sonication, the FCP 2D positions for (e) three offset apertures, and (f) three apertures summation.

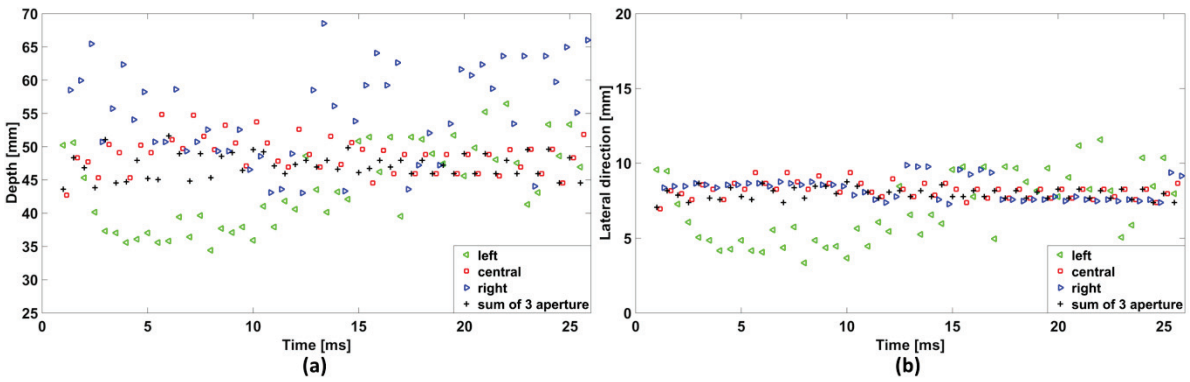

Figure III-37: The FCP localization temporal profile along 25 ms of sonication for both (a) depth and (b) lateral imaging direction.

III.2.6 Discussion

First of all, when comparing the PAM-PCF reconstructed cavitation maps for the three active apertures in Figure III-36.(a-c), the right active aperture (c) relative to the others two (a,b) has not a clear spot cavitation. It is similar to the cases in One-spot cavitation (III.1.1) with very high cavitation activity intensity (CI=40) displayed in Figure III-15, and in Multi-spots cavitation (III.1.3) with multi-bubble cloud generation represented in Figure III-27.(d-f) and Figure III-28.(d, e). As previously discussed, it is mainly caused by bubble interferences generating destructive and constructive wave fronts recorded afterwards by the imaging probe which could lead to incorrect reconstructed cavitation sources, commonly called artifacts. Furthermore, the axial resolution spot issue is also observed in every passive reconstructed cavitation maps ("tail" aspect). Moreover, the therapy focus position and spatial extension, corresponding respectively to the average and standard deviation of the FCP 2D positions on the entire 50 frames, were recovered. Then, the therapy focus positions (axial direction; lateral direction) for each three active aperture offset are as follows: left aperture = (43.96 ± 6.29; 6.93 ± 2.3) mm, central aperture = (48.74 ± 2.68; 8.2 ± 0.54) mm, right aperture = (55 ± 7.11; 8.29 ± 0.76) mm. None of them correspond to the expected positon of the ultrasound theoretical therapy focus which was set at (80, 0) mm, which could mean that the first interpretation of the PAM-PCF results shows that there could be a focalization problem during the ultrasound sonication therapy. Additionally, when investigating the FCP 2D positions (Figure III-36.e), the FCP localization accuracy mainly in the lateral imaging direction is greatly decreased for the source positioned outside of the active aperture (left aperture offset). This loss of localization accuracy is clearly noticed in Figure III-37.b where for the left active aperture (in green) the FCP positions were spread out with standard deviation of 2.3 mm at least three times higher relative to the other two active aperture. This effect was already explored by the validation process in Chapter II with the experiment on a wire. It is explained by the hyperbolic delay shape (time of arrival of the wave front to the corresponding element of the active aperture) which error sensibility is directional (steered towards the source). Likewise, the previously inspected axial low resolution of the cavitation spot, mainly dependent on the imaging probe characteristics, influences the FCP localization especially in the axial imaging direction (depth). It is noticed with the FCP positions directed towards its own cavitation spot direction and quantitatively outlined in Figure III-37.a, where the FCP depth dispersion for each offset aperture is high: left std = ± 6.29 mm, central std = ± 2.68 mm, and right std =± 7.11 mm. However because of the lack of cavitation power threshold operation, events with low- or no-cavitation activity are not omitted and hence some of them could be represented by these high dispersed FCP positions. Moreover, a clear difference is noticed between two consecutive active aperture offsets (example left then central aperture offset), reinforcing the active aperture characteristics dependency over the FCP position localization accuracy and hence shows the importance of the aperture choice which will be investigated in further studies in next Chapter.

Thanks to the particular "three offset aperture" acquisition sequence the cavitation source is for each offset laterally shifted relative to the corresponding active aperture. Hence, for each active aperture cavitation map reconstructed (Figure III-36.(a-c)), the direction of the source position is granted because of the spot steered direction. Thus, the axial predominant problem could be partially resolved here by using the "triangulation process". It consists in summing the three active aperture maps into one map called the "three aperture summation", displayed in Figure III-36.d, which possess an improved axial resolution. Therefore, the use of this three apertures summation cavitation map (triangulation process), is useful to bypass the FCP localization accuracy with

improved FCP position dispersion. Thus, from this point forward the FCP 2D positions investigation will be considered only with the summation cavitation maps and is displayed in Figure III-36.f. Therefore, the bubble cloud (cavitation source) generated during the ultrasound sonication therapy is localized at (axial direction; lateral direction) = (47.16 ± 1.87; 7.96 ± 0.39) mm.

The theoretical therapy focus, or theoretical bubble cloud bc_{th}, at (80; 0) mm is in reality not reached because of different ultrasound propagation mechanisms caused by the fluctuation of the speed of sound values in the different crossed medium: water, balloon material, skin, tissue, and blood. This variation in speed of sound generates first inaccurate interpolation of the distance relative to the time of flight used for the reconstruction of anatomical ultrasound B-mode images. Therefore the different anatomical structures, for example the femoral artery, are represented in the B-mode images, if the speed of sound considered is lower than the ground truth value, to be closer to the imaging probe than it really is (speed displacement artifact). It leads to bad targeting of the therapy focus at the thrombus and hence should be positioned deeper than it appears on anatomical images, which phenomenon was already observed and discussed by Poizat *et al.* [97]. Second, the refraction/reflection ultrasound propagation mechanisms could occur because of the water-balloon-skin-tissue interface existence and the incident ultrasound therapy waves striking the interface at a non-perpendicular angle θ_i. Therefore, because of the refraction mechanism, the transmitted therapy focus, or transmitted bubble cloud bc_t, is actually expected at approximatively 75 mm in depth instead of the theoretical 80 mm. Moreover, ultrasounds have difficulty to go through the water-balloon-skin-tissue interface and hence a high reflection mechanisms also arise and principally lead to the generation of a reflected therapy focus, or reflected bubble cloud bc_r, at approximatively (47; 8) mm which correspond very closely to the PAM-PCF FCP position recovered previously. The two expected focal cavitation spots (bc_t and bc_r) and the theoretical one (bc_{th}), induced by the ultrasound sonication therapy, are displayed in Figure III-38.

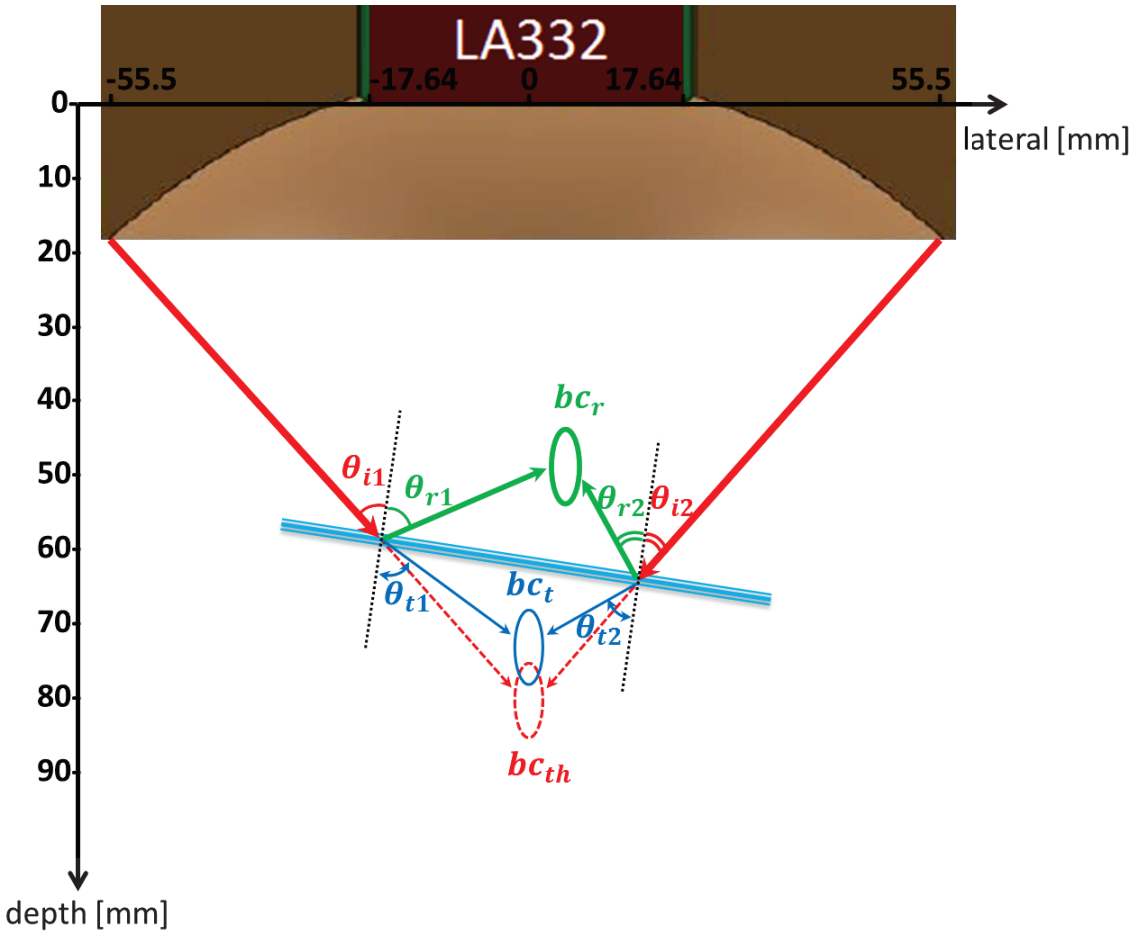

Figure III-38: Illustration presenting the refraction/reflection ultrasound propagation mechanism impact on the bubble cloud (therapy focus) generated by the ultrasound sonication therapy. bc_{th} = theoretical bubble cloud, bc_t = transmitted bubble cloud, and bc_r = reflected bubble cloud. The blue triple line corresponds to the water-balloon-skin-tissue interface.

The preliminary *in vivo* results mainly showed that more in-between steps before *in vivo* experiments need to be considered for better calibration of the therapy system. For example, along the 180 seconds of total therapy sonication time, only one second of passive pre-beamformed RF signals is recorded. Hence, a large lack of cavitation information is encountered which could impact the *in vivo* interpretations about the ultrasound destruction efficiency of the thrombus. Therefore, greater quantities of saved data are required, or even better the development of the real-time aspect of the cavitation map visualization system. Furthermore, when investigating on *in vivo* testing, the FCP ground truth position is not at all defined and therefore for more robust interpretation and results the passive ultrasound technique could be combined with another imaging modality as example MRI thermometry. Still the PAM-PCF cavitation maps are very coherent with the observation of the *in vivo* thrombolysis experiments and with the expected physical reflection-refraction US propagation mechanisms.

III.3Conclusions

In conclusion to these diverse cavitation experiments, the efficiency of the PAM-PCF reconstruction technique to accurately localize the focal cavitation point (FCP) position for simple cavitation situations as one-spot cavitation with moderate cavitation radiated intensity (CI ≤ 35 dB) is

partially asserted. However, for the majority of the other more complex situations as one-spot cavitation with CI = 40 dB, multi-spots cavitation, non-regulated cavitation, and especially *in vivo* testing the ground truth position of the cavitation sources is very difficult to validates with classic B-mode hyperechoic images or visual confirmation. Therefore, in parallel work more complex developments on ground truth validation protocol need to be considered which some are already used in research field as: the use of standing waves to trap and control the cavitation bubbles motion [127], or the use of nanocups to trap and stabilize gas [128].

Still, the majority of interpretations about the different PAM-PCF results were coherent with the known physical cavitation mechanisms. Therefore, these results supported the accuracy of the PAM-PCF technique and hence approve it as the referenced passive cavitation imaging technique of our monitoring device development. Thus, in the next chapter to get closer to a complete enhanced ultrasound therapy monitoring device, more optimizations process were investigated and developed.

Chapter IV : Optimization process

Even if the preliminary investigation and validation of PAM-PCF and therapy efficiency are promising more optimizations and improvements of the monitoring ultrasound cavitation therapy system needs to be considered and developed before going on with more complex and expensive *in vivo* or clinical testing of the innovative extracorporeal ultrasound thrombolysis therapy technique. Therefore a first step of three dimension imaging techniques development is investigated second, optimizations of the imaging probe characteristics with increased aperture size and number of active elements (thanks to new ULAOP-256 technology) third, frequency domain analysis is assessed and finally a real-time development of the PAM-PCF visualization is explored with early preliminaries results as well as a hybrid mode implementation by combining B-mode and passive mode images.

IV.1 3D passive imaging

The three dimensions (3D) implementation is a crucial step for real-time optimized monitoring of US therapy. First, for 3D positioning in anatomical active B-mode ultrasound imaging of the therapy focus on the thrombus. Second, as the cavitation spot is located and spreads in the three directions, the acoustic source information should, for passive cavitation maps reconstruction, be retrieved from the recorded RF signals in both lateral and elevation directions of the array. A two dimension (2D) array is therefore considered with an additional dimension corresponding to the elevation direction represented by the z axis in Figure IV-1. For 1D array (2D images), acoustic sources positioned outside of the field of view of the probe (meaning that they don't belong to the elevation plane of the probe) will emit ultrasound waves which could still reach the probe and, depending on the directivity sensibility of the element, could be recorded in the RF acoustic signals. Therefore these sources will be considered in the PAM beamforming algorithm and subsequently alter the cavitation sources localization maps. The hyperbolic delay shape observed in the pre-beamformed RF data becomes for 3D passive imaging a spherical surface shape. It increases the accuracy of PAM computation because unlike in 1D array, the PAM technique will acknowledge RF signals recorded in the elevation direction. Two dataset were used to assess the 3D passive reconstruction image technique: simulations considering an acoustic point source and cavitation water tank experiment.

IV.1.1 Materials and methods

First the same simulation tool used in Chapter II is considered to assess 3D PAM-PCF reconstruction technique. Simulated 3D pre-beamformed data were considered with an acoustic point source positioned at 4 cm from a 24x8 (lateral x elevation) 2D array with 400 µm pitch. Then, the PAM-PCF maps are reconstructed with similar image reconstruction and computation parameters used in the following 3D cavitation experiment and which will be presented afterwards.

Second, the same cavitation water tank experiment setup was used as in the previous Chapter III and is displayed in Figure IV-1. US cavitation (bubble cloud) was induced in a water tank by the regulated US-induced cavitation generator with a CI equal to 30 dB. The tank was filled with deionized-filtered (particles <5 µm) and degassed (3 mgO_2/L) water. A 2D matrix array of 24 by 8 elements (lateral by elevation dimension) with a 400 µm pitch and central frequency of 2.8 MHz is used. An agar gel was positioned 45 mm distance from the therapeutic transducer and in direct

contact with the 2D imaging probe. The bubble cloud was induced at 40 mm from the probe which images both cavitation transversal plane (x, y) and the cavitation frontal plane (z, y).

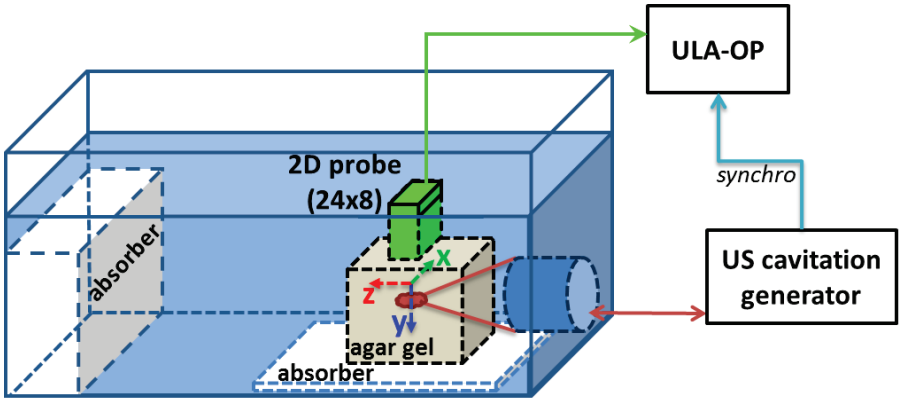

Figure IV-1: Cavitation water tank experiment setup using the regulated US-induced cavitation generator to induce a bubble cloud in an agar gel, with a CI=30dB. In addition, a 2D imaging matrix probe with 24 by 8 elements is combined with the ULA-OP synchronized with the ultrasound sonication pulses.

The 2D array is combined with the ULA-OP-64 which can only control simultaneously 64 channels maximum meaning that to be able to use the entire 192 elements of the 2D array a particular acquisition sequence is needed and is presented in Figure IV-2. The control over the 2D array is divided into three squared blocks of 8 by 8 elements and the active block alternates between each ULA-OP acquisition with an internal 3000 Hz PRF. Therefore, the total pre-beamformed RF signal acquired for the entire 2D probe corresponds to the juxtaposition in the lateral direction of the three RF signals acquired for each block. Moreover, the total juxtaposed RF signal is thereby acquired with a 1000 Hz PRF_{block}. The "Enable" synchronization configuration, useful to allow passive acquisitions just during the ultrasound sonication, was also considered with a τ_{Enable} set to 25 ms same width as the sonication pulse τ_{pulse}. A total of 300 block acquisitions were achieved corresponding to 100 total juxtaposed RF pre-beamformed signals, representing thereby 4 sonication pulses of 25 RF signals each.

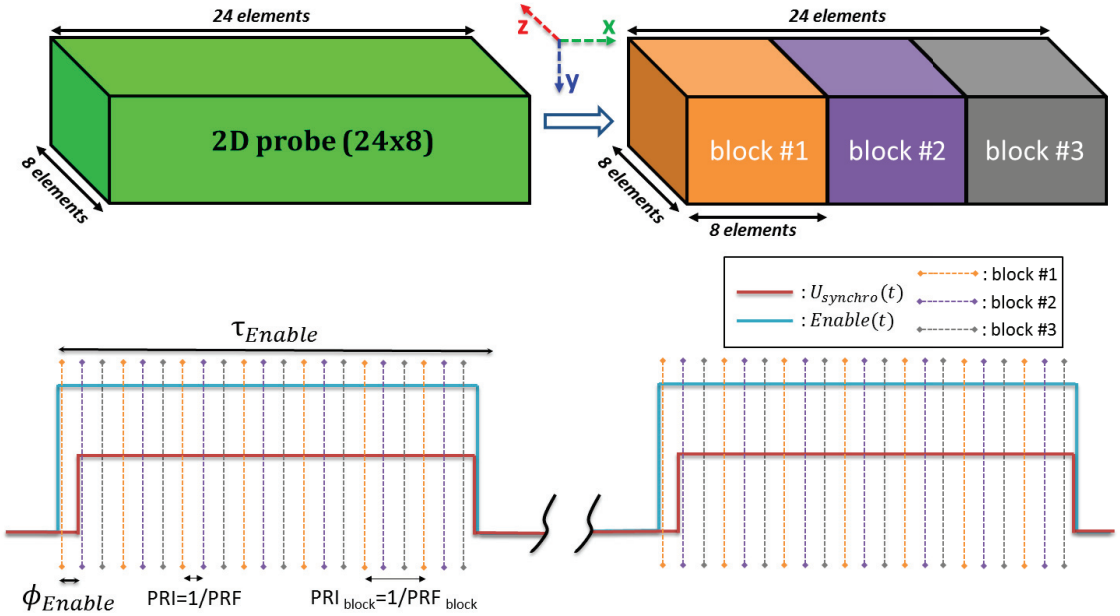

Figure IV-2: On top, the three squared block partition of the 2D matrix imaging array including 24 by 8 elements (192 total elements). Each 8x8 block corresponds to 64 simultaneously active elements. On Bottom, the "Enable" synchronization configuration established between the ultrasound sonication pulse (US cavitation generator) and the ULA-OP acquisition, combined with a particular block acquisition sequence. It consists in alternatively activating the three juxtaposed blocks. The first frame is acquired outside of each sonication pulse.

For each juxtaposed RF signal, one cavitation map was computed using PAM-PCF beamforming algorithm. The reconstruction parameters displayed in Figure IV-3, used to compute the different maps, were set as follows. A 30 mm × 20 mm x 20 mm images [axial × lateral × elevation direction] with 75 pixels × 50 pixels × 50 pixels were used corresponding to a 0.4 mm × 0.4 mm × 0.4 mm pixel resolution. The depth (axial imaging axis) ranged from 20 mm to 50 mm. The lateral imaging axis as well as the elevation imaging axis were centered at zero. The time Tused in the averaging process of TEA was set to 14.7 µs with a time step Δt of 64.52 ns corresponding to a TEA sampling frequency f_{TEA}= 15.5 MHz. Hence, 100 3D cavitation maps were reconstructed and the FCP is recovered for the three dimensions: depth, lateral and elevation.

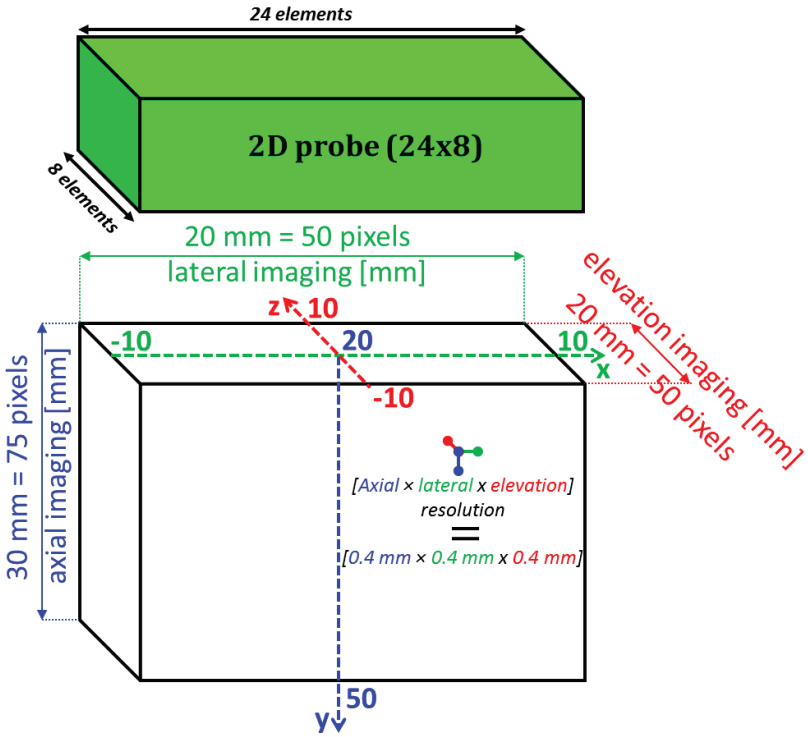

Figure IV-3: The image reconstruction parameters for the 2D matrix array imaging both cavitation transversal plane (x, y) = (lateral, axial) imaging direction and cavitation frontal plane (z, y) = (elevation, axial) imaging direction.

IV.1.2 Results and discussions

The isosurface at -3dB and two perpendicular cross-section planes (elevation=0 and lateral=0) are displayed for both dataset in Figure IV-4. The point source simulation in Figure IV-4.(a,b,c) and the cavitation experiment in Figure IV-4.(d,e,f) reconstructed maps exhibit very similar cavitation spot shape and resolution. Moreover, a wider cavitation spot is noticed for the elevation direction in Figure IV-4.(c,f). Indeed, it is related to the probe aperture size which in this direction is three times less than in the lateral direction. Hence, with the future use of higher aperture probes, the resolution should be improved. The FCP for the simulation is recovered at (42.30; -0.20; -0.20) mm which is closely equal to the theoretical FCP position at (40; 0; 0) mm. Along the 100 maps of the cavitation experiment, the FCP is equal to (36.15 ± 2.15; 6.40 ± 0.36; 4.27 ± 1.17) mm and its 3D positions are outlined in Figure IV-5. An offset is noted for FCP results in all three directions between the cavitation experiment and the theoretical reference. The ground truth, corresponding to the theoretical reference, was difficult to establish especially in this experiment because of the absence of active ultrasound images in 3D useful to check accurately the position of the 2D probe relative to the induced cavitation bubble cloud.

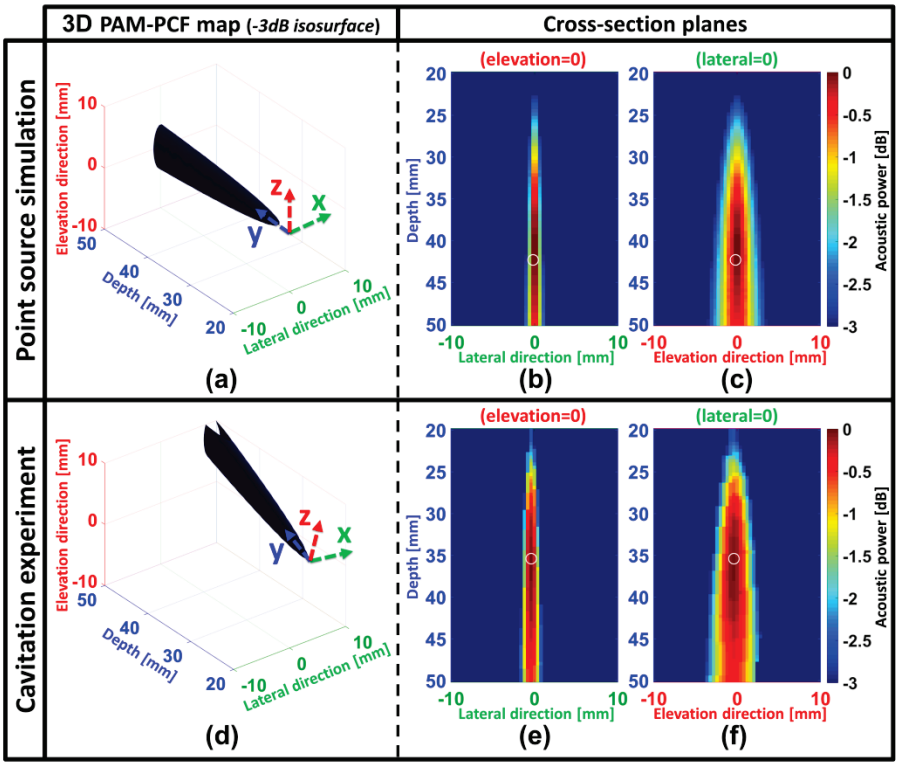

Figure IV-4: 3D passive acoustic maps reconstructed with PAM-PCF beamforming algorithm considering first, (a,b,c) simulation of an acoustic point source positioned at 4 cm from the array and second, (d,e,f) water tank cavitation experiment with a bubble cloud induced at 4 cm from the array. From left to right: (a,d) the isosurface at -3 dB dynamic, the perpendicular cross-section plane (b,e) for elevation=0, and (c,f) for lateral=0. The white circle corresponds to the FCP localization.

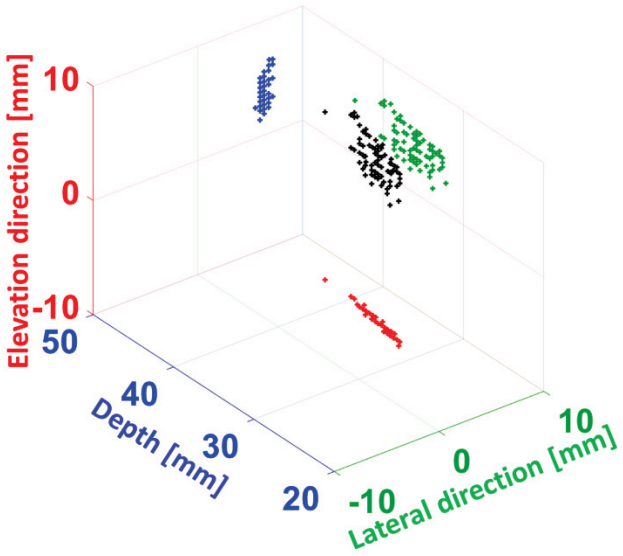

Figure IV-5: The FCP 3D positions recovered from the 100 PAM-PCF reconstructed maps for the cavitation experiment. The positions for the three directions are plotted in black. The position projections are plotted on the lateral direction (x=10) in green, on the depth direction (y=50) in blue, and on the elevation direction (z=-10) in red.

For further work, improved 3D cavitation maps will require echography system with higher number of channels simultaneously available. Nowadays, because of recent development in FPGA and digital signal processor (DSP) technologies, the highest available number of controlled channels increased up to 1024 with for example the synthetic aperture real-time ultrasound system (SARUS)

located in the University of Denmark which could manage up to 1024 channels [129]. Likewise, the use of four combined Vantage platform (Verasonics, Redmond, WA) each managing 256 channels allows the control of a total of 1024 channels [130]. Therefore, a 32x32 2D array matrix array could be connected and used. In the following, additional simulations on a punctual source positioned at 4 cm from the 2D probe with four different pitch values are achieved and the PAM-PCF 3D were reconstructed considering the same parameters as previously (image reconstruction and computation step). The PAM-PCF 3D cavitation maps as well as the two perpendicular cross-section planes (elevation=0 and lateral=0) are displayed in Figure IV-6. The different 2D imaging probe characteristics and the FCP recovered positions are outlined in Table IV-1. As expected, with higher pitch (meaning higher aperture), improved cavitation spot resolution as well as FCP position localization is noticed. Still even if the cavitation spot resolution linearly continue to progress, the FCP depth positions seems to converge to 40.27 mm value event for increasing aperture (pitch=800 µm or 1200 µm). Moreover, the lateral and elevation FCP positions values alternates between -0.20 mm and 0.20 mm which corresponds to one pixel resolution offset of 0.4 mm.

Table IV-1: 2D probe characteristics and FCP positions recovered for simulations of a punctual source at (40; 0; 0).

2D Probe (lateral x elevation)	Pitch	Aperture size (lateral x elevation)	FCP position (depth; lateral; elevation)
24 x 8 (192 elts)	400 µm	(9.6 x 3.2) mm^2	(42.3; -0.2; -0.2) mm
32 x 32 (1024 elts)	300 µm	(9.6 x 9.6) mm^2	(41.5; -0.2; -0.2) mm
32 x 32 (1024 elts)	400 µm	(12.8 x 12.8) mm^2	(40.7; 0.2; -0.2) mm
32 x 32 (1024 elts)	800 µm	(25.6 x 25.6) mm^2	(40.3; 0.2; 0.2) mm
32 x 32 (1024 elts)	1200 µm	(38.4 x 38.4) mm^2	(40.3; -0.2; 0.2) mm

Still for even efficient use of the imaging system, spiral or sparse arrays could be considered because of better imaging accuracy (better beam pattern) than for classical matrix arrays with the same number of elements [131]–[133].

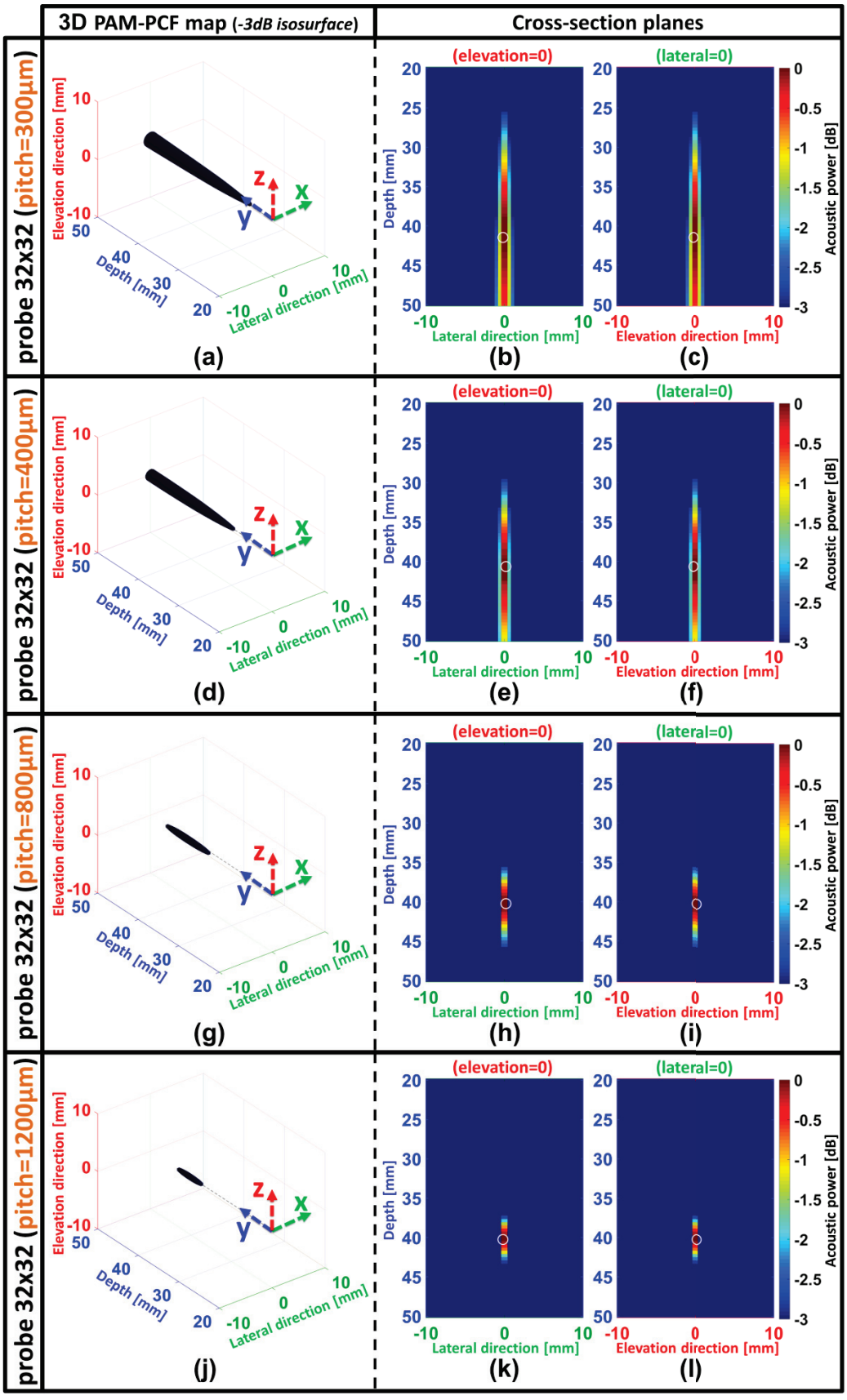

Figure IV-6: 3D passive acoustic maps reconstructed with PAM-PCF beamforming algorithm considering simulation of an acoustic point source positioned at 4cm from a 32x32 array and for 4 increasing pitch values from top to bottom: 300, 400, 800, and 1200 µm. From left to right: the isosurface at -3 dB dynamic, the perpendicular cross-section plane for elevation=0, and for lateral=0. The white circle corresponds to the FCP localization.

IV.2 Probe aperture

Probe imaging characteristics are relevant for the global performance of any ultrasound imaging technique and especially for passive cavitation imaging system. Therefore, its impact on the PAM-PCF reconstruction technique is explored.

IV.2.1 Principle

The number of active elements of the probe was constrained by the echography system (ULA-OP 64). Thanks to the recent addition of the newest ultrasonic platform ULA-OP 256 [134] to our laboratory platform, optimized imaging technique could be considered with especially higher aperture size thanks to greater number of active elements managed simultaneously (up to 256 channels controlled). The linear array LA523 was considered with its 192 total elements.

The F-number ($f_{\#}$) is a dimensionless value corresponding to the ratio between the distance to the focus (D) and the active aperture size (a) as presented in the following:

$$f_{\#} = \frac{D}{a} \tag{IV.8}$$

The more active elements used, the higher the aperture size, the lower the F-number, the narrower the beam and hence the better the resolution of the reconstructed image. Dynamic expanding aperture is keeping the F-number constant by growing the aperture with the imaging depth. This way the focus is the same in the entire depth. Thus, to assess this important imaging parameter and show the impact on the PAM-PCF mapping results, simulation of a point source and experiment on a wire were considered with four different aperture size models presented in Table IV-2. The 1/3 elements model, also namely “1 active element each 3” acquisition mode, corresponds to the activation of 1 element each 3 to allow the use of the entire probe’s aperture by using only 64 elements (situation available on the ULA-OP 64 platform). For all four models, the active elements were chosen in the way that the probe’s aperture was always laterally centered at zero.

Table IV-2: Probe imaging characteristics with F-number calculated for a fixed depth focus at D=80 mm.

Aperture model	Number of active elements	Pitch	Aperture size	F-number ($f_{\#}$)
64 elements	64	245 µm	15.68 mm	5.10
128 elements	128	245 µm	31.36 mm	2.55
192 elements	192	245 µm	47.04 mm	1.70
1/3 elements	64	245 µm	47.04 mm	1.70

Moreover, the sampling frequency (f_s) is also increased, thanks to higher hardware performance for quicker processing time, with a 78.125 MHz instead of initial 50 MHz. It enables mostly better delay resolutions. Its impact was not directly assessed but still the logical influence over enhanced PAM performance does not need to be confirmed and won’t be discussed in this study. However if an even higher f_s was considered then it would have been more interesting to investigate this parameter.

IV.2.2 Simulation on a point source

Simulations on a point source were achieved for the 4 different aperture models and using similar simulation tool parameters than in Chapter II but with this time an increased RF signal sampling frequency f_s= 78.125 MHz and decreased TEA sampling frequency f_{TEA}= 10 MHz. For better comparison process, both previous parameters were set to match the following "experiment on a wire" computation parameters in section IV.2.3. The point source was positioned at 80 mm from the imaging probe and laterally centered. The corresponding four PAM-PCF reconstructed maps are displayed in Figure IV-7.(a-d). Quantitative visualizations were considered with acoustic pattern profiles in both lateral and axial direction in Figure IV-7.(e,f), as well as FCP localization values in Table IV-3.

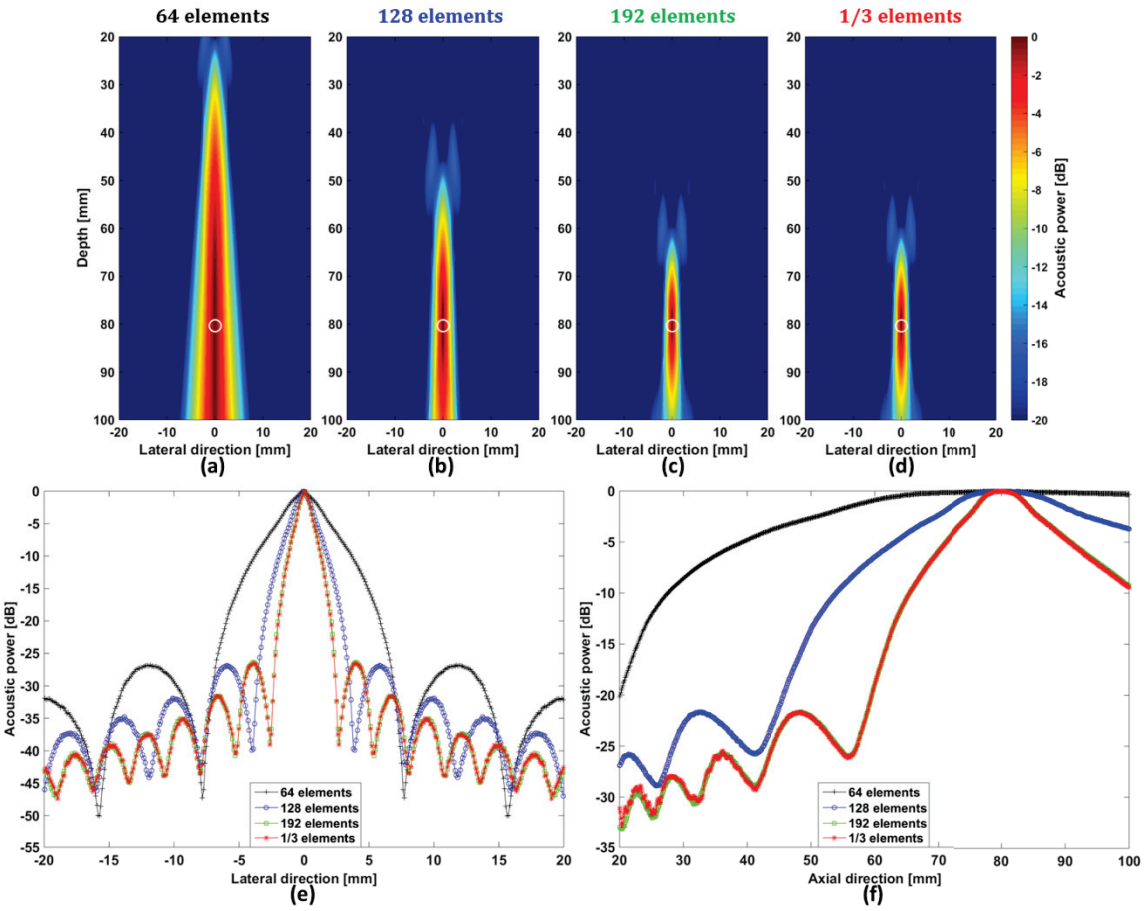

Figure IV-7: The dataset considered are pre-beamformed simulated RF signals emitted by an acoustic point source positioned at 80 mm from the imaging probe. On the top, PAM-PCF maps reconstructed using the four different aperture models: (a) 64 elements, (b) 128 elements, (c) 192 elements, and (d) 1/3 elements. In each subplot, the white circle corresponds to the FCP localization. On the bottom, the acoustic pattern profiles in the (e) lateral and (f) axial direction (depth) for the four different aperture models.

Table IV-3: FCP positions recovered for the four aperture models with simulation of a punctual source at (80; 0).

Aperture model	FCP position (depth; lateral)
64 elements	(80.38; 0.05) mm
128 elements	(80.38; 0.05) mm
192 elements	(80.38; -0.05) mm
1/3 elements	(80.08; -0.05) mm

When comparing the four PAM-PCF maps displayed in Figure IV-7.(a-d), the increase of the aperture size influences clearly the improvement of the focal spot resolution especially in the axial direction which is outlined in both axial and lateral acoustic pattern profiles (Figure IV-7.(e,f)). Likewise, the increase of the aperture size reduces the side lobes power but with a compromise of an increased side lobe's number. Lobes are even present in the axial direction when the number of elements increases (noticed for active number of elements higher or equal to 128). They could actually correspond to constructive interferences in reception of the US waves and also to artifacts caused by TEA computation when the acoustic radiated power is summed along a total time T. The 1/3 elements model have highly similar acoustic pattern than the 192 elements model. Yet, in this simple simulation case, the FCP position localization is not influenced by the aperture model characteristics, outlined in Table IV-3.

IV.2.3 Experiment on a wire

Similar methodology as in chapter II (section II.3.2) was explored with the experiment on a wire setup. Basically, a 0.1-mm-diameter nylon wire was placed perpendicular to the imaging probe and was excited by a mono-element transducer (5 MHz, IAHG051, Sofranel, Sartrouville, France). It was powered with the pulser/receiver (5052PR, Sofranel Panametrics-Olympus, Tokyo, Japan). Likewise, the same "Synchro Out" synchronization configuration was considered but this time in the opposite way meaning that the ULA-OP ultrasonic scanner worked as "master". It sends out a pulse signal "PRFout" synchronous with the ULA-OP internal PRF, which in this case is not a problem for therapy monopoly as it is omitted in experiment on a wire. Therefore, the ULA-OP controls the transmission of the transducer and hence the wire excitation. A time offset is set between pre-beamformed ULAOP acquisition and the wire excitation in a way that the scattering US waves are rightfully recorded. Then, the position of the wire with respect to the probe position was axially and laterally shifted by moving the probe using a three-directional motorized positioning system (OWIS, Staufen, Germany) in the three orthonormal axes (x, y, z), as shown in Figure IV-8. The wire was first positioned using B-mode visualization at (x = 0 mm; z = 20 mm). The y position was chosen so that the imaging plane remains in the transducer beam plane. Then, using the positioning system software (OWISoft), the imaging probe was shifted in 104 different positions: 13 lateral (in the x direction with an increment of +2 mm) and 8 axial (in the z direction with an increment of +10 mm). Because of the lateral symmetry of the probe, only positive offsets for the lateral direction (0 to 24 mm) were considered.

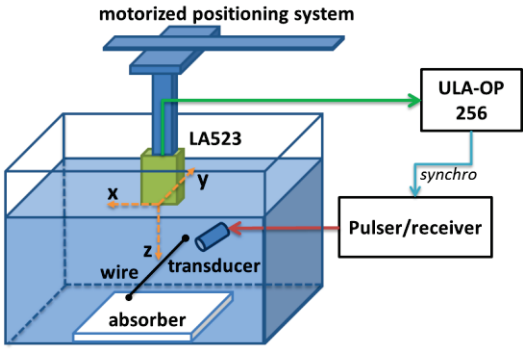

Figure IV-8: Same wire experiment setup considered in Chapter II with this time the ULA-OP 256 system controlling the synchronization configuration.

Additionally, by activating the total 192 elements of the LA523 linear imaging probe (thanks to ULA-OP 256), the entire probe's aperture was considered and therefore the pre-beamformed saved data involved 192 RF signals instead of the initial 64. Also, for each wire position, 100 passive acquisitions were recorded which corresponds to 100 wire excitations. Moreover, especially in this experimental protocol, the ground truth was recovered for each wire position thanks to I/Q active B-mode ultrasound images. The wire ground truth position was hence recovered by getting the maximum point coordinates in the I/Q post-beamformed logarithm compressed active image as example displayed in Figure IV-9, where the FCP ground truth for the (80; 0) mm theoretical wire position is recovered at (77.95; 0) mm. Therefore, the ground truth was much more accurate and closer to the reality.

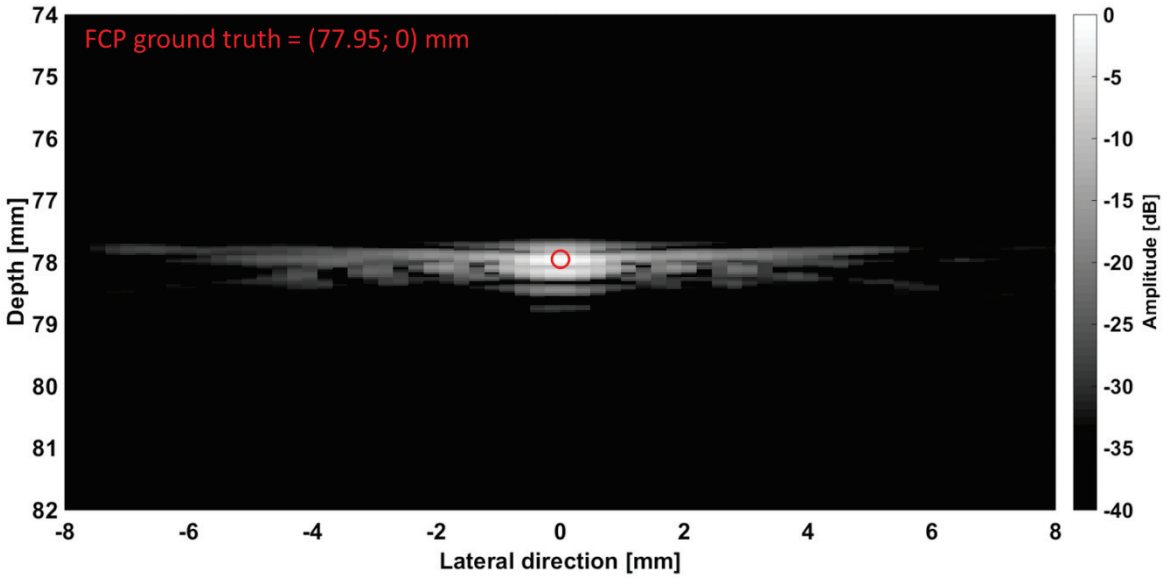

Figure IV-9: The In-phase and Quadrature (I/Q) post-beamformed image representing the wire cross-section used for FCP ground truth recovery. Here the theoretical (80; 0) mm wire position corresponds to a ground truth of (77.95; 0) mm.

The four different aperture model pre-beamformed dataset were built in post-processing step by choosing the right active elements in the original saved pre-beamformed data. After applying the PAM-PCF technique to the four different aperture model dataset, 100 passive maps were reconstructed for each model. Then, on each map, the position of the FCP corresponding to the wire position was extracted. Finally, the mean wire position was recovered and plotted in Figure IV-11 for all 104 positions. The time T used in the averaging process of TEA was set to 5 µs which for one cycle

wire excitation is high enough to capture the entire ultrasound scattered wave. The TEA sampling frequency was set to f_{TEA}= 10 MHz to decrease processing time of the reconstruction algorithm. To enable the comparison with the previous simulation on a point source results, the PAM-PCF map reconstructed for the four different aperture models are displayed specifically for the wire positioned at (80; 0) mm in Figure IV-10.(a-d) as well as the acoustic pattern profiles in both lateral and axial direction in Figure IV-10.(e,f). Likewise, the FCP recovered positions including the standard deviation values along the 100 passive maps are outlined in Table IV-4.

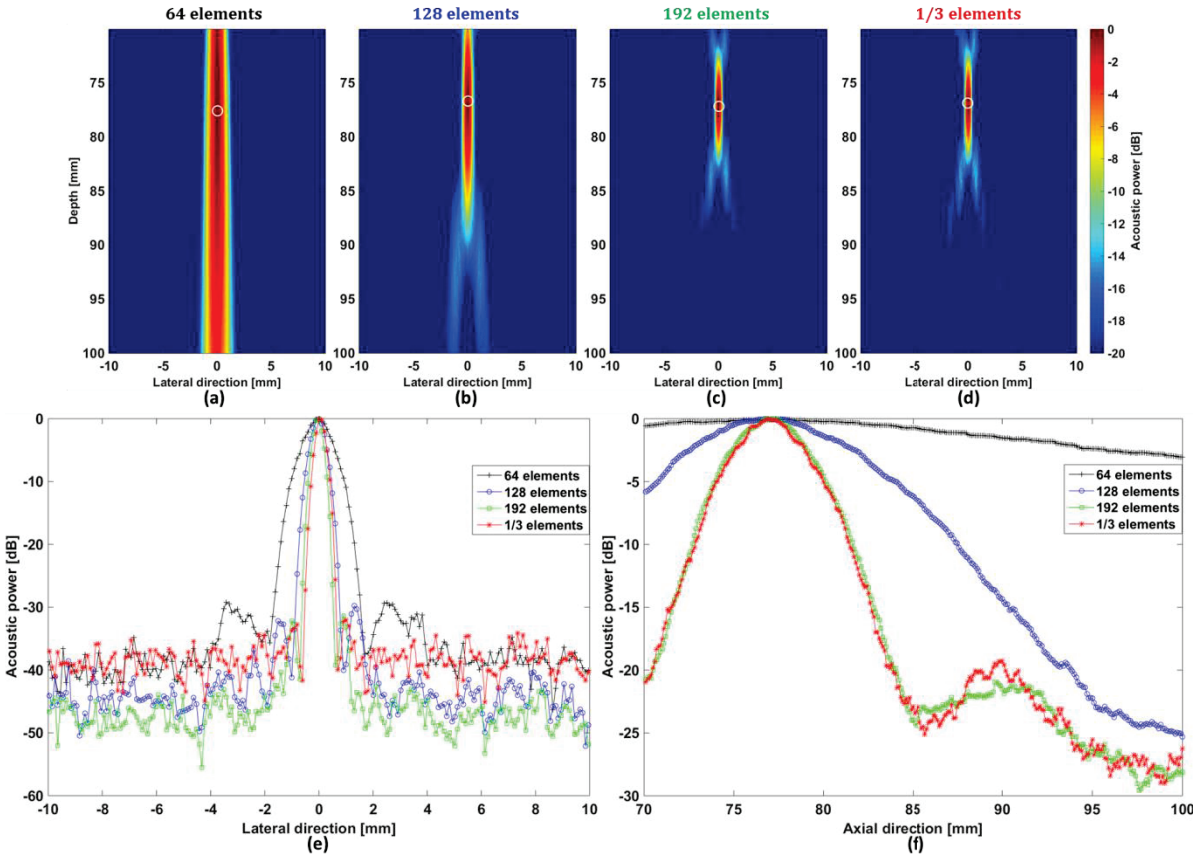

Figure IV-10: The dataset considered are pre-beamformed recoded RF signals emitted by the excited wire positioned at 80 mm from the imaging probe. On the top, PAM-PCF maps reconstructed using the four different aperture models: (a) 64 elements, (b) 128 elements, (c) 192 elements, and (d) 1/3 elements. In each subplot, the white circle corresponds to the FCP localization. On the bottom, the acoustic pattern profiles in the (e) lateral and (f) axial direction (depth) for the four different aperture models.

Table IV-4: FCP positions recovered for the four aperture models with wire experiment dataset including 100 RF recorded signals.

Aperture model	FCP position (depth; lateral)
64 elements	(76.37 ± 1.27; -0.02 ± 0.05) mm
128 elements	(76.68 ± 0.27; -0.05 ± 0.02) mm
192 elements	(76.82 ± 0.13; -0.05 ± 0.01) mm
1/3 elements	(76.80 ± 0.20; -0.03 ± 0.04) mm

Close observations are noticed to the ones in the previous simulation results with the clear improvements of the spot's resolution with increased aperture size. However, this time, on

opposition with the simulation results, when observing the side lobe power levels a minor benefit of the 192 elements model over the 1/3 elements model is observed in Figure IV-10.e. Moreover, the FCP averaged localizations are similar between each four models (Table IV-4) and are close to the ground truth value (77.95; 0) mm recovered in Figure IV-9. Furthermore, the FCP standard deviations decrease with higher aperture size and are clearly dominant for the 192 elements model.

For this ground truth wire positioned at (77.95; 0) mm, an averaged error difference of around 1.28 mm is noticed with the PAM-PCF recovered FCP. This error could be categorized in either ground truth or PAM-PCF error recovery. Many arguments could explain these errors. First the active ultrasound imaging is not the perfect method for ground truth establishment because of for example speed of sound value errors which cause an offset in the delay calculation which also intervene in the PAM algorithm. Second, there is still the propagation attenuation compensation term α outlined in Equation II.3, which was neglected until now because of the use of water as US propagation medium. Therefore, to get a higher accuracy, these ultrasound propagation mechanisms should be considered and investigated.

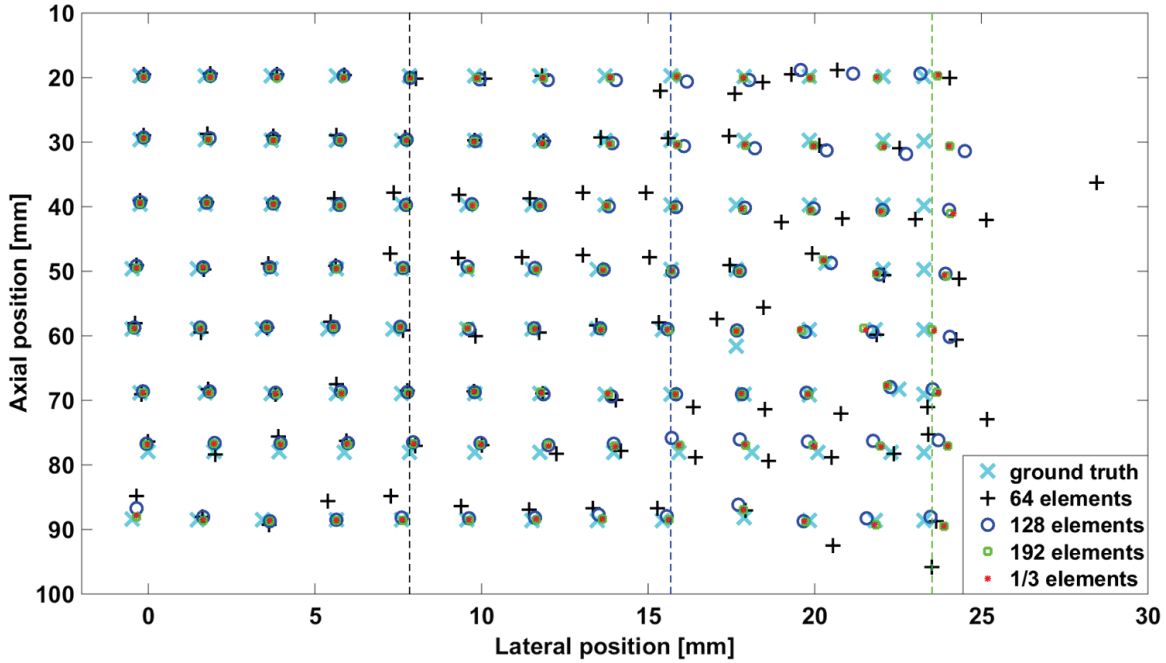

Figure IV-11: The wire position recovered with PAM-PCF and corresponding to the FCP position localization for the four different aperture models as well as for the ground truth position. The vertical dashed lines in black, blue, and green correspond to the half array aperture limit for the 64 elements, 128 elements, and 192 elements or 1/3 elements aperture model, respectively.

The Figure IV-11 first illustrate the issue, already observed in Chapter II, with the 64 central elements aperture causing inaccurate FCP recovery when the wire is positioned outside of the active aperture of the imaging probe and/or for higher depth. Second, it exhibits the obvious improvement of the FCP recovery accuracy for higher aperture size model because of the corresponding enlargement of the active aperture.

The recovery errors (mean ± standard deviation) in the axial and lateral direction shifts, corresponding to the difference between the ground truth and the PAM-PCF recovered wire positions, are computed for the four different aperture models and presented in Table IV-5.

Table IV-5: FCP recovery errors between PAM-PCF and ground truth FCP localization.

Aperture model	FCP recovery errors (depth; lateral) direction shift
64 elements	(1.33 ± 1.27; 0.42 ± 0.65) mm
128 elements	(0.58 ± 0.59; 0.19 ± 0.20) mm
192 elements	(0.41 ± 0.44; 0.15 ± 0.16) mm
1/3 elements	(0.39 ± 0.44; 0.15 ± 0.16) mm

These additional recovery errors results shows that both 192 elements and 1/3 elements aperture models are the most efficient and accurate in term of FCP localization because the FCP recovered positions are the nearest to the ground truth ones. It has the lowest FCP recovery errors average and standard deviations for the 100 total reconstructed PAM-PCF maps.

Therefore, both 192 elements and 1/3 elements aperture models are the best choices for PAM-PCF technique. Still, this general conclusion was actually easily expected because of the logical theory about the probe's aperture size. However, the interesting observation is that even if there is a slightly better side lobe power level decrease for the 192 elements model, the 1/3 elements could be considered in further studies. It has the advantages that first it can be tuned on the ULAOP-64 and second that it exhibits lower time consuming during PAM computation process because of three times less data to process. It was actually developed in the late stage of the PhD project and thus not considered in the previous chapters with cavitation experiments.

IV.3 Frequency domain analysis

The spectrum study and harmonics higher frequency imaging were neglected and not explored yet in the previous PAM computations. However it is a relevant step useful first for exclusive use of higher frequency enabling better spot resolution, and second mapping the different physical cavitation phenomena. For this study only the 64 central active elements were used and the one-spot cavitation experiment was considered with the same dataset and computation parameters than in section III.1.1. The LA523 linear probe is considered imaging the cavitation transversal plane (x, y) in degassed water and with a cavitation power level CI=20 dB. Only one frame (the 55th one) is investigated with a theoretical FCP reference localized at (depth; lateral) = (44; 0) mm. Moreover, in the previous PAM-PCF computations, the TEA sampling frequency (f_{TEA}) parameter never exceeded 15.5 MHz because high frequencies weren't the focus of the investigation. However, now a higher f_{TEA} needs to be set to be able to take in consideration higher frequencies of the pre-beamformed signal. Hence, in the following, the f_{TEA} was set at 18MHz for a corresponding maximum considered bandwidth of 8 MHz (f_{Max}) to respect Shannon principle ($f_{TEA} \geq 2f_{Max}$). The averaged spectrum along the 64 active elements of the pre-beamformed data is plotted in Figure IV-12.

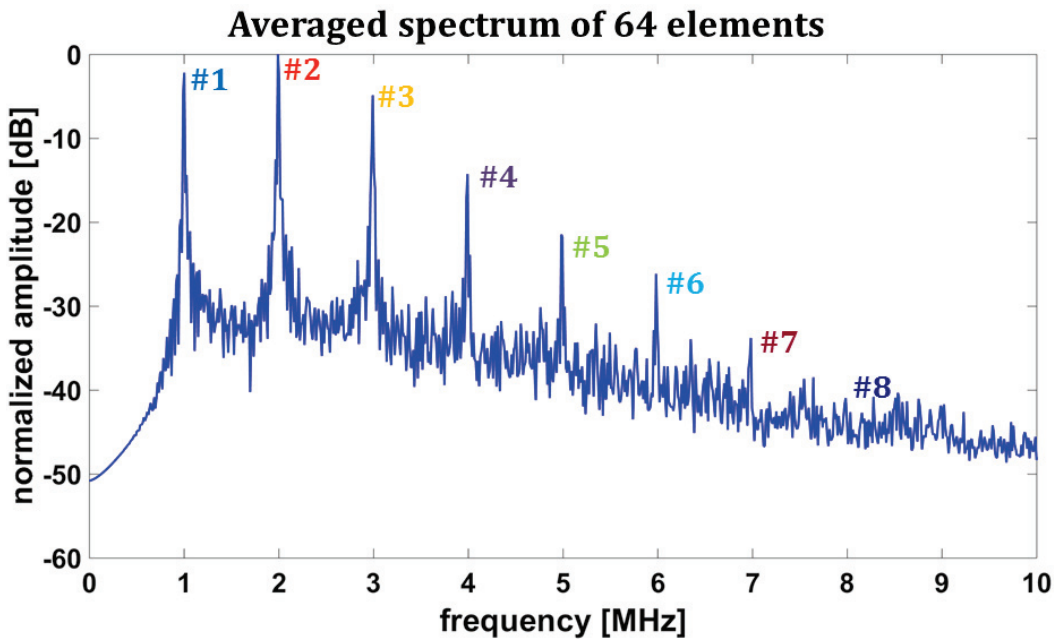

Figure IV-12: Averaged spectrum along the entire 64 active elements of the LA523 imaging probe before any additional frequency-harmonics filtering process with the harmonics number # (n_h) outlined on the plot. Harmonic #1 corresponds to the fundamental signal.

To assess the frequency impact over the PAM-PCF results, a filtering process was applied to the pre-beamformed dataset prior to the PAM-PCF computation. A band-pass Butterworth filter of 5th order and with two corresponding cutoff frequencies (f_{c1} and f_{c2}) is applied for each harmonic number choice (n_h). The cutoff frequency are set to exclusively keep in the filtered pre-beamformed signal the chosen frequency-harmonic with values calculated with Equation (IV.9):

$$\left[f_{c1};f_{c2}\right]=\left[\left(0.8+n_h-1;1.2+n_h-1\right)\right]\ MHz \qquad \text{(IV.10)}$$

In the following, the eight first n_h harmonic numbers were considered. The first harmonic number (n_h=1) corresponds here to the fundamental frequency f_0 = 1 MHz signal. The PAM-PCF technique was applied to the 8 bandpass filtered pre-beamformed signals and the corresponding reconstructed passive maps are displayed in Figure IV-13 as well as the corresponding lateral and axial acoustic pattern profile plotted in Figure IV-14.

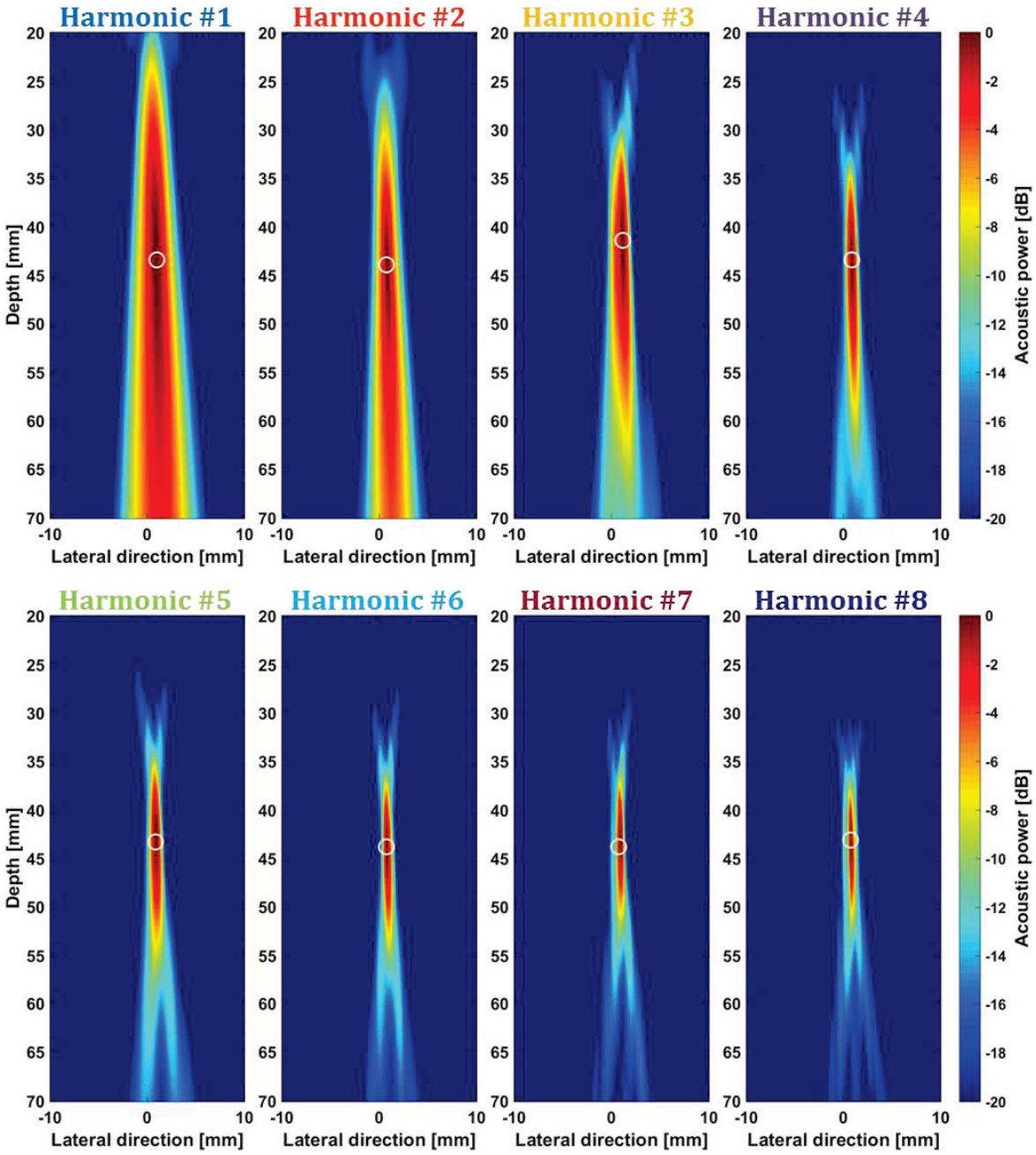

Figure IV-13: PAM-PCF reconstructed maps considering 8 pre-beamformed harmonic-filtered cavitation dataset. The bubble cloud was induced at 44 mm from the imaging probe. The white circle corresponds to the FCP localization. Harmonic #1 corresponds to the fundamental signal.

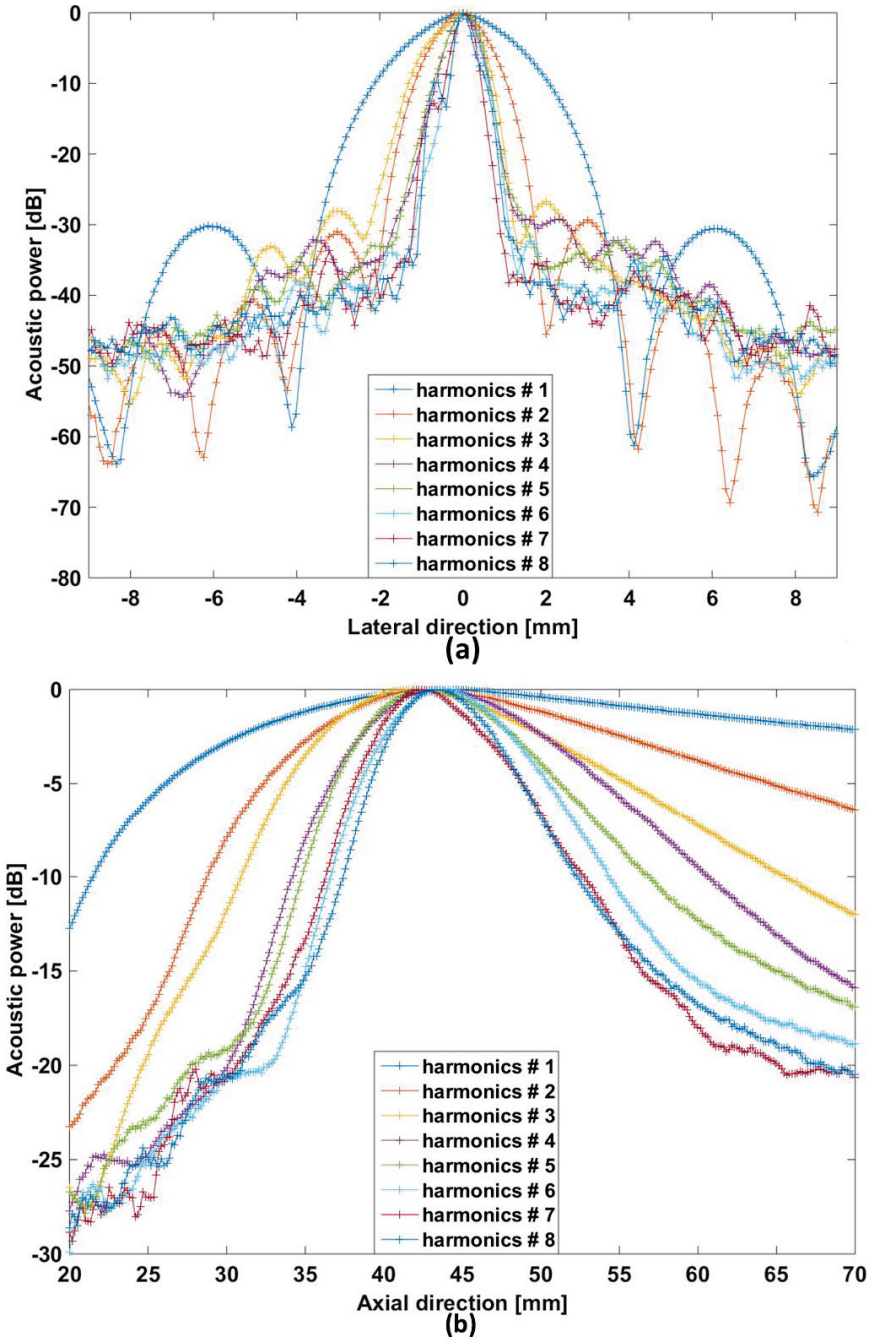

Figure IV-14: The acoustic pattern profiles in the (a) lateral and (b) axial direction for the 8 different harmonic number choices.

A clear improvement of the lateral and axial resolution with the increase of the harmonic choice is noticed in both Figure IV-13 and Figure IV-14. It is coherent with higher frequency ultrasound imaging principle. This increased spot resolution could be useful for multi-bubble localization for avoiding interference between cavitation spots. For each harmonic number choice (n_h), the 2D FCP positions were recovered as well as the recovery errors in both lateral and axial directions (Figure IV-15). The recovery errors correspond to the difference between the theoretical (44; 0) mm and PAM-PCF recovered FCP positions. Except that the FCP localization is not constant in both lateral and

axial directions, it doesn't exhibit any particular correlation with the harmonic number choice but both lateral and axial recovery errors have similar profile plot.

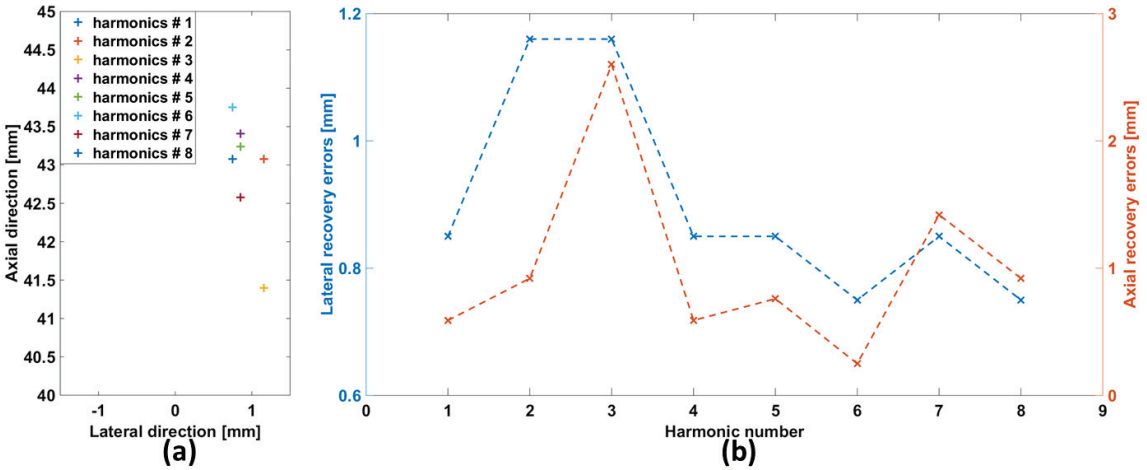

Figure IV-15: The (a) FCP 2D positions and the (b) lateral and axial recovery errors for the entire 8 harmonic number choice maps.

The frequency domain analysis process could be useful also if we want to separate the US waves scattered directly by the bubble cloud from the one emitted by the cavitation phenomenon. For more advanced frequency analysis, more enhanced filtering process needs to be considered as narrowband and broadband signal quantification methodology [135] or angular spectrum approach used for frequency-selective PAM reconstructions [136], [137].

IV.4 Real-time visualization and hybrid mode

The direct collaboration with the MSDlab allowed, during a stay of 3 months in their facility in Firenze, the development of first a preliminary "pseudo-PAM" real-time visualization tool, and second a hybrid mode combining B-mode with passive maps. The ULA-OP 256 new platform was available during my stay and the different developments were focused on.

IV.4.1Real-time visualization

Improved flexibility and processing power of the new ULA-OP 256 platform are guaranteed by the possibility of individually programming multiple digital signal processors (DSP) and field programmable gate arrays (FPGA). Therefore, the platform is able to incorporate a multiline beamformer (parallel beamforming ability) that allows obtaining post-beamformed images of maximum 96 lines by 2048 samples (focused points) at a frame rate of 720 Hz [134]. To implement the PAM technique in real-time, the use of the internal multiline beamformer of the ULA-OP 256 is considered. It enables dynamic focalization in reception (passive DAS) of a complete passive image.

First of all, the pre-beamformed RF signals are converted, thanks to analog-to-digital converters (ADC), into digitals signal sampled at f_s, with number of channels (N) by number of samples (N_s). It is presented in Figure IV-16.a. The pre-beamformed data are then beamformed using an internal ULA-OP beamformer "Pseudo-PAM" which consists in a compounded DAS in reception and is outlined in

Figure IV-16.b. The post-beamformed data corresponds to the passive images with number of lines (N_l) by number of focused points (N_p). The term "Pseudo" is used because there is actually a lack of steps omitted from the initial PAM algorithm previously presented in Chapter II and hence only the passive and compounding/summation aspects are here respected. The post-beamformed data (Figure IV-16.c.) are afterwards demodulated at a chosen demodulation frequency (f_M) into I/Q data which then pass thought an envelope detector (modulus operation) and finally are logarithm compressed and ready for real-time display (Figure IV-16.d.). In this example, the experiment on a wire setup was considered. The number of compound applied was k = 10 with a 500 Hz frame rate reached. The demodulation frequency was set at f_M = 2 MHz because the wire was excited with a 2 MHz transducer.

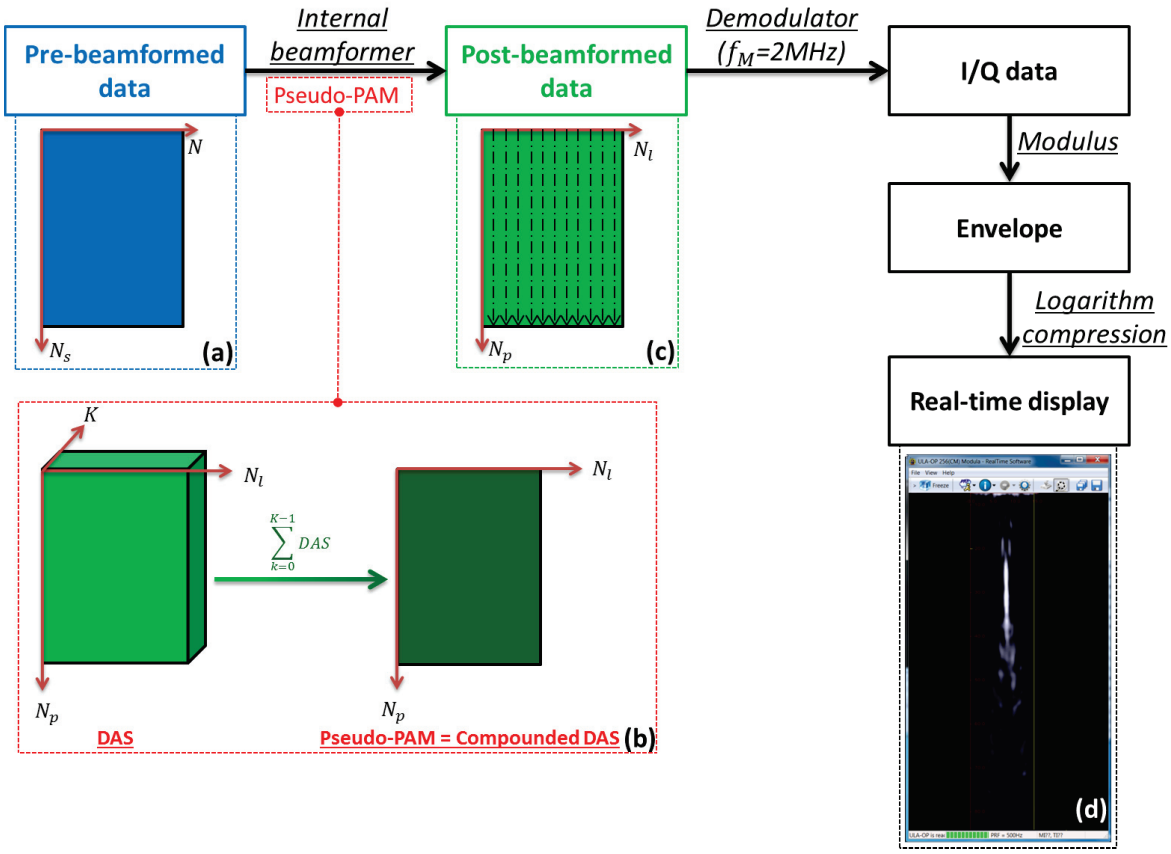

Figure IV-16: Real-time display implementation in the ULA-OP 256 platform of (b) the "Pseudo-PAM" technique passing from (a) pre-beamformed data to (c) post-beamformed data and finally to (d) passive images displayed in real-time (screenshot of the real-time visualization tool). The experiment on a wire was considered in this example for real-time display with a 500 Hz frame rate and k=10 (number of compound).

The use of the ULA-OP 256 platform allowed modifying the number of active elements of the LA523 imaging probe considered for the real-time "Pseudo-PAM" visualization. Therefore the three previous aperture models (64, 128, and 192 elements) outlined in Table IV-2 were assessed and the screenshots of the real-time visualization tool are displayed in Figure IV-17. The wire was positioned at 30 mm from the imaging probe.

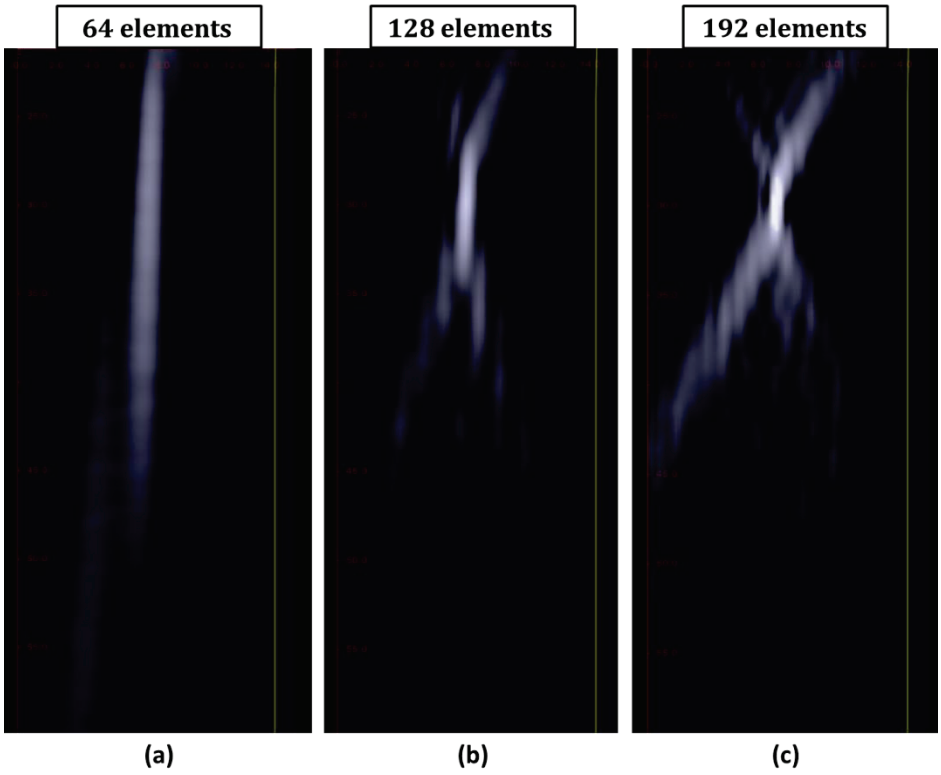

Figure IV-17: Screenshots of the real-time visualization tool during experiment on a wire positioned at 30 mm from the LA523 imaging probe with three different number of active elements chosen: (a) 64 elements, (b) 128 elements, and (c) 192 elements.

The improvement of the spot resolution is clearly observed as predicted in previous studies on the aperture size characteristic. Moreover, the presence of an I/Q representation of the post-beamformed data could be very useful for PCF real-time implementation. The instantaneous phase (φ) of the delayed signal needs to be computed for PCF optimization factor (see Equation II.5). Hence, thanks to I/Q data, φ can be easily recovered by getting directly the argument of the I/Q without passing necessarily by the analytical signal representation thanks to the Hilbert transform considered in classic post-processing offline step on Matlab.

This was a first preliminary test of the real-time display used to establish the possibility of PAM-PCF implementation in the ULA-OP platform. The quick stay at MSDlab didn't permit to go further on this real-time development. Therefore, more work is still needed in development of a complete PAM-PCF real-time display.

IV.4.2 Hybrid imaging mode

For a suitable monitoring therapy system, both active anatomical B-mode images and passive cavitation maps need to be displayed simultaneously during the therapy. Therefore, a combined hybrid imaging mode was developed consisting in merging both information. Thus, the transmission/reception sequence was investigated and tested for RF acquisitions.

The "Enable" synchronization configuration was considered with this time two different ULA-OP acquisition sequences: the passive or active acquisition. The passive acquisition is ON during the therapy ($U_{synchro}(t)$) and then the active acquisition takes over when the therapy is OFF. The

number of acquisitions, especially for the passive mode, needs to be set *a priori* to fit exactly $U_{synchro}(t)$ width. This ULA-OP acquisition sequence is displayed in Figure IV-18.

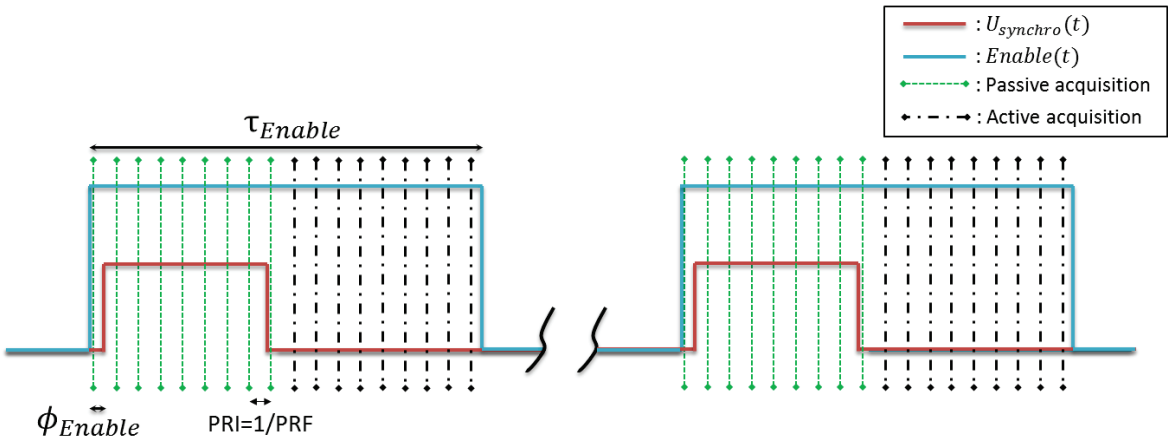

Figure IV-18: ULA-OP hybrid acquisition sequence including active and passive mode synchronized with the therapy signal thanks to the "Enable" configuration.

In parallel to this PhD project, a photoacoustic project is currently in progress in which Aneline DOLET (PhD student) was also able to stay in the MSDlab facility during 6 months to work on the development of a similar passive real-time hybrid imaging mode on the ULA-OP 256. It consisted in a more complex specific C++ and DSP programing process.

IV.5 Conclusions

In conclusion, first the 3D passive imaging implementation would be encouraging by considering a bigger 2D matrix array (32x32 elements). Likewise, this increased number of elements was also considered with the enhancement of the available linear probe characteristics by mainly increasing the aperture size thanks to the use of the optimized ULA-OP 256 platform. This aperture parameter allows mostly the increase of the cavitation spot resolution and hence should improve the multi-source localization accuracy. Additionally, a frequency domain analysis was considered which also improved the spot resolution by taking in consideration higher frequency by working with higher harmonics in the RF signals. Second, preliminary important expansions of the monitoring system were investigated with real-time passive visualization as well as hybrid mode implementations. However, the complete real-time implementation of the PAM-PCF algorithm was partially achieved. Moreover, an alternative or additional real-time implementation could be considered with the use of a very high frame rate acquisition technology paired with a perfectly synchronized configuration [138]. It would mostly allow omitting the TEA principle in the PAM computation step and therefore permit the real-time visualization of instantaneous PAM cavitation maps.

For further development work, a 3D hybrid real-time PAM-PCF imaging system should be developed and therefore would be useful for monitoring the cavitation activities for more *in vivo* ultrasound thrombolysis testing. Still, more optimization of the PAM-PCF technique need to be also assessed as: filtering process, impulse response consideration, electronic noise attenuation as well as time gain compensation (TGC).

CONCLUSIONS AND PERSPECTIVES

This PhD thesis focused on the development and integration of a monitoring ultrasound imaging system into a pre-existing regulated ultrasound-induced cavitation generator therapeutic device designed specifically for ultrasound thrombolysis.

Complex synchronization configurations were established between the therapeutic sonification signal and the ULA-OP acquisitions. During imaging system investigation, the cavitation maps reconstruction achieved with different passive ultrasound techniques were assessed and the passive acoustic mapping weighted with the phase coherence factor (PAM-PCF) method was validated thanks to simulations on a point source and experiments on a wire. Additionally, the focal cavitation point (FCP) recovery errors (axial direction; lateral direction) were considered and exhibit decent values as well as acceptable dispersions (0.44 ± 0.28 mm; 0.09 ± 0.04 mm) for sources positioned in the active aperture of the imaging probe and at low depth which is correlated respectively with steering sensitivity and F-number probe aperture. Subsequently, real cavitation experiments were considered with water tank protocol as well as diverse imaging probe, medium, and computation parameters. It includes one-spot cavitation or multi-spots cavitation generation for multi-sources localization assessment. Moreover, a non-regulated versus regulated cavitation generation protocol was developed to outline the regulation feed-back real-time loop system performance. Additionally, *in vivo* animal testing using an ovine model of acute limb ischemia asserted some already known physical focalization issues dependent to ultrasound propagation mechanisms as reflection and refraction at interfaces. It could cause bad focalization and serious damage of the surrounding tissue. Finally, preliminary optimizations of the previous developed passive ultrasound imaging system were promoted. The importance of 3D localization of the cavitation spot was outlined thanks to 3D imaging implementation assessed with simulations on a point source and cavitation experiments. In addition to 2D array consideration, linear imaging probes could be *a priori* enhanced in performance thanks to the use of higher aperture size influencing directly the focal cavitation spot resolution and FCP localization efficiency. The overall FCP recovery errors were particularly decreased for the 192 elements aperture model (0.41 ± 0.44 mm; 0.15 ± 0.16 mm) versus the 64 elements aperture model (1.33 ± 1.27 mm; 0.42 ± 0.65 mm). An initial frequency domain analysis of the cavitation signal signature was investigated by taking in consideration harmonics and high frequency imaging. It exhibited for high frequency-harmonic cavitation maps improved cavitation spot resolutions. Still the ground truth cavitation focal spot resolution is not accurately defined and therefore the enhancement of this spot characteristic is not that pertinent. Furthermore, a hybrid mode combining both active anatomical images and passive cavitation maps was developed and still needs to be assessed in cavitation experiments. Last but not least, a real-time implementation of a preliminary PAM passive technique was achieved in the ULA-OP 256 to permit real-time visualization of cavitation maps.

The main perspectives of this project would be to carry on the implementation of the monitoring system with a complete 3D hybrid real-time ultrasound imaging technique. Nevertheless, additional parallel works still need to be done as for example developing more accurate protocols for ground truth recovery of the cavitation sources. Indeed, thanks to optimizations, as higher aperture size or higher harmonics exploration, the cavitation spot resolution is clearly improved. However, it could be

indefinitely enhanced but still it cannot be compared to the exact ground truth spot resolution. Therefore, this cavitation spot resolution ground truth reference for the passive cavitation images needs to be exactly defined and hence better protocols for ground truth recovery need to be developed which some are already considered in research field as the use of standing waves to trap and control the cavitation bubbles motion [127], or the use of nanocups to trap and stabilize gas [128]. Moreover, the implementation of a high frame rate camera synchronized with the ULAOP passive acquisitions would be very useful for tracking optically and accurately the ground truth positions of the bubble cloud.

Furthermore, an enhanced simulation tool considering more complex and realistic cavitation bubble mechanisms and interactions is required, using for example the simple Rayleigh–Plesset equation governing the bubble dynamics subject to a pressure field. Otherwise, for a first step, a less evolved simulation tool could be developed with the use of a cavitation referenced RF signal, recorded by a hydrophone during a simple case of cavitation water tank experiment, which is then temporally dephased accordingly to the active element number of the considered imaging probe and finally used for the creation of the complete simulated pre-beamformed dataset. Moreover, the experiment on a wire was very helpful in this work to assess the accuracy of the passive imaging technique. It could be updated by adding multiple wires excited at different times by different transducers and hence would allow the investigation of multi-sources localization accuracy of the passive imaging techniques. Alternatively, a simpler protocol could be considered by using only one scattering wire shifted in many positions and by then summing the recorded RF pre-beamformed signals it would thereby generate a pseudo-multi-sources dataset.

Besides, for performance investigation PAM-PCF technique should be carefully compared with other PAM optimizations (as PAM-SCF, PAM-RCB, PAM-SCF-RCB [127]) and other passive techniques (as angular spectrum approach [136]). Additionally, the impulse response of the imaging probe should be considered and hence the frequency domain analysis should be assessed with more enhanced filtering processes or with the use of other frequency domain passive beamforming methods. Furthermore, thanks to parallel works on the distinct and specific regulation of the inertial or non-inertial cavitation activity, the regulated ultrasound-induced cavitation generator should be able to separate both cavitation mechanisms during the therapy and therefore isolates the mechanical from the thermal damage of the cavitation bubbles.

Original and innovative studies are being considered for ultrasound therapy and a lot of effort is put into action to develop a complete safe ultrasound therapeutic technique by focusing on the spatial monitoring system allowing during the sonification therapy to ensure the cavitation bubble cloud to be generated on the thrombus. Moreover, many inquiry lines of research remain to be explored and many issues remain to be solved before one can hope to test clinically this extracorporeal ultrasound thrombolysis device.

PERSONAL BIBLIOGRAPHY

Journal

P. Boulos, F. Varray, A. Poizat, A. Ramalli, B. Gilles, J.-C. Bera, and C. Cachard, “Spatial monitoring of a focused ultrasound-induced cavitation generator,” *IEEE Trans. Ultrason. Ferroelectr. Freq. Control*. (*submitted 2017*)

International conferences

P. Boulos, F. Varray, A. Poizat, M.A. Kalkhoran, B. Gilles, J.-C. Bera, and C. Cachard, “Passive cavitation imaging using different advanced beamforming methods,” *IEEE International Ultrasonics Symposium*, Tours, France, 2016, pp. 1–4. (*oral presentation*)

P. Boulos, F. Varray, B. Gilles, J.-C. Bera, and C. Cachard, “3D passive imaging of ultrasound cavitation using a 2D array,” *IEEE International Ultrasonics Symposium*, Washington, USA, 2017. (*poster presentation*)

National conferences

P. Boulos, F. Varray, A. Poizat, J.-C. Bera, and C. Cachard, “Passive cavitation imaging using an open ultrasonic system and time reversal reconstruction,” *Congrès Français de Mécanique*, Lyon, France, 2015. (*oral presentation*)

A. Poizat, **P. Boulos**, F. Varray, B. Gilles, C. Cachard, and J.-C. Bera,"Contrôle temporal et spatial de la cavitation ultrasonore pour des tests de thrombolyse ultrasonore extracorporelle," *Congrès Français de Mécanique*, Lyon, France, 2015. (*oral presentation*)

FRENCH SUMMARY

A. Introduction

Les ultrasons sont souvent utilisés pour l'imagerie diagnostique médicale en raison de ses avantages connus comme non-invasive, facilité d'utilisation, affichage en temps réel et coût limité. Des techniques novatrices de thérapie par ultrasons ont émergé récemment avec la technologie des ultrasons focalisés de haute intensité (HIFU) qui peut causer des dommages mécaniques ou thermiques induits par des mécanismes de cavitation acoustique. Cette technique a l'avantage principal de pouvoir traiter des organes profonds sans altérer les tissus présent entre le transducteur et son foyer. De telles modalités thérapeutiques ont déjà des applications cliniques comme par exemple le traitement des cancers de la prostate et la destruction des calculs rénaux. D'autre part, les maladies cardiovasculaires comme la thrombose qui se caractérise par des caillots sanguins obstruant les vaisseaux, sont actuellement traitées par des techniques de thrombolyse telles que: les traitements médicamenteux (anticoagulants ou agents thrombolytiques) et chirurgicaux (angioplastie par ballonnet, thrombectomie ou pontage). Pourtant, ces techniques ont un risque élevé d'échec causé la plupart du temps par des problèmes de saignement. Par conséquent, une nouvelle technique thérapeutique peu invasive est à l'étude: la thrombolyse ultrasonore extracorporelle en exploitant les dommages mécaniques des HIFU pour détruire le thrombus. Afin de contrôler l'activité de la puissance de cavitation, un prototype a été récemment conçu et amélioré avec une boucle de rétroaction en temps réel [97]. Cependant, cette technique thérapeutique nécessite toujours un système de suivi en temps réel qui serait essentiel pour assurer la destruction parfaite et complète du thrombus sans endommager les vaisseaux. Ce dispositif devrait être capable d'imager et de localiser le thrombus et ensuite de suivre et quantifier l'activité de cavitation dans les deux dimensions spatiale et temporelle. Ainsi, le travail présenté dans ce mémoire porte sur le développement et l'évaluation d'un système d'imagerie ultrasonore avancé intégré au traitement de la thrombolyse ultrasonore: l'imagerie ultrasonore de la thrombolyse ultrasonore.

B. Thrombose et thrombolyse

La thrombose est la formation d'un caillot sanguin, également appelé thrombus. Il est le résultat de l'agrégation de différents composants comme les plaquettes, les globules rouges et la fibrine. Il est formé dans les vaisseaux principalement pendant le processus d'hémostase correspondant à une réponse normale et naturelle à un vaisseau endommagé. Lorsque la surface de l'endothélium est endommagée, les plaquettes interagissent avec la surface sous-endothélium révélée, formant un thrombus pour arrêter le saignement. Après guérison, le processus naturel de fibrinolyse a lieu pour désintégrer chimiquement le caillot sanguin. La plupart du temps, le thrombus est localement limité dans la zone du vaisseau blessé et ne cause pas de risques d'ischémie majeure. Cependant, la thrombose pourrait apparaître de façon pathologique dans un vaisseau sain, provoquée par trois facteurs de risque interdépendants connus sous le nom de triade de Virchow qui inclut : une altération de l'endothélium (hémostase), une anomalie du flux sanguin (stase ou turbulence) et une hypercoagulabilité. Parfois, le thrombus peut même se détacher de la paroi du vaisseau et parcourir le système sanguin pour enfin obstruer un vaisseau sain, c'est ce qu'on appelle une embolie. Cette

pathologie est appelée thromboembolie. Il existe deux types de thrombose selon l'endroit où il se produit: la thrombose veineuse ou artérielle. Pour les thromboses veineuses, les retombées les plus graves sont la thromboembolie pulmonaire provoquée par l'obstruction du système artériel pulmonaire par un thrombus détaché en amont. Pour les thromboses artérielles, la sévérité est plus importante et peut résulter en un infarctus aigu du myocarde ou en une ischémie cérébrale correspondant respectivement au blocage de l'artère coronaire alimentant le muscle cardiaque ou du blocage de la carotide alimentant le cerveau. Des risques plus faibles, mais toujours élevés, peuvent être observés pour l'ischémie aiguë des membres correspondant au blocage de l'irrigation sanguine d'un membre. S'il n'est pas traité rapidement, il peut entraîner une invalidité permanente, l'amputation ou même la mort du patient. Ces pathologies nécessitent des traitements adaptés rapide, appelés thrombolyse, qui désagrègent chimiquement ou mécaniquement le caillot sanguin obstruant partiellement ou totalement le vaisseau. Selon la localisation, la gravité, la composition et l'âge du thrombus différents traitements adaptés peuvent être utilisés comme les médicaments ou la chirurgie invasive.

De nos jours, l'échographie (l'imagerie ultrasonore) a des applications dans de nombreux domaines et est utilisée principalement pour détecter, localiser et analyser les tissus et organes. Grâce à ses caractéristiques portatives, non-ionisantes, non-invasives et à coût limités, l'imagerie ultrasonore est majoritairement utilisée pour le diagnostic en médecine. D'un autre côté, les ultrasons de haute intensité peuvent être nocifs et même endommager les tissus. Lorsque les ultrasons se propagent dans le tissu, un mécanisme d'absorption se produit correspondant à la conversion de l'énergie acoustique en énergie thermique provoquée par la vibration et le frottement de la matière. Ce mécanisme est déjà considéré en imagerie ultrasonore avec la contribution partielle de l'atténuation en fonction de la profondeur des ultrasons alors que l'amplitude est beaucoup moins élevée que dans les applications thérapeutiques. Des contraintes mécaniques significatives peuvent également être observées comme la génération d'ondes de choc ou de micro-écoulement et micro-flux violents. Cependant, la cavitation acoustique est le principal phénomène intervenant dans la thérapie par ultrasons responsable de la plupart de ces mécanismes destructeurs.

Le phénomène de cavitation consiste premièrement en la nucléation de bulles (noyaux) induites dans un liquide exposé à une forte sous-pression provoquant une diminution rapide et significative de la pression locale à température constante. Par conséquent, la cavitation se produit lorsque la pression est inférieure à la pression de vapeur saturante. Ce phénomène est thermodynamiquement très similaire au phénomène d'ébullition où, au contraire, l'augmentation rapide de la température à pression constante génère des bulles. Cette sous-pression peut être générée soit par des ondes ultrasonores (cavitation ultrasonore), soit par un écoulement liquide très rapide observé par exemple sur les pales d'une hélice de bateau (cavitation hydrodynamique). Dans les travaux de cette thèse, seul le phénomène de cavitation par ultrasons est étudié. Lorsque les bulles sont soumises à un champ ultrasonore, leurs rayons varient inversement et proportionnellement à la pression (oscillation radiale) tant que la pression est faible: les sous-pressions favorisent la pénétration du gaz dans la bulle qui va donc s'étendre et au contraire les surpressions induisent la diffusion du gaz hors de la bulle et son diamètre se réduit. La quantité de gaz diffusée d'une phase à l'autre est proportionnelle à la surface de la bulle (surface d'échange). En raison de la différence de cette surface d'échange entre les cycles d'expansion et de compression, il y a en moyenne un net flux de gaz entrant dans la bulle. Donc, le rayon de la bulle a tendance à augmenter. Cette théorie est

appelée diffusion de masse rectifiée et permet à la bulle d'atteindre des tailles plus importantes que la taille du noyau initial. Une fois la nucléation amorcée, la cavitation peut évoluer en fonction de l'amplitude de pression du champ ultrasonore suivant différents régimes. Pour de faibles amplitudes, l'oscillation radiale de la bulle est stable et est décrite comme une oscillation linéaire. Pour des amplitudes plus élevées, la bulle oscille encore de manière stable, cependant elle tend à se comporter davantage comme un oscillateur non linéaire incluant une réponse harmonique et même sous-harmonique. Ces deux régimes représentant une oscillation radiale stable de la bulle est appelée la cavitation non inertielle. Dans ce cas, l'absorption par le tissu est renforcée par la diffusion de l'énergie acoustique à différentes fréquences harmoniques. Par conséquent, le mécanisme thermique est amplifié. Pour des amplitudes encore plus élevées, la bulle devient très instable et s'étend rapidement et chaotiquement jusqu'à atteindre une douzaine de fois son rayon initial, provoquant son effondrement violent suivi de nombreux rebonds. Cet effondrement provoque de nombreuses répercussions mécaniques (ondes de choc), thermiques (température locale jusqu'à 5000 K) et chimiques (radicaux libres). Ce régime est appelé la cavitation inertielle et est défini acoustiquement par un spectre large bande lié à la rapidité de l'effondrement. Ces différents régimes peuvent coexister dans le même nuage de bulles. Dans cette étude, l'appellation de cavitation est utilisée pour la nucléation, l'oscillation radiale et l'effondrement des bulles. Le phénomène de cavitation dépend d'un grand nombre de paramètres comme le champ ultrasonore (amplitude, forme et fréquence) et le milieu (impédance acoustique, température, impuretés et concentration de gaz dissous). C'est un phénomène complexe qui possède un caractère fortement aléatoire.

Ainsi, les ultrasons sont de plus en plus utilisés dans le domaine de la thérapie en raison de ses avantages évidents en permettant des traitements peu invasifs et peu coûteux. En clinique, les ultrasons sont déjà utilisés à des fins thérapeutiques comme la physiothérapie, l'hyperthermie et la lithotripsie. En phase de recherche, des techniques innovantes de traitement par ultrasons peu invasives sont toujours à l'étude pour des applications telles que la sonoporation, la délivrance ciblée de médicaments, l'histotripsie et la thrombolyse. Ce dernier utilise l'insonification HIFU pulsée transcutanée en s'appuyant sur le processus de cavitation inertielle. C'est ce qu'on appelle la thrombolyse ultrasonore extracorporel. Cependant, l'utilisation de la cavitation par ultrasons reste complexe et sa dynamique doit être temporellement contrôlée en temps réel durant la thérapie. Ainsi, plusieurs travaux de recherche ont été réalisés pour mettre en place un système de contrôle temporel de cavitation en temps réel. Récemment, un système de contrôle avec une boucle de rétroaction a été considéré en particulier pour le régime pulsé et la régulation de l'activité de cavitation inertielle. Il a été spécifiquement développé pour l'application de la thrombolyse ultrasonore pour mieux s'affranchir du caractère aléatoire de la cavitation ultrasonore [97]. Un transducteur thérapeutique (IMASONIC SAS, Voray, France) est excité avec un signal sinusoïdal à 1 MHz pulsé avec une répétition de pulse de 4 Hz et un rapport cyclique de 10%. Il est pré-amplifié par un amplificateur de puissance (69 dB, GN 1000, PRANA, Malemort, France). Ce générateur de cavitation à ultrasons focalisés est régulé en terme de la puissance acoustique transmise et un indice de cavitation inertielle (CI) a été défini comme la moyenne le long des fréquences de la compression logarithmique de la transformée de Fourier du signal acoustique mesuré en temps réel. Il représente le bruit acoustique large bande correspondant à la contribution de la cavitation inertielle. Cependant, il manque encore l'information spatiale de l'activité de cavitation. Par conséquent, afin de cibler spatialement le thrombus dans le vaisseau sanguin et de contrôler spatialement l'activité de cavitation, un système de surveillance approprié doit être développé.

Dans la recherche actuelle et aussi en clinique, la thérapie ultrasonore est normalement suivie avec les techniques de thermométrie par imagerie par résonance magnétique (IRM), avec des cartographies d'élévation de température ou par imagerie ultrasonore active en mode B avec les informations hyperéchogènes du nuage de bulles de cavitation qui permettent sa localisation. Cependant, les deux méthodes ne permettent pas de surveiller spatialement l'activité de cavitation en temps réel car elles ne peuvent pas fonctionner simultanément avec les outils de thérapie. De plus, l'IRM fournit une information de température qui n'est pas utile pour la thrombolyse où les dommages mécaniques prédominent sur les dommages thermiques. En imagerie ultrasonore active en mode B, le nuage de bulles de cavitation apparaît comme une zone hyperéchogène en mouvement qui, même si elle fournit des informations de localisation spatiale sur les bulles, ne donne pas d'informations quantitatives sur l'activité de cavitation. De plus, le nuage représente des « anciennes » bulles qui, lorsqu'elles sont détectées, ne cavitent plus. En effet, les deux méthodes peuvent être utilisées pour guider la thérapie en per-opération, mais elles ne sont pas adaptées pour le guidage de l'activité de cavitation en temps réel. Au contraire, l'imagerie passive ultrasonore est un bon candidat parce que premièrement, elle n'interfère pas avec les impulsions de thérapie et que deuxièmement, elle dispose de capacités de suivi en temps réel. Par conséquent, il pourrait fournir des cartographies d'activité de cavitation en temps réel pendant la thérapie ultrasonore.

Le but de cette thèse est de développer et d'intégrer un système de suivi spatial temps réel optimisé au système de thérapie préexistant. Il inclut une technique avancée d'imagerie ultrasonore passive fournissant une cartographie de l'activité de cavitation utilisée pour la localisation des sources de cavitation (nuage de bulles). Dans la partie suivante, le système d'imagerie développé pour l'imagerie de cavitation passive est présenté, y compris sa configuration générale et un protocole de validation.

C. Imagerie ultrasonore passive

Dans le mode brillance (mode B) d'imagerie classique, l'amplitude du signal acoustique écho est utilisée pour la modulation de la luminosité et le temps de propagation pour obtenir la position du diffuseur. En imagerie passive de cavitation, l'impulsion en transmission est désactivée et la sonde d'imagerie ultrasonore enregistre les signaux acoustiques émis par les bulles de cavitation au cours du temps. Le nuage de bulles génère des ondes sphériques représentées par des fronts d'ondes qui se propagent dans le milieu et sont collectées passivement par la sonde. Après l'enregistrement passif des données radio fréquences (RF) brutes, la cartographie d'activité de cavitation peut être reconstruite grâce à un algorithme de formation de voies (beamforming). Dans une étude préliminaire, trois méthodes de reconstruction par formation de voies ont été développées et testées spécifiquement pour la localisation des sources de cavitation: la méthode de retournement temporel (« time reversal method » TRM), la cartographie acoustique passive (« passive acoustic mapping » PAM) et le PAM pondérés avec un facteur de cohérence de phase (« phase coherence factor » PCF). Ils sont introduits à la suite et leurs performances sont de même discutées.

Les techniques de retournement temporelles reposent sur l'invariance de l'équation de propagation d'onde par inversion temporelle. Il a été introduit par Fink *et al.* [106] et est utilisé dans de nombreux domaines comme les télécommunications ou le médical. Dans les applications

médicales, quelques études ont été réalisées en utilisant un mécanisme de focalisation par retournement temporelle. La technique du miroir à retournement temporel consiste à utiliser un réseau de transducteurs piézoélectriques qui permet d'enregistrer le champ acoustique reçu, de l'inverser dans le temps, puis de le retransmettre par les mêmes transducteurs. En conséquence, l'onde ultrasonore se propage et se focalise à la source acoustique initiale. Dans notre étude, une méthode de retournement temporelle virtuelle (TRM) a été développée grâce à l'outil « k-Wave » conçue par Treeby *et al.* [119] dans le logiciel Matlab pour des simulations de propagations acoustiques dans le domaine temporel. Il comprend un algorithme flexible de reconstruction d'image par retournement temporel qui inverse temporellement les signaux acoustiques et propage virtuellement les ondes dans le milieu vers leurs sources. Cette méthode est appliquée aux données RF brutes passives. Il consiste à rétro propager les ondes acoustiques incidentes vers leurs sources et donc à localiser les sources d'origine (nuage de bulles).

L'algorithme de reconstruction de cartographie acoustique passive, traduit de l'anglais « passive acoustic mapping » (PAM), consiste à appliquer une focalisation dynamique en réception, c'est-à-dire l'algorithme sommation des retards (« delay–and-sum » DAS) [120]. Les retards τ_i à appliquer aux données RF de chaque élément i de la sonde pour le pixel spécifique (x, y, z) de la cartographie de cavitation à reconstruire sont calculés:

$$\tau_i(\boldsymbol{r}) = d_i(\boldsymbol{r}) / c_0 = \|\boldsymbol{r} - \boldsymbol{r_i}\| / c_0, \quad \text{avec} \begin{cases} \boldsymbol{r} = (x, y, z) \\ \boldsymbol{r_i} = (x_i, y_i, z_i) \end{cases} \tag{11}$$

où d_i est la distance de propagation entre le point $\boldsymbol{r}$ et le i^{th} élément positionné à $\boldsymbol{r_i}$ et c_0 la vitesse de propagation de l'onde ultrasonore. Cependant, étant donné que le système d'imagerie fonctionne sur des acquisitions passives et de même par faute de l'information temporelle du comportement de l'activité des bulles, le temps de propagation aller-retour de l'onde ultrasonore ne peut alors être utilisé. C'est pourquoi la limitation principale de l'imagerie ultrasonore passive est l'absence de l'information temporelle sur les conditions d'origine des signaux RF enregistrés. La force de source q à un instant $k\Delta t$ et pour le pixel localisé à $\boldsymbol{r}$ sont calculées en sommant les informations de pression récupérées à partir des signaux RF retardés:

$$q(\boldsymbol{r}, k\Delta t) = \frac{1}{N} \sum_{i=1}^{N} \alpha . s_i \left\{ k\Delta t + \tau_i(\boldsymbol{r}) - min\left[\tau(\boldsymbol{r}) \right] \right\} \tag{12}$$

où s_i est le signal RF enregistré par le i^{th} élément, α le terme de compensation pour l'atténuation de propagation et N le nombre d'éléments de la sonde. Pour surmonter le problème du manque de l'information sur le temps d'origine, le principe du temps d'exposition acoustique (« time exposure acoustic » TEA) [121] a été appliqué en calculant la moyenne du carré de la force de source q le long d'un temps $T = (K-1)\Delta t$.

k représente le nombre entier du pas temporel correspondant et K le nombre total de pas de temps calculés. Enfin, la puissance acoustique P_{PAM} est calculée pour chaque pixel:

$$P_{PAM}(\boldsymbol{r}) = \frac{1}{4\pi\rho_0 c_0} . \frac{1}{K} . \sum_{k=0}^{K-1} q^2(\boldsymbol{r}, k\Delta t) \tag{13}$$

où ρ_0 est la densité du milieu. Pour améliorer la suppression des lobes secondaires, corriger les points mal focalisés et corriger les artefacts d'interférence de bulles qui limitent la reconstruction PAM, un facteur de cohérence de phase [123] est implémenté (PAM-PCF). Il consiste en un facteur de pondération se basant sur l'estimation de la dispersion de la phase du signal retardé σ_φ, et est calculé de la façon suivante:

$$PCF\left(\boldsymbol{r},k\Delta t\right)=\max\left[0;1-\frac{\gamma}{\sigma_0}\sigma_\varphi\left(\boldsymbol{r},k\Delta t\right)\right] \tag{14}$$

où γ correspond à la sensibilité du facteur PCF. L'augmentation de la valeur γ favorise la suppression des données mal focalisées, et il est choisi égal à 1. φ est la phase instantanée du signal retardé et σ_0 est l'écart-type nominal d'une distribution linéaire dans $[-\pi;\pi]$ modulo 2π et est égal à $\frac{\pi}{\sqrt{3}}$. Enfin, la puissance acoustique $P_{PAM-PCF}$ est calculée pour chaque pixel:

$$P_{PAM-PCF}\left(\boldsymbol{r}\right)=\frac{1}{4\pi\rho_0 c_0}.\frac{1}{K}.\sum_{k=0}^{K-1}\left[PCF\left(\boldsymbol{r},k\Delta t\right).q\left(\boldsymbol{r},k\Delta t\right)\right]^2 \tag{15}$$

Deux types de données ont été utilisés pour l'étape d'étude des performances ainsi que la validation de ces trois algorithmes de formation de voies : des données de simulation considérant une source ponctuelle et des données enregistrées lors d'une expérience sur un fil excité par une source acoustique et immergé dans une cuve d'eau.

L'outil de simulation utilisé consiste en la création de données simulées en prenant en compte une source ponctuelle qui correspond à une seule source de cavitation. Cette source acoustique est défini par sa position, sa fréquence fondamentale f_0, et le nombre d'harmoniques supposés être générés par la non-linéarité. Dans cette étude, la source est caractérisée par une fréquence f_0=1 MHz et la présence de 7 harmoniques avec des fréquences nf_0, n={2;…;8}, et une diminution d'amplitude proportionnelle à $1/n$. La source ponctuelle est positionnée à 40 mm de la sonde d'imagerie et les trois algorithmes de formation de voies (TRM, PAM et PAM-PCF) sont ensuite appliqués aux données brutes simulées correspondantes. Finalement les cartographies sont reconstruites et affichées Figure 19.(a-c). De plus, pour une meilleure interprétation quantitative, les profils acoustiques suivant les directions latérale et axiale sont tracés pour les trois méthodes dans la Figure 19.(d, e).

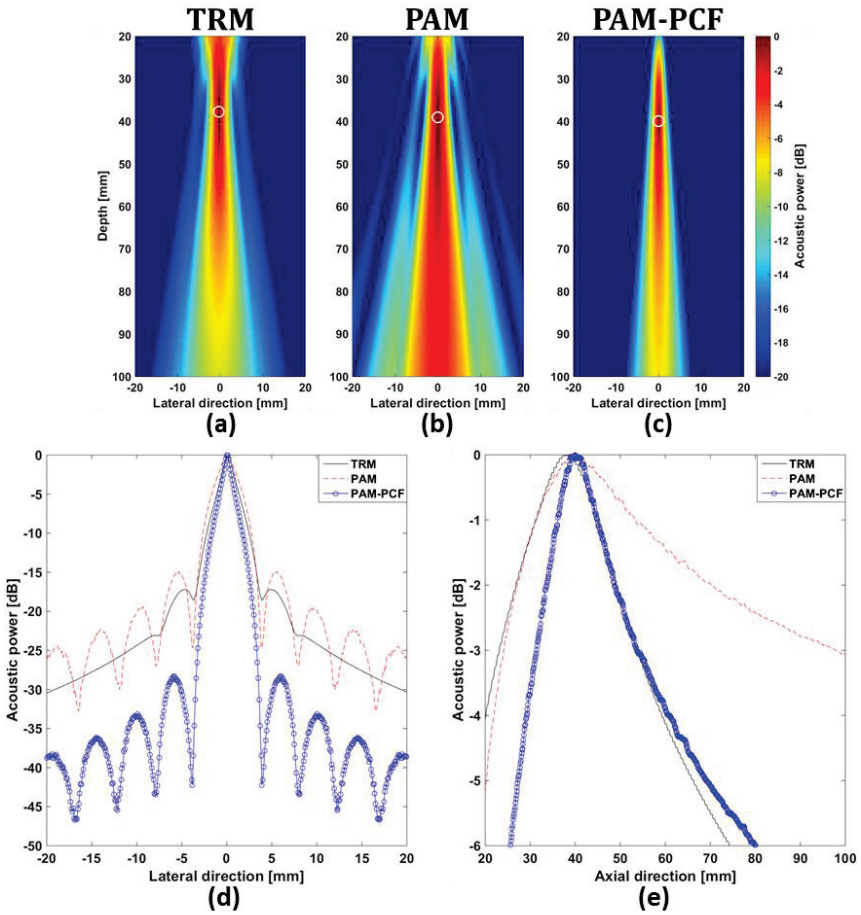

Figure 19 : Cartographies de puissance acoustique reconstruites à l'aide des trois algorithmes de formation de faisceau: (a) TRM, (b) PAM, (c) PAM-PCF appliqué aux signaux RF simulés bruts transmis par une source acoustique ponctuelle positionnée à 40 mm de la sonde d'imagerie. Dans chaque cartographie, le point focal mesuré est marqué par un cercle blanc, avec les coordonnées (latérale ; profondeur) en mm et la position théorique égale à (0; 40). Les profils acoustiques dans la direction (d) latérale et (e) axiale pour les trois algorithmes de formation de faisceau (TRM, PAM, PAM-PCF).

Dans les cartographies de puissance acoustique Figure 19.(a-c), pour les trois méthodes, un aspect de tâche focale prolongé dans la direction axiale aussi appelé « aspect en queue de comète » est observé, représentant une diminution latérale de la résolution en fonction de la profondeur. Il est quantitativement observé dans la Figure 19.(e) où son impact est plus fort pour PAM que TRM. Cet aspect pourrait s'expliquer principalement par le processus TEA lorsque dans PAM la puissance acoustique est sommé le long d'un temps (13). Grâce à l'implémentation du facteur de pondération PCF (PAM-PCF), la résolution a été améliorée dans les deux directions axiale et latérale, en particulier en diminuant ce problème de « aspect en queue de comète ». Pour le PAM-PCF, dans la direction latérale, une réduction de 13.4 dB pour les lobes secondaires est obtenue ainsi que pour le lobe principal à -20 dB diminué de 16.9 %. Dans la direction axiale, la largeur de la tâche focale à -3 dB a été réduite de 69.8 %. Dans la direction axiale (profondeur), le point focal (point d'intensité maximum) pour TRM, PAM et PAM-PCF est respectivement localisé à 37.7 mm, 39 mm et 39.9 mm. La localisation de la source ponctuelle est donc efficace et proche de la valeur théorique à 40 mm. Le PAM a cependant une meilleure efficacité de localisation que TRM et cela est confirmé lorsqu'on augmente la profondeur d'étude.

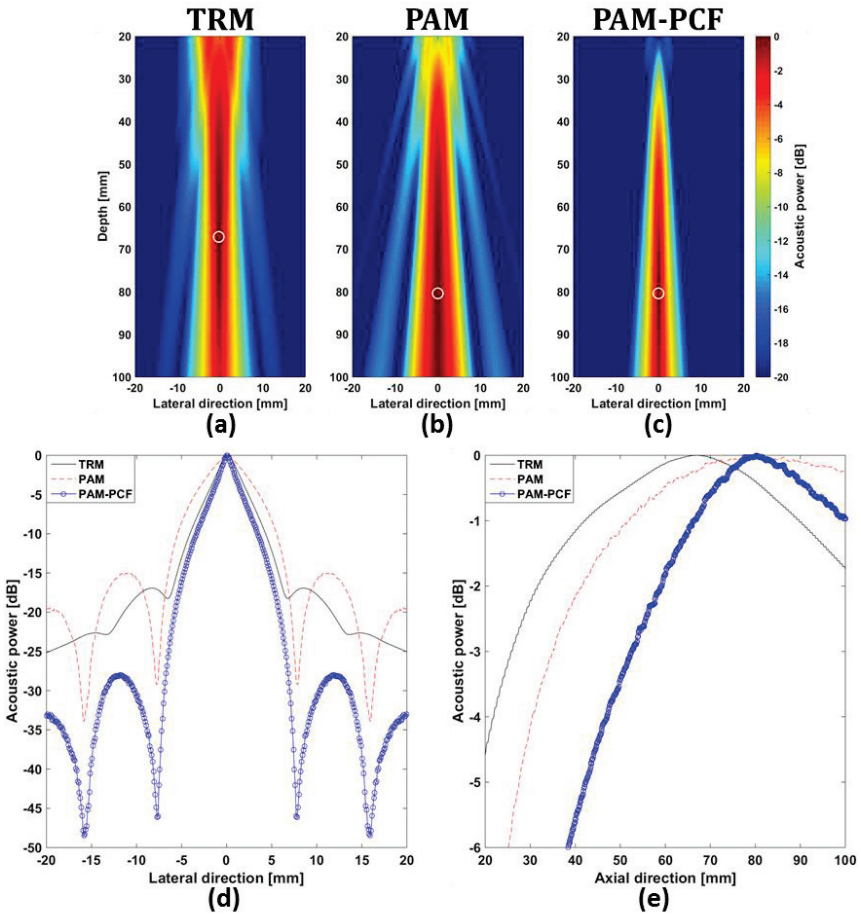

Figure 20 : Cartographies de puissance acoustique reconstruites à l'aide des trois algorithmes de formation de faisceau: (a) TRM, (b) PAM, (c) PAM-PCF appliqué aux signaux RF simulés bruts transmis par une source acoustique ponctuelle positionnée à 80 mm de la sonde d'imagerie. Dans chaque cartographie, le point focal mesuré est marqué par un cercle blanc, avec les coordonnées (latérale ; profondeur) en mm et la position théorique égale à (0; 40). Les profils acoustiques dans la direction (d) latérale et (e) axiale pour les trois algorithmes de formation de faisceau (TRM, PAM, PAM-PCF).

En effet, pour une source ponctuelle positionnée cette fois ci plus profondément à 80 mm de la sonde d'imagerie (Figure 20), les mêmes interprétations que précédemment (Figure 19) sont observées. Mais cependant dans ce cas, les résolutions, quand comparées à celles des cartographies de la source à 40 mm de la sonde, sont dégradées avec des largeurs de tâche focale plus grandes. Ce problème est lié directement à l'ouverture de la sonde et de la nécessité du maintien de la valeur du F-number. Par ailleurs, dans la direction axiale (profondeur), le point focal pour les 3 méthodes TRM, PAM et PAM-PCF est respectivement localisé à 67.1 mm, 80.4 mm et 80.4 mm. Ainsi, un problème de localisation de source est observé pour la méthode TRM lorsque la profondeur de la source acoustique augmente. Ce problème peut s'expliquer du fait que la technique de retournement temporelle utilisant l'outil de simulation « k-Wave » pour la rétro-propagation de l'onde ultrasonore à la source ponctuelle initiale est différente dans son processus de calcul par rapport aux signaux RF bruts simulés. C'est pourquoi la plupart des applications de retournement temporelle considèrent l'aspect physique réel de l'inversion du temps en retransmettant le signal inversé dans le milieu en utilisant spécifiquement le même transducteur physique qu'à l'aller pour des conséquences de précision de focalisation. Par conséquent, dans notre cas de reconstruction de cartographie passive

de cavitation, la supériorité de la méthode PAM par rapport à TRM est validée et donc TRM n'est plus utilisée ou discutée dans les travaux suivants.

Spécifiquement pour les expériences en cuve d'eau, un système d'imagerie ultrasonore, incluant la plateforme de recherche ultrasonore (ULA-OP) couplée à deux sondes d'imagerie linéaire LA523 et LA332, a été intégré au système préexistant de thérapie (le générateur de cavitation ultrasonore régulé). Ce système d'imagerie est synchronisé avec le générateur de cavitation de sorte que les signaux RF soit acquis à des moments précis durant la thérapie. La configuration générale est représentée dans la Figure 21.

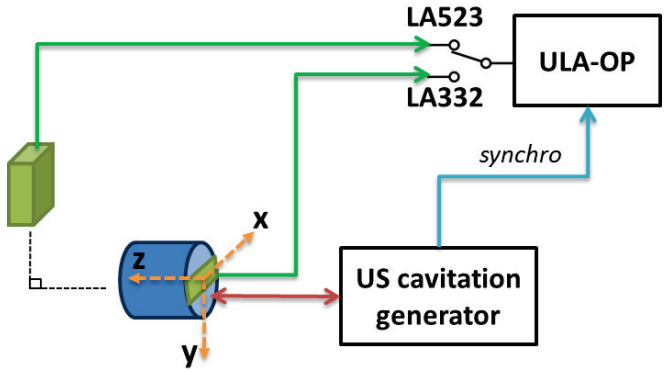

Figure 21 : Configuration générale utilisant à la fois le système thérapeutique (générateur de cavitation ultrasonore régulé) et le système d'imagerie avec un échographe ULA-OP couplé à deux sondes d'imagerie (LA523, LA332) synchronisées avec l'insonification thérapeutique ultrasonore.

Les deux sondes d'imagerie, LA523 et LA332 (Esaote S.p.A., Florence, Italie), sont utilisées séparément dans ce travail. Il s'agit de deux sondes linéaires à éléments piézo-électriques avec le même pas (distance entre deux éléments consécutifs) égal à 245 µm. Les deux sondes sont placés perpendiculairement l'une à l'autre. La sonde LA332 est incorporée dans le transducteur thérapeutique et est donc active suivant le même axe que celui du faisceau de thérapie. Les caractéristiques de ces deux sondes sont présentées dans le Tableau 1. Les 64 éléments centraux ont été utilisés sur les deux sondes, correspondant à une d'ouverture active de largeur égale à 15.68 mm.

Tableau 1: caractéristiques des sondes d'imageries

Sonde	Nombre total d'éléments	Bande passante	Dimensions
LA523	192	4–13 MHz	50x8 mm
LA332	144	3–11 MHz	36x8 mm

Pour examiner la précision de la technique d'imagerie passive (PAM-PCF), la fonction d'étalement ponctuel a été considérée en utilisant un fil de nylon de 0.1 mm de diamètre placé perpendiculairement à la sonde d'imagerie LA523. Un transducteur mono-élément (5 MHz, SL-0503-HP, Panametrics-Olympus, Tokyo, Japon) a été utilisé pour exciter le fil. Il était alimenté par un générateur émetteur/récepteur (5052PR, Sofranel Panametrics-Olympus, Tokyo, Japon), de sorte que le fil rayonnant imite une source ponctuelle à réponse fréquentielle large bande fournissant des

informations similaires à un événement de cavitation inertielle. Pour étudier l'efficacité de la localisation de la technique de reconstruction PAM-PCF, la position du fil par rapport à la position de la sonde a été modifiée axialement et latéralement en déplaçant la sonde à l'aide d'un système de positionnement motorisé tri-directionnel (OWIS, Staufen, Allemagne) à trois axes orthonormés (x, y, z), comme le montre la Figure 22. Pour le premier positionnement du fil à (x = 0 mm; z = 20 mm) la visualisation avec l'imagerie ultrasonore active en mode B a été utilisé. La position y a été choisie de sorte que le plan d'imagerie coïncide avec le plan du faisceau du transducteur. Ensuite, en utilisant le logiciel du système de positionnement (OWISoft), la sonde d'imagerie a été déplacée dans 154 positions différentes: 11 latérales (dans le sens des x) et 14 axiales (dans le sens des z). Ayant une symétrie dans la direction latérale de la sonde, seuls les décalages positifs pour la direction latérale (0 à 20 mm) ont été pris en compte. Pour chaque position du fil, 100 acquisitions passives synchronisées avec le générateur émetteur/récepteur ont été enregistrées. Après le post-traitement des acquisitions avec la méthode PAM-PCF, 100 images passives ont été reconstruites. Ensuite, sur chaque cartographie, la position du pixel d'intensité maximale correspondant à la position du fil a été extraite. Finalement, la position moyenne du fil a été récupérée et tracée sur la Figure 23 pour les 154 positions.

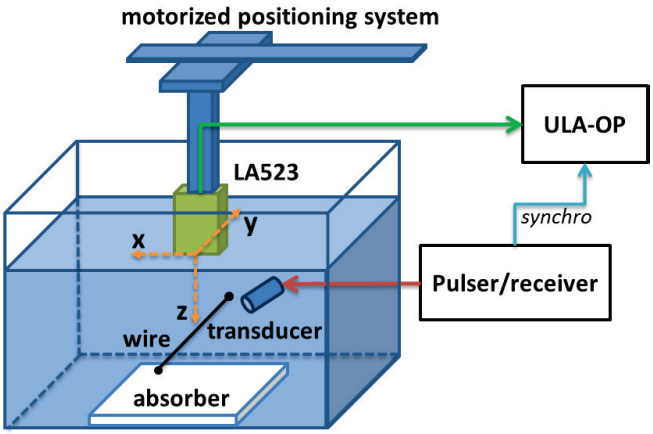

Figure 22 : Expérience en cuve d'eau sur un fil de nylon de 0,1 mm de diamètre excité par un transducteur alimenté par un générateur émetteur/récepteur. La sonde d'imagerie LA523, enregistrant passivement les signaux acoustiques transmis par le fil avec le système ULA-OP, est déplacée en utilisant un système de positionnement motorisé dans les deux directions (x = latéral et z = axial).

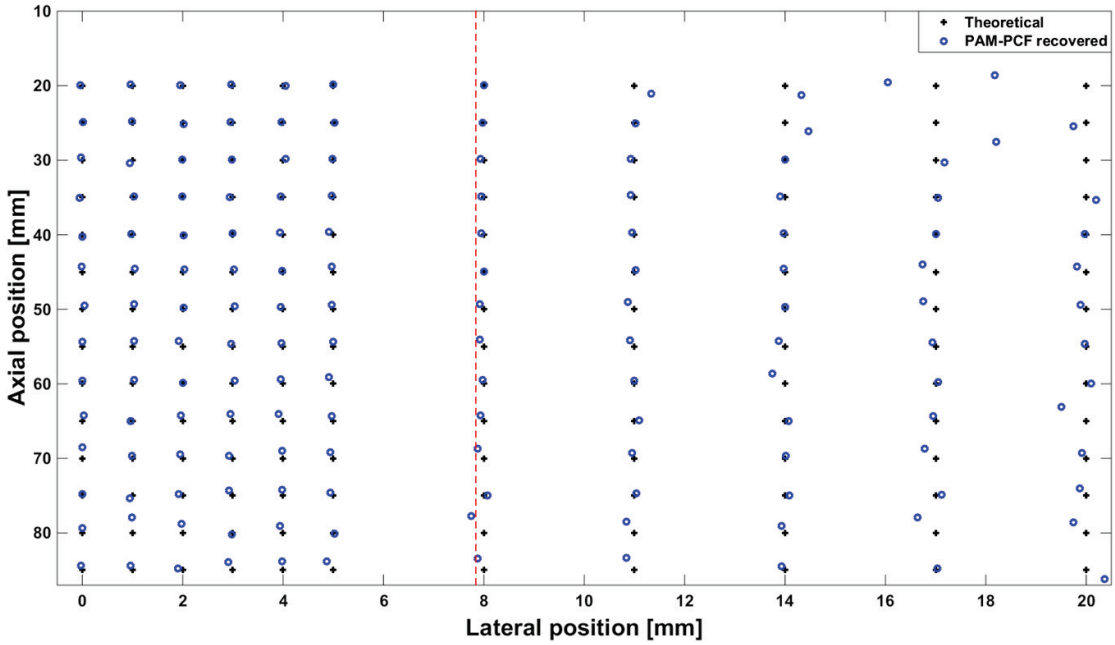

Figure 23 : Positions théoriques des fils (noir +) et celles calculées avec PAM-PCF (bleu o). La ligne pointillée rouge verticale correspond à la limite de la moitié de l'ouverture active de la sonde égale à 7.84 mm (32 éléments × 0.245 mm de pas).

Grâce à l'algorithme PAM-PCF, les positions des fils ont été obtenues avec une précision satisfaisante: les erreurs de mesure (moyenne ± écart-type), correspondant à la différence entre la position théorique et la position mesurées, sont respectivement égales pour les décalages dans la direction axiale et latérale à 0.64 ± 0.52 mm et 0.13 ± 0.21 mm. En outre, les positions des fils sont mieux localisées lorsque le fil est dans l'ouverture active de la sonde (positions latérales <7.84 mm) et proche de la sonde (positions axiales <70 mm). Dans cette région, les erreurs de mesure pour les décalages dans la direction axiale et latérale étaient respectivement de 0.44 ± 0.28 mm et 0.09 ± 0.04 mm. À de plus grandes profondeurs (positions latérales <7.84 mm et positions axiales ≥ 70 mm), la localisation est moins robuste et les erreurs de mesure pour les décalages dans la direction axiale et latérale sont respectivement de 0.80 ± 0.52 mm et 0.06 ± 0.03 mm. Cependant, pour des positions hors de la limite de l'ouverture active de la sonde (positions latérales> 7.84 mm), les positions mesurées sont moins précises et les erreurs de mesure pour les décalages dans la direction axiale et latérale sont respectivement de 0.76 ± 0.61 mm et 0.19 ± 0.30 mm. En effet, en raison de la sensibilité limitée de directivité de la sonde d'imagerie, les échos rétrodiffusés par le fil pourrait être négligés dans le signal RF enregistré.

En conclusion, la méthode passive de reconstruction PAM pondérée par le facteur de cohérence de phase (PAM-PCF) a été comparé aux méthodes TRM et PAM en considérant les deux protocoles de validation précédents (des simulations avec une source ponctuelle et une expérience sur un fil excité par un transducteur). En considérant d'abord les simulations avec une source ponctuelle, la méthode PAM domine la TRM par rapport à la localisation du point focal et la seconde méthode PAM-PCF améliore la méthode PAM avec une meilleure résolution de la tâche focale (réduction du lobe principal et secondaire). Ensuite, grâce à l'expérience sur fil, l'efficacité de la localisation du point focal en utilisant uniquement la technique PAM-PCF a été évaluée. Il a été montré que la précision est meilleure lorsque le fil est placé dans l'ouverture active de la sonde d'imagerie et à faible profondeur.

Dans la suite des travaux, la technique de formation de voies PAM-PCF est choisie comme la technique d'imagerie de cavitation passive de référence pour la reconstruction des cartographies d'activité de cavitation. Dans la partie suivante, des expériences de cavitation sont testées pour évaluer la technique d'imagerie passive dans une situation plus proche de la réalité ainsi que tester les performances du système de thérapie.

D. Expériences de cavitation

Pour une étape de validation plus poussé, des expériences de cavitation ont été menées d'abord pour évaluer des cartographies réalistes de cavitation d'imagerie passive, puis pour étudier et observer l'activité de cavitation avec son évolution et comportement spatio-temporelle. Des expériences *in vitro* en cuve d'eau ainsi que des expériences préliminaires *in vivo* ont été développées et réalisées.

Une méthode préliminaire d'étude de la cavitation est d'utiliser des expériences en cuve d'eau permettant directement une visualisation optique en temps réel de la génération du nuage de bulles et de ses déplacements. Un nuage de bulles de cavitation unique, avec différents paramètres du milieu ainsi que différentes intensités d'insonification ultrasonore (CI), est étudiée. Ensuite, l'activité de cavitation non-régulée par rapport à une activité régulée est évaluée. Finalement, deux nuages de bulles de cavitation générés séparément sont considérés pour évaluer les limitations de la technique PAM-PCF. La cavitation ultrasonore (un nuage de bulles) est déclenchée dans une cuve d'eau grâce au générateur de cavitation ultrasonore régulé. La cuve a été remplie d'eau filtrée, déionisée (particules <5 µm) et dégazée (3 mgO_2/L). La température ambiante de l'eau était constante et égale à 22° C. Des absorbeurs acoustiques ont été utilisés pour réduire les ondes d'échos multiples réfléchies par les parois de la cuve. Un gel d'agar, utilisé pour restreindre le déplacement du nuage de bulles au minimum, a été préparé avec de l'agar à 4% dissous dans de l'eau déionisée, chauffée à 85 °C et mélangée en utilisant un agitateur magnétique. Le mélange homogène a été versé dans un moule de 10 cm x 10 cm x 10 cm et ensuite refroidi dans un réfrigérateur pendant la nuit. Les signaux RF ne sont enregistrés que pendant les impulsions d'insonification ultrasonore avec une fréquence de répétition d'impulsions (PRF) interne de l'ULA-OP. L'indice de cavitation (CI) est utilisé pour contrôler l'intensité de l'activité de cavitation.

<u>Expérience avec un nuage de bulles de cavitation unique :</u>

Pour l'expérience avec un seul nuage de bulle présenté sur la Figure 24, différents cas expérimentaux ont été étudiés : avec ou sans gel d'agar, un CI croissant (10 à 40 dB avec un incrément de 5 dB) et les deux sondes d'imagerie (LA523 ou LA332). Lorsqu'il est utilisé, le gel d'agar est positionné à une distance de 40 mm du transducteur thérapeutique et en contact direct avec la sonde d'imagerie LA523. Le nuage de bulles a été généré à 44 mm de LA523 et à 80 mm de LA332. Ces positions ont été *a priori* vérifiées en utilisant la visualisation en mode B avec l'identification des régions hyperéchogènes correspondant au nuage de bulles. La sonde LA523 image le plan transversal de la tâche de cavitation (x, y) et la sonde LA332 le plan axial de la tâche cavitation (x, z) tel qu'illustré sur la Figure 24. Pour chaque cas, 1500 acquisitions passives ont été réalisées représentant, pour une PRF de 3000 Hz, 20 impulsions d'insonification ultrasonore de 75 signaux RF chacune. Pour chaque acquisition passive enregistrée, une cartographie de cavitation a été reconstruite en utilisant l'algorithme de formation de voie PAM-PCF. Ainsi, un total de 1500

cartographies a été reconstruit le long des 500 ms. Pour chaque cartographie, le point focal de cavitation (FCP) est défini comme le point à la puissance acoustique maximale et donc représente la position centrale du nuage de bulles de cavitation. Pour supprimer les événements à faible ou sans cavitation, un seuil de -40 dB a été appliqué aux valeurs de puissance acoustique du FCP. Exclusivement pour cette opération de seuillage, la puissance acoustique est auparavant normalisée sur la totalité des 1500 cartographies.

Les changements de position du FCP ont ensuite été calculés temporellement pour les deux directions d'imagerie : axiale et latérale. Un cas spécifique expérimental a été choisi dans cette section pour présenter ces différents résultats: utilisation de l'eau dégazée, gel d'agar, plan transversal de cavitation (LA523) et un indice de cavitation (CI) égal à 20 dB. La cartographie de cavitation reconstruite pour la 4ème image d'acquisition passive et la cartographie cumulée le long des 1500 cartographies reconstituées sont représentées sur la Figure 25.(a, b). La position dans les deux dimensions du FCP est affichée sur la Figure 25.c. De même, son profil temporel de localisation dans la direction axiale (profondeur) et latérale est représenté sur la Figure 25. (d, e).

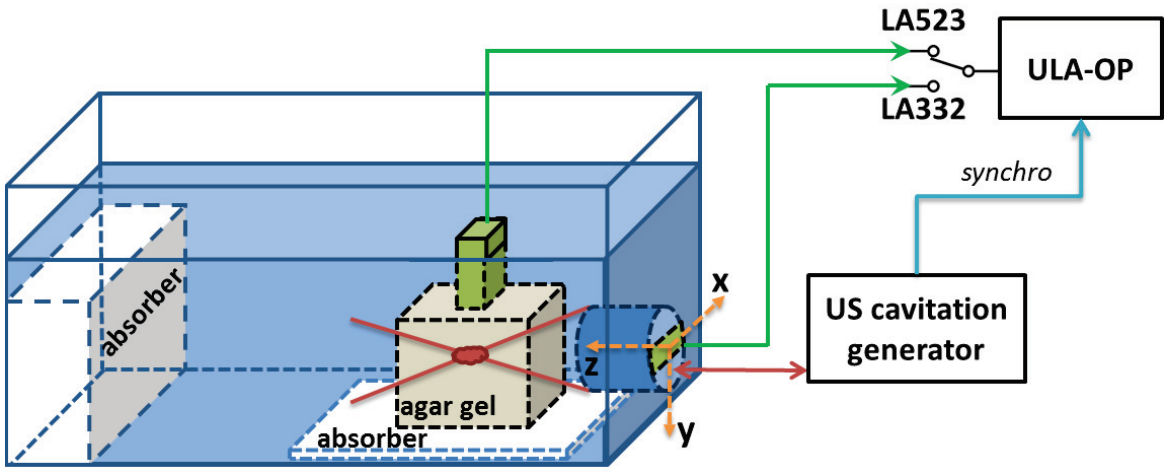

Figure 24 : Expérience de cavitation en cuve d'eau utilisant à la fois le système thérapeutique (générateur de cavitation ultrasonore régulé) pour induire un nuage de bulles et le système d'imagerie avec les deux sondes d'imagerie (LA523, LA332) synchronisées avec les impulsions d'insonification ultrasonore.

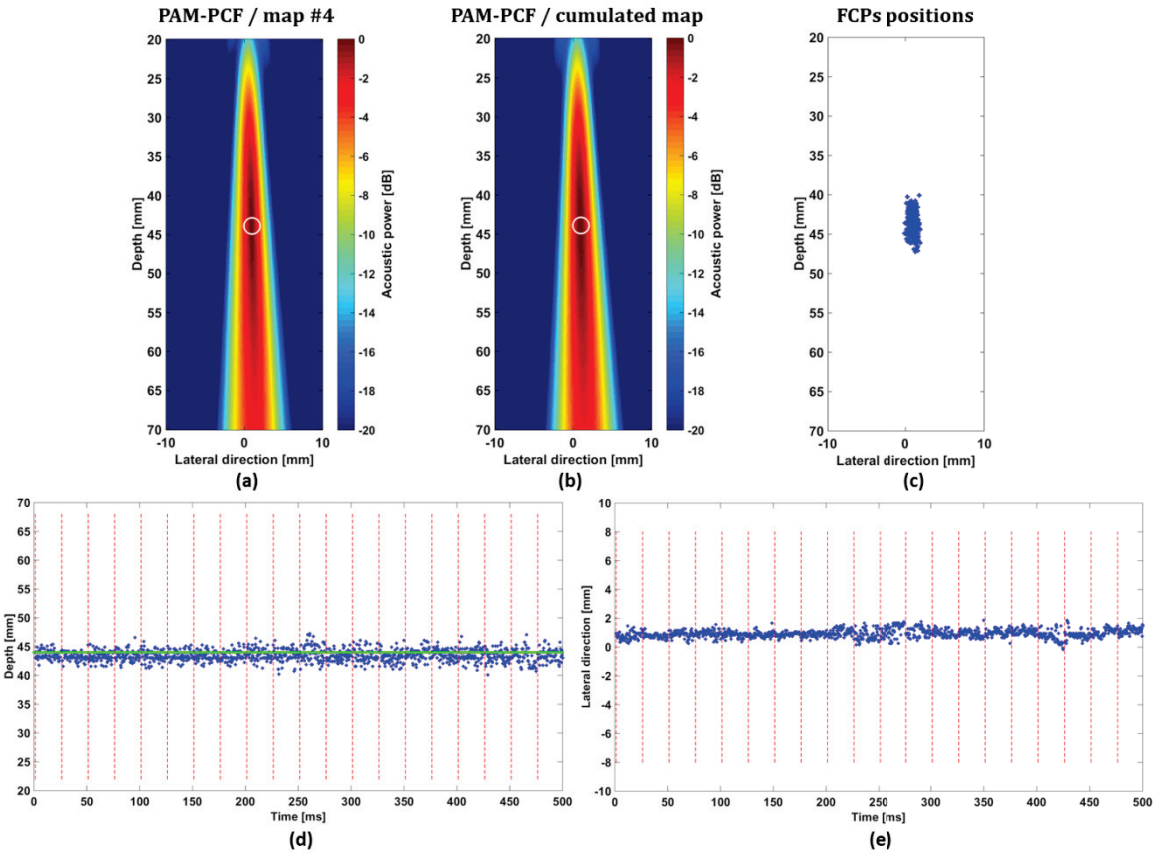

Figure 25 : Utilisation du gel d'agar et de la sonde d'imagerie LA523 avec CI = 20. (a) La cartographie de cavitation reconstruite avec la méthode PAM-PCF pour la 4ème image d'acquisition passive. (b) Cartographie cumulée le long de 1500 cartographies. Le cercle blanc correspond à la localisation FCP. (c) Les positions 2D du FCP. Le profil temporel de localisation du FCP le long des 500 ms d'insonification ultrasonore à la fois pour (d) la profondeur et (e) la direction d'imagerie latérale. La ligne verte horizontale représente la référence de profondeur théorique du FCP et la ligne pointillée rouge verticale correspond au début de chaque impulsion d'insonification ultrasonore.

Dans la section suivante, un aperçu des différents résultats des différents cas traités est présenté. Les positions FCP 2D le long des 500 ms d'insonification ultrasonore globale sont affichées pour les cas avec ou sans gel d'agar avec un CI croissant et pour les deux plans de cavitation sur la Figure 26 (plan transversal) et la Figure 27 (plan axial).

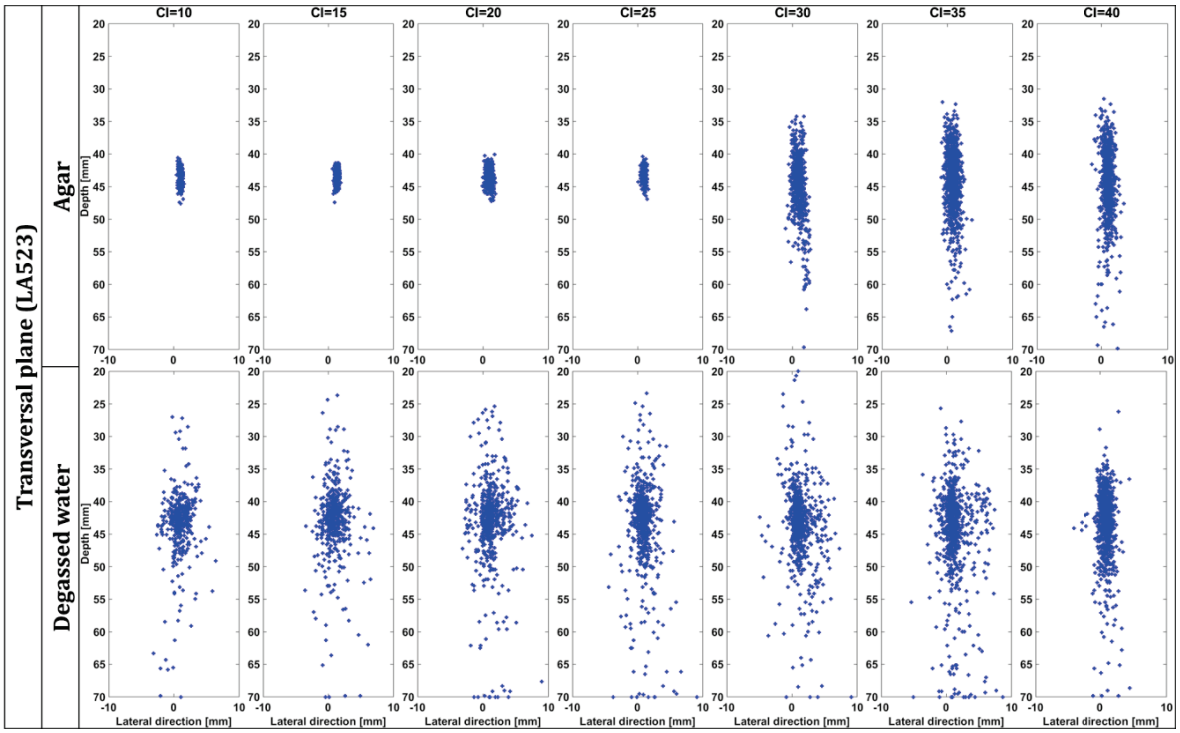

Figure 26 : Positions des points focaux de cavitation (FCP) dans les deux dimensions le long des 500 ms d'insonification ultrasonore globale pour le plan transversal de cavitation (LA523) avec ou sans gel d'agar et avec un indice de cavitation (CI) croissant.

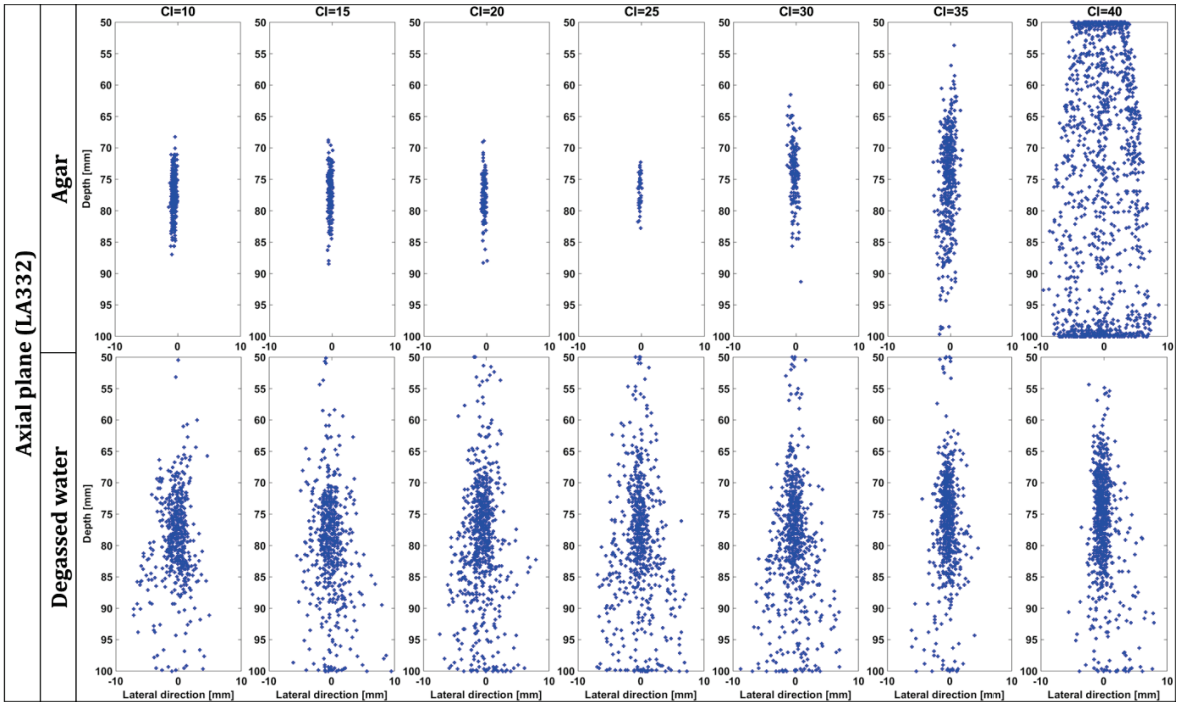

Figure 27 : Positions du point focal de cavitation (FCP) dans les deux dimensions le long des 500 ms d'insonification ultrasonore globale pour le plan axial de cavitation (LA332) avec ou sans gel d'agar et avec un indice de cavitation (CI) croissant.

Par rapport au comportement spatio-temporel, l'activité de cavitation ultrasonore générée a été étudiée en analysant la localisation spatiale du FCP en profondeur pour un CI croissant. Pour chaque CI, le FCP a été moyenné le long des 500 ms d'insonification ultrasonore. Le profil spatio-temporelle

est affiché pour la sonde d'imagerie LA523 correspondant au plan transversal de cavitation sur la Figure 28.(a, b) et pour la sonde d'imagerie LA332 correspondant au plan axial de cavitation sur la Figure 28.(c, d).

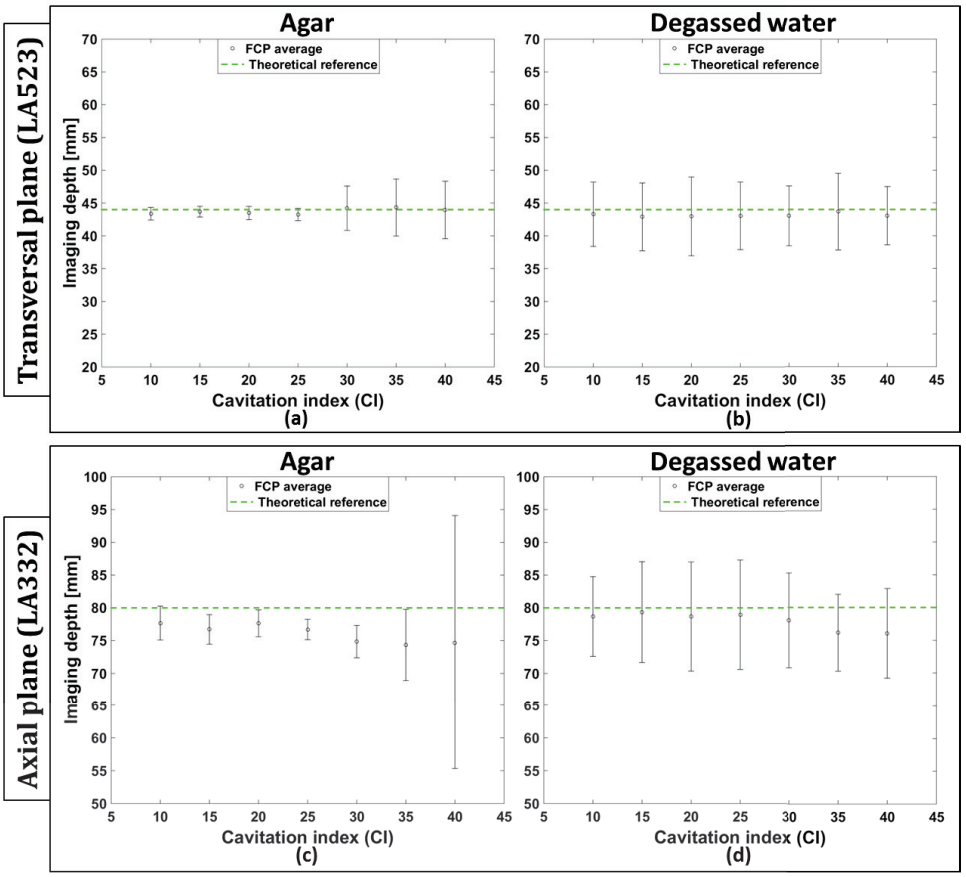

Figure 28 : Evolutions spatio-temporelles du FCP pour un CI croissant et les deux plans de cavitation transversal (LA523) et axial (LA332) avec ou sans gel d'agar. La ligne pointillée verte horizontale représente la référence théorique du FCP.

Ces résultats confirment dans un premier temps le comportement physique déjà connu de la cavitation ultrasonore. En effet, dans le plan transversal de cavitation, les positions du FCP convergent bien vers la valeur de référence théorique. En revanche, dans le plan axial de cavitation, les positions du FCP sont plus discontinues et s'éloigne de la référence théorique. Avec un CI croissant, le nuage de bulles tend à migrer vers le transducteur thérapeutique. Cette observation est cohérente avec le comportement spatial physique déjà connu du nuage de bulles dans cette direction [60]. De plus, les positions du FCP sont spatialement plus étendues dans le plan axial de cavitation que dans le plan transversal de cavitation ce qui est cohérent avec la forme ovale du faisceau d'insonification ultrasonore dans cette direction. Par ailleurs, le confinement du nuage de bulle dans le gel d'agar est clairement observé surtout dans la Figure 26 ainsi que la Figure 27. Quand le gel d'agar est utilisé, les bulles ne se déplacent pas librement en raison de la structure du gel qui restreint le déplacement du nuage de bulles dans une zone limité. Cependant, ceci n'est plus le cas pour des intensités de cavitation élevé (CI≥30) où une sur-dégradation du gel d'agar se produit, conduisant à un comportement de bulle assez similaire à celui avec de l'eau dégazée où les bulles sont plus libres de se déplacer. En outre, en utilisant l'intensité d'activité de cavitation la plus élevée (CI = 40), et spécifiquement pour le plan axial de cavitation (LA332), les positions du FCP fournies par

PAM-PCF varient dans une large gamme spatiale d'une dizaine de centimètres (Figure 28.c et CI=40). Ceci correspond à une situation où certaines bulles de cavitation sont parfois visibles sur l'interface eau-agar, à 40 mm de la sonde d'imagerie LA332 et sur le trajet du faisceau d'insonification ultrasonore, conduisant à la génération de multiples nuages de bulles de cavitation. Entre autres, des interférences destructives et constructives des ondes ultrasonores transmises par les sources de cavitation multiples ont été enregistrées par la sonde d'imagerie et augmentent donc directement les points mal focalisés correspondant à des faux positives sources de cavitation. Le fait qu'il ne soit remarqué qu'avec la sonde LA332 travaillant dans l'axe du faisceau thérapeutique et qu'avec la présence du gel d'agar confirme l'analyse sur l'interface eau-agar. De même, cette interface pourrait également refléter directement une partie de l'onde d'insonification ultrasonore incidente vers la sonde d'imagerie. Il convient donc de noter dans ce cas que PAM-PCF détecte un problème dans la position du nuage de bulles, qui devrait encore être largement localisé à la focale du transducteur thérapeutique. Fondamentalement, ces résultats et ces interprétations reconnaissent que cette intensité de cavitation CI = 40 dB doit être évitée pour limiter la création d'artefacts.

Expérience de cavitation non-régulée et régulée :

La prochaine expérience traite du comportement de l'activité de cavitation en terme de positions du FCP corrélées avec l'utilisation de deux stratégies de cavitation : non-régulée (boucle de régulation ouverte) et régulée (boucle de régulation fermée). Spécifiquement pour cette expérience, seule la sonde d'imagerie LA332 (plan de cavitation axiale) a été utilisée. Cependant, comme la cavitation est plus facile à amorcer avec un ratio de gaz dissous plus élevé, l'eau a été dégazée cette fois-ci à 7 mg d'O_2/L. Pour évaluer globalement une dispersion libre des positions du FCP et le comportement de la cavitation, aucun gel d'agar n'a été utilisé pour le confinement du nuage de bulles. Durant la stratégie de cavitation non-régulée, des valeurs de la puissance de cavitation très irrégulières sont attendues. C'est pourquoi, une opération de seuillage plus élaborée a été développée incluant quatre niveaux de seuillage correspondant à 4 couleurs assorties différentes:]-10;0] dB en noir,]-20;-10] dB en rouge,]-30;-20] dB en vert, et]-30;-40] dB en bleu. Les événements à faible ou sans cavitation sont comme précédemment *a priori* omis grâce à un seuillage de -40 dB. Durant la stratégie de cavitation régulée, le CI consigne est choisi puis l'algorithme de régulation de la cavitation temporelle définit en temps réel la tension d'amplitude $U(t)$ utilisée pour le transducteur thérapeutique. Le CI moyenné tout au long de l'insonification ultrasonore a été mesuré et il a toujours convergé vers la valeur consigne ($CI_{measured}$ = $CI_{desired}$). Dans le cas de la stratégie de cavitation non-régulée, une tension d'amplitude constante $U(t)$ est réglée manuellement et utilisé par le transducteur thérapeutique ensuite le CI moyenné tout au long de l'insonification ultrasonore est mesuré ($CI_{measured}$). Pour les deux expériences de cavitation régulée et non-régulée, les positions du FCP en 2D sont affichées sur la Figure 29.

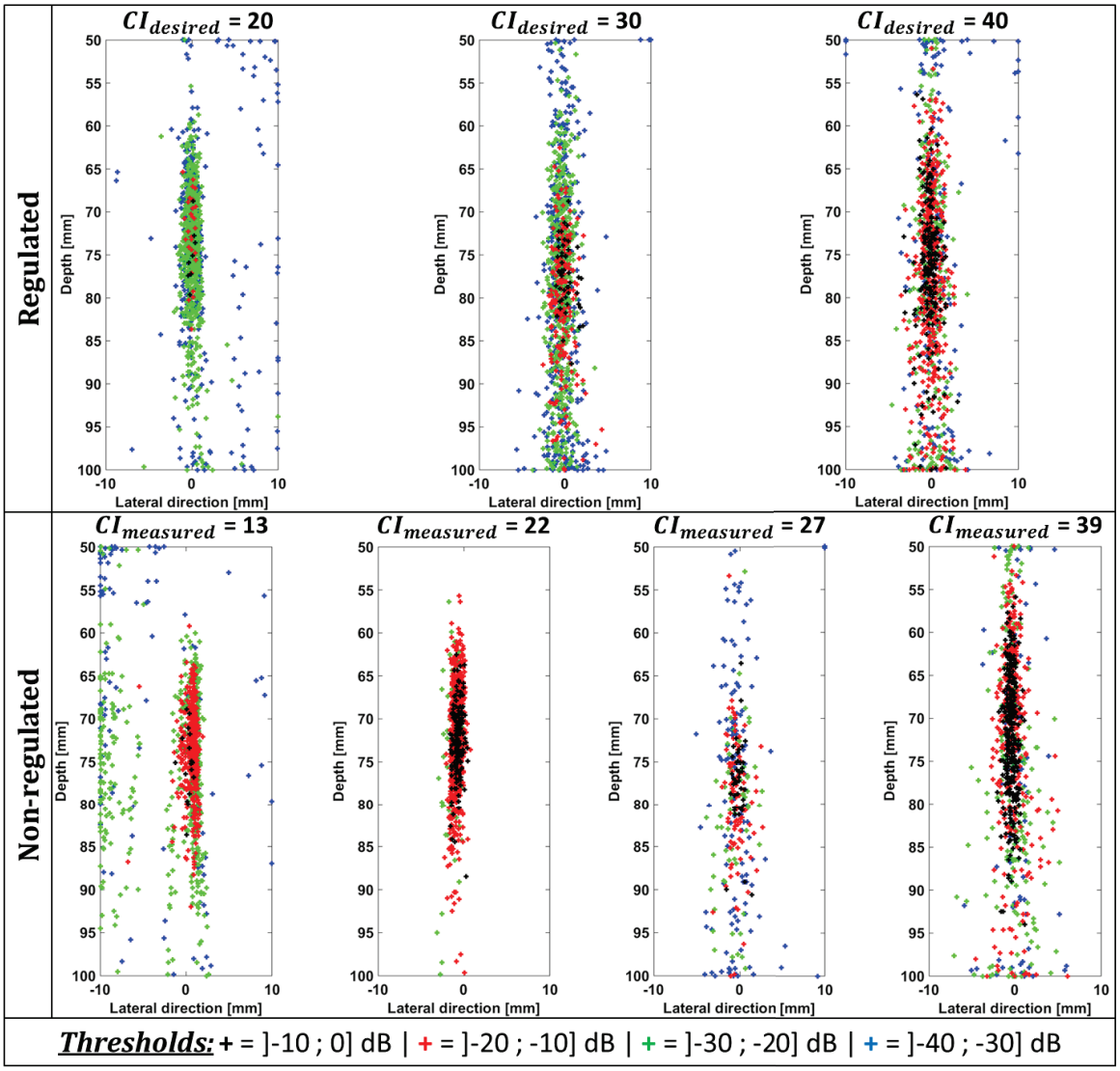

Figure 29 : Positions du FCP en 2D (en haut) pour la stratégie de cavitation régulée et (en bas) pour la stratégie de cavitation non-régulée. Quatre niveaux de seuillage de la puissance de cavitation ont été utilisés et représentés par quatre couleurs assorties.

Tout d'abord, pour tous les cas expérimentaux, la majorité des FCP à valeurs de puissance de cavitation les plus élevées (les points de couleur noire et rouge représentant un seuil de]-20; 0] dB) sont localisés au plus proche du foyer du transducteur thérapeutique. Par ailleurs, lorsque l'intensité de cavitation (CI) est augmentée, les FCP à valeurs de puissance de cavitation les plus élevées (point noir et point rouge) sont plus nombreux au foyer. Cependant, la dispersion globale des valeurs de puissance augmente avec un CI croissant. Cette dispersion est soulignée par l'augmentation de la diversité des couleurs dans la Figure 29. Cela induit que même si avec des CI croissant la puissance de cavitation augmente au foyer du transducteur thérapeutique, la puissance de cavitation globale est cependant étendu sur une plus grande zone autour du foyer. Par conséquent, un compromis doit être fait entre des puissances de cavitation élevées au foyer contre une faible dispersion de la puissance de cavitation globale. En plus, le désavantage principal du comportement de la cavitation avec la stratégie non-régulée est clairement remarqué dans le cas expérimental spécifique pour un $CI_{measured}$ = 27 dB, où un grand nombre d'événements à faible ou sans cavitation sont présent et de fait ont été omis lors de l'étape de seuillage.

Expérience avec plusieurs nuages de bulles de cavitation :

Jusqu'à présent, une seule source de cavitation correspondant à un seul nuage de bulles de cavitation était considérée. Cependant, pour des expériences plus réalistes avec des événements de cavitation hautement chaotique, des sources multiples différentes de bulles de cavitation doivent être étudiées pour évaluer la capacité de multi-localisation de sources de cavitation par la technique de formation de voies PAM-PCF. Par conséquent, un protocole plus complexe a été développé avec principalement l'intégration d'un deuxième générateur de cavitation ultrasonore indépendant.

Deux transducteurs thérapeutiques identiques à 1 MHz (IMASONIC SAS, Voray, France) focalisés à 8 cm ont été utilisés pour générer deux nuages de bulles de cavitation différents dans un gel d'agar. Comme un seul générateur de cavitation ultrasonore régulé est disponible, un générateur à double sortie (out_1 et out_2) est plutôt utilisé et couplé à deux amplificateurs de puissance différents liés à chaque sortie: Amp_1 (69 dB, GN 1000, PRANA, Malemort, France) et Amp_2 (66 dB, AMPAR 801, PRANA, Malemort, France). Par conséquent, pendant cette expérience, l'activité d'intensité de cavitation (CI) n'a pas été régulée et ainsi la reproductibilité de l'activité de cavitation n'a pas été prise en compte. Les deux sorties (out_1 et out_2) sont identiques et définis par un signal sinusoïdal à 1 MHz pulsé avec une répétition de pulse de 4 Hz et un rapport cyclique de 10% (similaire au signal de thérapie considéré dans les expériences précédentes). La sonde d'imagerie LA332, incorporée dans le transducteur thérapeutique, était exclusivement choisie. Le gel d'agar a été préparé avec le même protocole que précédemment. Cependant, comme cette fois, deux nuages de bulles distincts doivent être confinés, un moule plus grand (18 cm x 18 cm x 14 cm) a été utilisé. Le gel d'agar a été positionné à 35 mm de la sonde d'imagerie LA332. Les deux nuages de bulles ont été générés à 80 mm de chaque transducteur thérapeutique. Ainsi, le nuage de bulles (bc_1) généré par out_1 a été positionné à 80 mm de la sonde LA332 et centré selon à la direction d'imagerie latérale. Le nuage de bulles (bc_2) généré par out_2 a été positionné à 95 mm de la sonde LA332 et à 11,5 mm selon la direction d'imagerie latérale. La sonde LA332 image donc le plan (z, y) qui correspond au plan axial de cavitation du nuage de bulles (bc_1) et au plan frontal de cavitation du nuage de bulles (bc_2) comme indiqué sur la Figure 30.

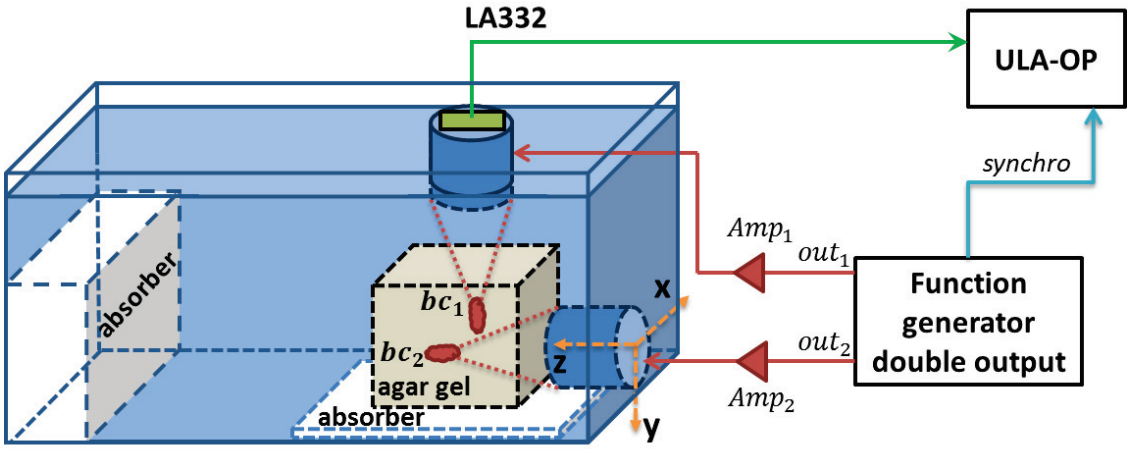

Figure 30 : Expérience de cavitation utilisant deux transducteurs thérapeutiques pour générer deux nuages de bulles différents et indépendants (bc_1 et bc_2). Le système d'imagerie avec la sonde (LA332) est synchronisé avec les deux impulsions d'insonification ultrasonore.

Les deux out_1 et out_2 ont été activés et un total de 616 acquisitions passives ont été enregistrées, représentant chacune 8 impulsions de 77 signaux RF. Deux tâches focales de cavitation différentes peuvent être observées cependant, la localisation du FCP ne les identifie pas tous les deux. Par conséquent, une méthode automatique de localisation multi-tâches focales de cavitation plus complexe a été développée. Cette méthode consiste en une segmentation par classe (labelling par composantes connectées) combinée à une opération de seuillage. Elle a été appliquée à l'ensemble des 616 cartographies de cavitation préalablement reconstruites, ensuite les positions du FCP en 2D ont été calculées. Les résultats sont présentés dans la Figure 31 avec différentes cartographies de cavitation reconstruites par PAM-PCF (Figure 31.(f-j)), les étapes de segmentation par classes correspondantes (Figure 31.(a-e)), la cartographie cumulée sur l'ensemble des 616 cartographies (Figure 31.k) ainsi que son étape de segmentation (Figure 31.l) et finalement les positions en 2D des FCP (Figure 31.m).

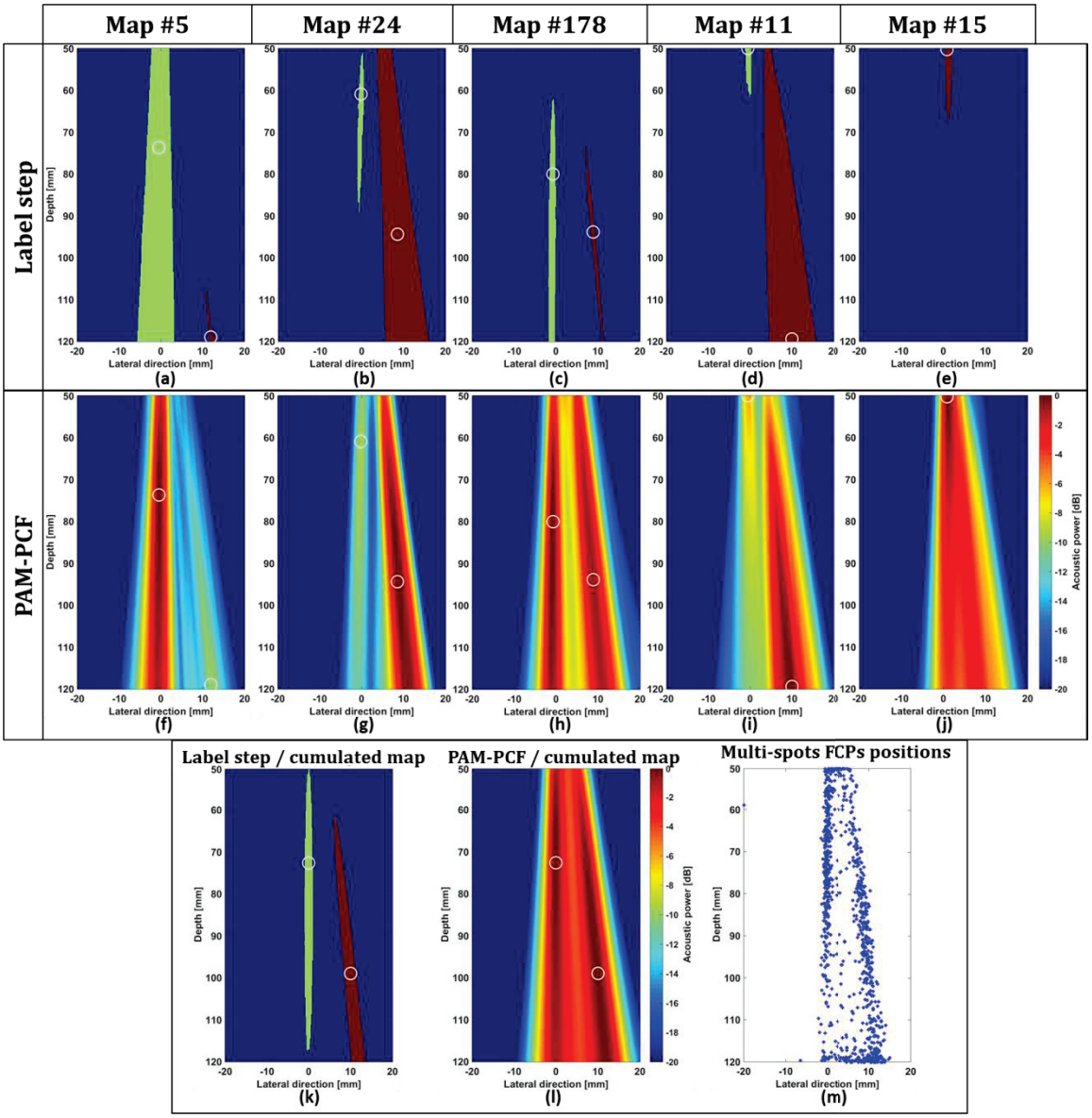

Figure 31 : Les deux out_1 et out_2 sont activés (les deux nuages de bulles bc_1 et bc_2 étaient générés). (a-e) L'étape de localisation multi-tâches focales avec l'application d'un seuillage puis de l'étape de segmentation par classe sur 5 cartographies de cavitation reconstruites préalablement par PAM-PCF. (f-j) Les 5 cartographies de cavitation correspondantes avec la localisation des FCP multipoints pour les deux spots de cavitation. Le cercle blanc correspond à

la position du FCP. (k) l'étape de localisation multi-tâches focales pour la cartographie cumulé et (l) la cartographie de cavitation multipoints. (m) Les positions globales des FCP en 2D, incluant toutes les tâches focales identifiées.

Les deux tâches focales de cavitation sont principalement observées pendant toute l'insonification ultrasonore, ce qui est confirmée par la cartographie cumulée (Figure 31.l). Cependant, les deux nuages de bulles de cavitation ne sont pas toujours générés simultanément à cause de l'insonification ultrasonore à stratégie de cavitation non-régulées et de l'absence d'une synchronisation parfaite entre les deux systèmes indépendants de génération de cavitation. Ceci est confirmé dans la Figure 31.(f, g) avec la présence d'un nuage de cavitation unique (bc_1 ou bc_2) alternativement dominant. La Figure 31.h. montre un exemple où les deux tâches de cavitation sont présentes et bien identifiées avec PAM-PCF. En plus, le même problème observé précédemment avec l'expérience dans le cas particulier avec une très forte intensité de cavitation (CI = 40 dB) est souligné dans la Figure 31.(i, j) où des interférences constructives et destructives des fronts d'ondes émis par différentes sources de cavitation sont pris en compte. Pour mieux comprendre ce cas et les problèmes d'interférence des émissions de bulles, une vérité terrain mieux contrôlée doit être développée.

Expérience in vivo :

Ayant l'opportunité d'effectuer des expériences *in vivo* de thrombolyse ultrasonore sur animal qui était disponible et programmé pour d'autres protocoles, l'utilisation de notre système d'imagerie passive incorporé dans un protocole *in vivo* a été réalisée. L'objectif principal de cette expérience *in vivo* était de tester la technique innovante de thrombolyse extracorporelle ultrasonore sur un modèle ovin afin de démontrer son efficacité en situation réelle. Spécifiquement pour cette expérience, une séquence d'acquisition d'images passives "trois décalages" a été développée. Elle consiste à utiliser indirectement la totalité de l'ouverture de la sonde d'imagerie LA332, qui contient au total 144 éléments, en effectuant trois décalages des positions des 64 éléments actifs choisis : à gauche (éléments #0 à #64), au centre (éléments #40 à #104), et à droite (éléments #80 à #144) respectivement représenté par un code couleur par le vert, le rouge, et le bleu sur la Figure 32.

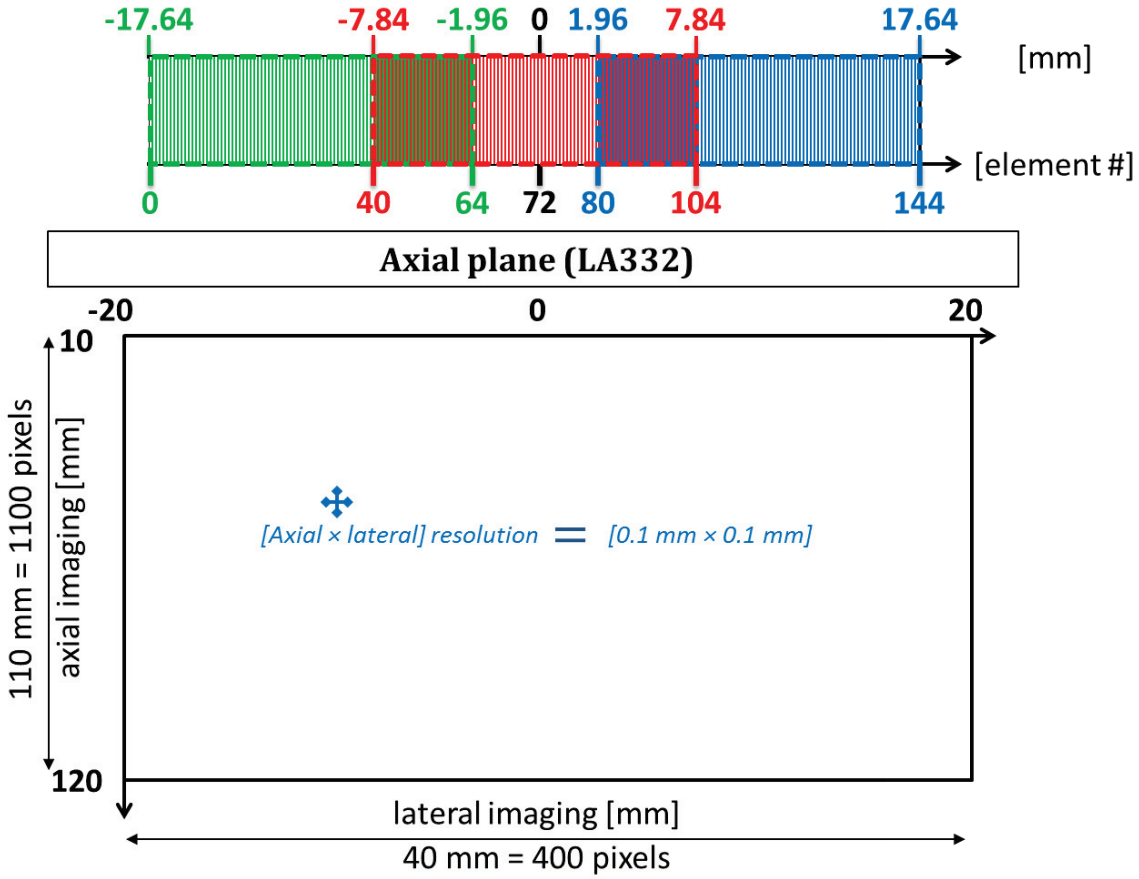

Figure 32 : En haut, illustration de la sonde d'imagerie LA332 avec les trois ouvertures actives correspondant à trois décalages différents: gauche (en vert), centrale (en rouge) et droite (en bleu). En bas, paramètres de reconstruction utilisés pour la reconstruction des cartographies PAM-PCF pour la sonde LA332 imageant le plan axial de cavitation (x, z).

Ainsi, 50 cartographies ont été reconstruites avec le PAM-PCF pour chacune des trois ouvertures actives et les positions en 2D du FCP ont été mesurées. En outre, un processus de triangulation a été réalisé en additionnant les 3 cartographies à différente ouverture active et en fournissant par conséquent une localisation focale plus précise. Les différents résultats sont représentés sur la Figure 33. Les cartographies de cavitation pour les trois ouvertures actives différentes sont affichées pour une seule acquisition parmi les 50 sur la Figure 33.(a-c) et la cartographie de cavitation de sommation des trois ouvertures est affiché sur la Figure 33.d. De plus, les positions FCP en 2D pour l'ensemble des 50 images reconstruites pour chaque ouverture active sont représentées sur la Figure 33. (e, f).

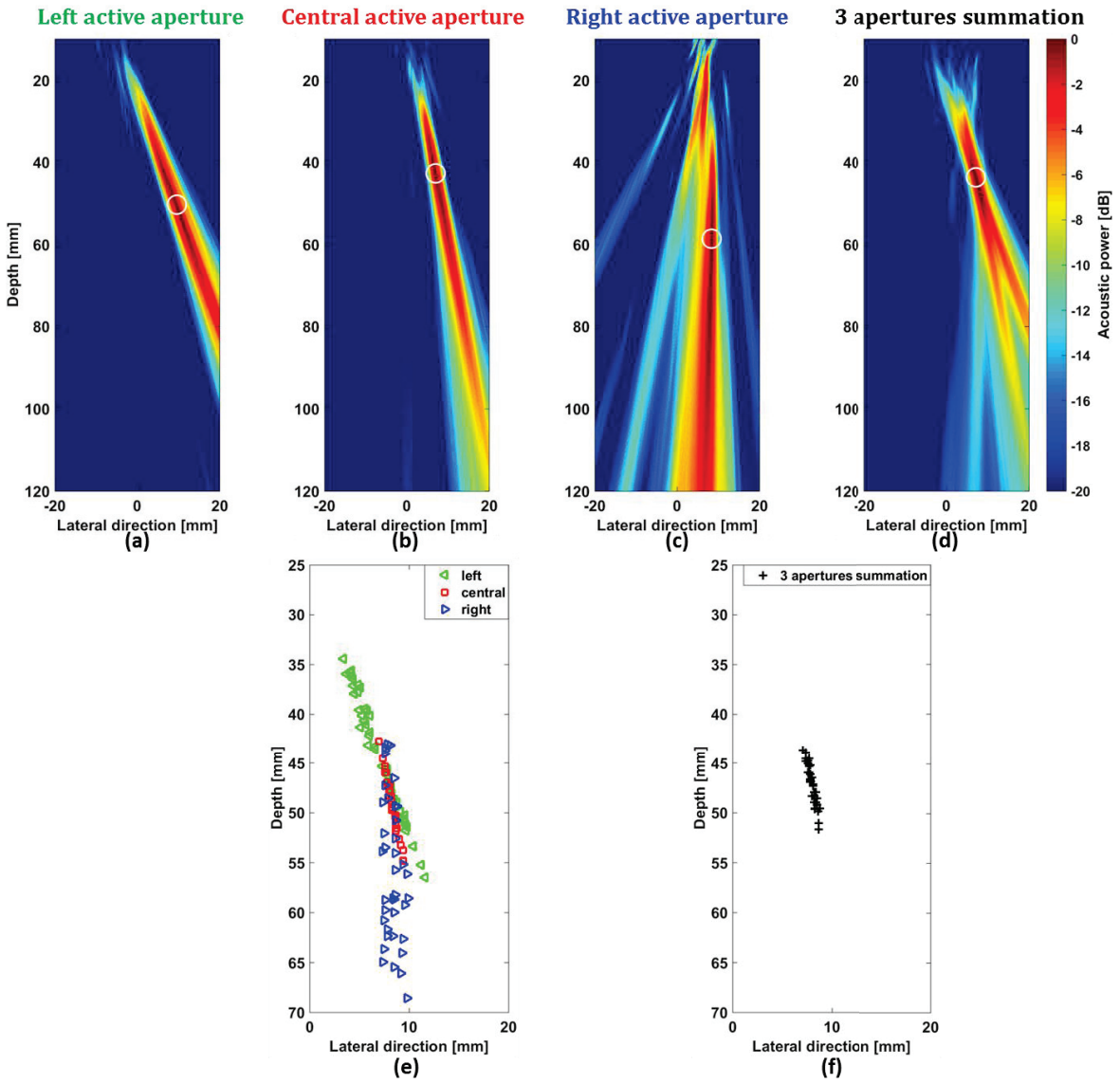

Figure 33 : Cartographies de cavitation reconstruites avec PAM-PCF pour une acquisition parmi 50 pour (a) l'ouverture active à gauche, (b) l'ouverture active centrale, (c) l'ouverture active à droite, et (d) la sommation des trois ouvertures. Le cercle blanc correspond à la localisation FCP. Pour l'ensemble des 50 images PAM-PCF reconstruites, le long de 25 ms d'insonification ultrasonore, les positions FCP en 2D pour (e) les trois ouvertures actives décalées, et (f) la sommation des trois ouvertures.

Les positions des foyers de thérapie (direction axiale, direction latérale) pour chaque décalage d'ouverture actif sont les suivantes : ouverture à gauche = (43.96 ± 6.29; 6.93 ± 2.3) mm, ouverture au centre = 48.74 ± 2.68, et ouverture à droite= (55 ± 7.11; 8.29 ± 0.76) mm. Aucun d'entre eux ne correspond à la position attendue du foyer de la thérapie théorique fixée à 80 mm, ce qui pourrait montrer qu'il pourrait y avoir un problème de focalisation lors de l'insonification ultrasonore thérapeutique. En effet, le foyer de thérapie théorique, ou le nuage de bulles théorique, généré à (80; 0) mm n'est en réalité pas atteint en raison des différents mécanismes de propagation des ultrasons provoqués par la variation de la valeur de la vitesse du son dans les différents milieux traversés: l'eau, le matériau du ballon, la peau, les tissus et le sang. Cette variation de la vitesse du son, cause d'abord une interpolation inexacte de la distance par rapport au temps de propagation des ondes ultrasonores utilisé dans la reconstruction d'images (entre autres pour le mode B active anatomique). Cela pourrait conduire à un mauvais ciblage du foyer de thérapie sur le thrombus.

Deuxièmement, les mécanismes de propagation ultrasonore de réfraction/réflexion pourraient se produire en raison de l'existence de l'interface eau-ballon-peau-tissu et du fait de l'existence d'un angle d'incidence non négligeable des ondes de thérapies focalisées sur l'interface.

Les résultats préliminaires *in vivo* ont principalement montré que plus d'étapes intermédiaires avant d'autres expériences *in vivo* doivent être envisagées pour un meilleur étalonnage du système de thérapie. De plus, dans le cadre d'une étude *in vivo*, la vérité terrain des positions du FCP n'est pas bien définie et, par conséquent, pour des interprétations et résultats plus robustes, la technique ultrasonore passive d'imagerie pourrait être combinée à une autre modalité d'imagerie. Cependant, les cartographies de cavitation PAM-PCF sont très cohérentes avec l'observation des expériences de thrombolyse *in vivo* et avec les mécanismes physiques de propagation ultrasonore de réfraction/réflexion attendus.

Pour conclure, la plupart des interprétations concernant les différents résultats du PAM-PCF sont cohérentes avec les mécanismes physiques connus de cavitation ultrasonore. Par conséquent, ces résultats soutiennent en partie la précision de la technique PAM-PCF et l'acceptent donc comme la technique d'imagerie passive de la cavitation référente pour le développement de notre dispositif de suivi en temps réel de la thrombolyse ultrasonore. C'est pourquoi, pour se rapprocher d'un dispositif complet de suivi en temps réel amélioré, l'étude et le développement de processus d'optimisation a été envisagé et réalisé. Par conséquent, une première étape du développement d'une technique d'imagerie en trois dimensions a été réalisée, ainsi que l'optimisation de l'utilisation des performances complètes de la sonde d'imagerie en considérant une largeur d'ouverture active et un nombre d'éléments actifs accrus (grâce à la nouvelle plateforme ULAOP-256). Une analyse préliminaire fréquentielle a été évaluée avec spécifiquement l'utilisation d'harmoniques et de fréquences plus élevés lors de la reconstruction des cartographies passives PAM-PCF. Ensuite, le développement de la visualisation PAM-PCF en temps réel est exploré avec des premiers résultats préliminaires ainsi qu'une mise en place d'un mode hybride combinant des images actives mode B et des cartographies passive de cavitation.

E. Conclusions et perspectives

Ce projet de thèse s'est focalisé sur le développement et l'intégration d'un système d'imagerie ultrasonore de suivi en temps réel au système préexistent thérapeutique, le générateur de cavitation ultrasonore régulé, conçu spécifiquement pour la thrombolyse par ultrasons.

Différentes configurations de synchronisation complexes ont été établies entre le signal d'insonification ultrasonore thérapeutique et les acquisitions passives. Lors de l'étude du système d'imagerie, la reconstruction des cartographies de cavitation réalisée avec différentes techniques ultrasonores passives a été évaluée et la méthode de cartographie acoustique passive pondérée par le facteur de cohérence de phase (PAM-PCF) a été validée dans un premier temps grâce à des simulations avec une source ponctuelle. De plus, les erreurs de mesure du point focale de cavitation (FCP) ont été considérées (direction axiale, direction latérale) et présentent des valeurs acceptables ainsi que des dispersions décentes (0.44 ± 0.28 mm; 0.09 ± 0.04 mm) pour les sources positionnées dans l'ouverture active de la sonde d'imagerie et à faible profondeur. Par la suite, des expériences de cavitation réelles ont été réalisées avec un protocole en cuve d'eau ainsi qu'avec divers paramètres de sonde d'imagerie, du milieu et de l'algorithme de calcul. Il inclut la génération d'un nuage de

bulles de cavitation unique ou bien la génération de nuages de bulles de cavitation multiples pour l'évaluation de la localisation multi-sources du PAM-PCF. De plus, un protocole de génération de cavitation non-régulée par rapport à une activité régulée a été développé pour évaluer la performance du système de régulation. Par ailleurs, une expérimentation animale *in vivo* utilisant un modèle ovin d'ischémie aiguë des membres a confirmé certains problèmes de focalisation physique ultrasonore déjà connus et liés aux mécanismes de propagation des ultrasons comme la réflexion et la réfraction aux interfaces. Cela pourrait causer une mauvaise focalisation du foyer thérapeutique et causer de graves dommages aux tissus environnants. Enfin, des optimisations préliminaires du système d'imagerie ultrasonore passive ont été proposées. L'implémentation 3D de l'imagerie passive a été effectuée et son importance et impact sur la localisation 3D de la tâche de cavitation a été soulignée. En plus de la prise en compte des sondes 2D, les sondes d'imagerie linéaire peuvent être *a priori* améliorées grâce à l'utilisation d'une plus grande largeur d'ouverture active de sonde influençant directement la résolution de la tâche focale de cavitation et l'efficacité de la localisation du FCP. Une analyse préliminaire fréquentielle de la signature du signal de cavitation a été étudiée en tenant compte des harmoniques et de l'imagerie haute fréquence. Il présente pour les cartographies de cavitation harmonique haute fréquence des résolutions de tâches de cavitation améliorées. En outre, un mode hybride combinant à la fois des images actives anatomiques et des cartographies de cavitation passive a été développé et doit encore être évalué dans des expériences de cavitation réelles. Enfin, une implémentation en temps réel de la technique passive PAM préliminaire a été réalisée avec la nouvelle plateforme ULA-OP 256 pour permettre la visualisation en temps réel des cartographies de cavitation.

Les principales perspectives de ce projet consisteraient à poursuivre le développement du système de suivi avec une technique d'imagerie ultrasonores 3D hybride en temps réel complète. Néanmoins, des travaux supplémentaires doivent aussi être effectués, par exemple en développant des protocoles plus précis pour la mesure de la vérité terrain des positions des sources de cavitation. En effet, grâce aux optimisations discutées précédemment, la résolution de la tâche de cavitation est nettement améliorée. Cependant pour une étude plus poussée et complète, il doit être simultanément comparé à la résolution référente réelle de la vérité terrain. Par conséquent, cet aspect de vérité terrain pour les images de cavitation passives doit être précisément défini. De ce fait, de meilleurs protocoles pour la caractérisation des valeurs de vérité terrain doivent être développés dont certains ont déjà été considérés dans le domaine de recherche comme l'utilisation des ondes stationnaires pour piéger et contrôler le mouvement des bulles de cavitation [127], ou l'utilisation de « nanocups » pour piéger et stabiliser le gaz dissous [128]. De plus, la mise en œuvre d'une caméra rapide à haute fréquence d'images synchronisée avec les acquisitions passives ULAOP serait très utile pour suivre de façon optique et précise les positions en vérité terrain du nuage de bulles.

De plus, un outil de simulation amélioré prenant en compte des mécanismes et des interactions de bulles de cavitation plus complexes et plus réalistes est nécessaire, en utilisant par exemple l'équation simplifiée de Rayleigh-Plesset régissant la dynamique des bulles soumise à un champ de pression. Sinon, dans un premier temps, un outil de simulation moins évolué pourrait être développé avec l'utilisation d'un signal RF de cavitation de référence, enregistré préalablement par un hydrophone lors d'un simple cas d'expérience en cuve d'eau de cavitation, qui est ensuite déphasé temporellement pour chaque éléments actifs de la sonde d'imagerie considérée et finalement utilisé pour la création de l'ensemble des données brutes complètes simulées. De plus, l'expérience sur fil a

été très utile dans ce travail pour évaluer la précision de la technique d'imagerie passive. Son protocole pourrait être mis à jour en ajoutant plusieurs fils excités à des moments différents par des transducteurs différents et donc permettrait l'étude de la précision de la localisation multi-sources des techniques d'imagerie passive. Par ailleurs, un protocole alternatif simplifié pourrait être envisagé en utilisant un seul fil décalé dans de nombreuses positions et en additionnant ensuite les signaux RF bruts enregistrés, pour générer un ensemble de données pseudo-multi-sources.

En outre, pour l'étude de performance d'imagerie passive, la technique PAM-PCF devrait être soigneusement comparée avec d'autres optimisations PAM (comme PAM-SCF, PAM-RCB, PAM-SCF-RCB [127]) et d'autres techniques passives de reconstruction de cartographies de cavitation comme l'approche angulaire spectrale (« angular spectrum approach » [136]). De plus, la réponse impulsionnelle de la sonde d'imagerie doit être prise en compte et l'analyse fréquentielle doit être évaluée avec des processus de filtrage plus évolués ou avec l'utilisation d'autres méthodes de formation de voies passives adaptées au domaine fréquentiel. De plus, grâce à des travaux parallèles sur la régulation distincte et spécifique de l'activité de cavitation inertielle ou non-inertielle, le générateur de cavitation ultrasonore régulé pourrait séparer les deux mécanismes de cavitation pendant la thérapie et isoler ainsi les dommages mécaniques des dommages thermiques causés par les bulles de cavitation.

Des études originales et innovantes sont envisagées pour la thérapie par ultrasons et beaucoup d'efforts sont mis en œuvre pour développer une technique thérapeutique ultrasonore sûre et précise en se concentrant sur le système de suivi spatiale permettant pendant la thérapie de générer le nuage de bulles de cavitation exactement sur le thrombus. C'est pourquoi, de nombreux axes de recherche restent à être explorer et de nombreux problèmes restent à être résolus avant de pouvoir tester cliniquement ce dispositif de thrombolyse ultrasonore extracorporelle.

REFERENCES

[1] G. D. Boon, “An Overview of Hemostasis,” *Toxicol. Pathol.*, vol. 21, no. 2, pp. 170–179, Mar. 1993.

[2] A. J. Gale, “Current Understanding of Hemostasis,” *Toxicol. Pathol.*, vol. 39, no. 1, pp. 273–280, 2011.

[3] J. M. Byers, “Rudolf Virchow--father of cellular pathology,” *Am. J. Clin. Pathol.*, vol. 92, no. 4 Suppl 1, pp. S2-8, Oct. 1989.

[4] D. R. Kumar, E. Hanlin, I. Glurich, J. J. Mazza, and S. H. Yale, “Virchow’s Contribution to the Understanding of Thrombosis and Cellular Biology,” *Clin. Med. Res.*, vol. 8, no. 3–4, pp. 168–172, Dec. 2010.

[5] G. J. Merli, “Pathophysiology of venous thrombosis, thrombophilia, and the diagnosis of deep vein thrombosis-pulmonary embolism in the elderly,” *Clin. Geriatr. Med.*, vol. 22, no. 1, pp. 75–92, viii–ix, Feb. 2006.

[6] C. W. Peterson, “Venous Thrombosis: An Overview,” *Pharmacother. J. Hum. Pharmacol. Drug Ther.*, vol. 6, no. 4P2, p. 12S–17S, Jul. 1986.

[7] D. Gailani and T. Renné, “Intrinsic Pathway of Coagulation and Arterial Thrombosis,” *Arterioscler. Thromb. Vasc. Biol.*, vol. 27, no. 12, pp. 2507–2513, Dec. 2007.

[8] J. E. Dalen, C. I. Haffajee, J. S. Alpert, J. P. I. Howe, I. S. Ockene, and J. A. Paraskos, “Pulmonary Embolism, Pulmonary Hemorrhage and Pulmonary Infarction,” 13-Jan-2010. .

[9] G. W. Reed, J. E. Rossi, and C. P. Cannon, “Acute myocardial infarction,” *The Lancet*, vol. 389, no. 10065, pp. 197–210, Jan. 2017.

[10] M. E. Raichle, “The pathophysiology of brain ischemia,” *Ann. Neurol.*, vol. 13, no. 1, pp. 2–10, Jan. 1983.

[11] T. G. Walker, “Acute Limb Ischemia,” *Tech. Vasc. Interv. Radiol.*, vol. 12, no. 2, pp. 117–129, Jun. 2009.

[12] P. B. Østergaard, B. Nilsson, D. Bergqvist, U. Hedner, and P. C. Pedersen, “The effect of low molecular weight heparin on experimental thrombosis and haemostasis - the influence of production method,” *Thromb. Res.*, vol. 45, no. 6, pp. 739–749, Mar. 1987.

[13] R. D. Lopes *et al.*, *Stroke Prevention in Atrial Fibrillation*. Rockville (MD): Agency for Healthcare Research and Quality (US), 2013.

[14] K. Werdan, R. Braun-Dullaeus, and P. Presek, “Anticoagulation in Atrial Fibrillation: NOAC’s the Word,” *Dtsch. Ärztebl. Int.*, vol. 110, no. 31–32, pp. 523–524, Aug. 2013.

[15] N. B. Norgard, J. J. Dinicolantonio, T. J. Topping, and B. Wee, “Novel anticoagulants in atrial fibrillation stroke prevention,” *Ther. Adv. Chronic Dis.*, vol. 3, no. 3, pp. 123–136, May 2012.

[16] D. Collen and H. R. Lijnen, “Thrombolytic agents,” *Thromb. Haemost.*, vol. 93, no. 4, pp. 627–630, Apr. 2005.

[17] The GUSTO Investigators, “An International Randomized Trial Comparing Four Thrombolytic Strategies for Acute Myocardial Infarction,” *N. Engl. J. Med.*, vol. 329, no. 10, pp. 673–682, Sep. 1993.

[18] S. Vedantham, G. Piazza, A. K. Sista, and N. A. Goldenberg, “Guidance for the use of thrombolytic therapy for the treatment of venous thromboembolism,” *J. Thromb. Thrombolysis*, vol. 41, pp. 68–80, 2016.

[19] I. K. Jang *et al.*, “Differential sensitivity of erythrocyte-rich and platelet-rich arterial thrombi to lysis with recombinant tissue-type plasminogen activator. A possible explanation for resistance to coronary thrombolysis,” *Circulation*, vol. 79, no. 4, pp. 920–928, Apr. 1989.

[20] V. J. Marder, “The Use of Thrombolytic Agents: Choice of Patient, Drug Administration, Laboratory Monitoring,” *Ann. Intern. Med.*, vol. 90, no. 5, p. 802, May 1979.

[21] National Institute of Neurological Disorders and Stroke rt-PA Stroke Study Group, “Tissue plasminogen activator for acute ischemic stroke,” *N. Engl. J. Med.*, vol. 333, no. 24, pp. 1581–1587, 14 1995.

[22] S. Schulman, R. J. Beyth, C. Kearon, M. N. Levine, and American College of Chest Physicians, “Hemorrhagic complications of anticoagulant and thrombolytic treatment: American College of Chest Physicians Evidence-Based Clinical Practice Guidelines (8th Edition),” *Chest*, vol. 133, no. 6 Suppl, p. 257S–298S, Jun. 2008.

[23] K. Peter Rentrop, M. Cohen, H. Blanke, and R. A. Phillips, “Changes in collateral channel filling immediately after controlled coronary artery occlusion by an angioplasty balloon in human subjects,” *J. Am. Coll. Cardiol.*, vol. 5, no. 3, pp. 587–592, Mar. 1985.

[24] P. W. Serruys *et al.*, “A comparison of balloon-expandable-stent implantation with balloon angioplasty in patients with coronary artery disease. Benestent Study Group,” *N. Engl. J. Med.*, vol. 331, no. 8, pp. 489–495, Aug. 1994.

[25] F. Ikeno, M. Buchbinder, and A. C. Yeung, “Novel stent and delivery systems for the treatment of bifurcation lesions: porcine coronary artery model,” *Cardiovasc. Revascularization Med. Mol. Interv.*, vol. 8, no. 1, pp. 38–42, Mar. 2007.

[26] B. Hiebl, E. Nennig, S. Schiestel, A. Kovacs, F. Jung, and H. Fischer, “Biocompatibility of a novel zinc stent with a closed-cell-design,” *Clin. Hemorheol. Microcirc.*, vol. 61, no. 2, pp. 205–211, 2015.

[27] R. B. Rutherford, “Clinical staging of acute limb ischemia as the basis for choice of revascularization method: when and how to intervene,” *Semin. Vasc. Surg.*, vol. 22, no. 1, pp. 5–9, Mar. 2009.

[28] M. J. A. Sharafuddin and M. E. Hicks, “Current Status of Percutaneous Mechanical Thrombectomy. Part II. Devices and Mechanisms of Action,” *J. Vasc. Interv. Radiol.*, vol. 9, no. 1, pp. 15–31, Jan. 1998.

[29] S. Goldman *et al.*, “Improvement in early saphenous vein graft patency after coronary artery bypass surgery with antiplatelet therapy: results of a Veterans Administration Cooperative Study,” *Circulation*, vol. 77, no. 6, pp. 1324–1332, Jun. 1988.

[30] S. Sarkar, H. J. Salacinski, G. Hamilton, and A. M. Seifalian, “The Mechanical Properties of Infrainguinal Vascular Bypass Grafts: Their Role in Influencing Patency,” *Eur. J. Vasc. Endovasc. Surg.*, vol. 31, no. 6, pp. 627–636, Jun. 2006.

[31] S. Sarkar, T. Schmitz-Rixen, G. Hamilton, and A. M. Seifalian, “Achieving the ideal properties for vascular bypass grafts using a tissue engineered approach: a review,” *Med. Biol. Eng. Comput.*, vol. 45, no. 4, pp. 327–336, Apr. 2007.

[32] S. M. Seedial *et al.*, “Local drug delivery to prevent restenosis,” *J. Vasc. Surg.*, vol. 57, no. 5, pp. 1403–1414, May 2013.

[33] “Quarkology - 82A Wave Model.” [Online]. Available: http://www.quarkology.com/11-physics/82-world-communicates/82A-wave-model.html. [Accessed: 27-Jun-2017].

[34] F. Varray, “Simulation in nonlinear ultrasound : application to nonlinear parameter imaging in echo mode configuration,” phdthesis, Université Claude Bernard - Lyon I, 2011.

[35] J. G. Lynn, R. L. Zwemer, A. J. Chick, and A. E. Miller, “A new method for the generation and use of focused ultrasound in experimental biology,” *J. Gen. Physiol.*, vol. 26, no. 2, pp. 179–193, Nov. 1942.

[36] W. J. Fry, “Ultrasound in Neurology,” *J. Acoust. Soc. Am.*, vol. 27, no. 5, pp. 998–998, Sep. 1955.

[37] S. Westermark, H. Wiksell, H. Elmqvist, K. Hultenby, and H. Berglund, “Effect of externally applied focused acoustic energy on clot disruption in vitro,” *Clin. Sci.*, vol. 97, no. 1, pp. 67–71, Jul. 1999.

[38] R. H. Liu, J. Yang, M. Z. Pindera, M. Athavale, and P. Grodzinski, “Bubble-induced acoustic micromixing,” *Lab. Chip*, vol. 2, no. 3, pp. 151–157, 2002.

[39] A. Ooi, P. Tho, and R. Manasseh, “Cavitation microstreaming patterns in single and multiple bubble systems,” *J. Acoust. Soc. Am.*, vol. 122, no. 5, pp. 3051–3051, Nov. 2007.

[40] J. Collis *et al.*, "Cavitation microstreaming and stress fields created by microbubbles," *Ultrasonics*, vol. 50, no. 2, pp. 273–279, Feb. 2010.
[41] O. A. Sapozhnikov, A. D. Maxwell, B. MacConaghy, and M. R. Bailey, "A mechanistic analysis of stone fracture in lithotripsy," *J. Acoust. Soc. Am.*, vol. 121, no. 2, pp. 1190–1202, Jan. 2007.
[42] P. Riesz, D. Berdahl, and C. L. Christman, "Free radical generation by ultrasound in aqueous and nonaqueous solutions.," *Environ. Health Perspect.*, vol. 64, pp. 233–252, Dec. 1985.
[43] K. S. Suslick, "The Chemical Effects of Ultrasound," *Sci. Am.*, pp. 80–86, Feb. 1989.
[44] V. S. Moholkar and A. B. Pandit, "Bubble behavior in hydrodynamic cavitation: Effect of turbulence," *AIChE J.*, vol. 43, no. 6, pp. 1641–1648, Jun. 1997.
[45] D. Hsieh and M. S. Plesset, "Theory of Rectified Diffusion of Mass into Gas Bubbles," *J. Acoust. Soc. Am.*, vol. 33, no. 2, pp. 206–215, Feb. 1961.
[46] S. F. Jones, G. M. Evans, and K. P. Galvin, "Bubble nucleation from gas cavities — a review," *Adv. Colloid Interface Sci.*, vol. 80, no. 1, pp. 27–50, Feb. 1999.
[47] M S Plesset and and A. Prosperetti, "Bubble Dynamics and Cavitation," *Annu. Rev. Fluid Mech.*, vol. 9, no. 1, pp. 145–185, 1977.
[48] T. G. Leighton, *The Acoustic Bubble*. Academic Press, 1997.
[49] A. Prosperetti, L. A. Crum, and K. W. Commander, "Nonlinear bubble dynamics," *J. Acoust. Soc. Am.*, vol. 83, no. 2, pp. 502–514, Feb. 1988.
[50] A. Eller and H. G. Flynn, "Generation of Subharmonics of Order One-Half by Bubbles in a Sound Field," *J. Acoust. Soc. Am.*, vol. 46, no. 3B, pp. 722–727, Sep. 1969.
[51] J. B. Keller and M. Miksis, "Bubble oscillations of large amplitude," *J. Acoust. Soc. Am.*, vol. 68, no. 2, pp. 628–633, Aug. 1980.
[52] L. A. Crum, "Surface oscillations and jet development in pulsating bubbles," *J. Phys. Colloq.*, vol. 40, no. C8, pp. C8-285-C8-288, Nov. 1979.
[53] W. Kreider, L. A. Crum, M. R. Bailey, and O. A. Sapozhnikov, "Observations of the collapses and rebounds of millimeter-sized lithotripsy bubbles," *J. Acoust. Soc. Am.*, vol. 130, no. 5, pp. 3531–3540, Nov. 2011.
[54] M. S. Longuet-Higgins, "Bubble noise spectra," *J. Acoust. Soc. Am.*, vol. 87, no. 2, pp. 652–661, Feb. 1990.
[55] J. Frohly, S. Labouret, C. Bruneel, I. Looten-Baquet, and R. Torguet, "Ultrasonic cavitation monitoring by acoustic noise power measurement," *J. Acoust. Soc. Am.*, vol. 108, no. 5, pp. 2012–2020, Nov. 2000.
[56] T. G. Leighton, "Bubble population phenomena in acoustic cavitation," *Ultrason. Sonochem.*, vol. 2, no. 2, pp. S123–S136, Jan. 1995.
[57] D. Miller, N. Smith, M. Bailey, G. Czarnota, K. Hynynen, and I. Makin, "Overview of Therapeutic Ultrasound Applications and Safety Considerations," *J. Ultrasound Med. Off. J. Am. Inst. Ultrasound Med.*, vol. 31, no. 4, pp. 623–634, Apr. 2012.
[58] V. J. Robertson and K. G. Baker, "A review of therapeutic ultrasound: effectiveness studies," *Phys. Ther.*, vol. 81, no. 7, pp. 1339–1350, Jul. 2001.
[59] S. Maluta *et al.*, "Regional hyperthermia added to intensified preoperative chemo-radiation in locally advanced adenocarcinoma of middle and lower rectum," *Int. J. Hyperthermia*, vol. 26, no. 2, pp. 108–117, Jan. 2010.
[60] C. C. Coussios, C. H. Farny, G. T. Haar, and R. A. Roy, "Role of acoustic cavitation in the delivery and monitoring of cancer treatment by high-intensity focused ultrasound (HIFU)," *Int. J. Hyperth. Off. J. Eur. Soc. Hyperthermic Oncol. North Am. Hyperth. Group*, vol. 23, no. 2, pp. 105–120, Mar. 2007.
[61] C. R. Hill and G. R. ter Haar, "High intensity focused ultrasound—potential for cancer treatment," *Br. J. Radiol.*, vol. 68, no. 816, pp. 1296–1303, Dec. 1995.
[62] L. Mearini and M. Porena, "Transrectal high-intensity focused ultrasound for the treatment of prostate cancer: Past, present, and future," *Indian J. Urol. IJU J. Urol. Soc. India*, vol. 26, no. 1, pp. 4–11, 2010.

[63] L. Poissonnier *et al.*, “Control of Prostate Cancer by Transrectal HIFU in 227 Patients,” *Eur. Urol.*, vol. 51, no. 2, pp. 381–387, Feb. 2007.

[64] K. Fischer, N. J. McDannold, C. M. Tempany, F. A. Jolesz, and F. M. Fennessy, “Potential of minimally invasive procedures in the treatment of uterine fibroids: a focus on magnetic resonance-guided focused ultrasound therapy,” *Int. J. Womens Health*, vol. 7, pp. 901–912, Nov. 2015.

[65] J.-F. Aubry *et al.*, “The road to clinical use of high-intensity focused ultrasound for liver cancer: technical and clinical consensus,” *J. Ther. Ultrasound*, vol. 1, p. 13, 2013.

[66] J. E. Lingeman, J. A. McAteer, E. Gnessin, and A. P. Evan, “Shock wave lithotripsy: advances in technology and technique,” *Nat. Rev. Urol.*, vol. 6, no. 12, pp. 660–670, Dec. 2009.

[67] H.-D. Liang, J. Tang, and M. Halliwell, “Sonoporation, drug delivery, and gene therapy,” *Proc. Inst. Mech. Eng. [H]*, vol. 224, no. 2, pp. 343–361, Feb. 2010.

[68] Z. Fan, R. E. Kumon, and C. X. Deng, “Mechanisms of microbubble-facilitated sonoporation for drug and gene delivery,” *Ther. Deliv.*, vol. 5, no. 4, pp. 467–486, Apr. 2014.

[69] W. G. Pitt, G. A. Husseini, and B. J. Staples, “Ultrasonic Drug Delivery – A General Review,” *Expert Opin. Drug Deliv.*, vol. 1, no. 1, pp. 37–56, Nov. 2004.

[70] J. M. Tsutsui, F. Xie, and R. T. Porter, “The use of microbubbles to target drug delivery,” *Cardiovasc. Ultrasound*, vol. 2, p. 23, Nov. 2004.

[71] J. T. Sutton, K. J. Haworth, G. Pyne-Geithman, and C. K. Holland, “Ultrasound-mediated drug delivery for cardiovascular disease,” *Expert Opin. Drug Deliv.*, vol. 10, no. 5, pp. 573–592, May 2013.

[72] E. Unger, T. Porter, J. Lindner, and P. Grayburn, “Cardiovascular drug delivery with ultrasound and microbubbles,” *Adv. Drug Deliv. Rev.*, vol. 72, pp. 110–126, Jun. 2014.

[73] Z. Xu *et al.*, “Controlled ultrasound tissue erosion,” *IEEE Trans. Ultrason. Ferroelectr. Freq. Control*, vol. 51, no. 6, pp. 726–736, Jun. 2004.

[74] W. W. Roberts, “Focused ultrasound ablation of renal and prostate cancer: Current technology and future directions,” *Urol. Oncol. Semin. Orig. Investig.*, vol. 23, no. 5, pp. 367–371, Sep. 2005.

[75] G. E. Owens *et al.*, “Therapeutic ultrasound to noninvasively create intracardiac communications in an intact animal model,” *Catheter. Cardiovasc. Interv.*, vol. 77, no. 4, pp. 580–588, Mar. 2011.

[76] X. Zhang, G. E. Owens, H. S. Gurm, Y. Ding, C. A. Cain, and Z. Xu, “Noninvasive thrombolysis using histotripsy beyond the intrinsic threshold (microtripsy),” *IEEE Trans. Ultrason. Ferroelectr. Freq. Control*, vol. 62, no. 7, pp. 1342–1355, Jul. 2015.

[77] G. Trübestein, C. Engel, F. Etzel, A. Sobbe, H. Cremer, and U. Stumpff, “Thrombolysis by Ultrasound,” *Clin. Sci.*, vol. 51, no. s3, p. 697s–698s, Jan. 1976.

[78] W. Steffen *et al.*, “High intensity, low frequency catheter-delivered ultrasound dissolution of occlusive coronary artery thrombi: An in vitro and in vivo study,” *J. Am. Coll. Cardiol.*, vol. 24, no. 6, pp. 1571–1579, Nov. 1994.

[79] S. Atar, H. Luo, T. Nagai, and R. J. Siegel, “Ultrasonic thrombolysis: catheter-delivered and transcutaneous applications,” *Eur. J. Ultrasound*, vol. 9, no. 1, pp. 39–54, Mar. 1999.

[80] S. Kaul, “Sonothrombolysis: a universally applicable and better way to treat acute myocardial infarction and stroke? Who is going to fund the research?,” *Circulation*, vol. 119, no. 10, pp. 1358–1360, Mar. 2009.

[81] A. Amaral-Silva, S. Piñeiro, and C. A. Molina, “Sonothrombolysis for the treatment of acute stroke: current concepts and future directions,” *Expert Rev. Neurother.*, vol. 11, no. 2, pp. 265–273, Feb. 2011.

[82] Y.-H. Chuang, P.-W. Cheng, and P.-C. Li, “Combining radiation force with cavitation for enhanced sonothrombolysis,” *IEEE Trans. Ultrason. Ferroelectr. Freq. Control*, vol. 60, no. 1, p. , Jan. 2013.

[83] R. D. Shlansky-Goldberg, D. B. Cines, and C. M. Sehgal, “Catheter-delivered Ultrasound Potentiates in Vitro Thrombolysis,” *J. Vasc. Interv. Radiol.*, vol. 7, no. 3, pp. 313–320, May 1996.

[84] R. J. Siegel *et al.*, “Noninvasive Transcutaneous Low Frequency Ultrasound Enhances Thrombolysis in Peripheral and Coronary Arteries,” *Echocardiography*, vol. 18, no. 3, pp. 247–257, Apr. 2001.

[85] T. R. Porter, R. F. LeVeen, R. Fox, A. Kricsfeld, and F. Xie, “Thrombolytic enhancement with perfluorocarbon-exposed sonicated dextrose albumin microbubbles,” *Am. Heart J.*, vol. 132, no. 5, pp. 964–968, Nov. 1996.

[86] Y. Birnbaum *et al.*, “Noninvasive In Vivo Clot Dissolution Without a Thrombolytic Drug,” *Circulation*, vol. 97, no. 2, pp. 130–134, Jan. 1998.

[87] U. Rosenschein *et al.*, “Shock-wave thrombus ablation, a new method for noninvasive mechanical thrombolysis,” *Am. J. Cardiol.*, vol. 70, no. 15, pp. 1358–1361, Nov. 1992.

[88] U. Rosenschein, V. Furman, E. Kerner, I. Fabian, J. Bernheim, and Y. Eshel, “Ultrasound Imaging–Guided Noninvasive Ultrasound Thrombolysis,” *Circulation*, vol. 102, no. 2, pp. 238–245, Jul. 2000.

[89] A. D. Maxwell, C. A. Cain, A. P. Duryea, L. Yuan, H. S. Gurm, and Z. Xu, “Noninvasive thrombolysis using pulsed ultrasound cavitation therapy - histotripsy,” *Ultrasound Med. Biol.*, vol. 35, no. 12, pp. 1982–1994, Dec. 2009.

[90] A. D. Maxwell, G. Owens, H. S. Gurm, K. Ives, D. D. Myers, and Z. Xu, “Noninvasive Treatment of Deep Venous Thrombosis Using Pulsed Ultrasound Cavitation Therapy (Histotripsy) in a Porcine Model,” *J. Vasc. Interv. Radiol.*, vol. 22, no. 3, pp. 369–377, Mar. 2011.

[91] C. Wright, K. Hynynen, and D. Goertz, “In Vitro and In Vivo High Intensity Focused Ultrasound Thrombolysis,” *Invest. Radiol.*, vol. 47, no. 4, pp. 217–225, Apr. 2012.

[92] K.-W. Lin *et al.*, “Histotripsy beyond the intrinsic cavitation threshold using very short ultrasound pulses: microtripsy,” *IEEE Trans. Ultrason. Ferroelectr. Freq. Control*, vol. 61, no. 2, pp. 251–265, Feb. 2014.

[93] I. Saletes *et al.*, “In Vitro Demonstration of Focused Ultrasound Thrombolysis Using Bifrequency Excitation,” *BioMed Res. Int.*, vol. 2014, p. e518787, Aug. 2014.

[94] A. Sabraoui, C. Inserra, B. Gilles, J.-C. Béra, and J.-L. Mestas, “Feedback loop process to control acoustic cavitation,” *Ultrason. Sonochem.*, vol. 18, no. 2, pp. 589–594, Mar. 2011.

[95] C. Desjouy, A. Poizat, B. Gilles, C. Inserra, and J.-C. Bera, “Control of inertial acoustic cavitation in pulsed sonication using a real-time feedback loop system,” *J. Acoust. Soc. Am.*, vol. 134, no. 2, pp. 1640–1646, Aug. 2013.

[96] A. Poizat, C. Desjouy, C. Inserra, B. Gilles, and J. C. Bera, “Regulation of cavitation activity in pulsed sonication with a real-time feedback loop system,” presented at the Acoustics, New Delhi, 2013.

[97] A. Poizat, “Contrôle temporel de la cavitation ultrasonore : application à la thrombolyse ultrasonore extracorporelle,” phdthesis, Université de Lyon, 2016.

[98] K. R. Gorny, N. J. Hangiandreou, G. K. Hesley, B. S. Gostout, K. P. McGee, and J. P. Felmlee, “MR guided focused ultrasound: technical acceptance measures for a clinical system,” *Phys. Med. Biol.*, vol. 51, no. 12, pp. 3155–3173, Jun. 2006.

[99] B. D. de Senneville, C. Mougenot, B. Quesson, I. Dragonu, N. Grenier, and C. T. W. Moonen, “MR thermometry for monitoring tumor ablation,” *Eur. Radiol.*, vol. 17, no. 9, pp. 2401–2410, Sep. 2007.

[100] S. Vaezy *et al.*, “Real-time visualization of high-intensity focused ultrasound treatment using ultrasound imaging,” *Ultrasound Med. Biol.*, vol. 27, no. 1, pp. 33–42, Jan. 2001.

[101] B. A. Rabkin, V. Zderic, and S. Vaezy, “Hyperecho in ultrasound images of HIFU therapy: Involvement of cavitation,” *Ultrasound Med. Biol.*, vol. 31, no. 7, pp. 947–956, Jul. 2005.

[102] T. Yu and C. Xu, “Hyperecho as the Indicator of Tissue Necrosis During Microbubble-Assisted High Intensity Focused Ultrasound: Sensitivity, Specificity and Predictive Value,” *Ultrasound Med. Biol.*, vol. 34, no. 8, pp. 1343–1347, Aug. 2008.

[103] M. Gyöngy and C.-C. Coussios, “Passive cavitation mapping for localization and tracking of bubble dynamics,” *J. Acoust. Soc. Am.*, vol. 128, no. 4, pp. EL175-EL180, Oct. 2010.
[104] C. C. Coussios, M. Gyongy, M. Arora, and R. A. Roy, “Mapping and characterization of cavitation activity,” EP2349483 A1, 03-Aug-2011.
[105] K. J. Haworth *et al.*, “Passive imaging with pulsed ultrasound insonations,” *J. Acoust. Soc. Am.*, vol. 132, no. 1, pp. 544–553, Jul. 2012.
[106] M. Fink, “Time reversal of ultrasonic fields. I. Basic principles,” *IEEE Trans. Ultrason. Ferroelectr. Freq. Control*, vol. 39, no. 5, pp. 555–566, Sep. 1992.
[107] S. Kim, W. A. Kuperman, W. S. Hodgkiss, H. C. Song, G. F. Edelmann, and T. Akal, “Robust time reversal focusing in the ocean,” *J. Acoust. Soc. Am.*, vol. 114, no. 1, pp. 145–157, Jul. 2003.
[108] A. Derode, A. Tourin, J. de Rosny, M. Tanter, S. Yon, and M. Fink, “Taking advantage of multiple scattering to communicate with time-reversal antennas,” *Phys. Rev. Lett.*, vol. 90, no. 1, p. 014301, Jan. 2003.
[109] M. Fink, G. Montaldo, and M. Tanter, “Time-Reversal Acoustics in Biomedical Engineering,” *Annu. Rev. Biomed. Eng.*, vol. 5, no. 1, pp. 465–497, 2003.
[110] J.-F. Aubry and M. Tanter, “MR-Guided Transcranial Focused Ultrasound,” in *Therapeutic Ultrasound*, Springer, Cham, 2016, pp. 97–111.
[111] N. Chakroun, M. A. Fink, and F. Wu, “Time reversal processing in ultrasonic nondestructive testing,” *IEEE Trans. Ultrason. Ferroelectr. Freq. Control*, vol. 42, no. 6, pp. 1087–1098, Nov. 1995.
[112] M. Pernot, G. Montaldo, M. Tanter, and M. Fink, “‘Ultrasonic stars’ for time-reversal focusing using induced cavitation bubbles,” *Appl. Phys. Lett.*, vol. 88, no. 3, p. 034102, Jan. 2006.
[113] J. L. Thomas, F. Wu, and M. Fink, “Time reversal focusing applied to lithotripsy,” *Ultrason. Imaging*, vol. 18, no. 2, pp. 106–121, Apr. 1996.
[114] J. Gâteau, L. Marsac, M. Pernot, J.-F. Aubry, M. Tanter, and M. Fink, “Transcranial ultrasonic therapy based on time reversal of acoustically induced cavitation bubble signature,” *IEEE Trans. Biomed. Eng.*, vol. 57, no. 1, pp. 134–144, Jan. 2010.
[115] L. Marsac *et al.*, “Ex vivo optimisation of a heterogeneous speed of sound model of the human skull for non-invasive transcranial focused ultrasound at 1 MHz,” *Int. J. Hyperthermia*, vol. 33, no. 6, pp. 635–645, Aug. 2017.
[116] C. Prada, F. Wu, and M. Fink, “The iterative time reversal mirror: A solution to self-focusing in the pulse echo mode,” *J. Acoust. Soc. Am.*, vol. 90, no. 2, pp. 1119–1129, Aug. 1991.
[117] M. Fink and C. Prada, “Acoustic time-reversal mirrors,” *Inverse Probl.*, vol. 17, no. 1, p. R1, Feb. 2001.
[118] M. Fink, “Time-Reversed Acoustics,” *Scientific American*, pp. 91–97, 1999.
[119] B. E. Treeby and B. T. Cox, “k-Wave: MATLAB toolbox for the simulation and reconstruction of photoacoustic wave fields,” *J. Biomed. Opt.*, vol. 15, no. 2, pp. 021314-021314-12, 2010.
[120] M. Gyongy and C.-C. Coussios, “Passive Spatial Mapping of Inertial Cavitation During HIFU Exposure,” *IEEE Trans. Biomed. Eng.*, vol. 57, no. 1, pp. 48–56, Jan. 2010.
[121] S. J. Norton and I. J. Won, “Time exposure acoustics,” *IEEE Trans. Geosci. Remote Sens.*, vol. 38, no. 3, pp. 1337–1343, May 2000.
[122] C. Coviello *et al.*, “Passive acoustic mapping utilizing optimal beamforming in ultrasound therapy monitoring,” *J. Acoust. Soc. Am.*, vol. 137, no. 5, pp. 2573–2585, May 2015.
[123] J. Camacho, M. Parrilla, and C. Fritsch, “Phase Coherence Imaging,” *IEEE Trans. Ultrason. Ferroelectr. Freq. Control*, vol. 56, no. 5, pp. 958–974, May 2009.
[124] P. Tortoli, L. Bassi, E. Boni, A. Dallai, F. Guidi, and S. Ricci, “ULA-OP: an advanced open platform for ultrasound research,” *IEEE Trans. Ultrason. Ferroelectr. Freq. Control*, vol. 56, no. 10, pp. 2207–2216, Oct. 2009.
[125] M. R. Bailey *et al.*, “Use of overpressure to assess the role of bubbles in focused ultrasound lesion shape in vitro,” *Ultrasound Med. Biol.*, vol. 27, no. 5, pp. 695–708, May 2001.
[126] M. Gyöngy and C. M. Coviello, “Passive cavitation mapping with temporal sparsity constraint,” *J. Acoust. Soc. Am.*, vol. 130, no. 5, pp. 3489–3497, Nov. 2011.

[127] S. Lu, A. Shi, B. Jing, X. Du, and M. Wan, “Real-time monitoring of controllable cavitation erosion in a vessel phantom with passive acoustic mapping,” *Ultrason. Sonochem.*, vol. 39, pp. 291–300, Nov. 2017.

[128] J. J. Kwan *et al.*, “Ultrasound-Propelled Nanocups for Drug Delivery,” *Small*, vol. 11, no. 39, pp. 5305–5314, Oct. 2015.

[129] J. A. Jensen *et al.*, “SARUS: A Synthetic Aperture Real-time Ultrasound System,” *IEEE Trans. Ultrason. Ferroelectr. Freq. Control*, vol. 60, no. 9, pp. 1838–1852, Sep. 2013.

[130] L. Petrusca *et al.*, “A New High Channels Density Ultrasound Platform for Advanced 4D Cardiac Imaging,” in *2017 IEEE International Ultrasonics Symposium (IUS)*, 2017.

[131] E. Roux, A. Ramalli, M. C. Robini, H. Liebgott, C. Cachard, and P. Tortoli, “Spiral array inspired multi-depth cost function for 2D sparse array optimization,” in *Ultrasonics Symposium (IUS), 2015 IEEE International*, Taipei, Taiwan, 2015.

[132] E. Roux, A. Ramalli, P. Tortoli, C. Cachard, M. C. Robini, and H. Liebgott, “2-D Ultrasound Sparse Arrays Multidepth Radiation Optimization Using Simulated Annealing and Spiral-Array Inspired Energy Functions,” *IEEE Trans. Ultrason. Ferroelectr. Freq. Control*, vol. 63, no. 12, pp. 2138–2149, Dec. 2016.

[133] E. Roux, A. Ramalli, H. Liebgott, C. Cachard, M. C. Robini, and P. Tortoli, “Wideband 2-D Array Design Optimization With Fabrication Constraints for 3-D US Imaging,” *IEEE Trans. Ultrason. Ferroelectr. Freq. Control*, vol. 64, no. 1, pp. 108–125, Jan. 2017.

[134] E. Boni *et al.*, “ULA-OP 256: A 256-Channel Open Scanner for Development and Real-Time Implementation of New Ultrasound Methods,” *IEEE Trans. Ultrason. Ferroelectr. Freq. Control*, vol. 63, no. 10, pp. 1488–1495, Oct. 2016.

[135] E. Lyka, C. Coviello, R. Kozick, and C.-C. Coussios, “Sum-of-harmonics method for improved narrowband and broadband signal quantification during passive monitoring of ultrasound therapies,” *J. Acoust. Soc. Am.*, vol. 140, no. 1, p. 741, Jul. 2016.

[136] C. Arvanitis, N. McDannold, and G. Clement, “Fast passive cavitation mapping with angular spectrum approach,” *J. Acoust. Soc. Am.*, vol. 138, no. 3, pp. 1845–1845, Sep. 2015.

[137] C. D. Arvanitis, C. Crake, N. McDannold, and G. T. Clement, “Passive Acoustic Mapping with the Angular Spectrum Method,” *IEEE Trans. Med. Imaging*, vol. 36, no. 4, pp. 983–993, Apr. 2017.

[138] J. Gateau, J.-F. Aubry, M. Pernot, M. Fink, and M. Tanter, “Combined passive detection and ultrafast active imaging of cavitation events induced by short pulses of high-intensity ultrasound,” *IEEE Trans. Ultrason. Ferroelectr. Freq. Control*, vol. 58, no. 3, pp. 517–532, Mar. 2011.

Ultrasound imaging of the ultrasound thrombolysis

Ultrasound therapy techniques emerged very recently with the use of high intensity focused ultrasound (HIFU) technology. Extracorporeal ultrasound thrombolysis is one of these promising innovative low-invasive treatment based on the mechanical destruction of thrombus caused by acoustic cavitation mechanisms. It is a poorly controlled phenomenon and therefore a better control of cavitation activity during the ultrasonic treatment and especially its localization during the therapy is an essential approach to consider the development of a therapeutic device. A prototype has already been designed and improved with a real-time feedback loop in order to control the cavitation power activity. However, to monitor the treatment in real-time, an ultrasound imaging system needs to be incorporated into the therapeutic device. It should spot the blood clot, position the focal point of the therapy transducer, track the destruction of the thrombus, and evaluate in real-time the cavitation activity. Present work focusses mainly on the development of passive ultrasound techniques used to reconstruct a cavitation activity map. Different beamforming algorithms were investigated and validated through point source simulations, experiments on a wire and cavitation in a water tank. It was demonstrated that among many beamforming algorithms tested the most accurate for focal cavitation point localization is the passive acoustic mapping weighted with the phase coherence factor (PAM-PCF). Additionally, *in vivo* testing on an animal model of acute limb ischemia was assessed. Finally, some optimizations of the previous developed imaging system were carried out as 3D imaging, real-time implementation, and hybrid imaging combining active anatomical images with passive cavitation maps.

Imagerie ultrasonore de la thrombolyse ultrasonore

Les techniques de thérapie par ultrasons sont apparues très récemment avec l'usage des ultrasons de haute intensité focalisée. La thrombolyse ultrasonore extracorporelle en fait partie et se base sur la destruction mécanique du thrombus causée par la cavitation acoustique. C'est un phénomène mal contrôlé et ainsi un meilleur contrôle de l'activité de cavitation et sa localisation pendant la thérapie est essentiel pour considérer le développement d'un dispositif thérapeutique. Un prototype a déjà été conçu et amélioré avec une boucle de rétroaction en temps réel afin de contrôler l'activité de puissance de cavitation. Cependant, pour surveiller le traitement en temps réel, un système d'imagerie ultrasonore doit être incorporé dans le dispositif thérapeutique. Il doit localiser le thrombus, positionner la focale du transducteur thérapeutique, suivre la destruction du thrombus, et évaluer en temps réel l'activité de cavitation. Le travail actuel se focalise principalement sur le développement de techniques d'imagerie ultrasonore passive utilisées pour reconstituer la cartographie d'activité de cavitation. Différents algorithmes de formation de voies ont été examinés et validés par des simulations de sources ponctuelles, des expériences sur fil et de cavitation dans une cuve d'eau. Il a été démontré que parmi plusieurs algorithmes de formation de voie testés le plus précis pour la localisation du point focale de cavitation est la technique de cartographie passive acoustique pondérée avec le facteur de cohérence de phase (PAM-PCF). En outre, des tests *in vivo* sur un modèle animal d'ischémie des membres aigus ont été évalués. Enfin, certaines optimisations du système d'imagerie développé précédemment ont été réalisées comme l'imagerie 3D, l'implémentation en temps réel et l'imagerie hybride combinant l'imagerie active anatomique avec les cartographies de cavitation passive.